

Hydrogen Supply-Chain Optimisation

Wind-Based Hydrogen Supply Chain Optimisation For Non-Stationary Storage Applications In An Early Market Development Stage

M.M. Kooter



Hydrogen Supply-Chain Optimisation

Wind-Based Hydrogen Supply Chain Optimisation For Non-Stationary Storage Applications In An Early Market Development Stage

by

M.M. Kooter

In fulfilment of the requirements for the degree of
Master of science Sustainable Energy Technology
at the Delft University of Technology.

To be defended publicly on Mar 24th, 2021.

Student number:	4443020	
Project duration:	May, 2021 – March, 2022	
Thesis committee:	Prof. dr. ir. A. (Ad) Van Wijk,	TU Delft, chairman
	Prof. dr. ir. Z. (Zofia) Lukszo,	TU Delft, 1st supervisor
	Dr. ir. M. B. (Michiel) Zaaijer,	TU Delft, 2nd supervisor
External coach:	Ir. H. (Hugo) Groenemans	HYGRO

This thesis report is confidential



Preface

This Thesis completes my Master of Science in Sustainable Energy Technology at the University in Delft. Starting the final part of my Master degree on the topic of a hydrogen refuelling infrastructure for the mobility sector. Mapping the optimal value chain design from well to tank and future demand for a yet to be developed market, while simultaneously optimising the production process, hydrogen distribution and thereby determining the optimal storage units to be used. Together with the decision to develop a model with an for me, unused modelling technique has created a challenging but motivating journey for past few months. Therefore, I want to thank my graduation committee: Ad van Wijk, Zofia Lukzso and Michiel Zaaijer for their support and reflecting upon my progress with their expertise in separate stages of my research.

I would like to thank Hugo Groenemans, for providing me with the time to perform my independent research while reflecting on the progress in our weekly meetings, and talk together extensively on interesting observations made along the journey. While also guiding me in personal development conducting this research project. Additionally, I want to thank all the colleagues at HYGRO for being able to provide me with all the answers to my questions and showing me the world of a developing hydrogen market and the challenges that come with.

*M.M. Kooter
The Hague, March 2022*

Summary

Implementing green alternatives in the heavy-duty mobility market is required to reach the set climate goals and decrease greenhouse gas emissions. As of 2021, heavy-duty vehicles contribute significantly to the overall emissions of the road transport sector and have a negligible number of emission-free vehicles on the road. Refuelling infrastructures based on alternative fuels such as hydrogen are not sufficiently available, which pose a barrier for large scale implementation and investment in new emission-free heavy-duty fuel cell vehicles.

This Master Thesis project aims to design, describe and review a future hydrogen value chain based on the levelised cost of hydrogen (LCOH) from well-to-tank, considering a refuelling infrastructure for the heavy-duty vehicle market. Non-stationary storage units are considered to transport and provide on-site storage for the hydrogen value chain infrastructure. An optimisation model focused on the operational decision-making level is proposed to answer the main research question:

”What impact does the type of non-stationary storage unit have on the levelised cost of hydrogen in the wind dominated hydrogen value chain?”

A Mixed Integer Linear Programming (MILP) optimisation model has been adopted to simulate a small scale hydrogen value chain dominated by hydrogen production directly from wind energy at the wind turbine location. Early market value chain configurations and low refuelling station demand levels are researched and evaluated. Additionally, a method to define future demand for two separate end-user categories at a hydrogen refuelling station is proposed. The spatial configuration of the researched infrastructure is based on a ”Hub” and ”Satellite” concept with distributed production locations. Five main scenarios are considered with different spatial configurations and demand levels that give insight into the gradual LCOH development of a hydrogen refuelling infrastructure. Input parameters are varied in a scenario analyse and sensitivity analyses to determine their relative impact on the total LCOH.

The results show that distribution of hydrogen is cost-optimal for implementing large 20ft Multi-Element-Gas-Containers despite the lower distribution efficiency and extra storage capacity required to ensure distribution flexibility compared to small High-Pressure-Swappable-Containers.

With the current market pricing of all value chain components, cost parity with diesel fuel is reached if the total production capacity of the value chain is utilised. Future cost development will result in a lower total cost for hydrogen per kg than the diesel fuel equivalent. The hydrogen refuelling infrastructure based on wind energy is resilient against increased energy price fluctuations by an expected increase in installed capacity of renewable energy sources.

It can be concluded that the operational decision-making process regarding the hydrogen production process is generally independent of the distribution system size and spatial configuration, and type of non-stationary storage container. Four parameters that define the most cost-optimal hydrogen production process s the ratio between the turbine power capacity, grid connection capacity, electrolyser production capacity and average hydrogen demand within a specified time frame.

This research only considers an optimisation model based on the total cost of hydrogen production, distribution and storage. Other objectives should be taken into account in future research, such as reliability, safety, or environmental objectives. Grid interaction on different energy markets can be explored and possibly reduce the total production cost of hydrogen while providing balancing services to the local power grid. Additionally, separate markets for the non-stationary storage units should be evaluated.

Contents

Summary	v
Abbreviations	ix
1 Introduction	1
1.1 Wind Dominated Green Hydrogen Refuelling Infrastructure	2
1.2 Research Methodology	5
1.3 Research Problem	6
1.4 Research questions	6
1.5 Thesis outline	7
2 Hydrogen Supply chain System Design	9
2.1 Wind Energy	10
2.2 Grid Connection	18
2.3 Hydrogen Production	20
2.4 Hydrogen Compression	30
2.5 Hydrogen Transport/Storage	38
2.6 Hydrogen Refuelling Station	46
2.7 Hydrogen Demand	50
3 Case Study The Netherlands	55
3.1 Wind energy	55
3.2 Grid Connection	66
3.3 PEM Electrolyser	69
3.4 Compressor	74
3.5 Distribution Network and Storage	75
3.6 Hydrogen Refuelling Station	82
3.7 Demand Model	85
4 Optimisation Model	91
4.1 Modelling Approach	91
4.2 Objective Function	92
4.3 Hydrogen Production	92
4.4 Hydrogen Storage	94
4.5 Hydrogen Transportation	97
4.6 Total Cost Function	100
4.7 LCOH Cost Function	102
4.8 Parameter Overview	103
5 Results	107
5.1 Optimisation Scenarios	107
5.2 Main Scenario Results	109
5.3 Scenario Analysis	118
5.4 Sensitivity analysis	125
6 Discussion	131
6.1 Hydrogen Production	131
6.2 Hydrogen Storage	132
6.3 Hydrogen Distribution	133
6.4 Model Limitations	134
6.5 Uncertainty	134
6.6 Multi-Objective Optimisation	135

7 Conclusion	137
8 Recommendations	139
Bibliography	141
A Appendix: Balance OF Plants PEM Elctrolyser	153
B Appendix: Model Overview	163
B.1 Objective function163
B.2 Constraints163
B.3 Total Cost Function166
C Appendix: Correltations Matrices	167
D Appendix: Detailed Cost Overview Base Scenarios	169

Abbreviations

AC	Alternating Current
ADR	Agreement on international transport of Dangerous goods by Road
AEL	Alkaline Electrolyser
BEV	Battery Electric Vehicle
BOP	Balance of Plants
CAPEX	Capital Expenditure
CCUS	Carbon Capture, Use and Storage
CFD	Computational Fluid Dynamics
CG	Coal Gassification
CI	Compression Ignition
COP	Coefficient Of Performance
DC	Direct Current
DECOM	Decommissioning Cost
DFV	Dual-Fuel Vehicle
DSO	Distribtuon System Operator
FCEV	Fuel Cell Electric Vehicle
FCET	Fuel Cell Electric Truck
GHG	Greenhouse gas
GDL	Gas Diffusion Layer
HSC	Hydrogen Supply Chain
HDV	Heavy-Duty Vehicle
HHV	Higher Heating Value
HPSC	High Pressure Swappable Container
IEC	International Electrotechnical Commission
KPI	Key Performance Indicator
KNMI	Koninklijk Nederlands Meteorologisch Instituut
LCOE	Levilised Cost Of Electricity
LHV	Lower Heating Value
LH2	Liquid Hydrogen
LCOH	Levilised Cost of Hydrogen
LOHC	Liquid Organic Hydrogen Carrier
MEGC	Multi-Element Gas Container
MCP	Market Clearing Price
MEA	Membrane Electrode Assembly
MILP	Mixed Integer Linear Programming
NHN	Noord Holland Noord
OPEX	Operational Expenditure
O&M	Operation & Management
PPA	Power Purchase Agreement
PEM	Proton Exchange Membrane
SAE	Society Automotive Engineers
SC	Supply Chain
SI	Spark Ignition
SMR	Steam Methane Reforming
SOC	State Of Charge
SOE	Solid Oxide Electrolyser
SSE	Sum Squared Error
TPED	Transport Pressure Equipment Directive
TSO	Transmission System Operator
TTW	Tank-To-Wheel
WACC	Weighted Average Cost of Capital
WTT	Well-To-Tank

Introduction

With the introduction of renewable energy sources, the energy sector's greenhouse gas (GHG) emissions have decreased significantly. GHG reduction in the energy sector has led to an overall decrease in GHG on the European continent. However, it does not resemble the increase of GHG emissions of the mobility sector. The CO₂ emissions have increased from 5.8 Gigaton to 8.2 Gigaton from 2000 up into 2020 (Teter et al., 2020). To become fully net-zero by 2050 (EU Commission, 2018) and comply with the European Union emission reduction goals, the biggest challenge for emission reduction lies in the mobility sector. The mobility and transport sector can be divided into road transportation, maritime, inland waterways, rail, and aviation. Road transportation is the most significant contributor to overall GHG emissions. The road transport sector contributes 21% towards the total GHG emissions in the European Union (EEA, 2017). The significant contribution to GHG emissions is due to fossil-based fuels, and accordingly, greener alternatives must be used.

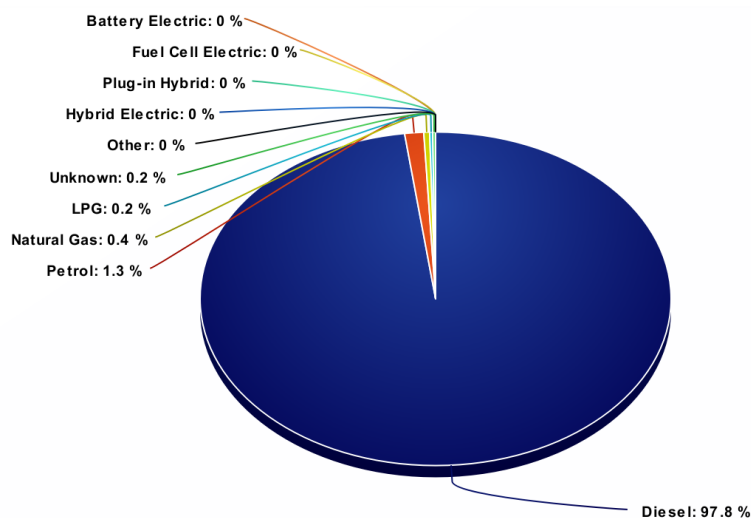


Figure 1.1: Medium and heavy duty commercial vehicles in use by fuel type, as of January 2021 (ACEA, 2021)

Renewable energy sources such as wind, solar, geothermal and biomass can supply the energy for alternative fuels. The problem arising with these types of energy production methods is the energy carrier. Fossil fuel-based road vehicles cannot use the energy carrier produced by renewable energy sources as they rely on the Internal Combustion Engine (ICE). Therefore other drivetrain technologies must be considered to help the transition to green alternatives and reduce the CHG emissions in the mobility sector.

The Battery Electric Vehicle (BEV) and the Fuel Cell Electric Vehicle (FCEV) have introduced new drivetrain technologies and opened up a market to incorporate non-fossil-based energy sources in the

mobility sector. A well-to-wheel energy analysis has shown that the FCEV with hydrogen produced by steam methane reforming has a decrease in overall energy use between 5%-35% and a GHG emission reduction of 15%-45% (Liu et al., 2020). With renewable energy sources, the percentage of GHG reduction will increase to almost 100%. However, only 3.5% of all registered vehicles in Europe are electrified (EEA, 2020), and a negligible percentage of vehicles are based on other alternative fuels. Focussing only on heavy-duty transport vehicles, almost all vehicles are fossil-fuel-based as can be seen in Figure 1.1.

According to Offer et al. (2010), the most critical barriers to the implementation of greener alternatives can be categorised by technical, economic and infrastructural barriers. The technical barrier for a BEV is the low-energy density of batteries. Compared to current fossil-based technologies, a large, heavy and expensive battery will be required to achieve equal travel distance before charging. The large battery capacity is especially required for the transportation of goods and is therefore unsuitable for such applications. The chemical energy density of hydrogen mitigates the low-energy density of the battery. However, on the contrary, hydrogen has a very low volumetric density. This results in bulky hydrogen storage tanks, which must provide storage under high pressure than fossil fuel-based tanks.

Handwerker et al. (2021) mentions that the integration of charging stations for BEVs could pose another challenge at putting strain on the electricity grid's capacity if all vehicles would become BEVs. Long-distance travelling and fast charging required by the heavy-duty vehicle industry is a significant barrier to implementing battery-electric drivetrains and poses a critical disadvantage. As of 2021, a limited amount of heavy-duty vehicles based on a battery-electric drivetrain are commercially available (van Sloten et al., 2020). Adequate distribution of different drivetrain technologies is required to reduce infrastructure barriers. Other alternatives such as hydrogen-powered vehicles could pose the solution.

Marcinkoski et al. (2016a) has researched the suitability of converting a representative sample of medium and heavy-duty vehicles into FCEVs. Truck performance based on range, payload, acceleration, speed, gradability and fuel economy were considered. The research concluded that no significant technological barriers on the drivetrain side exist to achieve the same performance characteristics of conventional fossil-fuel-based heavy-duty vehicles. Therefore, if the economic and infrastructural barriers are minimised, the heavy-duty mobility sector will heavily implement FCEVs due to the use characteristics of long-distance travelling and the need for short refuelling times. Hydrogen can, therefore, provide an alternative and contribute to the decarbonisation of the entire mobility sector.

Handwerker et al. (2021) notes that the most notable downside for hydrogen is the absence of the refuelling infrastructure. It must be presented as an attractive alternative for a fast implementation of hydrogen as a fuel in the mobility sector. The two main barriers for hydrogen to be adopted and widely used as an alternative fuel source in the heavy-duty mobility sector is the cost of the hydrogen fuel compared to current fossil fuels and the lack of infrastructure not able to provide sufficient hydrogen refuelling stations, consequently with inadequate coverage for long-distance travelling. The question arises, how to supply the rising demand for heavy-duty hydrogen vehicles cost-competitively?

1.1. Wind Dominated Green Hydrogen Refuelling Infrastructure

This master thesis will focus on the rollout of a hydrogen refuelling infrastructure in an early market development stage. The entire hydrogen value chain is treated from Well-To-Tank (WTT). The infrastructure considered is focused on supplying hydrogen to heavy-duty vehicle categories, which are expected to be large consumers of hydrogen fuel. A distinction is made between two technologies that adopt hydrogen to propel vehicles.

Providing a cost-competitive green alternative is the biggest challenge for an early-stage rollout of the hydrogen refuelling infrastructure. According to Glenk & Reichelstein (2019), the production of hydrogen from a renewable energy source can be cost-competitive in the upcoming years Due to the sharp decrease in renewable energy generation costs, positively influencing the business case. In this research, the primary source of energy for hydrogen production is considered to be wind energy.

The development of complete refuelling infrastructure, primarily based on renewable energy sources, requires significant capital investments without the guarantee of success. Therefore across the value chain, the costs regarding each section will be identified individually.

Consequently, the cost regarding each section of the value chain will be used as a lead decision parameter to define the technological layout and design of the hydrogen value chain. The aim is to provide insights into a detailed cost structure of a wind dominated hydrogen value chain. A simplified diagram of the value chain considered is shown in Figure 1.2

An approach adopted in this research is the distinction between two end-user categories of hydrogen fuel at the refuelling station. Heavy-duty vehicles adopting dual-fuel technology is the first end-user category considered utilising hydrogen. Dual-fuel technology uses an injection of alternative clean fuel in the internal combustion engine and contributes towards an overall emission reduction. Dual-fuel technology has encountered several problems in spark ignition (SI) engines. However, compression ignition (CI) engines, mostly known as the diesel engine, it has shown promising results as the efficiency of the engine increases with 5.3% at 55% engine load, in the case of hydrogen addition (Cernat et al., 2020). Hydrogen cannot solely be used as fuel in a CI engine, as the temperature due to compression is not high enough to overcome the activation barrier and initiate combustion. An ignition source is required. Diesel will contribute as the primary fuel and ignition source for hydrogen. A significant part of the energy is taken from the combustion of diesel, and the rest is provided by green hydrogen (Saravanan et al., 2008).

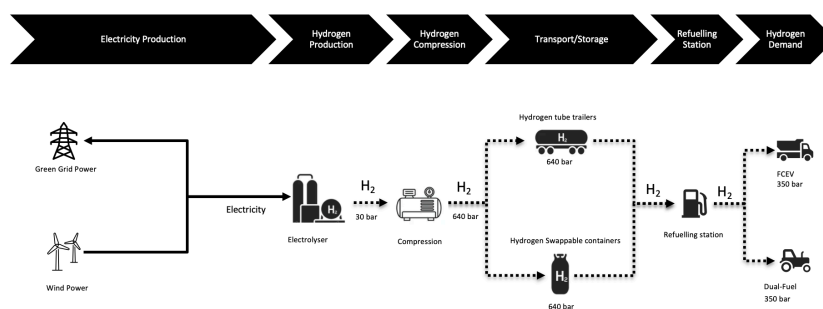


Figure 1.2: Overview value chain considered in this research

The Dual-Fuel Vehicle (DFV) is a solution that can directly be implemented into the mobility industry without relying on a constant hydrogen energy source. A reduction of NO_x by 75% and a 22% reduction of CO_2 emissions for the hydrogen dual fuel vehicle built by H_2 Dual Power (H2DualPower, 2021) shows a good starting point for early-stage development of alternative fuels such as hydrogen. Integrating hydrogen with current fossil fuels could help start an infrastructure based on green alternatives.

The second end-user category considered is the Fuel Cell Electric Truck (FCET). The FCET utilises a Proton Exchange Membrane (PEM) fuel cell to electrochemically convert hydrogen into electric power, which drives an electric motor to provide momentum to the vehicle.

The value chain considered in this research includes a grid connection. The grid connection would overcome the need for long-term storage and provide power to the electrolyser at reduced wind speeds. However, it would also negatively influence the cost of hydrogen as power must be purchased at a premium from the grid. Therefore the main question arises how the interaction of the grid connection and the energy production by the wind turbine would influence the value chain's strategic design choices and operational decision-making and if considering a grid connection would lead to better results.

Hydrogen is in a gaseous state at atmospheric pressure and standard room temperature (293K). However, it must be converted by either compression, liquefaction, or liquid organic hydrogen carriers (LOHC) to have economic, efficient transportation or storage of hydrogen. LOHC utilises a two-step

cycle: (i) the hydrogenation of the organic carrier to store hydrogen in the liquid and (ii) the dehydrogenation when the hydrogen is retrieved from the carrier liquid. Both processes involve the covalently bounding and release of hydrogen from the liquid carrier fluid (Niermann et al., 2019). Advantages of LOHC are the ambient state and properties of the hydrogen carrier that result in the ability for long-term storage. The LOHC has similar properties as oil and can therefore be stored in similar manners and use existing infrastructures. The downside of LOHC is the high energy-intensive process of dehydrogenation, as this process is endothermic. Hurskainen & Ihonen (2020) has compared the LOHC against compressed hydrogen transportation by truck and concluded that greater hydrogen demands and significantly longer transportation distances were shown to favour the LOHC concept over compressed gas. The cost of the LOHC system is mainly based on processing cost, while the compressed hydrogen delivery method is the distribution cost. Subsequently, for short-distance early development refuelling infrastructure studied in this thesis, LOHC is not a suitable transportation or storage method.

Liquifying hydrogen is first done by compression, expansion and throttling processes (Peschka, 2012; Ratnakar et al., 2021; Scott et al., 2013). Liquid hydrogen boils at 20.4K at atmospheric pressure with a critical temperature of 30.2 K and 12.97 bar (Ratnakar et al., 2020). The advantage for liquid hydrogen in transport is the high density in which LH2 can be transported. LH2 trucks are capable of carrying up to 4 times more H₂ compared to compressed hydrogen when considering weight (He et al., 2021). The high-capacity trucks and shorter transfer times reduce delivery costs per hydrogen unit. A second advantage is a high throughput at low dispensing cost (Petitpas et al., 2018). The biggest challenge is the high energy-intensive liquefaction process and the boil-off rate of the liquid hydrogen, which results in significant losses across the entire supply chain (Ratnakar et al., 2021).

Stöckl et al. (2020) modelled a green hydrogen refuelling supply chain based on renewable energy and concluded that liquid hydrogen tends to have the highest share in the optimal solution for large-scale refuelling infrastructures. As Li et al. (2020) performed a cost analysis on light and heavy-duty FCEVs and stated that there is a trade-off present based on the choice of liquified hydrogen transportation and compressed hydrogen transportation. For smaller distances, the higher transportation cost due to the lower truck capacity results in more trips outweighs the cost for hydrogen liquefaction. Reuß et al. (2019) concluded that distribution of hydrogen regarding low penetration of fuel cell vehicles should be supplied by compressed hydrogen tube trailers. Therefore this research aims to get a more detailed understanding of the distribution of gaseous hydrogen, as distances in the value chain are relatively short between the considered locations in combination with low overall demand.

A centralised or decentralised storage approach can be taken, as seen in research conducted by Seo et al. (2020). Centralised storage reduced the Levelised Cost Of Hydrogen (LCOH) for the entire value chain due to the economy of scale. A different and not much-researched approach is non-stationary storage. This approach shows promising results towards decreasing the overall cost of transportation and storage. Research from He et al. (2021) has proposed a new method by combining storage and transportation and considering transportable storage vessels. According to He et al. (2021), 'The advantage of gas trucks over stationary pressure vessel storage is that it can travel and be shared across the whole HSC to provide on-demand storage service and meet spatial-temporal varying energy supply and demand'. It can make intermittent hydrogen production by the wind turbine more cost-effective, as partial truckloads with transportable storage can be distributed compared to large tube trailer systems.

A system developed by NPROXX (2021), one of the leading companies in hydrogen storage, can be seen as an example. Twenty-two swappable hydrogen units containing 53 kg each are placed on the back of a 40ft trailer and can be interchanged at the Hydrogen Refuelling Station (HRS). When regionally great demand is expected, it can be transported from the production locations and other demand sites. Considering the combination of storage and transportation as one integral part of the supply chain could pose a critical cost reduction and gain traction towards cost-competitive hydrogen at the HRS.

This research focuses on the design of a wind dominated hydrogen refuelling infrastructure located in the Netherlands, generating an understanding of the cost development of the entire value chain

for different demand scenarios regarding the end-user categories and their demand characteristics, the spatial distribution of the refuelling infrastructure, and choice on transport and storage sizing. The ability to give insight into the cost structure and to compare different scenarios, the Levelised Cost Of Hydrogen (LCOH) will be taken as the main focal point in this research from which the most optimal integral non-stationary storage technology will be chosen for hydrogen distribution.

1.2. Research Methodology

An optimisation approach is adopted to answer the research questions that arise with the design and implementation of a hydrogen refuelling infrastructure. A MILP optimisation model will be based on cost minimisation of the production and transportation costs from Well-To-Tank (WTT). The cost minimisation by the optimisation model in combination with the required investment costs provides the opportunity to create a tool that provides an insight into the total cost structure for different value chain topologies, demand situations, and transport/storage applications. Thereby aiding strategic and operational design choices for future infrastructure development projects. By adjusting cost parameters, and infrastructure design, the total cost effect on the individual cost components of the value chain can be mapped. Comparison between value chain configurations will be based on the concept of LCOH. The LCOH describes the total cost for a single kg of hydrogen up to the hydrogen fuel tank of the consumer vehicle. The LCOH will be compared to fossil fuel-based alternatives and will answer the questions of the value chain would be more cost-competitive and what components contribute the most towards the LCOH. The project Duwaal developed by HYGRO will be taken as a reference and provide the base of the hydrogen value chain considered in this research.

1.2.1. Scientific Research Gap

Research towards the hydrogen value chain and supply chain infrastructures are often researched on national-scale or large-scale projects where the focus is laid upon the choice of the hydrogen state in transport (gaseous, liquid or LOHC) and the corresponding transportation technologies. The research of Almansoori & Shah (2006) is taken as a seminal paper, whereafter most research is based on the approach taken in the paper. Thereby large-scale generalisations are made. The power production capacity of wind turbines is often assumed by yearly power production rates for entire wind turbine parks. The hydrogen demand is based on s-shaped technology development curves, where the current number of fossil-fuel-based vehicles is used to express the expected number of hydrogen vehicles.

The issue arising with this approach is an overestimation of the hydrogen demand in an early-stage market as not all vehicles are expected to use hydrogen as an alternative fuel. Also, in the early market development stage, project-based rollout strategies with a minimal number of hydrogen vehicles can be assumed as the chicken-and-egg paradox is present. The chicken-and-egg paradox in the case of the hydrogen value chain corresponds to the need for an existing refuelling infrastructure to implement many hydrogen-powered vehicles (chicken). However, an adequate demand is required to provide a positive business case for developing the hydrogen refuelling infrastructure (egg). The second problem is that the s-shaped technology development curve approach does not consider the characterisation of different types of consumers and research what impact this could have on the value chain strategic and operational decision-making processes.

As of 2022, in the early-stage development market for the hydrogen refuelling infrastructure, this nationwide generalisations and value chain configurations are not assumed realistic and do not aid strategic decision making in an early-stage developing market. Considering small projects with single wind turbines combined with several refuelling stations with limited hydrogen demand is expected to be a suitable approach. To the author's best knowledge, research towards the design and optimisation of a wind-dominated hydrogen value chain in the early-stage development market, with a particular focus on the choice of optimal non-stationary storage solutions based on a model taking into account a great detail operational decision-making process, is not yet conducted.

The contribution towards science is to provide insight into the strategic and operational decision-making processes when developing a wind dominated hydrogen value chain transporting gaseous hydrogen. Determining if modelling a small-scale value chain with a high level of detail and defining the impact of every component of the value chain can provide new insights for future research directions and policy decisions.

In conclusion, to fill in the research gap, this thesis aims to provide several value chain configurations that prove to be cost-competitive with fossil fuel-based alternatives or show significant potential to reach cost competitiveness while simultaneously providing insight into the total LCOH cost breakdown and possible future focus points of the refuelling infrastructure. First, the value chain design is determined theoretically, whereafter the research objective is provided by an overview of the most suitable value chain configurations. Assumptions and generalisations are made in several areas of the infrastructure to ensure the ability to model the complete interaction from well-to-tank of the value chain.

1.3. Research Problem

First, the value chain components will be researched theoretically, where scientific literature and expert knowledge from HYGRO will be used to identify the optimal choices regarding the value chain design and possible variations and decision parameters for the optimisation model. When the value chain configuration is established, the mathematical formulation of the optimisation model will be discussed with experts, whereafter implemented with the Python programming language using a commercial solver.

Fundamental research aspects are:

- Demand characterisation for different end-user categories
- Transport/storage alternatives
- Cost optimization modelling
- Small-scale refuelling infrastructure development
- Value chain cost performance insights

1.4. Research questions

As discussed, this research aims to model a wind dominated hydrogen value chain and create a decision support tool to determine the most optimal infrastructure rollout strategy based on the performance characteristics of non-stationary storage applications and a cost objective function that gives insight into the LCOH of the value chain.

This leads to the main research question:

- What impact does the type of non-stationary storage unit have on the levelised cost of hydrogen in the wind dominated hydrogen value chain?

To determine the correct research approach, it is essential to consider all technological and behavioural characteristics that correctly model the value chain. To answer the main research question, multiple subquestions are formulated. The sub-questions pave the way by creating a structured approach to the optimisation model and finalising a comprehensive answer to the main research question. The following subquestions are:

- What are the techno-economic characteristics of a wind dominated hydrogen value chain?
- How to define the hydrogen demand for the dual-fuel vehicles and fuel cell electric trucks?

- How to define the hydrogen value chain optimisation problem while integrating non-stationary storage, and what is the appropriate optimisation technique?
- What characterises uncertainty in each step of the value chain, and how does this affect the strategic and operational decision-making process?
- What can be recommended regarding choosing between the available non-stationary storage technologies and the spatial distribution of hydrogen refuelling stations?

1.5. Thesis outline

The research outline provides an overview of the chapters provided in this thesis. It creates a structure based on the previously mentioned sub-questions and main research question.

2. Hydrogen Supply Chain System Design

This chapter provides background information on the design and system components that need to be considered when designing a hydrogen value chain regarding a refuelling infrastructure for the mobility sector. The chapter provides an answer to subquestion one. Several technology options are examined for every section of the value chain, whereafter the optimal choice is presented. The chapter structure is based on sections of the hydrogen value chain starting at the production location, including energy production, hydrogen production, and hydrogen compression, followed by hydrogen transport with possible distribution strategies. Finally, the refuelling station is discussed with the distinction between the two end-user categories.

3. Case Study The Netherlands

A case study is presented based on the technology decisions from chapter 2. A similar chapter setup is adopted. The case study is based on the Duwaal project proposed by HYGRO, for which an additional turbine location can be added. The chapter describes the power production model created to model estimate power availability to produce hydrogen. The sizing of the distribution vehicles and available storage units are discussed, whereafter the layout of the refuelling stations are defined. Finally, a stochastic demand model is described, which provides the input for both end-user categories for the optimisation model. The demand modelling approach described in this chapter provides the answer to subquestion two.

4. Optimisation Model

This chapter describes the entire mathematical formulation of the optimisation model. The objective function of minimising the total cost of the value chain, taking into account the operational cost, where a time frame of a single year is discussed. The input parameters for the optimisation model are described by chapter 3. The optimisation model is based on a production routing problem incorporating the period and quantity of hydrogen at the production locations, hydrogen transport between several production locations and refuelling stations and Inventory balancing in the entire value chain. This chapter provides the answer to subquestions three.

5. Results

The results for several scenarios based on distribution strategies, transport/storage sizing, demand characteristics, and spatial distributions are presented. Five main scenarios are considered. The expansion of a single turbine and two refuelling stations is gradually increased to more refuelling stations up to a system with two turbines and four refuelling stations. The demand is increased with the system size to determine the cost development of the LCOH for two non-stationary storage technologies. The results show a detailed overview of the operational decision-making process based on cost minimisation. The second result presented is visualising the cost breakdown of the individual value chain components and the contribution to the total LCOH. The chapter concludes with a sensitivity analysis

for the distribution topology with the most cost-competitive results based on spatial distribution, transport technology, and total hydrogen demand. The visualisation of the value chain performance based on the stochastic demand and performance results from the sensitivity analysis will answer subquestion five.

6. Discussion

The findings from the previous chapter are summarised. Insights on the effect on the value chain performance are discussed, whereafter the limitations of the optimisation model are presented.

7. Conclusion

The final chapter answers the main research question and concludes the overall results of the hydrogen value chain considered.

8. Recommendations

This research concludes with recommendations for research towards a similar value chain design and provides recommendations for future research on this topic for other modelling approaches and research towards other target markets.

2

Hydrogen Supply chain System Design

This chapter presents the value chain configuration adopted in this research. The system design for the entire well-to-tank value chain is based on literature review, scientific publications and supported with the help of expert knowledge from HYGRO. This chapter aims to give background knowledge on each section of the value chain considered in this research and provides an answer to the first sub-question: What are the techno-economic constraints of a dominant wind-based hydrogen value chain? A dominant wind-based hydrogen value chain can be divided into multiple sections. The sections present in a dominant wind-based hydrogen value chain for the mobility market are:

- Power Source
- Hydrogen Production
- Compression
- Transportation
- Refuelling Station
- Demand

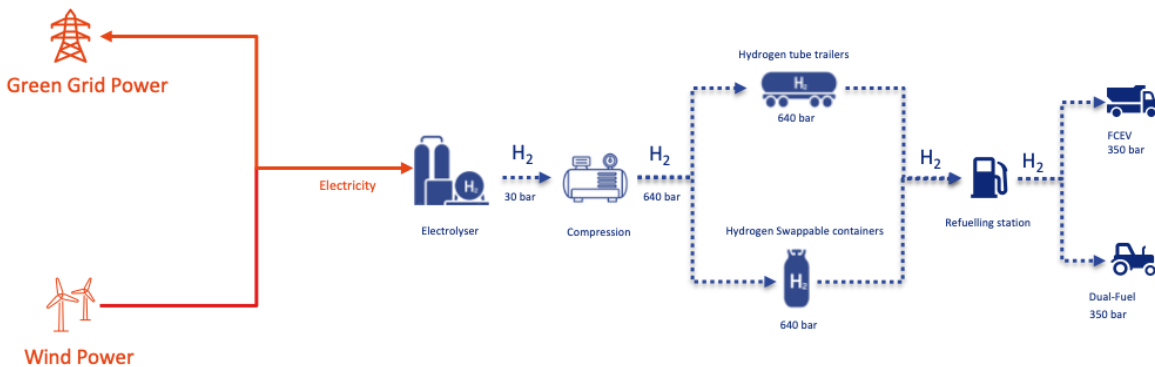


Figure 2.1: Value chain overview

For each echelon of the supply chain, the technical properties, physical configuration, impact on efficiency on the conversion processes and the cost components are examined. First, in section 2.1 the production of electricity from the onshore wind turbine is described. The interaction with the electricity grid is discussed in section 2.2. These two sections combined make up the power source for hydrogen production. In section 2.3 the different types of hydrogen production technologies are examined, the

most suitable electrolyser technology for this supply chain configuration based on the technical characteristics is determined. section 2.4 studies the compression technologies of gaseous hydrogen. ?? addresses the different transport technologies and their technological constraints. In the final stage of the well-to-tank value chain, the hydrogen refuelling station is defined in section 2.6. This chapter concludes with distinguishing between the two considered end-user applications and their demand characteristics.

2.1. Wind Energy

Harnessing energy from the wind converts the kinetic energy present in air motion to electrical energy. The first conversion process is to transform kinetic energy into mechanical energy. The second conversion step is to convert the mechanical energy into electrical energy using generators. The most widely used wind turbine technology in the commercial sector is the three-bladed horizontal-axis wind turbine (Taylor et al., 2020). In Figure 2.2 the horizontal axis wind turbine is shown. The wind turbine can be divided into two sections. The first section contains the moving parts, often referred to as the rotor-nacelle assembly. This section contains the blades, the rotor holding the blades, the drivetrain containing the generators and the gearbox to convert the mechanical energy into electrical energy. The second section of the wind turbine can be seen as the support structure of the wind turbine containing the tower and the foundation.

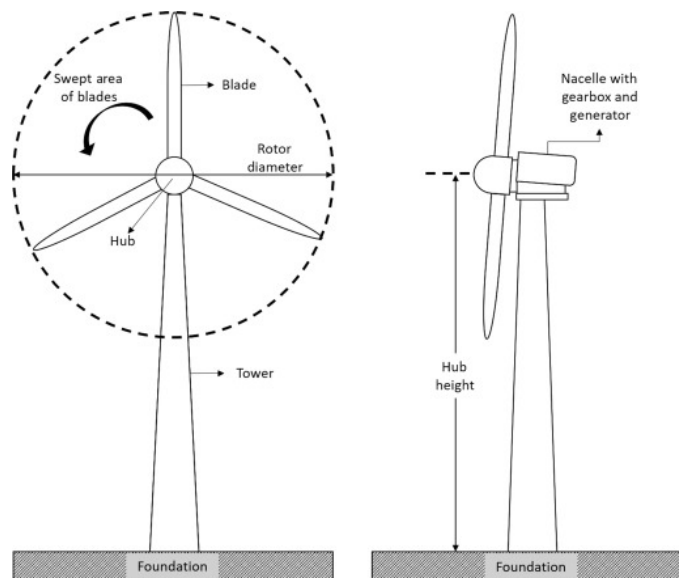


Figure 2.2: Overview horizontal axis wind turbine (Contreras Montoya et al., 2021)

The power energy conversion from the wind can be calculated with the momentum theory (Garcia-Sanz & Houppis, 2012). The number of energy particles or objects has due to their motion, through a cross-sectional area is defined by kinetic energy (E_k) and the mass flow (\dot{m}), both defined by Equation 2.1 and Equation 2.2, respectively. The amount of power through a cross-sectional area per unit of time is derived from the derivative of the kinetic energy equation and the mass flow equation into Equation 2.3. Power harnessed from the wind, as shown in Equation 2.4, is therefore proportional to the density of the air (ρ), the cross-sectional area of the rotor also referred to as the rotor swept area (A), the wind speed (U) cubed, and the power coefficient C_p . The power coefficient is the ratio between the mechanical power obtained by the wind turbine and the original energy present in the free stream flow of air (Garcia-Sanz & Houppis, 2012).

The power coefficient is limited by a theoretical limit, the Betz limit (Ackermann, 2012). The Betz limit depicts the maximal theoretical efficiency possible for converting the kinetic energy in the wind to mechanical power. The maximum theoretical efficiency is equal to $\frac{16}{27}$. More losses occur in converting kinetic energy to mechanical and electrical energy. These will be discussed in subsection 2.1.2.

$$E_k = \frac{1}{2} \rho A v^2 \quad (2.1)$$

$$\dot{m} = \rho v A \quad (2.2)$$

$$P = \frac{1}{2} \rho A v^3 \quad (2.3)$$

$$P = \frac{1}{2} \rho A U^3 C_p \quad (2.4)$$

The power curve describes the conversion from wind energy to electrical energy. The power curve shows the relationship between the output power of the wind turbine and the wind speed. Some explicit wind speeds define the transition points in the shape of the power curve. The first characteristic wind speed is the cut-in wind speed. The cut-in wind speed is the minimum wind speed required for the turbine to operate and is defined as the lowest wind speed at which power is being produced (Wright & Wood, 2004). Operating at wind speed lower than the cut-in wind speed can result in power consumption instead of power production due to all the conversion losses. The second characteristic wind speed is the cut-out wind speed. The cut-out wind speed is the wind speed at which the wind turbine stops operating due to protection against extreme mechanical stresses that can result in damage to the wind turbine (Jelavić et al., 2013). The third characteristic of wind speed is the rated wind speed. At this wind speed, the maximum conversion capacity of the generator is reached. The power output is limited and kept constant between the rated wind speed and the cut-out wind speed. Either pitch control (rotating blades along the longitudinal axis) or stall control (regulation of power output by the aerodynamic design of the turbine blades) controls the constant power (Ackermann, 2012). In between the cut-in wind speed and the rated wind speed, the power conversion process is optimised, and C_p therefore maximised (Wright & Wood, 2004). The wind turbine's power output is directly proportional to the wind speed cubed. Therefore the power curve between cut-in and rated wind speed increases with the power of three with increasing wind speed.

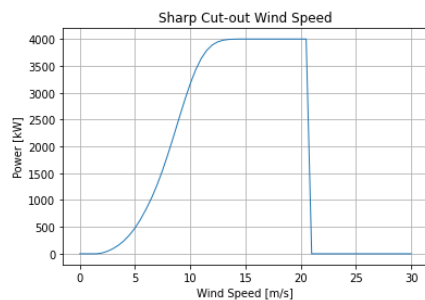


Figure 2.3: Power curve sharp cut-out wind speed Enercon E-126-EP3 4000 kW

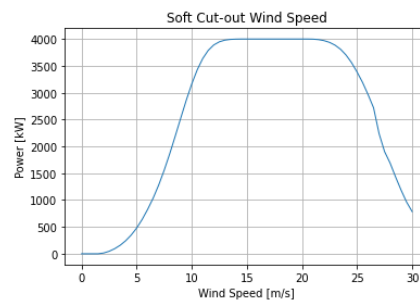


Figure 2.4: Power curve soft cut-out wind speed Enercon E-126-EP3 4000 kW

A typical power curve shows a sharp cut-out wind speed at which the turbines shuts off. Typically, this cut-out wind speed is at 25 m/s (Jelavić et al., 2013). The wind turbine requires a drop in wind speed with a couple of meters per second before the turbine is put in operation again. This is called the hysteresis loop (Ackermann, 2012). A sudden drop in power can have adverse effects on the grid connection (Jelavić et al., 2013). A different method is the use of a soft cut-out wind speed as at which the power is gradually reduced with increasing wind speed. In Figure 2.3 and Figure 2.4 both a sharp and soft-cut out wind speed is shown, respectively. A soft-cut out wind speed is preferred in a large wind park where sudden power drop of all wind turbines can result in a large power deficit in the electricity grid.

2.1.1. Power Electronic Configurations

The drivetrain and power electronics system define the backbone of the wind turbine. The choice in drivetrain configuration can significantly influence the cost and the reliability of the wind turbine (Taherian-Fard et al., 2020).

Three power electronic system designs for the conversion from wind to electricity for hydrogen production are proposed by HYGRO. The first design utilises commercially available wind turbines designed to be connected to the grid. The wind turbine is connected to the electrolyser system without any alterations to the internal power electronics system (Figure 2.5). The second phase, known as the 'Hybrid turbine', incorporates a wind turbine with alterations to the wind turbine's internal power electronics. Nonetheless, a connection to the grid is still present (Figure 2.6). The final design utilises a wind turbine that is no longer connected to the electricity grid and where the turbine design is optimised based on a minimised Levelised Cost of Hydrogen (LCOH) production instead of a minimised LCOE as in the previous two designs. This turbine is referred to as the 'Hydrogen turbine'. This research focuses on the first design and implementation of currently available wind turbines. Nonetheless, a schematic overview of all three wind turbine drivetrain designs and power electronic configurations are provided to give technical insight into the expected development and implementation of the wind turbines in the hydrogen value chain.

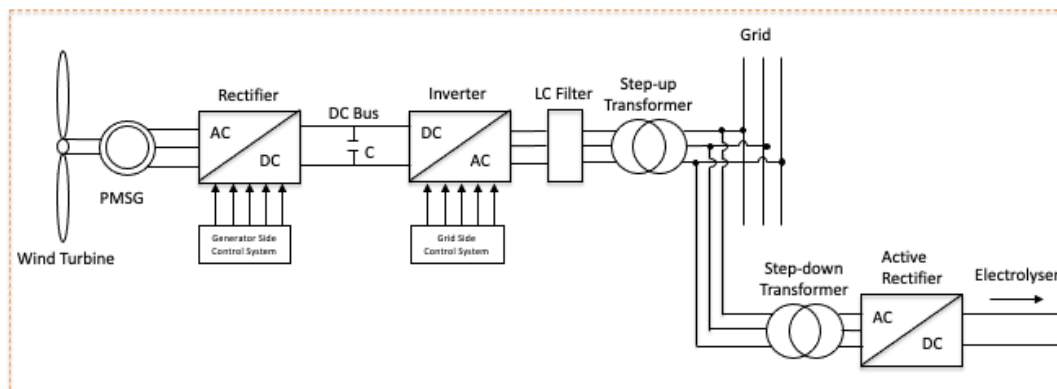


Figure 2.5: Simplified electrical line diagram commercial turbine with back-to-back converter

The first phase uses all standard components of a typical horizontal axis wind turbine. In Figure 2.5 the drivetrain power electronics of a permanent magnet direct drive turbine is pictured. The AC power generated by the generator is converted into DC power, whereafter it is converted back into AC power. This AC to DC and back to AC conversion is called a back-to-back converter process. Two sides of the conversion process are distinguished. The generator side involves the conversion from AC to DC, and the grid connection side includes the conversion from DC to AC. The generator side is used to apply torque control on the wind turbine rotational speed and vary the rotational speed to maximise power output with the use of various Maximum Power Point Tracking (MPPT) strategies (Apata & Oyedokun, 2020; Kasem Alaboudy et al., 2013). The grid side converter ensures a stable connection to the grid by regulating the current and voltage to match the grid voltage and frequency levels. The DC link provides a connection between the generator side and the grid connection side where the objective is to provide power to the grid with minimal losses (Kasem Alaboudy et al., 2013).

In the second design proposed by HYGRO, the electrolyser is directly connected to the DC link between the rectifier of the generator side and the inverter of the grid connection side. The power capacity of the converter and cables on the grid conversion side is reduced compared to the power electronics conversion capacity in the first design. The connection directly to the DC cables in the wind turbine poses a few advantages. The first advantage is fewer conversion steps between electricity production by the wind turbine and the electrolyser. Fewer conversion steps result in a lower power electronic loss factor, and therefore more hydrogen is produced with the same amount of energy harnessed by the

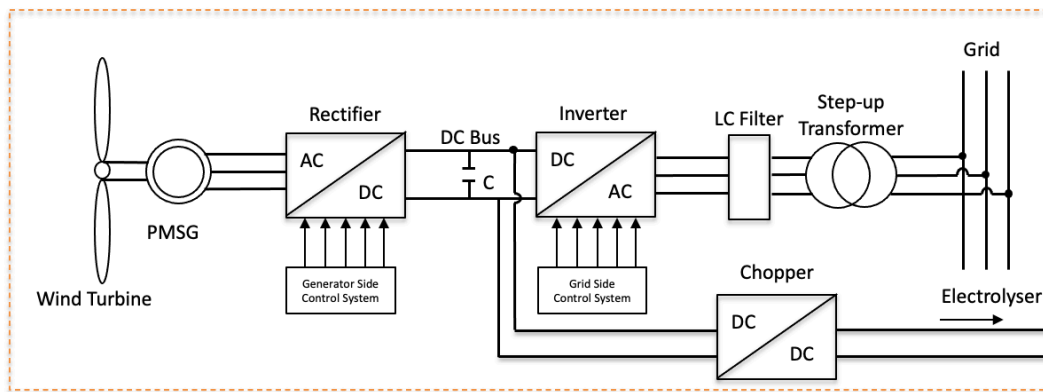


Figure 2.6: Simplified electrical line diagram hybrid turbine with back-to-back converter

wind turbine. The second advantage is the downsizing of the power electronics requirements within the wind turbine and the connection with the grid. The downsizing of electrical components results in an overall capital investment cost reduction without compromising the ability to convert wind energy into hydrogen or electricity. The third phase configuration shows no grid connection, and therefore there is no need for the DC-AC power inverter and step-up transformer to provide grid voltage levels. The electrolyser is connected to the rectifier of the generator side with a DC-DC converter. The system introduces a battery, fuel-cell, and DC-AC converter to provide essential and backup power for the operating systems and AC power for all AC powered equipment on the production site.

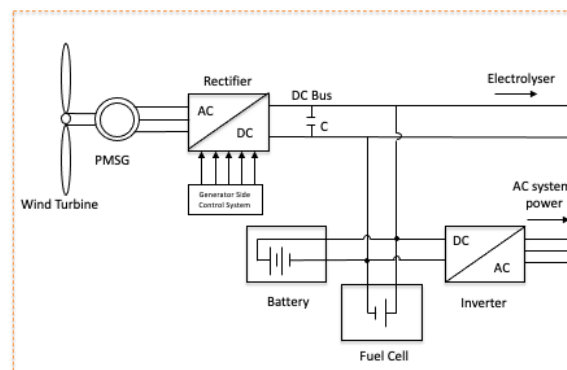


Figure 2.7: Simplified electrical line diagram hydrogen turbine

2.1.2. Wind Turbine Operation

It is of great importance to consider all the occurring losses to obtain a realistic prediction of the output power of the wind turbine. According to Ackermann (2012) these losses are described by categories:

- Drivetrain
- Turbine environment
- Maintenance & operation

The first category of losses in the power production from the wind turbine originates from cable losses and conversion steps by the installed power electronics and mechanical losses in the drivetrain. The power electronics configuration defines the amount of electrical power loss in the system. As shown, the three designs by HYGRO have different electrical configurations and, therefore, different measures of power losses. The first phase has the most conversion steps and the highest electrical

loss factor. This research only focuses on the first phase system proposed by HYGRO. The clear differences in power efficiencies of the three proposed systems will not be discussed. Mrčela et al. (2016) has shown that with a simulation model of the back-to-back power converter, LC filter and the step-up transformer with the operation of a wind turbine, an average power electronics efficiency is reached of 98% for different operating levels. A simplified analysis on the losses occurring at an onshore wind park based on different Weibull parameters has shown that electrical losses in the annual power production are in between 2% and 3% (Colmenar-Santos et al., 2014). On average total electrical losses on power production are 2%-5% annually (Ackermann, 2012; Colmenar-Santos et al., 2014; Diaz-Dorado et al., 2007)

A wind park's wake effect can be defined as the cumulative power loss of neighbouring wind turbines. The wake effect results in a loss due to fluctuation in wind speed by the interplay of the installed wind turbines. The wind speed is reduced for the downstream wind turbine due to the extraction of energy from the wind by the wind turbine placed upstream. Wake losses are one of the more significant contributors to loss in power production when considering a wind park. The annual loss of power production can range between 5% and 15% depending on the wind turbine park design and location (Ackermann, 2012). It is therefore important to consider all wind turbine locations individually to determine the total loss as this depends on many site-dependent parameters.

Wind turbines are explicitly arranged with a certain distance in the streamwise and spanwise directions to minimise the losses and maximise power production per unit area. Stevens et al. (2016) has researched the effect of different spatial configurations of wind turbine parks and their inter turbine spacings. Interestingly, a staggered layout with small inter turbine spacing resulted in the highest energy output. This energy output is due to the compensation of more turbines producing power per unit area than the energy loss caused by wake effects. However, a wind turbine park design often minimises the LCOE and does not maximise the production per unit area. Therefore, the spacing between wind turbines is often close to 5-10 times the rotor diameter (5-10D), both spanwise as streamwise direction (Meyers & Meneveau, 2012; Stevens, 2016).

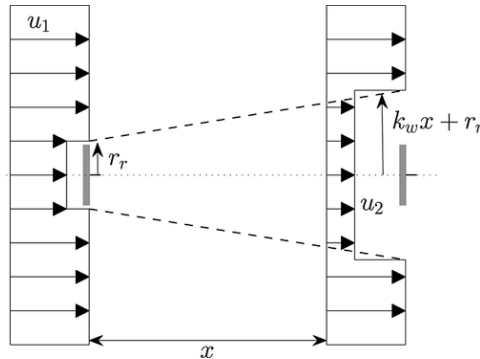


Figure 2.8: Jensen Wake model 'top-hat' velocity profile (Shakoor et al., 2016)

A distinction is made between near wake and far wake. Near wake depicts the effect on the wind speed by the wind turbine directly behind the rotor, typically up to one to five rotor diameters (Veena et al., 2020). As the wind speed gradually regains speed as one moves further downstream from the wind turbine, far wake is modelled differently. As mentioned earlier, wind turbines in a wind park are placed typically around five to ten rotor diameters apart. Therefore, only the far wake effect will be considered in this research. The Jensen far wake model was developed in 1983 (Jensen, 1983). The model has been extended and improved throughout the years to predict better the wake effect on the wind speed behind the wind turbine rotor. The model considers asymmetrical wake expansion proportional to the distance behind the rotor, taking the rotor diameter as the input for the wake model (Veena et al., 2020). A 'top-hat velocity profile is created due to the assumption of constant velocity throughout the wake in lateral and vertical directions. The simplicity of this model and the ability to calculate the reduction in wind speed behind the rotor for specific distances allows estimating wake losses to a certain extent. More extensive models are available to correctly model all parameters influencing and

determining the wake effect on the wind speed. However, these models are considered to be too complex for this research and application, increasing the computational and complexity of the wind power production model proposed in chapter 3.

The Jensen model considers that the wake symmetric expands proportionally with the flow after the turbine, where the initial wake diameter is taken as the turbine rotor diameter. The wake effect on the wind speed behind the turbine is described by the equation developed by Jensen by Equation 2.5 and Equation 2.6.

$$1 - \frac{U_w}{U} = \frac{1 - \sqrt{1 - C_t}}{(1 + 2ks)^2} \quad (2.5)$$

$$k = \frac{0.5}{\ln\left(\frac{z}{z_0}\right)} \quad (2.6)$$

In the Equation 2.5, U_w is the new wind speed due to the wake effect. U is the ambient wind speed without any influence of the wind turbine. C_t is the thrust coefficient of the wind turbine. k_w is the wake decay constant. This constant is affected by the environment around the wind turbine and describes the recovery of the wind speed and wake diameter expansion, as shown in Figure 2.8. For onshore wind parks, this parameter in most cases is set at 0.075 (Kollwitz, 2016). The wake decay constant can also be calculated with Equation 2.6, where z_0 equals the surface roughness and z the hub height of the wind turbine. The final variable in the equation s describes the dimensionless distance between the wind turbines.

When observing Equation 2.5, it is seen that for a decreasing C_t and approaching zero, the right side of the equation will also approach zero. Therefore, a decrease in trust coefficient means that the ratio between U_w and the undisturbed wind speed U goes to one. The result is that for a decreased trust coefficient, the wake effect on the wind reduces to almost negligible values. A decreased thrust coefficient is observed at higher wind speeds. The wake effect is thus most significant at lower wind speeds.

To precisely predict the losses on the power production due to the wake effect, extensive modelling of the wind turbine park is required, and a wake analysis must be conducted. To determine the effect of wake losses on the power production of a single wind turbine, as is considered in this research, a simplified method is proposed. This method is described in chapter 3 where the area around the considered wind turbine is analysed and determined if wake losses will occur due to neighbouring wind turbines. In the case of the turbine being part of a wind park, the simplified method will be validated against reported average losses due to wake from the specific wind park. Equation 2.5 will be used to determine the new wind speeds for wind directions where wake losses occur.

The third and final loss factor considered in this research is the loss in power production due to scheduled maintenance and unexpected system failure. The wind turbine cannot operate when under maintenance or a mechanical or electrical failure in the turbine has occurred. This results in a decrease in potential power produced and can have a negative effect on the operational cost of the system. Power from the grid must be supplied to be able to produce hydrogen, and in the case of a system with a limitation on-grid power availability, this can lead to the requirement of increased safety stock at the turbine or at the refuelling station, subsequently increasing the investment cost and operational cost of the value chain.

According to an extensive analysis of downtime data from multiple sources focused on the onshore wind turbines by Pfaffel et al. (2017) an average percentage of time-based reliability is equal to 95%. By most turbine manufacturers, 95% uptime performance is guaranteed, contractually. A single database shows results of 80% time-based reliability of the onshore wind turbines. However, this result is based on data from 30-year wind turbine performance. The time-based availability of onshore wind turbines will be used in this paper to model downtime due to O&M. The implementation of the wind turbine downtime in the system is explained in more detail in chapter 3.

2.1.3. Cost Breakdown Wind Turbine

Renewable energy sources are characterised by high capital investment costs and low operation and management costs compared to other energy production technologies. A correct overview and consideration of all costs considered with the instalment of a wind turbine are necessary to obtain a valid input for the cost calculation of the hydrogen value chain. A wind turbine's life cycle and cost components can be divided into three sections. Before the turbine is operational, the upfront cost is also known as Capital Expenditure (CAPEX). Costs associated with the operation and maintenance of the wind turbine, Operational Expenditure (OPEX). At the end of the life, after typically 20 years of operation for onshore wind turbines and often 25 years for offshore wind turbines, a third cost component is added to the total cost structure, known as Decommission Cost (DECOM) (Alsubal et al., 2021). A detailed cost structure is given by Figure 2.9. This cost structure shows a detailed breakdown of each of the three components.

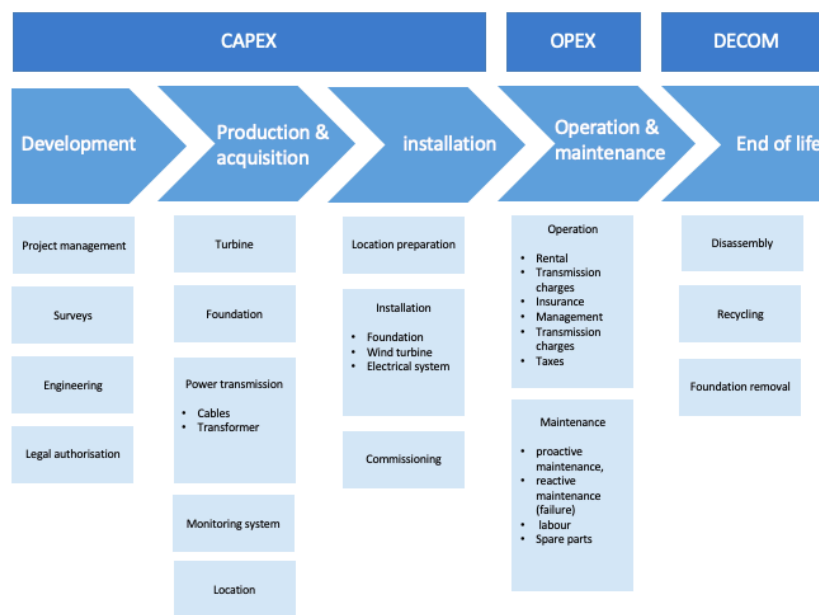


Figure 2.9: Breakdown of cost structure for a wind turbine (Blanco, 2009; Taylor et al., 2020)

CAPEX Wind Turbine

The CAPEX cost of a wind turbine installation can be divided into five segments according to the cost breakdown shown in Figure 2.11. The most significant cost component is the wind turbine. This cost component includes the blades, nacelle, tower and transformers. Civil works include the preparation of the site and all necessary to place and install the turbine at a specific location. Grid connection cost consists of the ability for the turbine to be connected to the power grid. The final cost component includes all other capital investments needed to ensure an operational wind turbine. These costs consist of labour costs for project management, construction site costs and investment costs for control systems (Renewable Energy Agency, 2012).

The onshore capital investment cost has decreased over the past years. In Figure 2.10 an analysis of the global weighted-average of the total installation cost is depicted for onshore wind turbines until 2020 (Taylor et al., 2020). The figure, however, shows an average for the entire globe. A significant difference in total cost is present for various parts of the world. Therefore, it is essential when analysing the cost of the wind turbine to determine the CAPEX for the area of interest. CAPEX differ significantly due to manufacturing cost or even shipment cost if the location for the wind turbine is remote. Research from Taylor et al. (2020) into turbine instalment cost for the year 2020 shows that the highest average CAPEX cost per kW per region is found in Other Asia, this does not include China and India, with 2475 USD/kW, and the lowest overall CAPEX is found in India, reaching 1038 USD/kW.

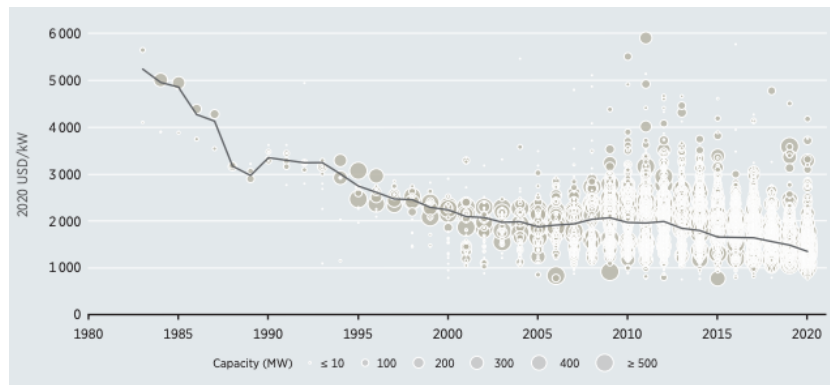


Figure 2.10: Global weighted average total cost, capacity factors and LCOE until 2020 for onshore wind turbines (Taylor et al., 2020)

The weighted average price for an onshore wind turbine in Europe is 1515 USD/kW (Taylor et al., 2020).

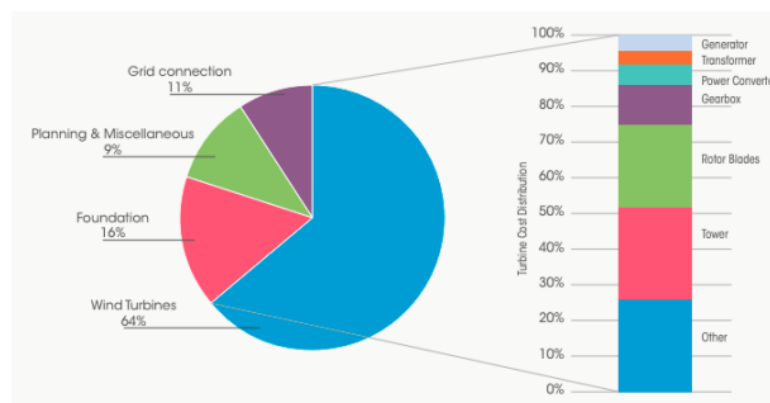


Figure 2.11: Capital expenditure cost breakdown wind turbine (Renewable Energy Agency, 2012)

OPEX Wind Turbine

Parameters that define the OPEX cost components are scheduled and unscheduled maintenance, the balance of plant O&M costs, land rental and property costs, taxes, the connection to the electrical grid, insurance, labour cost for operation and control of the wind turbine and more (Wiser et al., 2019). Around 20 to 35% of the LCOE of the wind turbine consists of OPEX (Taylor et al., 2020; Wiser et al., 2019). OPEX cost differs significantly for each location of the wind turbine. Many strategies are developed to minimise the total O&M cost during the lifetime of the wind turbine (Krokoszinski, 2003). For this research, an average yearly cost per MW for O&M cost is taken to represent all cost components.

DECOM Wind Turbine

DECOM are all costs associated with the life-ending phase of the wind turbine. The DECOM state cost of the removal, recycling of the wind turbine and restoring the site to its original state. The DECOM cost varies significantly from location and wind turbine type as these cost components are built up from a cost perspective and a revenue perspective. Revenue is created from decommissioning a wind turbine by either reselling or recycling and receiving funds for the wind turbine components. From a cost perspective, the decommissioning cost is dependent on turbine size, location and grade of restoration of the production location (Aldén & Barney, 2015). As each wind turbine's site and salvage value is different, this cost component should be evaluated for each specific case. As decommissioning costs are principally neglected in most studies, some studies say that the revenue of the old turbine is equal

to the cost of decommissioning, and therefore left out. (Thomson & Harrison, 2015). Other methods use a percentage of capital cost and are integrated into the CAPEX cost of the wind turbine, or a price per kW is determined (Schwabe et al., 2011). This research assumes that the residual price of the turbine is equal to the decommissioning costs and therefore left out of the equation.

2.2. Grid Connection

The electricity used for hydrogen production is predominantly supplied by the wind turbine in the hydrogen supply chain. In the case of a power deficit, the grid connection is used to buy electricity to produce hydrogen. However, it can also be used to sell electricity when excess electricity is available. The possibility of selling power to the grid results in a cost reduction due to revenue generated from the excess power production capacity of the wind turbine.

When considering a grid connection in the hydrogen value chain, there are several important factors. The first factor is the size and power requirements of the grid connection located at the turbine. The DSO can pose restrictions on the size of the grid connection or the amount of energy sold at certain moments throughout the year. Consequently, the DSO limits the ability of backup power supplied by the grid and the ability to sell excess electricity, increasing the overall cost of hydrogen at the refuelling station. With a restricted grid connection, it is expected that more storage capacity in the value chain is necessary to overcome less windy periods and limited backup power. The second factor is the cost structure considered for the grid connection and who is responsible for the extra costs for installing and using the grid connection. Thirdly the cost structure of selling and buying power on the electricity market should be considered and what cost structures apply to the local power market. Actively controlling the interplay between the grid connection and the power produced by the wind turbine for hydrogen production can reduce the LCOH. A final factor to examine is electric cable losses due to transmission between the wind turbine, grid connection and the electrolyser.

2.2.1. Electricity Market

This research focuses on the market structure for the electricity market in Europe. The market structure is shown in Figure 2.12. The electricity market is not singular but divided into different sub-markets with each their specific time frame before the moment of delivery of the electricity to the consumer. The most extended timescale considered in the electricity market is the wholesale market, with a timescale of the year up to a month before the delivery time. These markets include the forward energy market, forward transmission markets and balancing capacity markets for long term security of supply (Meeus, 2020).

A blind auction operates the day-ahead market. The mechanism of the day-ahead market operates for every hour of the day. The day-ahead market has two types of participants, buyers and sellers. They send their orders to the order book. Using all buy and sell orders, a demand curve based on the buy orders and a supply curve based on the sell orders is composed. The price for an MWh for which these lines cross is called the market-clearing price (MCP). This MCP is the price for a single MWh for that hour established one day before the delivery time. The buyers who submitted a bid higher than the MCP will get filled, and all sellers who submitted a sell order for lower than the MCP will get filled. All buyers and sellers will have to pay or receive the MCP (EPEX SPOT, 2021). On a shorter timeframe, the intraday market operates 24 hours a day to overcome the differences between the expected supply and demand on the day-ahead market and the actual supply and demand. Five minutes before the delivery time, the TSO takes over and balances the market to ensure that supply meets demand and provides security of supply. It is possible to participate in the balancing market; however, it is not guaranteed that the service will be used and, therefore, not sure if the hydrogen electrolyser in the supply chain can exploit this ancillary service to the power grid by producing hydrogen when there is a power surplus in the electricity grid. This complex grid integration mechanism is not included in this research.

A renewable energy developer as HYGRO can use power purchase agreements (PPA) for the ex-

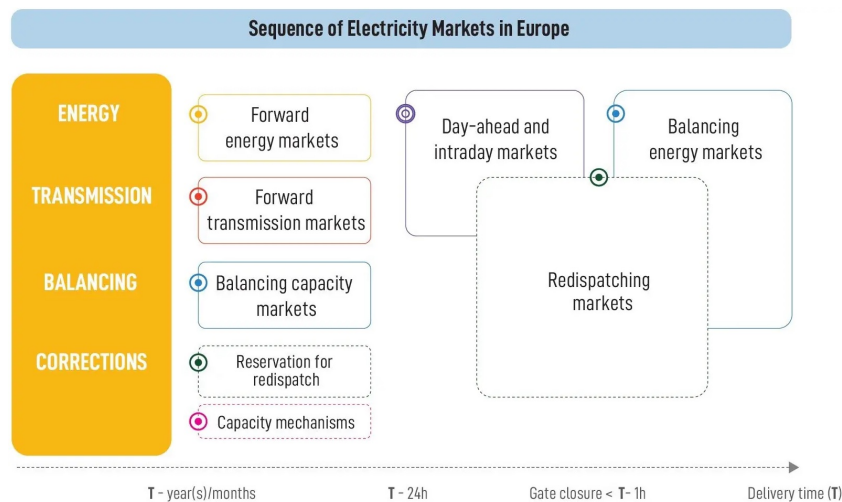


Figure 2.12: Overview of electricity market structure with timescale (Meeus, 2020)

cess electricity produced by the wind turbine. A PPA is a bilateral contract between an energy producer and an arbitrary company. The core principle is the agreement of a fixed price for a unit of energy (kWh or MWh) (Ghiassi-Farrokhfal et al., 2021). A PPA could pose valuable for the power producer (HYGRO) as uncertainty from fluctuating electricity prices is eliminated. The goal, however, for this value chain is to produce hydrogen, and it is uncertain how much excess energy will be produced. Also, the ability to control hydrogen production based on expected electricity prices in the market makes it possible to produce hydrogen for the lowest cost by picking the moment of production. It is, therefore, of no interest to use PPA in a wind-based hydrogen supply chain system as production quantities can not be guaranteed to the buyer of the excess electricity. This research will use the day-ahead market price for the cost/revenue calculation of excess power sold and bought from the power grid.

2.2.2. Cost Breakdown Grid Connection

The costs associated with the grid connection are divided into different cost structures according to Swider et al. (2008). *Shallow costs* are considered to cover the overall cost for connecting the supply chain to the power grid up to the medium voltage grid connection. Any cost associated with necessary grid reinforcement is not considered and will not be paid by the developer. The distribution system operator or the transmission system operator are accounted for the costs of grid reinforcement or other alterations to the power grid. The result of this cost structure is the ability to install a wind turbine inexpensively as no extra grid costs are considered. An onshore wind turbine installed in a country with an extended power grid often does not pose a problem as the power grid can supply sufficient connection points. However, when considering offshore wind turbines, it is less acceptable that all costs for expensive offshore grid installation and reinforcement are socialised, therefore not paid by the wind turbine park developer.

The second cost structure is referred to as *Deep costs*. This cost structure represents all costs associated with installing the wind turbine, including the need for any grid reinforcement or alterations. The wind turbine developer is expected to pay these extra costs. A benefit of this cost structure is that the developer is forced to optimise the wind turbine park's layout and electric cabling structure. It is, however, not fair to expect that the wind turbine developer is charged for the entire grid expansion as this might benefit other users as well (Swider et al., 2008). A third cost structure is the *super shallow costs*. The developer is not expected to pay anything for the electrical connection, and the end-consumers pay all costs. In reality, a hybrid approach from these three cost structures is frequently used. In this research, the shallow cost structure is taken into account. The hydrogen supply chain developer is only charged for connecting to the grid and all electrical components within the supply chain.

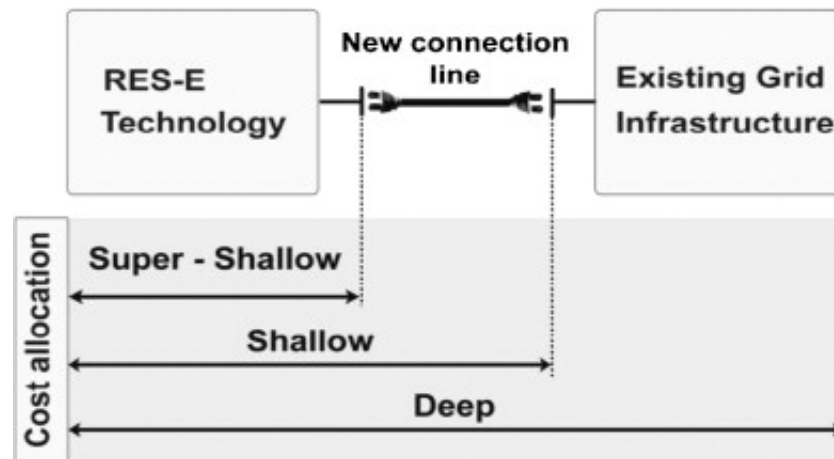


Figure 2.13: Different costs structure for renewable energy developers according to Swider et al. (2008)

The CAPEX costs of the grid connection consist of the installation fees and components needed to establish a secure grid connection for the value chain. OPEX cost entails all costs associated with the use of the electricity grid. Fixed OPEX considers yearly payments to the DSO for using the electrical equipment needed for the grid connection. Variable costs are also present with the use of the electricity grid. The variable components mainly depend on the peak power delivered to or taken from the power grid and the transmission costs per unit of energy bought or sold.

2.3. Hydrogen Production

Three leading hydrogen water electrolysis technologies can be distinguished. The first technology is the Proton Exchange Membrane (PEM) electrolyser technology. The second electrolyser technology is the Alkaline Electrolyser (AEL), and the final hydrogen electrolyser technology is the Solid Oxide Electrolyser (SOE). This section discusses all three electrolyser technologies, hydrogen production principles and technical limitations. The most suitable electrolyser technology for the wind-based value chain is determined based on a list of KPIs for the electrolysers system adopted in this value chain. The KPIs adopted in this research:

- Efficiency
- Flexibility
- Reactivity
- Gas Purity
- Pressure Range
- Current Density
- CAPEX/OPEX

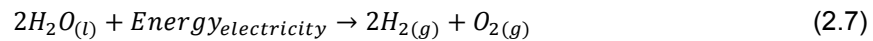
Multiple process steps are required to obtain high-purity, low-cost hydrogen from water electrolysis. In Appendix A the balance of plants (BOP) of the most suitable electrolyser system for the wind-based value chain is discussed in detail. Each component of the BOP and corresponding processes of the electrolyser is explored.

2.3.1. Hydrogen Electrolyser Technologies

The fundamental principle of water electrolysis is the electrochemical process of splitting water into hydrogen and oxygen using electricity. The overall reaction of water electrolysis is given by Equation 2.7. To produce green hydrogen, the energy for the electrolysis process has to come from a renewable

energy source. A DC energy source is required for the electrolysis process. Two advantages can be noted considering a green energy source with water electrolysis. The first advantage is the lack of polluting by-products in the conversion process, where the second advantage of using water electrolysis to produce hydrogen is the high purity that can be reached by the conversion process (Shiva Kumar & Himabindu, 2019).

In comparison with other hydrogen production technologies, water electrolysis can reach a purity of 99.99% when using PEM electrolyzers, whereas hydrogen production via steam methane reforming or coal gasification only reaches a purity of 94.3% (Khatib et al., 2019; Zhao et al., 2020). The high purity of hydrogen is essential for fuel cell applications. Fuel cells require high purity hydrogen due to the fuel cell catalyst poisoning if low purity hydrogen is adopted. The poisoning of the fuel cell catalysts result in performance in combination with lifetime degradation of the fuel cell (Khatib et al., 2019).



The splitting of water into oxygen and hydrogen is an energy disfavoured reaction. Energy is required to drive the reaction. The energy for the decomposition reaction is supplied by the potential difference between the cathode and the anode. The Gibbs Energy equation shown in Equation 2.8 can be used to determine the reversible voltage needed to split water with the help of electricity. The equation to determine the reversible voltage is shown in Equation 2.9, where n is the number of electrons shifted and F is Faraday's constant. At ambient conditions (25 C°), the reversible voltage to split water into hydrogen and oxygen is equal to 1.23V. The reversible voltage assumes that all components in the reaction are in a gaseous state. With water electrolysis, water is typically not in a gaseous state. Extra energy input is required to split water into hydrogen and oxygen. The voltage required to split water in a liquid state is defined by the thermal neutral potential, at ambient conditions equal to 1.48V and defined by Equation 2.10. Overpotential is applied to increase the electrolysis process as electrolysis at 1.48V is a slow process, and higher voltages are required to be able to split water due to system inefficiencies (Chisholm & Cronin, 2016). No reaction occurs when electrolysis is performed at a lower voltage than the reversible voltage. If the voltage potential is between the reversible and the thermal neutral voltage, heat is required to perform the reaction. finally, if the voltage potential is more significant (overpotential) than the thermal neutral potential, the reaction creates heat (Coutanceau et al., 2018).

$$\Delta G^\circ = \Delta H^\circ - T\Delta S^\circ \quad (2.8)$$

$$V_{ref} = -\frac{\Delta G^\circ}{nF} \quad (2.9)$$

$$V_{Tn} = -\frac{\Delta H^\circ}{nF} \quad (2.10)$$

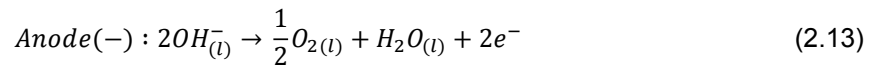
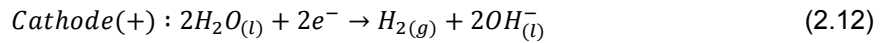
Two types of efficiencies in the process of electrolysis can be identified. The first efficiency in the water electrolysis process is the Faradaic efficiency. The Faradaic efficiency is the ratio between the amount of charge bypassed and the number of moles of hydrogen produced. Typically, a 100% Faradaic efficiency is assumed as in reality this efficiency is slightly lower, due to parasitic electrochemical processes (Chisholm & Cronin, 2016). The second efficiency is the energy efficiency of the electrolyser. The energy efficiency is calculated by the amount of hydrogen produced multiplied by the higher heating value (HHV), divided by the energy necessary to produce hydrogen. The electrolysis efficiency is often presented in $\frac{kWh}{m^3}$ and defined by Equation 2.11. The efficiency of the entire electrolyser system, including the BOP, is often denoted as the system efficiency (η_{sys}) and includes all system losses. In AEL and PEM electrolysis, a higher heating value (HHV) has to be used. The water used in the electrolysis process is liquid, which requires extra energy to split water. With SOE, the Lower

Heating Value (LHV) can be used as the water used in the electrolysis process is in a gaseous state.

$$\eta_{eff} = \frac{mole_{H_2} \cdot HHV_{H_2}}{I \cdot V \cdot t} \quad (2.11)$$

Alkaline Electrolyser

The first electrolyser technology examined in this research is the Alkaline electrolyser. The AEL is the most mature electrolyser technology. The basic principle of the AEL is the separation of the oxygen and hydrogen in water via supplying direct current to a cathode and an anode. The reaction equations are shown in Equations 2.12, 2.13 and 2.14.



At the cathode, the water dissociates into hydrogen and two hydroxyl ions. The hydrogen is formed in a gaseous state, and the hydroxyl ions transfer to the anode side under the influence of the electrical circuit through a porous diaphragm (Keçebaş et al., 2019). Simultaneously, oxygen is formed at the anode, and a water molecule is created. When a water molecule dissociates at the cathode, a new water molecule is created at the anode. The AEL typically utilises an electrolyte of 25-40 wt% of potassium hydroxide (KOH) or sodium hydroxide (NaOH) varying on the working temperature and operating pressure of the electrolyser cell (Ursúa et al., 2012). Figure 2.14 schematically shows the alkaline electrolysis process.

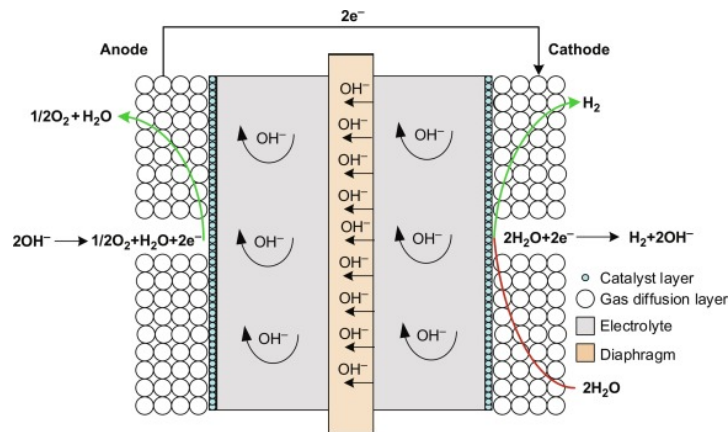


Figure 2.14: Alkaline electrolysis process (Keçebaş et al., 2019)

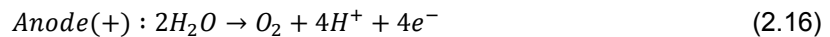
The typical operating temperature of alkaline electrolysis is below 100 C°. At higher operating temperatures, an increase in alkali electrode corrosion is present and reduce the lifetime of the electrolyser (Sheffield et al., 2014). A porous diaphragm separates the two electrodes. The material properties of the porous diaphragm influence the transportation of hydroxide ions and water between the electrodes and the operating pressure of the electrolyser. The operating pressure is typically lower than 30 bar and is limited by the material strength of the diaphragm in between the electrodes. Also, crossover gasses are increased by increased operating pressure and low operating loads. The latter is a limitation for the AEL. Decreased oxygen production and an increased concentration of hydrogen results in dangerous

levels of hydrogen and oxygen mixture (Chisholm & Cronin, 2016).

The lower dynamic range is defined by a percentage in which the electrolyser must operate to function relative to its total load capacity. The alkaline electrolyser must operate at least 10% of its total load capacity. The response time of the AEL is minutes up to hours depending on the standby operation or cold start-up (Lehner et al., 2014). Therefore, the alkaline electrolyser is interesting for applications with non-fluctuating loads properties and constant operation requirements.

PEM Electrolyser

The second electrolyser technology is the PEM electrolyser. The PEM electrolyser is a less mature technology than the AEL but is well established and commercially available. The operating principle of the PEM electrolyser is shown by Figure 2.15, where a polymer membrane separates the anode and cathode of the electrolyser. Water is supplied via an inlet at the anode surface and decomposed into protons (H^+) and oxygen (O_2). The polymer membrane permeates protons but rejects electrons. The PEM must be saturated with water to allow protons to permeate. Hydrogen and oxygen have weakly permeability through the membrane. This results in minor undesired diffusion and mixing of hydrogen and oxygen, also known as gas-cross over. The produced oxygen is presented at the flow plate's outlet on the anode side. The protons dissipated through the polymer membrane are recombined on the cathode's surface, where simultaneously electrons are supplied by electricity. The protons combine to form hydrogen and result in hydrogen flow at the outlet of the flow plate on the cathode side. The reaction equations are shown by Equations 2.15, 2.16 and 2.17.



The membrane used in the PEM electrolyser is dependent on the conditions of the electrolysis process. High-pressure, low load and frequent stop and start events result in a thicker membrane for the PEM electrolyser to withstand the pressure, reduce gas crossover or supply enough material for membrane degradation (Chisholm & Cronin, 2016). The thinner the membrane, the higher the efficiency of the electrolyser, so a trade-off is present between efficiency and durability of the PEM electrolyser.

The catalyst material choice on the surface of the electrodes is limited due to the high acidic nature of the PEM electrolyser (Coutanceau et al., 2018). Rare materials such as Platinum, Iridium, Rhodium or Ruthenium are used. The use of rare materials increases the cost of the PEM electrolyser (Millet & Grigoriev, 2013). The membrane and the electrocatalysts combined are called the Membrane Electrode Assembly (MEA). Figure 2.16 shows the components of the MEA and the flow plates located at either side of the MEA. The electrode is either directly or indirectly coated on the membrane or coated on the porous transport layers. In practice, the electrode layer is often coated on the membrane resulting in higher stability against gas evolution (Stolten & Emonts, 2016).

The gas diffusion layer (GDL) between the catalyst and bipolar flow plates has multiple purposes. The GDL help distribute water evenly over the catalyst layer. The GDL helps remove hydrogen and oxygen from the catalyst layer. Structural support is provided against differential pressure between the sides of the membrane and assembly pressure. The gas diffusion layer between the MEA and the bipolar plates increase the electrical conductivity, which results in improved transport of water and the produced gasses (Millet & Grigoriev, 2013) and the GDL helps to conduct the heat generated by the electrolysis process at the catalyst layer to the water in the bipolar flow plates providing thermal management for the PEM electrolyser cell (Omrani & Shabani, 2019).

The bipolar plates in the fuel cell accommodate the water flow to the GDL cell and remove the reactants from the electrolyser cell. Also, the bipolar plates allow electron conduction. The bipolar plates electrical often made of Titanium due to their high corrosive resistance, low electric resistance and long-term durability (Omrani & Shabani, 2019).

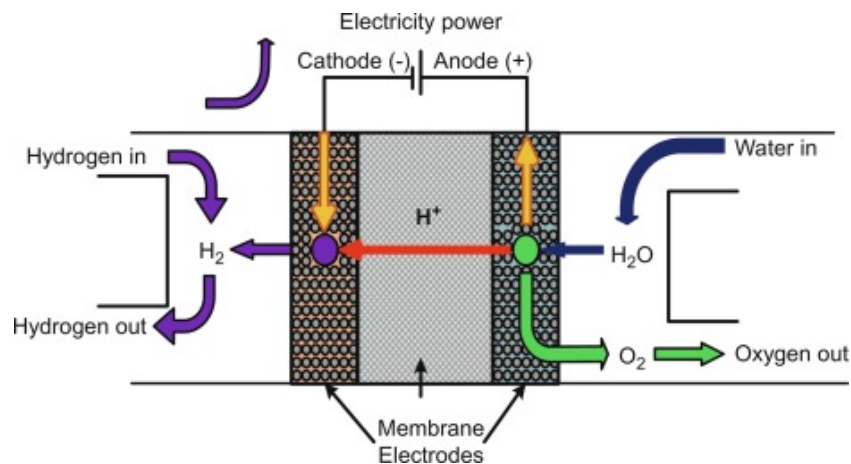


Figure 2.15: Operating principle PEM electrolyser (Keçebaş et al., 2019)

As the PEM electrolyser does not apply an electrolyte but an ion-conducting polymer membrane, de-ionised water is the only reactant. The sole use of the de-ionised water results in high purity gasses, and only limited purification processes are needed after the hydrogen production (Millet & Grigoriev, 2013). However, the PEM electrolyser needs purified water to operate as impurities can lead to a less purified output of hydrogen, unpurified water also leads to more maintenance and a decreased lifetime of the electrolyser (Millet & Grigoriev, 2013). An advantage is the application of the zero-gap cell. A zero-gap cell is defined by the electrodes only being separated by the separator, in the case of the PEM electrolyser the polymer membrane. The zero-gap cell decreases the ohmic conductivity, and as a result, the overall efficiency is increased. Due to the efficiency increase, higher current densities can be applied to the electrolysis cell. The efficiency of the electrolysis process is negatively influenced by the current density applied as the permeation of hydrogen increases with increased current density (Trinke et al., 2017). The efficiency decreases with an increased current density, resulting in an economic trade-off to be made. An optimum exists for each case where the extra hydrogen produced due to increases in current density outweighs the loss in performance. Two optimums can be defined for the PEM electrolyser. The first optimum is the electrolyser efficiency achieved at low current densities. The second optimum is the economic optimum, where the increase in hydrogen production due to increased current density outweighs the efficiency loss of the electrolyser system. The optimum size and current density applied are specific for each application.

The ability for the PEM electrolyser to operate at higher pressures than the Alkaline and the SOE results in fewer compression stages. The limitation for hydrogen production at high pressures originates from the gas crossover. As pressure increases, gas crossover increases, resulting in dangerous levels of the hydrogen-oxygen mixture inside the electrolysis system. Also, more gas crossover across the membrane results in lower gas purities which is not preferred when producing hydrogen for fuel cell applications.

The significant advantage of using PEM electrolyzers in combination with renewable energy sources is the rapid response time and extensive dynamic range of the PEM electrolyser. The quick response time of PEM electrolyzers is a result of the electrolyte (solid) and the permeability of the protons (Coutanceau et al., 2018). The response time of PEM electrolyzers equals a few milliseconds, and the dynamic range spans from 0 to 100%. The most significant drawback of the PEM electrolyser is the use of rare earth materials, which result in a significant cost increase of the electrode components of the electrolyser. The rare materials in the electrodes, titanium flow plates and the polymer membrane define the high price of the PEM electrolyser system. The challenge is to find alternative materials

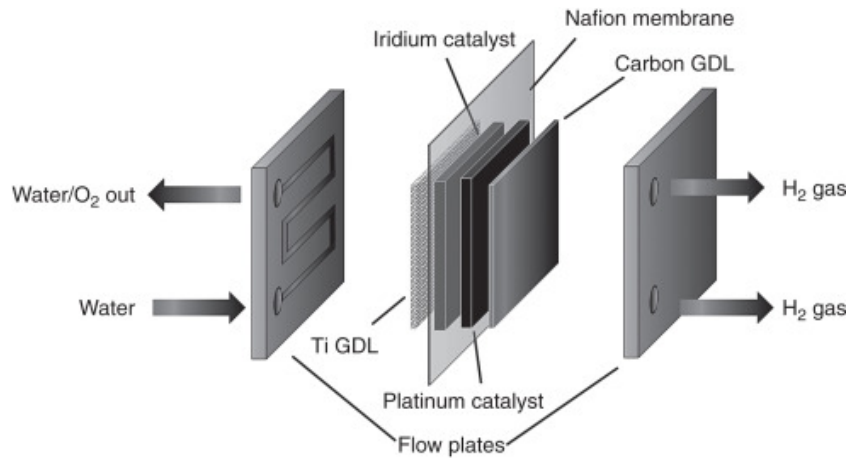
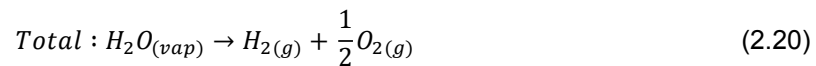
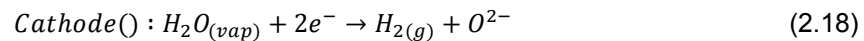


Figure 2.16: Cell structure PEM electrolyser (Chisholm & Cronin, 2016)

for these components without decreasing the overall efficiency of the electrolyser (Coutanceau et al., 2018; Millet & Grigoriev, 2013).

Solid Oxide Electrolyser

The third and final electrolyser considered as an option in this research is the Solid Oxide Electrolyser. The SOE operates at high temperatures at which water electrolysis is performed with water vapour instead of water as a liquid. The operating temperature of the SOE is in the range of 700-1000 °C (Chisholm & Cronin, 2016; Coutanceau et al., 2018). The SOE splits the water into hydrogen and oxygen according to Equations 2.18, 2.19 and 2.20. Figure 2.17 shows a schematic of the reaction process.



The SOE works according to the same principle as the PEM electrolyser, ionic conduction through a membrane separating the electrodes. A solid membrane is located between the anode and the cathode. The membrane separates the two compartments and ensures that no gas cross over occurs and therefore prevents recombination of the reaction products (Millet & Grigoriev, 2013). The two main differences to PEM electrolysis is the water vapour used at the cathode and the high temperature of operation. Also, the SOE transmits oxides instead of protons Figure 2.18 shows the energy split for water decomposition where the temperature of the process is shown on the horizontal axis. As the heat increases, less electricity is required, and more energy is obtained from the heat of the reaction. The reduced and improved kinetics in the electrode reactions result in an energy requirement of $3 \frac{kWh}{Nm^3}$ H_2 at 900°C and $4 \frac{kWh}{Nm^3}$ H_2 at 80°C (Keçebaş et al., 2019; Millet & Grigoriev, 2013). Ceramic materials are often used for the separator, which reduces the ohmic losses as much as possible (Millet & Grigoriev, 2013).

The main advantage of an SOE is the low electrical energy input required making the technology suitable for applications where energy in the form of heat is available. The high-temperature operation results in a high energy efficient electrolysis process. The major drawbacks for the SOE technology are fast degradation in performance due to the high heat and, therefore, the short lifetime of the electrolyser. The SOE technology is as mature as PEM or Alkaline and available on a small scale. The solid oxide electrolysis process is not appropriate for intermittent electrolyser operation (Millet & Grigoriev,

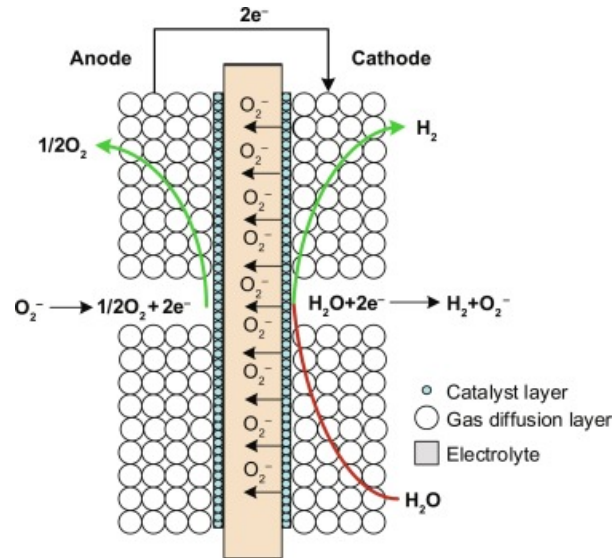


Figure 2.17: Solid electrolyser electrolysis process (Keçebaş et al., 2019)

2013).

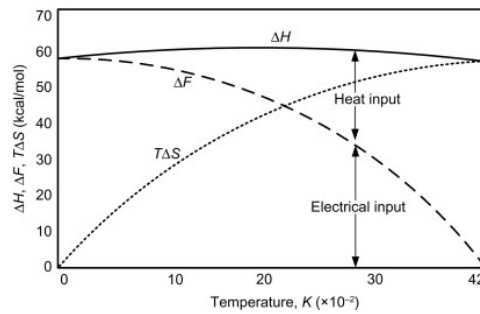


Figure 2.18: Heat and electrical requirement for splitting water as function of temperature (Keçebaş et al., 2019)

Conclusion

The optimal hydrogen electrolyser is chosen based on the KPIs mentioned at the beginning of this subsection. An overview of all electrolyser technologies and their constraints is given by Table 2.1. The efficiency of the electrolyser determines the amount of energy required for a single mass unit or volume unit of hydrogen. Both AEL and PEM show similar energy consumption where SOE has the highest system efficiency and requires little electrical energy input. The SOE, however, requires heat as energy input which is not defined by the table.

Flexibility refers to the operation set point of the electrolyser. High flexibility ensures any given operation point about the electrolyser's total capacity. A lower dynamic range of 10% and response time of seconds shows that the AEL is not suitable for an application with an intermittent energy source. Similar to the AEL, The SOE also has a lower dynamic range of 30%, implying that a combination with an intermittent energy source is not preferred. This results in a required baseload to keep the electrolyser operational and prevent long start-up times.

The reactivity defines the switchability from different operating points based on the alternating power supply. Both SOE and AEL need seconds to adjust to a different load applied to the electrolyser, whereas the PEM electrolyser can change within milliseconds. The fast reactivity of the PEM electrolyser makes it suitable for the intermittent power supply of the wind turbine. The gas purity of the hydrogen production process is the highest for the PEM electrolyser. The use of highly de-ionised wa-

Specification	Unit	AEL	PEM	SOE
Electrolyte	-	Aq. Potassium Hydroxide 20 - 40 wt% (KOH) or Sodium Hydroxide (NaOH)	Polymer membrane	Yttria stabilised Zirconia
Anode	-	Ni, Ni-Mo alloys	Pt, Pt-Pd	Ni/YSZ
Cathode	-	Ni, Ni-Co alloys	RuO ₂ , IrO ₂	LSM/YSZ
Mobile species	-	OH^-	H^+	O^{2-}
Operating temperature	C°	60-80	50-80	650-1000
Current density	$\frac{A}{cm^2}$	0.2-0.4	0.6-2.0	0.3-2.0
Operating pressure	<i>bar</i>	<30	<200	<25
Cell voltage	<i>V</i>	1.8-2.4	1.8-2.2	0.7-1.5
Voltage efficiency	%	62-82	67-82	<110
Cell area	m^2	<4	<0.3	<0.01
Production rate	$\frac{m^3 H_2}{h}$	<760	<40	<40
Stack energy	$\frac{kWh}{m^2 H_2}$	4.2-5.9	4.2-5.5	>3.2
System energy	$\frac{kWh}{m^3 H_2}$	4.5-6.6	4.2-6.6	>3.7
Gas purity	%	>99.95	99.99	99.9
Lower dynamic range	%	10-40	0 - 10	>30
Response time	-	seconds	Milliseconds	Seconds
Cold start time	<i>minutes</i>	<60	<20	<20
Stack lifetime	<i>hours</i>	60.000-90.000	20.000-60.000	<10.000
Technology maturity	-	Mature	Commercial	Demonstration
Capital cost	$\frac{\text{€}}{kW}$	1000-1200	1860-2320	>2000

Table 2.1: Characteristics of alkaline, PEM and Solid oxide electrolyzers (Schmidt et al., 2017)

ter for the electrolysis process results in the high purity of hydrogen output. The AEL electrolyser has a low current density resulting in a large system size requirement and therefore a large footprint. Next to the wind turbine, often on leased land, space is limited. A small electrolyser system is preferred. The PEM electrolyser can cope with the highest current density, which results in the smallest system size.

No heat source is present at the wind turbine, making the SOE electrolyser a less suitable option. The system's response time and lower dynamic range of the PEM electrolyser make it the best suitable option for the wind-based value chain. Also, the gas purity of the PEM electrolyser has an advantage over the AEL and results in a less extensive purification process to reach fuel cell quality hydrogen. The elevated operating pressure of the PEM electrolyser in comparison with the other water electrolysis technologies also creates the opportunity to produce and directly store the hydrogen in high-pressure tanks. Overall it can be concluded that the PEM electrolyser is the most suitable application for the wind-based hydrogen value chain.

2.3.2. Electrolyser Balance of Plants

Appendix A discusses the PEM electrolyser system adopted in this research. The subsection reviews the balance of plant (BOP) and all necessary system components to obtain high-quality hydrogen for fuel cell applications. The PEM electrolyser production process is examined.

2.3.3. Cost Breakdown Hydrogen Electrolyser

The production cost of hydrogen can be quantified and defined by the Levelised Cost Of Hydrogen (LCOH) (Badgett et al., 2021). The cost components of the PEM electrolyser contains the CAPEX,

fixed OPEX and variable OPEX. The fixed OPEX consists of all expenditures regardless of the amount of hydrogen produced. The variable OPEX cost is proportional to the amount of hydrogen produced. The variable OPEX includes cost factors such as electricity cost, materials, replacement of equipment and water. All cost factors are divided by the annual hydrogen production, which results in an LCOH defined by the unit of $\frac{\text{€}}{\text{kg}}$.

For each application, it is crucial to design the PEM electrolyser to obtain the lowest LCOH. Key characteristics that define and influence the cost function for the electrolyser can be identified. An overview of all components that define the cost of hydrogen is shown in Figure 2.19. The three main categories are the economic parameters, performance parameters and manufacturing parameters. Both performance parameters and manufacturing parameters are dependent on the electrolyser system and stack design.

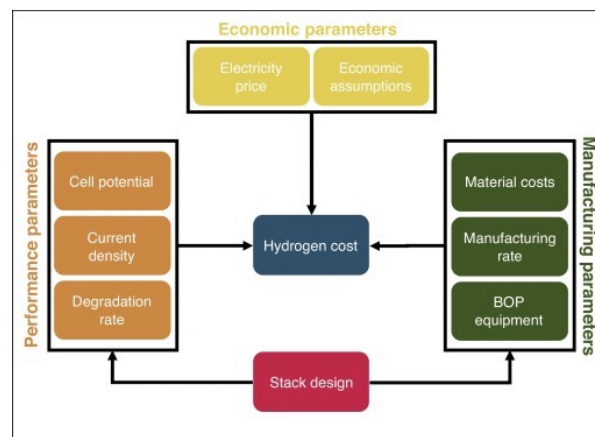


Figure 2.19: Cost components that define the LOCH from the electrolysis process (Badgett et al., 2021)

Electrolyser Cost Trend

According to Badgett et al. (2021) four categories can be identified that define LCOH cost reduction for electrolyser systems and can obtain a greater economic potential for the entire hydrogen value chain. The four categories that define historical and future electrolyser cost reduction are:

- Learning by Doing
- Economies of scale
- Reduced material consumption
- Electrolyser performance

Learning by doing is defined by the historical trend in cost reduction of electrolyser systems. The historical cost reduction trend for similar system size and electrolyser technology shows the economic development and gives insight into the future expected cost for the electrolyser. The learning power curve law often quantifies the estimate for future cost reduction for electrolyser systems. The future cost can be defined by Equation 2.21 where the C_0 and P_0 are the initial cost and production capacity/rate of the electrolyser system trend. The P_t is the production capacity or rate for which the cost estimate is required, and α is the learning curve that defines the slope of the learning power curve law (Schoots et al., 2008). The difficulty of this approach is to know the exact cost structure of all the historically developed and implemented electrolyser systems. Such Data is often not publicly available and therefore make a cost estimate based on a learning curve unpredictable and challenging (Schoots et al., 2008).

$$C = C_0 \cdot \left(\frac{P_t}{P_0}\right)^{-\alpha} \quad (2.21)$$

Total system cost can be reduced by producing system components and materials based on mass production and is defined as the economics of scale. The total capital and fixed operation and management costs for the BOP component manufacturing companies are distributed over more units with increased production capacity. The cost of every single component is therefore reduced and result in total electrolyser BOP cost reductions. Mayyas et al. (2019) has conducted a bottom-up system component cost analysis for PEM electrolysers. An important finding was that smaller cost reductions are expected in the economics of scale as there is already a significant amount of balance of plant components producers producing on a mass production basis. Another important finding was that the electrolyser stack materials costs are dominant for larger PEM electrolyser systems (>1MW). This is a result of the rare-earth materials used in the PEM electrolyser.

The use of the rare earth materials for the electrolyser stack components results in a large part of the total system cost for the PEM electrolyser. Therefore, in the upcoming years, research towards new electrolyser materials must be conducted to reduce system costs further. The aim is to optimise the material used by reducing the material needed or finding other materials without reducing the electrolyser performance (Badgett et al., 2021). The materials contributing the most towards the total system cost are the iridium and platinum used in the catalysts. The price of iridium has increased four times from 2018 to 2020 to over roughly 200.000 \$/kg Mayyas et al. (2019). The bipolar plates between the electrolyser cells are often made from titanium due to their high corrosive resist acne in the acidic environment of the PEM electrolyser. Around 15%-50% of the electrolyser, stack cost originates from the bipolar plates. A key driver to reduce the electrolyser system cost is to search for new materials that can replace the currently applied materials and reduce the total system cost by reducing the electrolyser stack cost component (Badgett et al., 2021; Mayyas et al., 2019).

Another method to reduce cost is focussing on improving the performance of the electrolyser system. An increase of the denominator while maintaining constant numerator results in a lower overall LCOH. The overall performance of the electrolyser is defined by the lifetime, degradation and overall system efficiency (Shiva Kumar & Himabindu, 2019). A better voltage efficiency leads to less power consumed per produced kg f hydrogen. Operating at higher current density with similar system efficiency results in more minor stack requirements and a longer lifetime, and smaller system degradation contributes to less maintenance cost and higher production capacity over the lifetime of the electrolyser system.



Figure 2.20: IRENA (2020a)

The extensive BOP cost analysis of (Mayyas et al., 2019) For the PEM electrolyser concluded that about two-thirds of the total 1MW system that was analysed consisted of the BOP components, with half of the BOP costs originating from the power electronics. The economics of scale for the electrolyser stack and the BOP system components can reduce the total system cost. An overall cost potential reduction for all the BOP components of the PEM electrolyser is shown in Figure 2.20. The figure depicts the fraction of the cost of the system as a function of the highest cost reduction potential. Power

electronics contribute the most towards the fraction of the total system cost and have the highest cost reduction potential. It is, therefore, crucial to focus the cost reduction of the PEM electrolyser on the power electronics to supply green and affordable hydrogen.

The two most important factors and dominant in the cost function are the cost of electricity and the capital cost of the electrolyser system. Typical operational expenditure adopted in research lies between 1-3% of the total system CAPEX (ICCT, 2020). Deloitte Monitor (2021) has conducted an analysis of the CAPEX cost for PEM electrolyser systems over past years. The total CAPEX trend in $\frac{\text{€}}{\text{kWh}}$ is shown in Figure 2.21. The current expected CAPEX cost for the PEM electrolyser system is between $800\text{-}1800 \frac{\text{€}}{\text{kWh}}$ and will reduce to an expected $600\text{-}1400 \frac{\text{€}}{\text{kWh}}$ in 2030.

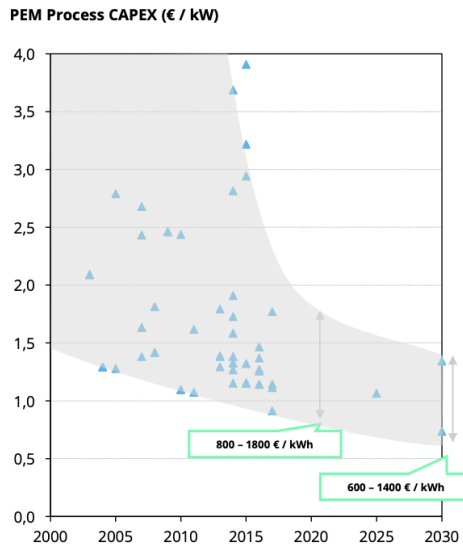


Figure 2.21: PEM cost development curve Deloitte Monitor (2021)

In this research, the electrolyser's system cost and performance optimisation is conducted by HY-GRO and outside the scope of this research. An analysis on the system components done to a specific extent as the electrolyser system topology used in the wind-based hydrogen value chain is confidential. Their PEM electrolyser system production model is used to convert electrical energy into kilograms of hydrogen produced in the case study. The cost of the components, the configuration of the PEM electrolyser and performance is discussed in chapter 3.

2.4. Hydrogen Compression

This section defines the different types of hydrogen compression technologies available and suitable for intermittent hydrogen production in a wind-based hydrogen value chain. The thermodynamic principle of hydrogen compression is discussed, whereafter an overview of compression technologies is provided. The drawbacks and advantages of the three most commonly used compression technologies are discussed both technically and economically. Finally, the end of this section will provide an overall conclusion on the most suitable compression technology for the wind-based hydrogen value chain. The conclusion will be based on a list of KPIs suitable for compression modules in a dominant wind-based hydrogen value chain.

Hydrogen can be transported in different material phases. As can be seen in the phase diagram shown in Figure 2.22 hydrogen is in a gaseous state under atmospheric conditions (1 bar, 20 °C). The phase diagram shows the pressure and temperature of the material on the vertical axis and the horizontal axis, respectively. The location in the phase diagram presents the phase of the material. Either

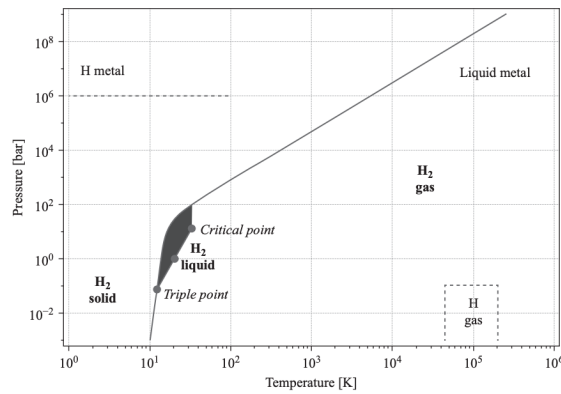


Figure 2.22: Phase diagram hydrogen (Makridis, 2016)

pressure has to be increased, or temperature has to be lowered to obtain hydrogen in a solid or liquid phase. The biggest drawback of hydrogen as an energy carrier is the low volumetric density. Hydrogen gas at atmospheric conditions (1 bar, 20C°) is equal to 0.09 kg/m³ (Makridis, 2016). It is crucial for the economic viability of the hydrogen value chain and the application of hydrogen as a fuel that the volumetric density of hydrogen is increased. Comparing the energy density of petrol and hydrogen at atmospheric conditions results in 26 MJ/L and 0.01 MJ/L, respectively (U.S. DOE & Energy, 2017). The volumetric density for multiple pressure levels is depicted in Figure 2.23 as a function of the temperature. Figure 2.24 depicts the volumetric and gravimetric density of multiple fuels. Hydrogen has the highest gravimetric energy density but the lowest volumetric energy density. It is, therefore, crucial to compress hydrogen and increase the volumetric energy density to make it a suitable alternative for fossil-based fuels.

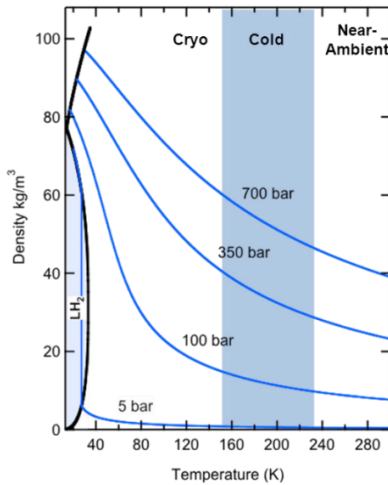


Figure 2.23: pressure temperature density (U.S. DOE & Energy, 2017)

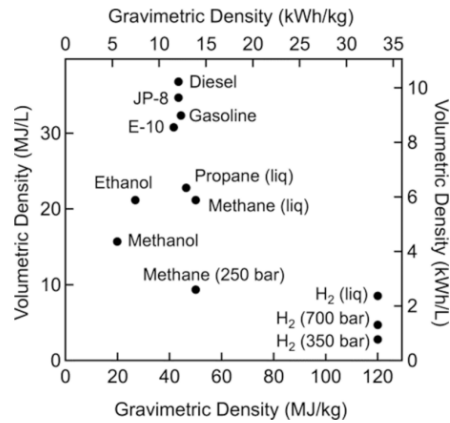


Figure 2.24: Density fuels (U.S. DOE & Energy, 2017)

Either the hydrogen is transported as a liquid or gas, or liquid organic hydrogen carriers (LOHC) are utilised. When comparing the carriers, the volumetric density of liquid hydrogen (1 bar, 20K) and gaseous hydrogen (700 bar, 293K) equals 38.7 kg/m³ and 70.8 kg/m³, respectively. The wt% of LOHC is typically in between 5-7 % (Hurskainen & Ihonen, 2020). In a fuel cell, hydrogen is utilised in a gaseous state. Liquid hydrogen requires cryogenic storage as it boils off at a temperature of 20K (Makridis, 2016). Storing hydrogen as a compressed gas in vehicles is therefore preferred despite its lower volumetric energy density (Hochgraf, 2009). For different applications, each carrier has its advantages and drawbacks. When considering short-distance transportation and low-energy demand,

as can be expected with the dominant wind-based hydrogen value chain, hydrogen transportation in a gaseous phase is most economically competitive (Pudukudy et al., 2014). Therefore, in this research, only the compression of gaseous hydrogen is considered.

The compression of a gas can be estimated by the ideal gas law and the principles of thermodynamics. The ideal gas law is shown by Equation 2.22. P denotes the pressure of the gas, V is the volume occupation of the considered gas. n is the number of atoms or moles of the gas considered. R is the ideal gas constant, and T is the gas temperature in Kelvin. To correctly estimate the compressed volume of hydrogen, a compressibility factor has to be included. Hydrogen does not precisely follow the ideal gas law and always results in a more spatial occupation than the ideal gas law estimates (Makridis, 2016). The compressibility factor is added to ideal gas law and shown in Equation 2.23. The value for the compressibility factor for different temperature levels can be seen in Figure 2.25. The ideal gas law can be used to determine the volumetric density of the hydrogen gas.

$$P \cdot V = n \cdot R \cdot T \quad (2.22)$$

$$P \cdot V = n \cdot Z \cdot R \cdot T \quad (2.23)$$

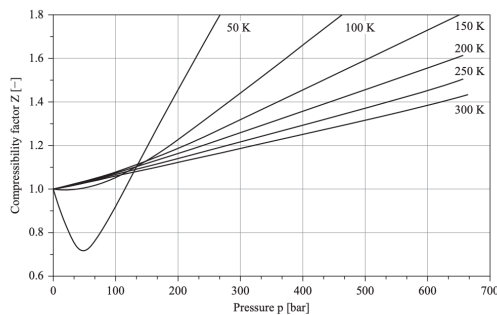


Figure 2.25: Density fuels(Makridis, 2016)

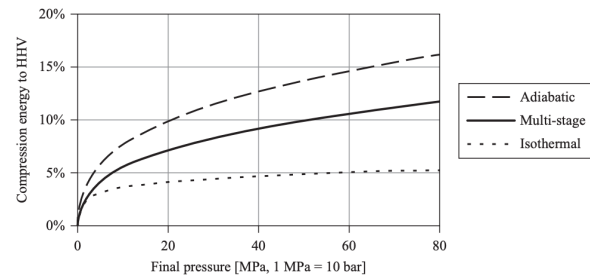


Figure 2.26: pressure temperature density (Makridis, 2016)

To compress hydrogen to a desired pressure level for either transportation or storage, energy is required. The amount of energy required to reach the desired pressure level depends on the gas mixture. In Figure 2.26 the work that must be applied to compress hydrogen gas as a function of the desired output pressure is shown. The work is defined as a percentage of the HHV of hydrogen. The work applied for the compression of a gas is translated into heat. Figure 2.26 shows the energy requirement of isothermal compression and adiabatic compression. With isothermal compression, the temperature of the gas remains constant throughout the compression process. With adiabatic compression, no heat or mass is exchanged with the surroundings. Adiabatic compression, therefore, implies that the work applied to the compression of the hydrogen translates into a temperature increase of the gas (Makridis, 2016). As can be seen in Figure 2.26, the compression of hydrogen gas isothermally requires less energy than the compression performed adiabatically. The lowest compression energy is required for ideal isothermal compression. It is crucial that cooling is applied with the compression of hydrogen to reduce the thermodynamic energy consumption. Often hydrogen cooling is done in between compression stages where cooling plates or other cooling mechanisms are applied (Lugo-Méndez et al., 2021). The total energy demand for hydrogen compression consists of the thermodynamic energy requirement combined with compressor system inefficiencies, also known as mechanical efficiency. The adiabatic compression energy can be described by Equation 2.24. The required work for adiabatic compression for multiple combinations based on the initial pressure levels and final pressure level is shown in ??.

$$W = \left[\frac{\gamma}{\gamma - 1} \right] \cdot P_0 \cdot V_0 \cdot \left[\left(\frac{P}{P_0} \right)^{\frac{\gamma-1}{\gamma}} - 1 \right] \quad (2.24)$$

Where W is the amount of work necessary for compression, $\gamma=1.41$ is the adiabatic coefficient, P is the desired pressure (Pa) and $V_0=11.01$ the initial volume of the compressed gas (m^3/kg) (Stolten & Emonts, 2016)

Initial pressure (bar)	Final pressure (bar)	Energy Demand (% of HHV)	Energy Demand (MJ)	Energy Demand (kWh)
1	350	12.1	17.16	4.77
1	500	13.7	19.46	5.41
1	640	14.7	21.0	5.83
1	700	15.4	21.85	6.07
30	350	2.81	3.98	1.11
30	500	3.41	4.84	1.34
30	640	3.83	5.43	1.51
30	700	4.04	5.73	1.59

Table 2.2: Energy requirement for adiabatic compression calculated with Equation 2.24

The hydrogen obtained at the outlet of the electrolyser considered in this research has a pressure of 30 bar, as can be seen in Table 2.2 compression from 30 bar to the desired storage pressure requires less energy than from atmospheric pressure. The compression stage is located at either the production location next to the wind turbine or a nearby hydrogen refuelling station supplied by a short distance pipeline. More system components increase the value chain's size and economic footprint. An increase in system size and complexity can harm the overall system cost. Therefore, placing the compression module at the refuelling station or the production location is preferred. Operating two compression modules, one at the hydrogen production location to a medium pressure level and one at the hydrogen refuelling station to a high-pressure level, would increase the complexity of the hydrogen value chain. The pressure in the hydrogen pipeline therefore remains similar to the output pressure of the hydrogen electrolyser.

The total pressure difference between the electrolyser outlet and the desired pressure for transportation determines the total compressor system size. Not all compressors can overcome and compress the gas to the desired pressure in a single compression stage. Each compression technology has compression ratios at which the technology is limited. The compression ratio is the ratio between the inlet pressure of the compressor and the outlet pressure for a single compression stage. Another important factor is the total energy consumption of the compression module. The total electricity consumption will be defined in this research as $\frac{kWh}{kg_{H_2}}$. The power consumption impacts the OPEX costs of the electrolyser, which together with the CAPEX is an important KPI that directly define the total compression system cost.

The most economical favourable compression technology is desired to minimise the value chain total system cost and provide low-cost hydrogen at the refuelling station without compromising compression efficiency. Some compression technologies contaminate the hydrogen gas as the hydrogen gas is put into contact with other materials, which can dissolve into the hydrogen gas (Sdanghi et al., 2019). After the hydrogen is purified for the fuel cell application, it is crucial that during compression, transport and refuelling, no contamination takes place as this could damage the fuel cell vehicles of the customers at the refuelling station (Cheng et al., 2007). The hydrogen production is based on an intermittent energy source. The compression technology must provide flexibility in compression rate based on the intermittent hydrogen supply from the electrolyser system. A technical-economic trade-off must be made between the KPIs to ensure the most suitable compression technology for the wind-based hydrogen value chain. Sdanghi et al. (2019) has extensively reviewed different hydrogen compression

technologies, which will be used as a basis for determining the most suitable hydrogen compressor. The list of KPIs to evaluate the different compression technologies is:

- Pressure Range
- Stages required
- Energy Consumption
- Compression Efficiency
- Hydrogen Contamination
- CAPEX & OPEX
- Durability
- Flexibility
- Technology readiness level

2.4.1. Hydrogen Compression Technologies

A distinction can be made for two types of compression principles of hydrogen. Mechanical compression technologies or non-mechanical compression technologies (Sdanghi et al., 2019). The reciprocating compressor technology, the diaphragm compression technology and the ionic compression technology will be extensively discussed. A general overview of mechanical & non-mechanical compression technologies are

Mechanical Compressors

- Reciprocating compressors
- Diaphragm compressors
- Linear compressors
- Liquid compressors

Reciprocating Compressors

Most hydrogen compressors work on the principle of positive displacement. Positive displacement entails compression of the hydrogen gas by reducing the volume of the compartment containing the hydrogen with a piston. The exact amount of hydrogen molecules in a smaller volume results in higher gas pressure. The reciprocating compression system works based on a piston-cylinder system. The compression cycle starts with the movement of the piston to its most downward position in the cylinder, creating a vacuum inside the cylinder. The hydrogen enters the cylinder via the inlet valve, after which the inlet valve is closed. The piston is moved up towards the cylinder head, reducing the cylinder compartment containing the hydrogen. The hydrogen is compressed by the reduction of volume inside the cylinder. Once the hydrogen in the cylinder reaches the desired pressure level, the outlet valve opens and releases the compressed hydrogen from the cylinder. This process repeats itself where the flow rate of the cylinder is defined by the cylinder size and the operating speed of the compression cycle. A schematic of the reciprocating compressor can be seen in Figure 2.27. Top Dead Centre (TDC) and Bottom Down Centre (BDC) define the top and down position of the piston.

The reciprocating compressor can be either single-stage or multistage (Sdanghi et al., 2019). With multistage compressors, the reliability is increased, and the size of the compressor stages is lowered as the differential pressures, and operating temperatures are lowered (Witkowski et al., 2017). With each reciprocating compressor stage, the pressure level is increased until the desired pressure is achieved.

Non-Mechanical Compressors

- Cryogenic compressors
- Metal-Hydride compressors
- Electrochemical compressors
- Adsorption compressors

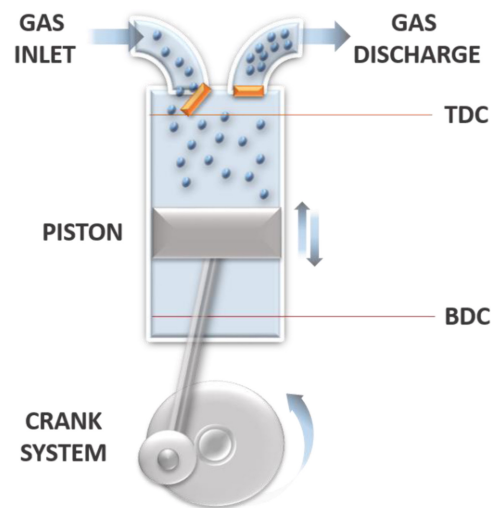


Figure 2.27: Reciprocating compressor schematic (Sdanghi et al., 2019)

Flow rates of reciprocating compressors are limited. The flow rate is dependent on the cylinder's dimension and the number of cycles per unit of time. An increase in system size results in increased component size and, consequently, higher inertia stresses. Lower operating speeds are required to cope with the increased stresses. High compression speeds are therefore only available for small cylinders limiting the flow rate of the compressor (Sdanghi et al., 2019). The limited flow rate flexibility of the reciprocating compressor makes it challenging to match with the variable hydrogen flow rate obtained from the wind power operated electrolyser.

The most significant impact on the durability of the reciprocating compressors is the embrittlement of the metals used inside the compressor unit. Hydrogen embrittlement refers to damage inflicted on metals due to hydrogen penetration and causing a loss in ductility and tensile strength (Karlsdóttir, 2012). To improve hydrogen embrittlement under high pressure, unique materials or coatings inside the compressor have to be used, described by the API 618 Standard.

A distinction is made between lubricated and non-lubricated reciprocating compressors. The reliability and durability of the reciprocating compressor depend on the correct lubrication of the piston, packing rings, rider bands, cylinder liner and compressor valves (Barton et al., 2020). No lubrication will lead to faster wear rates of the compressor. The biggest drawback for lubricated reciprocating compressors is the mixing of the lubricating oil and the hydrogen gas. As for fuel cell vehicles, very high purity levels are required. No hydrogen contamination is preferred. Non-lubricated reciprocating compressors use rider bands that prevent contact between the piston and the cylinder and reduce wear. Significant non-uniformity of pressure distribution has led to rapid failure of the non-lubricated compressors. With the high-pressure operation, gas leakage from the cylinder forms a major drawback resulting in increased hydrogen embrittlement in the cylinder and therefore a reduced lifetime (Sdanghi et al., 2019). The non-lubricated reciprocating compressors are primarily suitable for low-pressure levels. Therefore to obtain high enough pressure levels for hydrogen fuel cell application, lubricated reciprocating compressors would be the first choice (Dasilveira, 2002).

The energy requirement to compress hydrogen from 20 bar to a pressure of 350 or 700 bar isothermally is equal to 1.05 kWh/kg and 1.36 kWh/kg, respectively (Platzer & Sarigul-Klijn, 2021). When considering the wind-based hydrogen value chain, the wind turbine can produce roughly 1000 kg of hydrogen per day. According to Parks et al. (2014) reciprocating compressor with a flow rate of 1000 kg/day achieve a compression efficiency of 56% and a motor efficiency of 92%. The compression efficiency is often denoted as either adiabatic efficiency or isotropic efficiency. Isentropic efficiency is defined as the ratio between the work required to compress the hydrogen under an isentropic process and the actual work supplied to compress the hydrogen considering the same inlet and outlet pressures. With an isentropic process, the entropy of the gas/fluid is constant. An isentropic process can

be considered a reversible adiabatic process. In both cases, no heat exchange with the surroundings is assumed. Machine efficiency, also known as mechanical efficiency, is defined as the efficiency loss by secondary compression processes. These losses contain power losses in the power electronics and mechanical losses such as friction losses between the cylinder and the piston. Considering a total efficiency of 52%, the total energy consumption for compression equals 2 kWh/kg up to 350 bar and 2.6 kWh/kg up to 700 bar. A leading company in compression technology, Burkhardt compression (Burkhardt Compression, 2021), focused on hydrogen refuelling stations and hydrogen MEGC filling stations supply an oil-free piston compressor with a flow rate of 95 kg/h and a rated power capacity of 180 kW, which results in 1.89 kWh/kg compression energy consumption. These values are based on the inlet pressure of 20 bar up to compressed hydrogen at 450 bar. The energy consumption and efficiency of the reciprocating compressor is heavily dependent on the flow rate and compressor system design; however, a typical energy consumption between 2-4 kWh/kg hydrogen can be assumed (Parks et al., 2014).

Diaphragm Compressors

The diaphragm compressor is based on the principle of positive displacement, similar to the reciprocating compressor. A crank system drives a piston. In comparison with the reciprocating compressor, the piston of the diaphragm compressor is not in direct contact with the hydrogen gas. The piston is in contact with a hydraulic fluid used to cause a deflection in a diaphragm placed between the hydraulic fluid and the hydrogen gas. The displacement of the diaphragm results in expansion and reduction of the hydrogen compartment and ensures the compression of hydrogen. A perforated plate is placed between the hydraulic fluid reservoir and diaphragm to ensure evenly distributed load across the diaphragm membrane and prevent local stresses (Sdanghi et al., 2019). The piston in the compressor is moved downward in the cylinder, which creates a lower pressure on the hydraulic fluid side of the diaphragm. The membrane is forced against the bottom of the compressor cavity. Hydrogen fills the compression cavity via the inlet valve. The piston is moved upward, which forces the hydraulic fluid against the diaphragm, increasing the pressure applied to the hydrogen gas in the cavity. The movement of the membrane reduces the hydrogen cavity. The hydrogen gas is compressed by reducing the volume of the cavity and released as the desired pressure is reached. A schematic of a diaphragm compressor is shown in Figure 2.28.

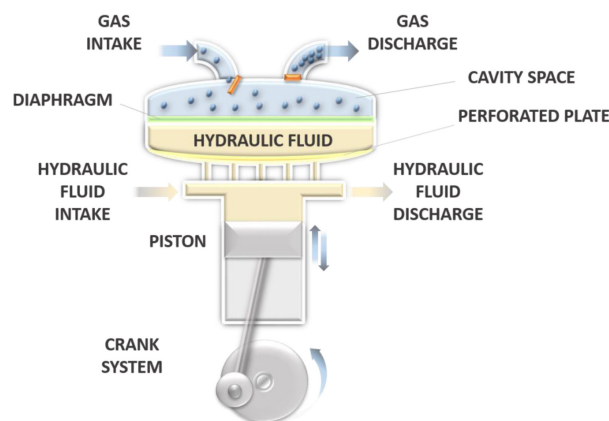


Figure 2.28: Diaphragm compressor schematic (Sdanghi et al., 2019)

The diaphragm of the compressor is composed of three plates. The processing plate is located on the hydrogen side of the diaphragm. The hydraulic plate comes into contact with the hydraulic side of the diaphragm. The middle plate ensures stability in between the process plate and the hydraulic plate (Bloch, 2006). The middle plate is also used to detect possible leaks and give support to the diaphragm (Sdanghi et al., 2019). The oil utilised in the reciprocating compressor was used to lubricate the piston-cylinder system, whereas the oil in the diaphragm compressor directly controls the compression process. Therefore, the oil in the diaphragm compressor must be managed, and the correct oil pressure is maintained to perform efficient compressor operation. The high heat conductivity of the

oil is a second advantage of the diaphragm compressor. The oil ensures high coolant properties and therefore improves the compression efficiency as more isothermal compression is performed (Zhang et al., 2005). The most significant advantage of the diaphragm compressor is the complete separation of hydrogen gas and hydraulic fluids in the compressor. Due to a closed system, high purity hydrogen gas is essential with a value chain for fuel cell applications. The inability of contamination removes the need for a purification process after the compression process.

The biggest drawback for the diaphragm compressors is the durability of the diaphragm. High flow rates reduce the lifetime of the diaphragm, and therefore the compressors are primarily suitable for low flow rate operation Sdanghi et al. (2019). The size of the hydrogen cavity in the compressor is also limited by the diaphragm material properties and therefore limits the flow rate of a single compression cycle. Intermittent operation compressor reduces the lifetime of the diagram resulting in increased maintenance costs and more downtime. The short lifetime of the diaphragm is seen as the biggest hurdle for developing economic compression systems in the hydrogen value chain (Rohatgi & Northwest, 2015). The Pacific Northwest National Laboratory (PPNL) and PDC, a leading diaphragm compressor manufacturer, investigated the main contributors to the lifetime degradation. They concluded that debris and contamination from fretting caused increased wear on the membrane surface. Improper priming when restarting the compressor resulted in increased radial stresses on the membrane, which eventually led to early membrane rupture. Both problems were identified as the cause of a reduced lifetime under intermittent operation Rohatgi & Northwest (2015).

A solution to this problem of intermittent hydrogen supply could either be a hydrogen buffer storage between the electrolyser and the compression module or a modular compression system with reduced size compressors and introduce variation of hydrogen flow rate by turning single compressors on and off in the modular set-up. Turning on and off the compressors variates the total compression flow rate, increasing the system's flexibility. A drawback of the modular system is to increase the CAPEX and OPEX costs of the compression process as the total system components and complexity increase.

PDC, a leading diaphragm compressor manufacturer, supplies a three-stage diaphragm compressor with a flow rate of 50 kg/h and an outlet pressure of 950 bar. Like the reciprocating compressor of Burkhardt compressors, a power rating of 180 kW is adopted for the diaphragm compressor. Despite a somewhat lower flow rate, a much higher pressure level at the compressor outlet is achieved. High compression is desired, especially when considering transportation under high pressure and a cascade filling system regarding fuel cell vehicles operating on 700 bar. Due to the high gas purity and high energy efficiency, the diaphragm compressors are preferred when considering the hydrogen-based value chain (Hu et al., 2017). In chapter 3 the total compressor system topology will be analysed and defined for this research. The compression efficiencies will be defined and total flow rate capacity given.

Ionic compressors

The Ionic liquid compressor is based on the principle of replacing the piston in the previous two compression technologies with an almost incompressible ionic liquid. The advantage of the adoption of ionic compressors is the improved operation due to good lubricant and thermal coolant properties of the ionic liquid (Sdanghi et al., 2019). Similar to the diaphragm compressor, no lubrication is required in combination with the almost negligible hydrogen solubility in ionic liquids (Mellein et al., 2021) results in little to no hydrogen contamination. The use of ionic liquids for hydrogen compression also ensures low energy consumption, long service life, low material costs and low noise emission. However, due to embrittlement by the ionic liquid, increased maintenance cost can be expected compared to the other compression technologies (Sdanghi et al., 2019).

The company The Linde Group (2020) has been the lead manufacturer of ionic compression technology. Due to the use of ionic liquids, low energy consumption, long service life, and low equipment cost can be expected (Sdanghi et al., 2019). In the next section, the ionic compressor by the The Linde Group (2020) is compared to the diaphragm compressor proposed by HYGRO.

Conclusion compressor

To define the compressor technology most suitable for the value chain considered in this research, two leading compressor manufacturers with two different compression technologies are considered. The first technology is the ionic compressor developed by (The Linde Group, 2020). The second technology is the diaphragm compressor developed by (Howden, 2021). In Table 2.3 both performance specifications are presented for compressor sizes with similar flow rates. Both the ionic and diaphragm compressor applies a three-stage compression process. The energy efficiency is calculated based on the ratio of the adiabatic compression energy required to compress hydrogen from 30 bar to 640 bar for the Howden compressor and up to 500 bar for the Linde compressor as 500 bar is the upper compression limit for this specific compressor. The adiabatic energy required is calculated with Equation 2.24, and the energy consumed in $\frac{kWh}{kg_{H_2}}$ for compression is obtained from both manufacturers.

When comparing the compression efficiency, the diaphragm compressor utilises less energy per kWh. This is in contradiction with literature on the comparison of the diaphragm and ionic liquid compressors (Sdanghi et al., 2019). Ionic liquid compressors have a higher compressor efficiency than diaphragm compressors due to the high heat conductivity and almost isothermal compression capabilities (Sdanghi et al., 2019). The lower efficiency regarding the Linde IC50 compressor could be a result of a much lower mechanical efficiency. This assumption can not be verified due to the lack of detailed technical data on both compressor technologies.

For compressors suitable for the wind-based value chain, a maximum flow rate of roughly 50 kg/h is assumed, limited by the electrolyser capacity. The costs regarding both compressors are obtained by expertise knowledge of Hygro, and an ionic compressor is almost twice as expensive as the diaphragm compressor for similar flow rates. It is therefore assumed in this research that the diaphragm compressor is the most suitable solution. Consequently, in this research, the application of the diaphragm compressor system is assumed in further analysis of the value chain.

Technological Parameters	Linde IC50	Howden
Design	ISO Container	-
Footprint	15 m ²	-
Compression stages	3	3
Rated Power	95 kW	84 kW
Inlet pressure range	6-200 bar	20-400 bar
Approximate flow rate	44 kg/h	44 kg/h
Max. Compression pressure	500 bar	640 bar
Ambient Operating Temperature	-20 to +45	-
Electricity consumption	2.2-2.9 kWh/kg	1.9 kWh/kg
Adiabatic Compressor efficiency	61%	79%
Pre-cooling	Not Required	-
Estimated CAPEX Cost	900.000	500.000

Table 2.3: Technical parameter comparison Linde IC50 Ionic compressor (The Linde Group, 2020) Howden 64MPa diaphragm compressor (Howden, 2021)

2.5. Hydrogen Transport/Storage

In this research, two transportation technologies are adopted. The section starts with the application of Multi-Element Gas Containers (MEGC), whereafter High-Pressure Swappable Containers (HPSC) are discussed. Both transportation technologies are based on the principle of hydrogen storage in composite high-pressure storage vessels. Each transportation technology in this research is considered an integral part of the storage system of the entire hydrogen value chain. The storage capabilities for

each transportation technology will be considered. The distribution network topology adopted in this research is discussed in this section.

2.5.1. Multi Element Gas Container Trailer

The multi-element gas container is defined by the European Agreement on international transport of Dangerous goods by Road (ADR) as (Ministerie I&W, 2021): 'UN Multiple-element gas containers (MEGCs) are multimodal assemblies of cylinders, tubes and bundles of cylinders which are interconnected by a manifold and which are assembled within a framework. The MEGC includes service equipment and structural equipment necessary for the carriage of gases. Service equipment means measuring instruments and filling, discharge, venting and safety devices. Structural equipment means the reinforcing, fastening, protective and stabilising members external to the elements.'

A tube trailer consists of horizontally placed tubes, whereas vertically placed tubes are often referred to as MEGC (Mair et al., 2021). The pressure vessels inside the MEGCs are designed to store and transport compressed hydrogen at a specific rated pressure. The tubes can either be fixed to the trailer or packaged in a detachable container. Typical transportation pressures for MEGC trailers range between 200 bar and 500 bar. This pressure range results in a transportable payload of 250-1100 kg of hydrogen when considering 40ft trailers (Reddi et al., 2018). Many MEGC trailer configurations exist. It is, therefore, crucial to perform a techno-economic trade-off between the different possible configurations.

A list of key performance indicators that help define the most suitable MEGC configuration (Hydrogen Europe, 2020):

- Operating Pressure
- Vessel Type
- Trailer Size
- Lifetime
- CAPEX
- OPEX

The pressure vessels of the MEGCs are either filled at the production location near the wind turbine or the Hydrogen Refuelling Station (HRS), also referenced as the hub station. The hydrogen compression unit feeds a hydrogen filling terminal with multiple docking bays. An empty MEGC must always be present at the loading terminal to provide a storage buffer for hydrogen production. The MEGC are transported by a truck to the distributed HRSs. At each HRS, an unloading bay is present. The unloading bay and valve panel are connected to the fuel dispenser providing the local storage at the HRS. The MEGC are consequently also considered as an integral part of the storage system at the HRS. The filled MEGC is interchanged with the empty MEGC already present at the HRS and transported back to the production location.

The size and configuration of the docking bays, valve panels, and the total amount of MEGCs required in the value chain heavily depend on the implemented MEGC type and their corresponding technological parameters. Also, the total hydrogen demand at the refuelling stations determines the allocation and sizing of the distribution system. The technical configuration of the valve panels, the layout of the docking bays and the service equipment of the MEGC is outside the scope of this research.

A distinction is made between three leading technological factors defining the total amount of transportable hydrogen in kg per MEGC. The pressure level of the hydrogen stored in the MEGC defines the volumetric density of the hydrogen gas and, therefore, the maximum amount of hydrogen stored in the storage vessels. In this research, a single transportation pressure level is adopted to decrease the

complexity of the possible distribution system configurations.

The second technological parameter is the selection of the vessel type. The vessel type is defined by the working pressure of the hydrogen storage. The vessel type also defines the manufacturing process, wall thickness and other physical attributes of the storage vessels. Consequently, the vessel type determines the total vessel weight, volume, payload capacity and material of which the vessel is composed (Reddi et al., 2018). The choice of vessel type impacts the cost and lifetime of the storage vessels and the CAPEX and OPEX of the distribution system.

Typically a distinction is made between the five vessel types. An overview obtained from Barthélémy (2012) of the five vessel types is given below. The parameters defining the different vessel types are the material, size and way of manufacturing (Reddi et al., 2018). Each pressure vessel has its unique physical characteristics due to the material choice and different manufacturing processes. Type I pressure vessels are mainly used in stationary industrial applications due to cheap and heavy materials such as metal and the implementation for low-pressure applications. The typical pressure for type I pressure vessels is around 200 bar with a maximum of 350 bar (Barthélémy, 2012). If higher storage pressure levels are required, type II vessels are implemented. Type II pressure vessels have a slightly different design which results in more strength and higher operating pressures. Type III and Type IV vessels are manufactured from composite materials.

The use of composite materials reduces the weight of the pressure vessels significantly, making them a suitable option for transportation purposes. As a result of the manufacturing processes and the properties of the composite materials, the allowable pressure is much higher, reaching 700 bar (Barthélémy, 2012). Compared to the Type I and Type II vessels, the downside of composite materials is the increased cost due to the material choice and manufacturing processes. However, the composite material based pressure vessels are more resilient, have a longer lifetime and require less maintenance (Mair et al., 2021). Also, no hydrogen embrittlement is present, as can be observed with the metal-based Type I and Type II pressure vessels (Barthélémy, 2012). Type V pressure vessels are manufactured without a liner, decreasing the pressure vessel's weight even further. Typical applications for type V pressure vessels are space applications where weight is the most critical factor. However, research towards the application of type V vessels in the distribution of hydrogen is being conducted

For compressed hydrogen transportation, the Type IV pressure vessel is often chosen due to its high-pressure storage capability and cost competitiveness compared to the Type V pressure vessel (Barthélémy, 2012). The CAPEX of type IV pressure vessels is lower due to commercialisation and economics of scale by larger production volumes. The type V pressure vessel and its capacity to store hydrogen up to 1000 bar provide an exciting solution for transporting and distributing hydrogen for passenger vehicles. A passenger vehicle requires at least 700 bar filling pressure. The transportation of hydrogen with a pressure level more considerable than the filling pressure results in eliminating compression systems at every HRS, reducing the cost of the total value chain. As is applied in this research for heavy-duty vehicles, the principle of a cascade filling could become possible for passenger vehicles and high-pressure filling applications (700 bar). Filling vehicles at 700 bar and very high-pressure distribution considering type V pressure vessels are outside the scope of this research.

- Type I: Pressure vessel made of metal
- Type II: Pressure vessel made of thick metallic liner hoop wrapped with a fibre resin composite
- Type III: Pressure vessel made of a metallic liner fully wrapped with a fibre-resin composite
- Type IV: Pressure vessel made of polymeric liner fully wrapped with a fibre-resin composite
- Type V: Linerless, all-composite pressure vessel

The third and final factor determining the amount of hydrogen transported in a single trip is the size of the trailer. Hydrogen MEGCs are available in different trailer sizes. This research considers three

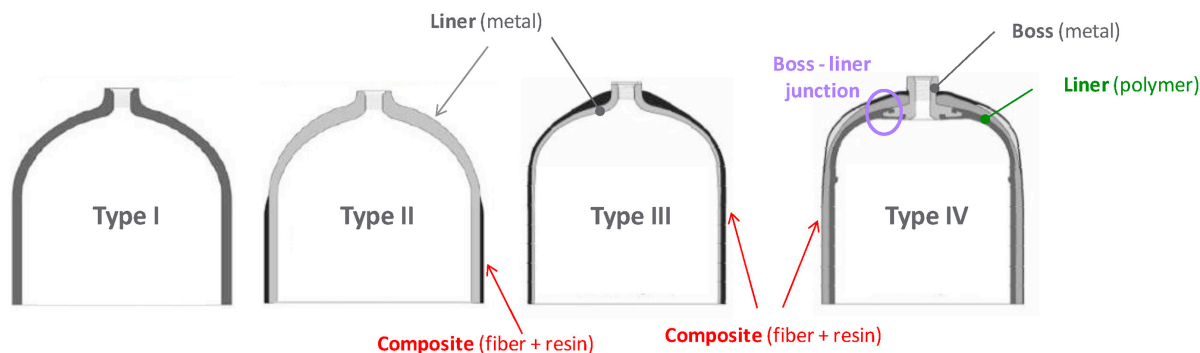


Figure 2.29: Pressure vessel classification (Barthelemy et al., 2017)

trailer sizes with ISO sized 10ft, 20ft, 40ft containers. Where after one is adopted in the model described in chapter 4. Research towards the efficiency of different composite tube configurations and payloads concluded that hydrogen transport vehicles with smaller sized and more significant numbers of composite tubes have a larger payload capacity than larger sized MEGCs with a fewer number of storage vessels (Reddi et al., 2018). MEGCs with smaller sized pressure vessels are considered in this research.



Figure 2.30: 20ft MEGC NPROXX (2021)

NPROXX (2021) is a leading manufacturer of different hydrogen MEGCs configurations with vertically placed pressure vessels. The technical data applied in this research for all three trailer lengths are further elaborated in chapter 3 and based on MEGC developed by NPROXX. Reddi et al. (2018) has researched two different stacking configurations for a pressure vessel diameter range of 9-36 inches and a pressure range of 200-500 bar, fitted inside an 8x8x40ft ISO container. The configuration comparison was based on two parameters, capital cost and maximum hydrogen payload. All vessel types were included in the comparison. The capital cost was influenced by material properties of the vessel type, fraction of safety, operating pressure, vessel diameter and packaging scheme. The research concluded that a 3x3 array configuration with composite pressure vessels diameter 30 inches and 500 bar pressure is the most economically beneficial configuration. Defining the vessel packing configuration is outside the scope of this study.

Where there are no limitations to the pressure or quantities of hydrogen transported by road. The UN model regulations of transport and dangerous goods, An European Agreement concerning the international carriage of Dangerous goods by Road (ADR) and the Transportable Pressure Equipment Directive (TPED), limit the amount of hydrogen carried by the application of a safety factor for the com-

posite pressure vessels. The safety factor is defined as the ratio between the operating pressure and the burst pressure with a fixed safety factor of 3 for composite gas cylinders (DeliverHy, 2013; HyLAW, 2019). A fixed pressure vessel safety factor for gas cylinders and tubes of composite materials limits the total operating pressure to 500 bar as the burst pressure of a type IV composite pressure vessel lies typically around 1500 bar (Berro Ramirez et al., 2015). Recommendations from HyLAW (2019) include that the fixed safety factors should be re-evaluated, and current regulations in place must be revised to allow higher working pressure and larger storage volumes in composite compressed gas cylinders. The increase in payload with the same pressure vessels decreases the overall cost of transportation and therefore increase the economic viability of industrial transport or large quantity hydrogen refuelling infrastructures (DeliverHy, 2013). Current type IV pressure vessels with working pressures of 700 bar are already available and applied in onboard fuel cell vehicle storage. To decrease the total transportation system's cost, 700 bar must also be granted permission to operate compressed hydrogen transportation by road. Based on information from Hygro, ADR regulation on the safety factor is expected to change by 2022. The expected reduction in safety factor results in operating pressure of 640 bar equal to a safety factor of 2.35 compared to 3 previously adopted. Therefore in this research, an operating pressure of 640 bar is adopted for each transportation technology.

2.5.2. High-Pressure Swappable Containers

The second transportation technology considered is the High-Pressure Swappable Container (HPSC). The HPSC applies the same storage technology as the MEGC. A bundle of four type IV composite pressure vessels is used. The technical parameters to store the hydrogen gas in a single pressure vessel of the MEGC and HSPC are assumed similar. The operating pressure of the swappable container unit is 640 bar and can hold a weight of up to 53 kg of hydrogen (NPROXX, 2021). In Figure 2.31 the swappable container unit is represented.

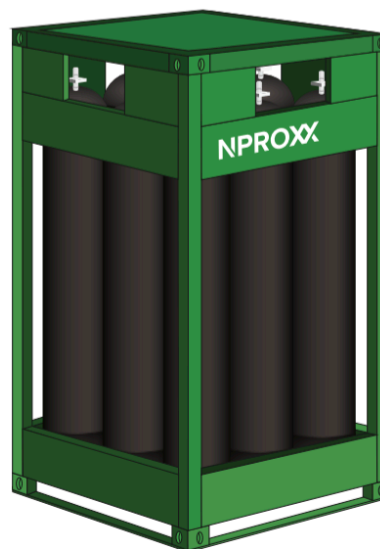


Figure 2.31: Swappable container (NPROXX, 2021)

The most significant difference and a possible advantage in an early market hydrogen value chain is the increased distribution flexibility due to partial unloading/loading of the container units. A single 40 ft trailer can stack 22 swappable containers creating the same payload size as the single 40ft MEGC system. Regarding a MEGC-based distribution network, each MEGC, disregarding its trailer length, must be left at the HRS and swapped with the empty MEGC as the MEGCs are an integral part of the storage system the HRS.

The HPSC applies a similar approach to the MEGCs but on a much smaller scale where the truck and trailer holding the HPSCs can partially unload the transported hydrogen. Consequently, an advantage is the ability to replenish the HRS on a much smaller scale and replenish multiple HRSs in a single trip requiring fewer system operators and transportation equipment. The reduction in the need for system operators and transport movements can impact the total system cost of the value chain.

The downside of the HPSC units is the increase in handling time and complexity of the valve panel at the production location and the HRS. Each container must be unloaded/loaded individually and connected individually to the valve panel. The increase in operating time increases OPEX cost as each container must be loaded/unloaded and connected to the valve panel. A proposed method for offloading and loading the containers is a trailer with a portable forklift.

2.5.3. Pipeline

Compressed hydrogen can be transported via pipeline, similar to natural gas. Typical applications that utilise hydrogen pipelines are large industrial consumers of hydrogen. Hydrogen pipelines are especially suitable for effective flow rates and geographically concentrated demands.

A solution in early-stage development of a refuelling station network existing gas pipelines can be utilised with minor alterations, or hydrogen blending with natural gas could be applied (Hydrogen Council, 2020; Wang et al., 2020) when the hydrogen demand for the refuelling stations increases, an upgrade towards a new and pure hydrogen distribution network could be considered. Due to the scale of the distribution network considered, it is not expected that blending hydrogen in the natural gas network is a viable option for this small-scale application.

A distinction can be made between a low-pressure hydrogen distribution system and a high-pressure pipeline distribution system. A high-pressure pipeline distribution system would require a compression system at the production location but mitigates the need for a compression module at the hydrogen refuelling station. Penev et al. (2019) has researched the economic viability of high-pressure distribution in urban areas. A comparison between a low-pressure distribution and high-pressure distribution was conducted. The research concluded that the distribution in urban areas with high-pressure pipelines was economically advantageous due to the decrease in overall system cost by mitigating the need for a compression module at every HRS.

Some side notes regarding this research are; a centralised production and compression location. In a wind-based hydrogen value chain, centralised compression is not possible as the value chain is based on decentralised production and compression. Also, future expansion with additional production locations in the wind-based hydrogen value chain would compromise the centralised storage and compression location and diminish the advantage gained. Centralised compression, therefore, reduces the flexibility of expansion of the hydrogen value chain.

A second hurdle in applying high-pressure pipelines is the technical feasibility, as most operating pressures of pipelines do not exceed 100 bar. Also, higher pressures lead to more hydrogen embrittlement, and it is mainly unknown what such high operating pressure is due to the durability and lifetime of the pipeline (Penev et al., 2019). Especially in urban areas, regulation on the maximum pressure level and safety standards must be re-evaluated as this in most cases; high-pressure pipelines are not allowed. It can be concluded that high-pressure pipelines could have economic benefits compared to low-pressure pipelines, but too much technological development is necessary. Also, the regulatory framework must be adjusted before implementation is possible in the short term.

Therefore, this research only considers the possibility of a low-pressure pipeline between the hydrogen production location and a hydrogen refuelling station nearby, also referenced as a 'hub' refuelling station. The implementation of the hydrogen pipeline between the production location and a nearby refuelling station tries to answer the question of a short distance pipeline outweighs the transportation

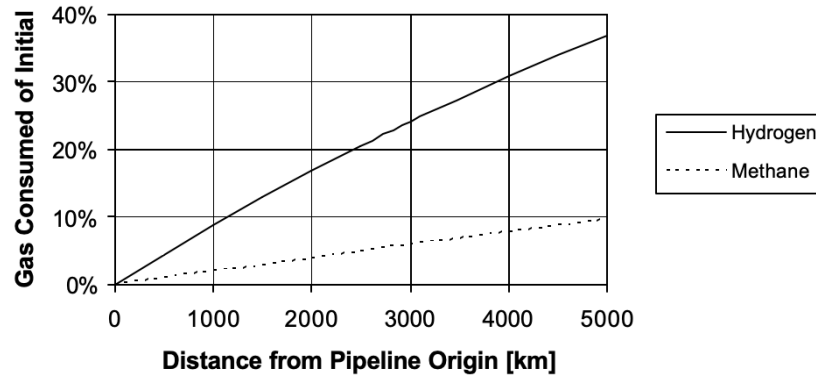


Figure 2.32: Gas consumed as function of distance transported by pipeline (Bossel, 2004)

cost by truck.

Similar to transportation by road, the pipeline distribution network has two purposes. The first application is the transportation of hydrogen gas to the nearby HRS. The second application is the ability to provide a small storage buffer for the distribution network. The storage capacity of the pipeline network is dependent on the length and diameter. When considering low-pressure pipelines, mostly PVC-enriched polyethylene (PE) pipes are used (Gondal, 2016).

Hydrogen transport through pipeline occurs due to pressure difference induced flow. The amount of hydrogen transported can be defined by the flow rate. The flow rate describes the amount of hydrogen mass flow through the cross-sectional area of the pipe per time unit, defined by $[\frac{kg}{h}]$. The flow rate of a pipeline is dependent on physical properties of the gas, pipe dimensions, gas temperature, pressure as well as pressure drop (Gondal, 2016). In this research, no extensive flow rate analysis for the pipeline is included as only a short distance between the PEM electrolyser and the refuelling station is considered.

Energy losses occurring in a pipeline due to transportation result in a pressure drop compared to the inlet pressure at the hydrogen production location and the outlet pressure at HRS. Pressure drop in a pipeline is the result of internal friction between the gas molecules and friction between the gas molecules and the pipe inner wall (Aka et al., 2017). When pressure drop is too significant for long distances, a recompression station is required. A typical distance between compression units is 80-100 km (Gondal, 2016). In this research, distances of only a few km are assumed; therefore, recompression stations are not considered. Only a compression unit at the hub refuelling station is considered to increase the hydrogen pressure to fill up the high-pressure storage vessels.

Bossel (2004) compared the energy required to transport hydrogen for a distance of 150 km. The result was compared to the energy required to transport natural gas. For natural gas, 0.3% of its gas content is consumed to be transported over a distance of 150km. Hydrogen uses 1.4% of its gas content to be transported at a similar distance. This results in a gas content loss of 0.009% km. In Figure 2.32 a comparison of gas content consumed for methane and hydrogen as a function of distance is shown. The energy required to transport hydrogen at very small distances is almost negligible therefore not taken into account in this research

The second application of the pipeline is the ability to operate as a storage buffer for the value chain. The total volume and pressure in the pipeline system define the amount of hydrogen present in the pipeline system. The storage capacity in the hydrogen pipeline network for a single-phase compressible gas is also referred to as line packing (Gondal, 2016). Due to the property of compressibility of the hydrogen gas, certain flexibility exists in the amount of hydrogen present in the pipeline system. In the case of overproduction by the electrolyser and a demand deficit at the HRS, the amount of hydrogen present in the pipeline is increased and 'packed', resulting in a slightly increased operating

pressure. The compressibility of the hydrogen gas can therefore provide short term storage and meet peak demand or an intermittent demand pattern (Karolyt , 2017). A more significant line packing ability results in a more extensive buffer storage. Equation 2.25 depicts the formula to determine the line pack in a pipeline. p_m is calculated by Equation 2.26

$$V_{storage,n} = V_{geom} \cdot \left(\frac{p_m}{K_m} - \frac{p_{m'}}{k_{m'}} \right) \cdot \frac{1}{p_n} \cdot \frac{T_n}{T} \quad (2.25)$$

$$p_m = \frac{2}{3} \cdot \frac{p_1^3 - p_2^3}{p_1^2 - p_2^2} = \frac{2}{3} \cdot \left(p_1 + p_2 - \frac{p_1 \cdot p_2}{p_1 + p_2} \right) \quad (2.26)$$

$V_{storage,n}$ is the volume of stored gas referenced back to 'normal' conditions at p_n and T_n . p_m is calculated by Equation 2.26. K_m is the compressibility factor of the gas considered. V_{geom} is the geometric volume of the pipeline section. The p_m and $p_{m'}$ denote the upper and lower mean pressure of the pipeline section. The sum of all pipeline sections n defines the total line pack volume. The line packing volume for the hydrogen value chain in this research is further elaborated in chapter 3, where the flow rate, demand and operating pressure of the pipeline system define the total line pack volume.

The CAPEX cost for a typical hydrogen distribution pipeline is estimated between 0.2 and 0.6 million euros per km. The CAPEX cost can be divided into two sections. The material cost for the pipeline and the civil works necessary to install the pipeline distribution network. The total CAPEX cost for a pipeline distribution network heavily depends on the environment of the installation. Due to either built areas or the need to cross waterways or highways, the cost of installation of a new pipeline distribution network can be increased drastically. Repurposing existing gas infrastructure could reduce this value by 10-35%. The estimated cost for transportation of a single kg of hydrogen with a distance of 1000 km is estimated 0.11-0.21 euro (ENTSOG et al., 2021). The technical and economic constraints of the pipeline considered in this research between the production location and the hub station are presented in chapter 3

2.5.4. Distribution Network Topology

A single distribution network configuration is taken into account in this research. ?? reflect the value chain topology schematically. The compression and filling of the MEGC or HPSC are located at the hub refuelling station.

The value chain contains the following components from the hydrogen production location contains to the filling process of the MEGCs or HPSCs:

- PEM electrolyser
- Distribution Pipeline
- Diaphragm compression module
- Valve panel
- MEGC/HPSC loading bays

As previously discussed, the diaphragm compressor maintenance increases and the lifetime of the diaphragm decreases with intensive start-stop cycles due to an intermittent flow rate (Rohatgi & Northwest, 2015). The pipeline utilises the principle of line packing and provides buffer storage for the hydrogen compression module. The combination of a pipeline as buffer storage and the compression module is assumed to provide the minimum flow rate required to encounter the intermittent hydrogen production at the electrolyser. For model simplification, the compression module is assumed to handle

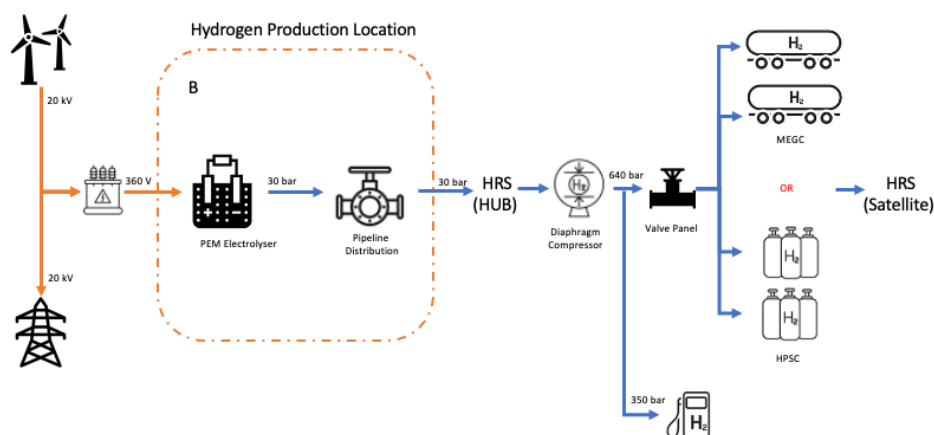


Figure 2.33: Simplified topology of distribution network layout

the intermittent hydrogen production adequately, and no minimum flow rate is required.

The compression module compresses the hydrogen up to the desired working pressure level for transportation. As discussed in section 2.4 the diaphragm compressor is applied in this research based on a trade-off between a commercially available ionic and diaphragm compressor. The valve panel is the backbone of the filling station. The valve panel controls the filling process and monitors the safety of the entire filling process. The MEGC or HPSC are connected to the valve panel for filling the composite pressure vessels. The MEGC or HPSC trailers are placed in the docking bays where a connection to the valve panel is present. A single connection between the MEGCs and the valve panel is assumed. The mechanics behind the loading/unloading of the different sized MEGCs the HPSC is outside the scope of this research. All CAPEX and OPEX components and operation parameters are described in chapter 3.

2.6. Hydrogen Refuelling Station

This section describes the components considered at the hydrogen refuelling station. Two types of refuelling stations are discussed the hub refuelling station and the satellite refuelling station. The refuelling station's topology is designed by Hygro and taken as reference.

Hub Station

The hub HRS is supplied directly from the production location via a hydrogen pipeline. The topology of the hub station is depicted in Figure 2.34. An overview of system components at the hub HRS is:

- Diaphragm compressor
- Valve panel
- MEGC or HPSC storage
- Pre-cooler unit
- 35 & 70 MPa hydrogen dispenser
- Electricity grid connection
- stationary storage 98 Mpa
- 98 Booster compressor

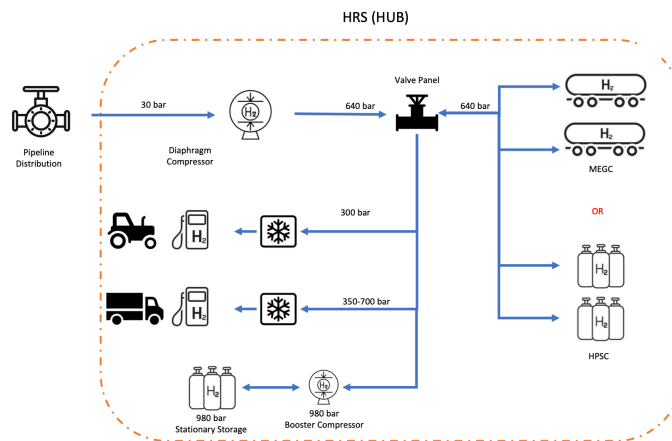


Figure 2.34: Simplified diagram hub refuelling station

At the hub station, the hydrogen is compressed from the low-pressure hydrogen distribution pipeline up to a pressure level suitable to fill the MEGC or the HPSC. The transportable storage considered at the hub HRS provides storage for vehicle filling or is transported to satellite stations in the area.

The valve panel is the backbone of the hydrogen refuelling station. It interconnects the compressor module with 350 bar and 350/700 bar hydrogen dispensers and the MEGC or HPSC storage containers. The hub station layout designed by Hygro includes a 700 bar filling application. The application of refuelling up to 700 bar is not considered in this research. However, Long haul heavy-duty fuel cell trucks may adopt 700 bar storage tanks instead of 350 bar storage tanks due to increased travel range as more hydrogen can be stored in the same storage volume. Therefore the layout designed by Hygro has the option for 700 bar filling purposes taken into account for possible long haul heavy-duty vehicle filling purposes and other hydrogen vehicles that apply 700 bar hydrogen storage tanks. The investment cost for the extra 98 MPa stationary storage vessels and a single small-sized booster compressor to reach a pressure level of max 98 MPa for the 70 MPa filling process is small compared to the entire refuelling station.

Next to facilitating the hydrogen connection between the dispenser and the transportable storage units, electronic valve connections are assumed to facilitate the ability of a cascade system operation. The total size of the valve panel is dependent on the amount of MEGC or HPSC connection points. Numerous measurement equipment is present within the hydrogen refuelling station to measure the hydrogen gas's pressure, temperature, and mass flow. Extensive hydrogen flow modelling within the hydrogen refuelling station is outside the scope of this study.

Satellite Station

The topology of the satellite HRS is slightly different to the hub HRS. No pipeline connection between a production location and the HRS is present. The compressed hydrogen is supplied to MEGC or HPSC at a high-pressure level from the hub refuelling station. The valve panel connects the MEGC or HPSCs with the hydrogen dispenser, and similar to the hub HRS configuration, electronic actuators are assumed to provide cascade system operation directly from the MEGCs or HPSCs. A list of HRS system components is:

- Valve panel
- MEGC or HPSC storage
- Pre-cooler unit
- 35 MPa hydrogen dispenser

- Electricity grid connection

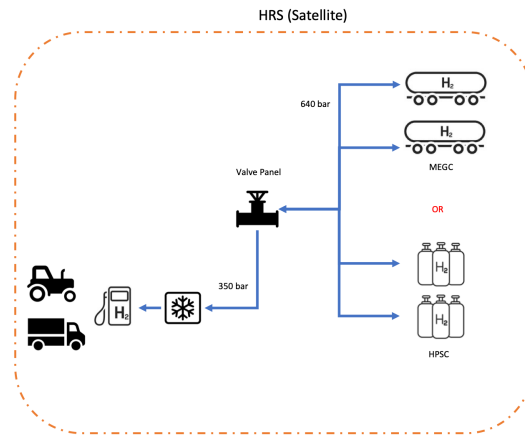


Figure 2.35: Simplified Topology Satellite refuelling station

The Hydrogen Refuelling Station's (HRS) primary function is to supply fuel to the hydrogen-powered vehicles in the most cost and energy-efficient manner while providing a high level of safety regarding the handling of the compressed hydrogen gas. Different technical HRS configurations are defined based on the hydrogen production location and the pressure level of the hydrogen supplied by the distribution network. A technical representation of the valve panel from the MEGC or HPSC storage vessels up to the hydrogen dispenser is described by Figure 2.36.

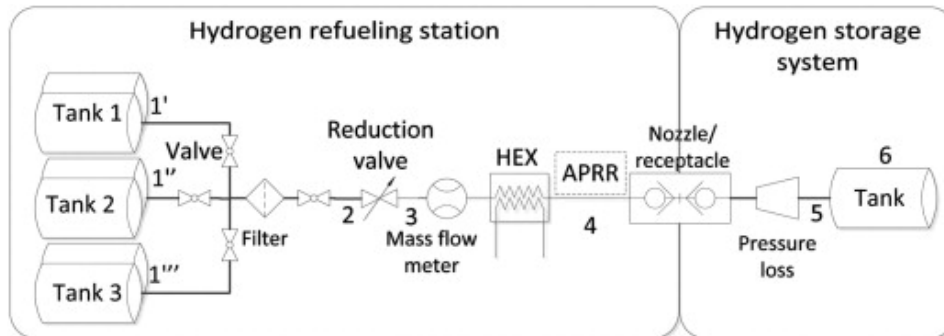


Figure 2.36: Piping diagram cascade filling process (Rothuizen et al., 2013)

In this research, the adoption of a cascade filling system is assumed. To perform proper cascade filling, the storage is sectioned into at least 3-4 sections (Rothuizen & Rokni, 2014). The MEGC or HSPC are an integral part of the HRS storage system and, therefore, part of the cascade filling system. The filling process starts with filling up the vehicle's fuel tank from the high-pressure storage vessels with the lowest operating pressure. When the HRS storage vessel and the fuel tank of the hydrogen vehicle reach the same pressure level, the second high-pressure storage vessel with the subsequent highest operating pressure starts filling up the vehicle's fuel tank. This process repeats until the SOC of the vehicle's fuel tank reaches the desired level. The SOC is defined as the ratio between the target density at ambient temperature conditions and the actual density in the hydrogen fuel tank (Rothlauf, 2011). Compared to a single storage vessel system, a higher mass flow can be achieved before the last storage vessel drops below the target pressure (Bauer et al., 2019). Rothuizen et al. (2013) has concluded that the application of a cascade filling system could reduce the need for compression by 17% and the energy consumption for cooling by 12% when comparing a cascade filling operation from multiple sections with a single storage system.

An example of the pressure levels, temperature levels, mass flow and cooling demand at an HRS during the process of cascade filling a 70 MPa hydrogen vehicle fuel tank is depicted in Figure 2.37. The graphs are obtained from Rothuizen et al. (2013), where the numbers correspond to the locations in Figure 2.36.

During fast refuelling of the hydrogen fuel tank, heat is generated. Two factors influence the total heat built up in the hydrogen fuel tank. The first factor is the heat created by adiabatic hydrogen compression by increasing the pressure inside the hydrogen fuel tank. The second heat source is caused by the Joule Thompson effect. The Joule-Thompson coefficient is negative for the considered pressure and temperature ranges of the hydrogen filling process and results in heat built up upon gas expansion (Rothuizen & Rokni, 2014). When considering a cascade filling system, the relative pressure difference between the HRS storage and the hydrogen vehicle’s fuel tank is lowered for each cascading stage. The lowered pressure difference results in less cooling of the hydrogen gas as the Joule-Thompson effect is reduced, which is dependent on the pressure difference (Rothlauf, 2011).

The total electricity demand for cooling the hydrogen gas to the desired temperature can be described by Equation 2.27, where Q is the cooling demand, and COP is the coefficient of performance of the refrigeration unit (Rothuizen & Rokni, 2014). Nistor et al. (2016) indicate based on empirical data that the cooling requirement from 15°C to -20°C or to -40°C is equal to $0.18 \frac{kWh}{kg_{H_2}}$ and $0.33 \frac{kWh}{kg_{H_2}}$, respectively. Hygro has conducted extensive analysis on the hydrogen dispensing units adopting the cascade filling process. According to HYGRO, an average of $0.1345 \frac{kWh}{kg_{H_2}}$ is required during the filling process. Taking into account a COP of 1.0 the electrical demand is equal to $0.1345 \frac{kWh}{kg_{H_2}}$ dispensed. In further calculations in this research, the average value obtained from Hygro’s thermodynamic model for cooling the hydrogen gas is considered.

$$W = \frac{Q}{COP} \tag{2.27}$$

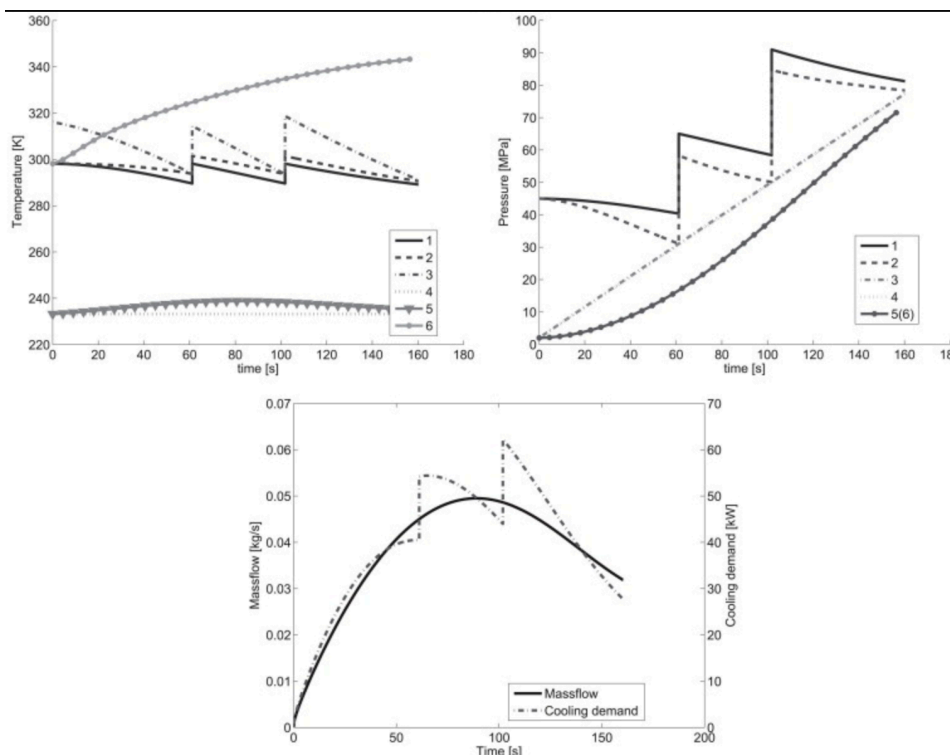


Figure 2.37: Example cascade filling process (Rothuizen et al., 2013)

For refilling of hydrogen fuel tanks, either a table-based or formula based protocol is applied. The

J2601 protocol is developed by the Society for Automotive Engineers (SAE) and ensures the ability to provide fast refilling of hydrogen fuel tanks without exceeding the operating limits of the hydrogen storage tanks. The protocol describes the filling process to reach up to 100% State Of Charge (SOC), without surpassing the fuel tank temperature range between -40 and 85 degrees Celsius and pressure limits not higher than 125% the nominal working pressure under ambient temperature conditions defined as 15c. (Miguel et al., 2017). The protocol describes two pressure ratings, H35 and H70, and four dispensing temperatures, A, B, C and D (Rothuizen et al., 2013). An overview of the possible dispenser pressure ratings and dispensing temperatures is given by Table 2.4. The SAE J2601-2 describes filling speeds for heavy-duty vehicles with hydrogen storage tanks larger than 10 kg. The three proposed filling speeds are 1.8, 3.6 and $7.2 \frac{kg_{H_2}}{min}$. In this research, it is assumed that a filling speed of $7.2 \frac{kg_{H_2}}{min}$ is adopted for the filling process up to 35 MPa. This corresponds to the average cooling requirements of $0.1345 \frac{kWh}{kg_{H_2}}$ mentioned previously.

Dispenser Configuration	Pressure [bar]	Temperature [C°]
A70	700	-40
A35	350	-40
B70	700	-20
B35	350	-20
C35	350	0
D35	350	Ambient

Table 2.4: Hydrogen dispenser ratings according to SAE J2601 (Rothuizen et al., 2013)

2.7. Hydrogen Demand

This research applies an approach where a distinction is made between the fuel demand of two different heavy-duty end-user categories. The first heavy-duty end-user category adopts fuel cell electric drivetrain technology, whereas the second heavy-duty end-user category adopts a dual-fuel combustion engine. The goal is to translate current diesel fuel demand into future hydrogen demand patterns based on the two different hydrogen drivetrain technologies.

To get a good understanding of the hydrogen fuel demand pattern for both end-user categories, a comparison must be made on drive train topology and drivetrain efficiency in reference to their diesel-powered alternatives. This section aims to define the working principle of both heavy-duty end-user drive train topologies and define their hydrogen demand characteristics regarding power consumption compared to the conventional internal combustion diesel engine. Detailed demand modelling based on actual demand data of both end-user categories is discussed in chapter 3.

Table 2.5 shows an overview of the general vehicle classification defined by the European Union (?). The vehicle class for transporting goods is denoted by N, and the vehicle class containing agricultural equipment is denoted by T. Multiple subcategories can be identified based on weight, size, and vocational use when considering commercial heavy-duty transport vehicles. Heavy-duty vehicles are further categorised based on gross vehicle weight, shown in Table 2.6. The large subset of categories results in a large design space for the Fuel Cell Electric Truck (FCET) drivetrain (Marcinkoski et al., 2016b). Therefore, in this research, a generalisation is made for all heavy-duty vehicles and their different weight classes are neglected. A reference FCET truck is defined based on several commercially available FCETs and further adopted to compare diesel-powered heavy-duty vehicles and the FCET.

2.7.1. Diesel Internal Combustion Engine

Currently, both end-user categories rely on the propulsion and operation of the diesel fuel. The diesel-powered vehicles are fitted with ICE and utilise the chemical process of converting energy from a fuel

General Vehicle Categories	
Class	Description
M	Vehicles carrying passengers
N	Vehicles carrying goods
L	2- and 3-wheel vehicles and quadricycles
T	Agricultural and forestry tractors and their trailers
O	Trailers

Table 2.5: European general vehicle categories (EU, 2021)

Goods Transportation Vehicle Categories	
Class	Description
N1	Carriage of goods, Gross-Weight < 3.5 t
N2	Carriage of goods, Gross-Weight > 3.5 t, < 12 t
N3	Carriage of goods, Gross-Weight > 12 t

Table 2.6: European heavy duty transport vehicle categories (EU, 2021)

and air mixture into mechanical work (Marcinkoski et al., 2016b). The combustion of the diesel-air mixture results in the movement of a piston inside a fixed cylinder that drives a crankshaft. A connection through a gearbox ensures the rotation of the wheels and provide propulsion to the vehicle.

Two types of internal combustion engines can be identified. The spark ignition (SI) and the compression ignition (CI) (Marcinkoski et al., 2016b). Both heavy-duty vehicle categories considered in this research use CI engines. The CI engine uses the concept of compression and heat built up to ignite the diesel-air mixture inside the engine cylinder. Due to the higher energy content of diesel of 10-15% compared to petrol and higher powertrain efficiency, the diesel CI engine is preferred for heavy-duty vehicles (Marcinkoski et al., 2016b). In Figure 2.38 the working principle of a CI engine is shown.

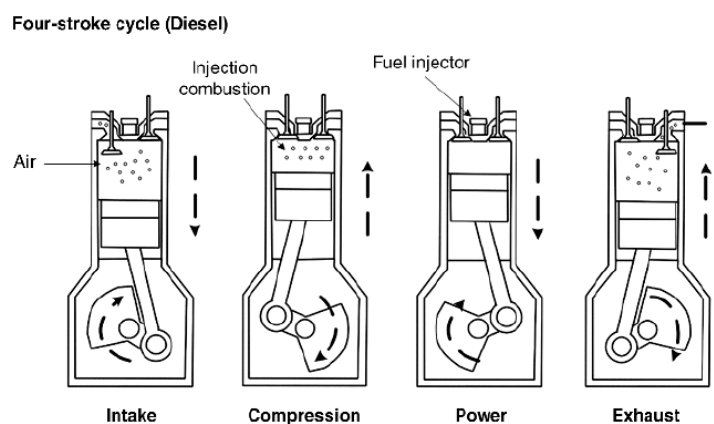


Figure 2.38: Working principle compression ignition engine (Fallah, 2014)

2.7.2. Fuel Cell Electric Truck

Figure 2.40 depicts a typical system topology for an FCEV drive train. The FCEV adopts compressed hydrogen as an energy carrier and utilises a fuel cell to convert the compressed hydrogen gas stored in the pressure vessels into electrical energy. An electric motor converts the electrical energy into mechanical work and provides propulsion for the vehicle. A battery bank in the FCEV is present as a buffer storage to decrease the peak energy demands and ensure the stable operation of the FC. Less dynamic operation of the fuel cell increases the lifetime of the fuel cell. The battery bank is also used



Figure 2.39: Fuel Cell Truck

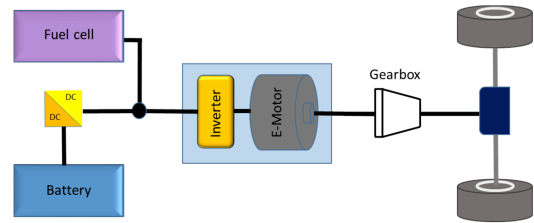


Figure 2.40: FCEV drivetrain topology (Röck et al., 2020)

to store energy from recuperative braking (Röck et al., 2020).

Hyzon motors is one of the leading companies bringing heavy-duty fuel cell trucks to the market. An overview of the proposed FCETs from HYZON Motors and their technical specifications is shown in Table 2.7. Currently, the first HyMax-450 trucks are being implemented in the Netherlands. Further considerations of the FCET end-user category are based on the technical parameters of the Hyzon HyMAX-450 FCET with a hydrogen storage capacity of 35 kg at a storage pressure of 350 bar.

Hyzon FCET			
Parameter	HyMax-160	HyMax-250	HyMax-450
Chassis weight [tonne]	19	25-40	40+
Electric Motor [kW]	160	250	450
Fuel cell [kW]	30	45	60
Storage pressure [bar]	350	350	350
Hydrogen storage [kg]	15	20	30-65
Battery [kWh]	70	140	140
Battery voltage [V]	450	140	700

Table 2.7: Overview Hyzon Motors FCET

2.7.3. Dual Fuel Vehicle

Dual-fuel technology uses an injection of alternative clean fuel in the internal combustion engine and contributes towards an overall emission reduction. In spark ignition (SI) engines, dual-fuel technology has encountered several problems. However, for compression ignition (CI) engine, it has shown promising results as the efficiency of the engine increases at specific loads (Cernat et al., 2020). Hydrogen cannot solely be used as fuel in a CI engine, as the temperature due to compression is not high enough to overcome the activation barrier and initiate combustion. An ignition source is required. Diesel will contribute as the primary fuel and ignition source for hydrogen. The combustion of diesel provides a significant part of the energy, and the rest is supplied by green hydrogen (Saravanan et al., 2008). The Dual-Fuel Vehicle (DFV) is a solution that can directly be implemented into the mobility industry without relying on a constant hydrogen energy source. A reduction of NO_x by 75% and a 22% reduction of CO_2 emissions for the hydrogen dual fuel vehicle built by H_2 Dual Power (H2DualPower, 2021) shows a good starting point for early-stage development of alternative fuels such as hydrogen. Blending in hydrogen with current fossil fuels could help transition towards an infrastructure based on solely green alternatives.

The demand for hydrogen for the dual-fuel vehicle is not fixed due to the ability to operate solely on diesel fuel if necessary. When considering the wind-based hydrogen value chain, hydrogen production costs are kept at a minimum when hydrogen production is obtained from the wind turbine compared to grid energy. Demand flexibility agreements between the customer utilising dual-fuel vehicles and

the value chain operator could reduce operating costs for the hydrogen value chain operator. Consequently, operating cost reduction could lead to lower hydrogen cost at the HRS for the customer.

The commercial application of the dual-fuel hydrogen tractor developed by H2DualPower (2021) is taken as a reference to represent the second heavy-duty end-user category. The hydrogen dual-fuel tractor can be used for either agricultural applications or contractor work. An overview of technical parameters of the dual-fuel tractor is shown in Table 2.8. The dual-fuel tractor from H2DualPower is based on a New Holland t5.140 AutoCommander with an 11.5 kg hydrogen storage container. During operation, the hydrogen is mixed in a ratio with diesel fuel between 15-60% dependent on the operation circumstances (Scholman & Scholman, 2020). For high load operation, the low-energy density of hydrogen is not sufficient to provide enough power, and more diesel is consumed. On average 40% hydrogen is injected into the fuel system before combustion (Scholman & Scholman, 2020). The hydrogen is injected on an 8 bar pressure level. The average injection of 40% is taken as a reference for further calculations on hydrogen demand for this end-user category.

H2 Dual Power Duel Fuel Tractor	
Parameter	New Holland H2 T5.140
Diesel Engine [kW]	103
Fuel Cell [kW]	x
Storage pressure H2 [bar]	350
Hydrogen storage [kg]	11.5
Diesel storage [L]	180

Table 2.8: Technical details H₂DualPower dual-fuel hydrogen tractor (Scholman & Scholman, 2020)

Quantifying the energy consumption of an internal combustion engine, fuel cell drivetrain or Dual-fuel engine is a complex task. The fuel consumption is dependent on multiple parameters. Some parameters of influence on fuel consumption are the weight of the transportable load, travelling speed, vehicle size, engine temperature and ambient environmental conditions such as drag and ambient temperature conditions (Hjelkrem et al., 2020). The individual comparison of many parameters of influence on the energy consumption of heavy-duty vehicles when comparing the drivetrain topologies and the operating conditions are considered outside this study's scope.

A more straightforward approach is taken to analyse current diesel demand for both end-user application categories and translate the demand to the future hydrogen demand. A constant value representing an average energy consumption efficiency from Tank-To-Wheel (TTW) ensures the ability to translate current diesel demand data into expected hydrogen fuel demand patterns on a large scale. The average TTW efficiency includes all losses in the combustion engine, fuel cell or Dual fuel drivetrain topology (Röck et al., 2020).

This research determines an average TTW energy consumption efficiency for both ends user categories based on literature findings. For the heavy-duty FCET category adopted in this research, the extensive TTW analysis for heavy-duty vehicles conducted by the Joint Research Center of the European commission is taken as reference (Röck et al., 2020). The study reports an extensive TTW energy consumption analysis on two heavy-duty FCET configurations compared to conventional diesel-based ICE. The study compares drive train topologies for a rigid truck with 18 tons of gross vehicle weight, designed for regional delivery. As well as a tractor-semitrailer combination with 40 tons gross vehicle weight, designed for long-haul transportation applications.

An overview of the results from the conducted study by the JRC is shown in Figure 2.41 and Figure 2.42. The average TTW energy consumption is depicted in $\frac{MJ}{tkm}$. The essential findings relevant for this research is the improvement of the TTW energy consumption when comparing the heavy-duty FCET to the conventional diesel ICE vehicles. The TTW of a conventional diesel engine is estimated at 23% (Cunanan et al., 2021). A decrease in TTW energy consumption by 20% is observed when

comparing FCET for long-haul applications, and a decrease of 35% in TTW energy consumption is observed when comparing FCET for regional delivery applications. In this research, the energy demand for the FCET is based on waste collection vehicles. The application of waste collection vehicles corresponds to the regional delivery application with a 35% reduction in TTW energy consumption. A decrease in fuel demand of 35% is assumed for the FCET heavy-duty end-user category.

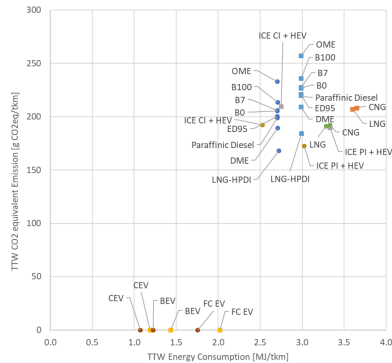


Figure 2.41: TTW research results for the regional delivery truck for multiple drivetrain technologies (Röck et al., 2020)

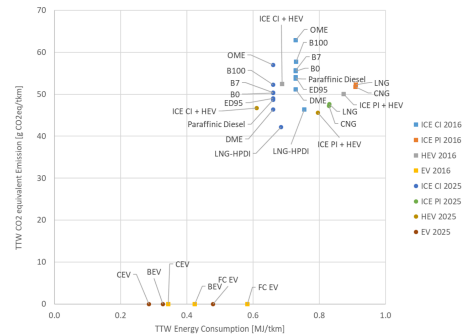


Figure 2.42: TTW research results for the long haul delivery truck for multiple drivetrain technologies (Röck et al., 2020)

Karagöz et al. (2016) has performed research on the effect on performance emission when the hydrogen-diesel mixture is used in a diesel ICE. Hydrogen was injected into the intake manifolds to create a dual-fuel mixture with the ratios of the hydrogen energy content of 25% and 50%. 0% hydrogen injection was taken as pure diesel operation. The amount of injected hydrogen was determined based on energy content compared to the replaced diesel fuel. Notable findings were that for both hydrogen-diesel fuel mixtures, power loss was observed. Under the operation of 25% hydrogen-diesel mixture, an 8.1%-15.1% power reduction was noticed as for the 50% hydrogen-diesel mixture. A 10.8%-25.4% power reduction was observed compared to only diesel fuel operation. However, the research shows a decrease in engine performance but does not describe the change in overall TTW energy efficiency. Due to inadequate literature on the overall efficiency TTW performance on hydrogen dual-fuel engines, no change in TTW efficiency is assumed for the dual-fuel vehicle.

3

Case Study The Netherlands

This chapter introduces a case study to model and research the optimal choice of storage aim to determine the levelised cost of hydrogen at the refuelling station. The case study is based on the future development of the DUWAAL project conducted by HYGRO in North Holland in the Netherlands. The case study will provide input parameters to research the effect of different spatial configurations of the value chain in combination with different non-stationary storage technologies. An optimisation model is created to model the entire value chain and minimise the objective function based on the total system cost. The results from this optimisation problem will be used to develop a recommendation for the optimal roll-out strategy given specific spatial configurations and demand applications.

A similar chapter layout is adopted as chapter 2. The two first sections will discuss the power source for hydrogen production. Technical and economic constraints for the wind turbine and grid connection used in the value chain are characterised, and an extensive description of the model determining the power production by the wind turbine is discussed. This section also describes the interaction with the electricity market. The third section defines the conversion process of the PEM electrolyser and its corresponding technical and economic constraints. The constraints for the compression module are treated in section 3.4. The two different transport containers and their corresponding techno-economic constraints for the case study are described in section 3.5. The Hydrogen Refuelling Station (HRS) for the case study is characterised in section 3.6. A stochastic model that defines the demand at the HRS is discussed in section 3.7.

3.1. Wind energy

This section discusses the technical and environmental constraints of the wind turbine used in the case study. A simplified method to calculate the wake effect by neighbouring wind turbines is proposed and validated by comparing the model output values with a comprehensive energy yield calculation report conducted by Pondera Consult for the ECN Wieringermeer wind park. Data used for the climate model and input data for the power production by the wind turbine is obtained from the ERA5 reanalysis database and validated by regression analysis with measured data from the ECN Wieringermeer wind park. Finally, the cost function of the wind turbine is defined.

3.1.1. Technical constraints Wind turbine

The most significant impact on the choice of a wind turbine is the site conditions and corresponding site constraints. Factors limiting the choice of the wind turbine relies upon the type of wind class at the production site's location and the site-specific constraints proposed by the wind turbine site developer. An international standard sets the wind classes by the International Electrotechnical Commission (IEC). Three parameters distinguish the IEC wind turbine classes. The turbulence intensity, average wind speed and maximum wind gust occur once every fifty years. Other influential factors on the choice of the wind turbine are the site-specific constraints. Some site-specific constraints are noise constraints,

the maximum hub height, the maximum height of the rotor blades, rotor diameter and environmental constraints. The case study is limited to the province of North Holland in the Netherlands. Figure 3.1 shows the current and expected feasible locations for wind turbine installations. The green dots picture currently installed wind turbines. The blue shaded area shows potential wind turbine locations, where the yellow shaded area shows potential future locations for solar and wind energy combined NHN (2021).

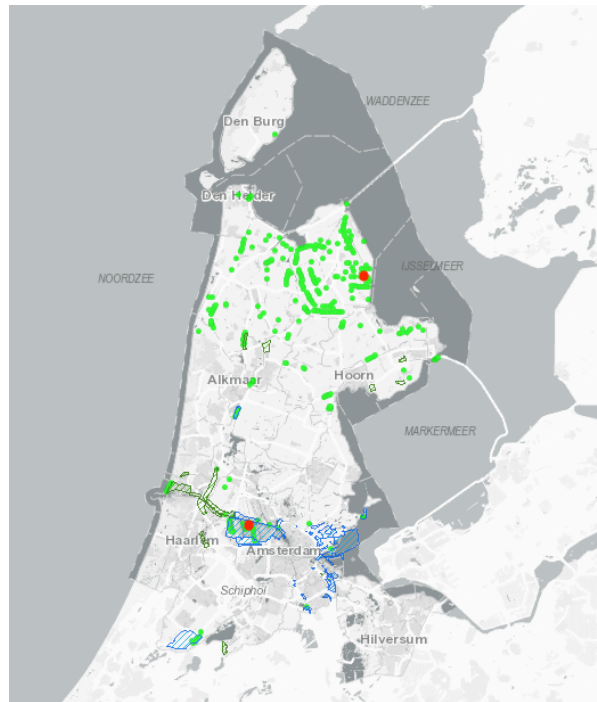


Figure 3.1: Map of the Province of Noord-Holland and the wind turbine locations (NHN, 2021)

In the case study, two wind turbine locations are determined. The first wind turbine location is located in the northern part of the province. HYGRO has installed a wind turbine at this site, and local wind speed measurement data is available. Measurement data from a nearby meteoromast creates the ability to validate the wind climate model proposed in the following subsection. A second wind turbine location is determined. A large spatial distribution of the two wind turbines results in the opportunity to model and research extended and short-distance value chain configurations. The second location is in the blue shaded area in the Port of Amsterdam. The Port of Amsterdam provides an exciting location as both turbines are spatially distanced. The second motivation for this location is a practical implementation of heavy-duty vehicles in the Port of Amsterdam. Placing a wind turbine in an area of high-demand results in shorter transportation distances between the hydrogen production site and the refuelling station, which can be economically beneficial. The locations of the wind turbines used in the case study are shown by a red dot in Figure 3.1.

The wind turbine installed and located at the ECN Wieringermeer wind park will be taken as a reference to create the wind climate model and power production model. The output of the power production model will be used as input for the optimisation model. The power production model is based on historical data. The same power production model will be used for the turbine location in The Port of Amsterdam. The wind climate model will be validated by using multiple wind data sources. The power production by wind turbine will be validated with a site analysis report commissioned by HYGRO. The assumption is made that the turbine and surrounding power electronic systems installed in the Port of Amsterdam is identical to the wind turbine installed at the ECN Wieringermeer wind park. Site-specific parameters such as wind speeds, surface roughness and neighbouring turbines that define the overall power production and adjacent wake effect will be analysed independently. General system efficiency losses are taken from a confidential site analysis report by Pondera Consultancy for the wind turbine

located at the ECN Wieringermeer wind park. The overall system losses are identical at both wind turbine locations. General efficiency losses include turbine reliability, electric cable losses, the internal electricity consumption of the wind turbine, blade degradation due to icing and contamination, hysteresis and shadow flicker.

The decision made by HYGRO is to implement the Enercon E126-EP3 4MW wind turbine based on the site-specific constraints of the ECN wind park. This turbine is used in the case study for both locations. Technical parameters of the Enercon E126-EP3 wind turbine are given by table Table 3.1.

Technical Parameters	Wind Turbine
Wind Turbine Type	Enercon E-126 EP3-4000
Rotor Diameter [m]	127
hub Height [m]	116
Tip Height [m]	179.5
Rated Capacity [kW]	4000
Operating mode	0s
Wind Class	IEC IIA
Turbine type	Gearless, variable speed, single blade adjustment

Table 3.1: Technical Parameters ENERCON E126-EP3 4000kW Wind Turbine (HYGRO, 2021)

3.1.2. Wind climate model

The average hourly wind speeds and overall wind climate is site-specific. A detailed modelling approach will be discussed in this section, in which an overview is presented with site-specific parameters and general system parameters. The first site-specific parameter is the surface elevation of the wind turbine. The second site-specific parameter is the surface roughness factor. The surface roughness factor describes the environment and surface terrain around the wind turbine on the wind speed. Wind speed follows a logarithmic profile with increasing height. The surface roughness factor describes the logarithmic profile's shape and depends on the surface terrain. The terrain around the wind turbine located in the ECN Wieringermeer wind park is described as flat agricultural farmland and results in a small surface roughness factor. The surface roughness factor for the location in the Port of Amsterdam is higher as this turbine is placed in a built environment which results in a more considerable impact on the wind speed. The surrounding buildings will influence the overall wind speed and reduce power production. The surface roughness factor for both locations is taken from the Corine Land Cover 2018 Database. The ECN Wind park surface roughness is estimated to be 0.05 m, and the surface roughness factor at the port of Amsterdam is equal to 0.5 m (Silva et al., 2007). The third site-specific parameter includes the surrounding obstacles and neighbouring wind turbines. Obstacles and neighbouring wind turbines negatively affect the wind speed and reduce the overall power output of the wind turbine. In this research, only neighbouring wind turbines are taken into account. Site-specific obstacles that could influence the wind speed are not considered in the wind climate model.

The ECN Wieringermeer wind park will be used as a reference to explain the wind climate model and wake effects caused by the surrounding wind turbines. The ECN wind park and the hydrogen turbine is shown in Figure 3.2. For the ECN Wieringermeer wind park, two sources are used to obtain site-specific climate data. The first source is wind data provided by ECN and measured at a nearby meteorological mast. The meteorological mast is located 1.8 km from the hydrogen turbine location. The measurements are taken in a 10-minute timeframe. Both wind speed and wind direction measurements are recorded at different heights. Figure 3.2 shows a layout of the wind turbine park. The purple dot indicates the location of the wind turbine used in this case study. The red dots represent the locations of the wind turbines that are part of the ECN wind park. Blue dots represent existing turbines installed before the development of the wind park, and the black dots represent turbines in the area but are not included in the wake model. The orange square shows the location of the MM4 Meteorological Mast of which the wind

speed and wind direction measurement data is available.

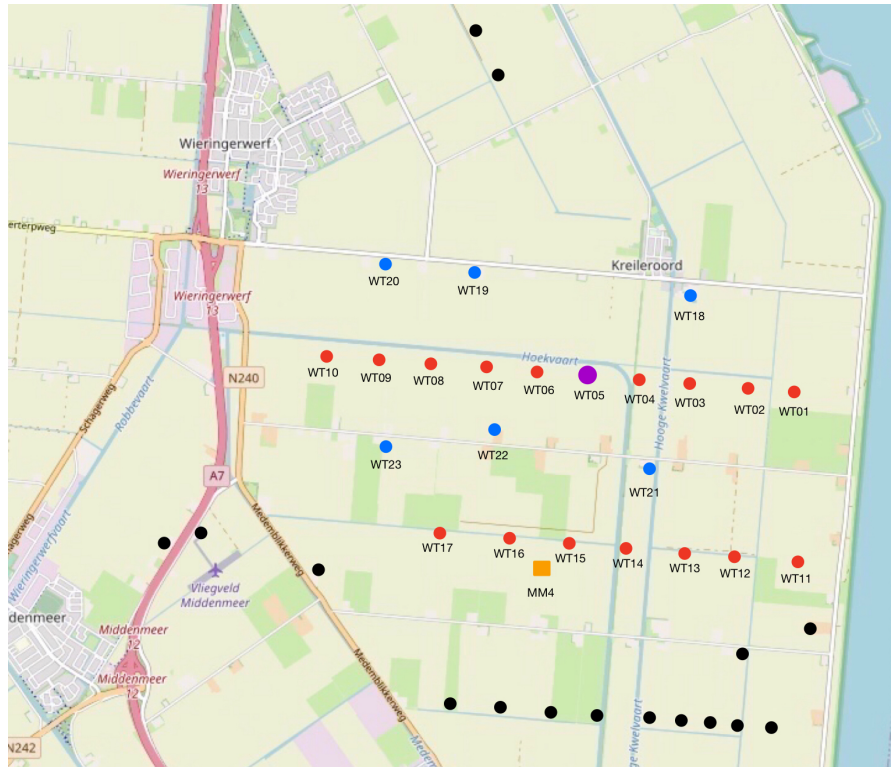


Figure 3.2: Turbine location ECN Wind park Wieringermeer (OSM)

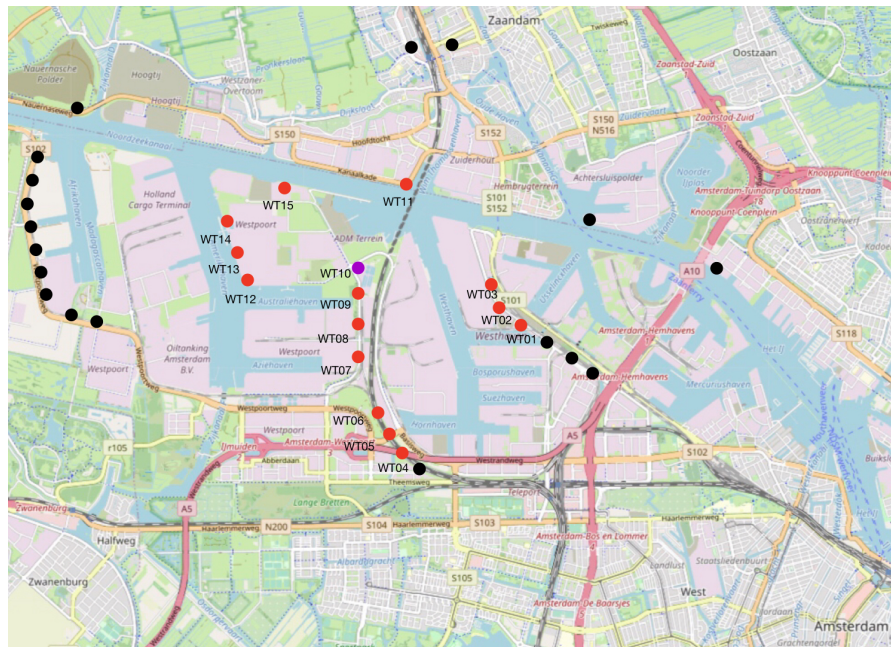


Figure 3.3: Turbine location Port of Amsterdam (OSM)

The second climate data source used in this research is the ERA5 reanalysis model developed by the European Center for Medium-range Weather Forecasts (ECMWF). The ERA5 reanalysis is the 5th generation reanalysis model of the ECMWF. The ERA5 creates a numerical estimation of the climate

around the globe based on past observations and weather prediction models to create a consistent time series for multiple atmospheric parameters. The ERA5 reanalysis data is publicly available and provides a spatial resolution of 0.25° in latitude and longitude direction. Data is available on an hourly timescale from 1979 until five days before real-time. The wind speeds are depicted in a North directional component and an East directional component. Wind speeds are available for multiple pressure levels ranging from 100 hPa to 0.01 hPa and single height levels such as 100-meter height. ERA5-land reanalysis database contains a higher spatial resolution up to 9km in latitude and longitude direction. However, The ERA5-Land database only provides hourly wind speeds and directions at 10-meter height. It is decided to use the ERA5 climate data source with lower spatial resolution as this climate model can provide wind speeds closer to the hub height of the wind turbine and thereby reduce calculation errors. A 5.5 km spatial resolution reanalysis model is being developed for the European continent. The Copernicus European Regional ReAnalysis (CERRA) model will result in a more accurate climate data source and could be used as input in future case study research. An overview of both wind data sources is given in Table 3.2

Data Source	MM4 ECN METMAST	ERA5 REANALYSIS
Type	Meteorological Measurements Mast	Reanalysis Model
Location (Latitude,Longitude)	(52.8162 , 5.0664)	(52.75 , 5)
Resolution	Single location	30x30km Grid
Distance to RW05 [km]	1.8 km	-
Measurement Height [m]	100	100
Data Period	30/05/2011 14:00 - 19/10/2016 23:00	01/01/1980 00:00 - Present(-5 days)
Used Data Period	30/05/2011 14:00 - 19/10/2016 23:00	01/01/1980 00:00 - 31/12/2020 23:00
Time step	10 Minutes	1 Hour

Table 3.2: Input for the climate model and case study

Two models can be adopted to describe the wind speed in a vertical direction. The first model is the logarithmic law. The logarithmic law is described by the function shown in Equation 3.1, where u^* is the friction velocity, κ is the Von Karman constant, z is the height, z_0 is the surface roughness length in meters. The stability component $\Psi(\frac{z}{L})$ is a function of the height z and Monin-Obukhov length L (Barthelmie et al., 2020). The stability factor ensures that turbulence created by stratification is taken into account (Xu et al., 2018). Equation 3.2 shows the relation to calculating wind speeds from a certain measurement height to the desired hub height. The second model is the power law, shown in Equation 3.3. The power law shows an empirical relationship between the height of the measured wind speed and the height of the desired wind speed. The shear exponent factor α is strongly dependent on the stability of the atmosphere and the surface roughness length (Mwanyika & Kainkwa, 2009). In general, a value of 0.143 for the wind shear exponent is used at higher elevations (Werapun et al., 2017). To implement a dynamic shear factor dependent on the ambient conditions, data on 10m height wind speeds and 100m height wind speeds is used to determine the hourly wind shear factor. Both climate data sources have measurements up to 100m height at which the influence of the local surface roughness is limited. The power law is often used between 100m and 200m (Schelbergen et al., 2020). When wind speed measurements are only available at low altitudes, the surface roughness should be considered, and the logarithmic law must be used. In the case study, the power law is used for both data sources to translate the wind speed from measurement height (100 m) to hub height of the wind turbine (116 m)

$$U(z) = \frac{u^*}{\kappa} \left[\ln\left(\frac{z}{z_0}\right) + \Psi\left(\frac{z}{L}\right) \right] \quad (3.1)$$

$$U(z) = U(z_{ref}) \cdot \frac{\ln(z/z_0)}{\ln(z_{ref}/z_0)} \quad (3.2)$$

$$U(z) = U(z_{ref}) \cdot \left(\frac{z}{z_{ref}}\right)^\alpha \quad (3.3)$$

An R^2 regression analysis is performed to validate the ERA5 database against the local measurements of the ECN MM4 Meteomast and determine if the ERA5 database can represent local wind speed climate. The correlation coefficient depicts the correlation between two datasets. A typical correlation coefficient threshold is set at 0.75 or 75% (Humpage, 2000). It can be seen in Figure 3.2 that the meteomast is located in the vicinity of two wind turbines. These wind turbines are located in the North-West and North-East direction about the ECN meteomast. The two neighbouring wind turbines could result in distorted wind speed measurements for the corresponding wind directions due to the wake effect inflicted on the meteomast. The influence of the wake effect will result in an underestimation of actual wind speed at the location of the wind turbine used in the case study. Using a more generalised wind data source as the ERA5 database is preferred to obtain realistic wind speeds for further power calculations. The R^2 regression analysis is performed for the entire timespan of measurement data for the meteomast and the ERA5 database. The ECN meteomast 10-min measurements are averaged to an hourly timeframe to match the hourly timeframe of the ERA5 data. The data used for the regression analysis contains the year 2011 up to 2016. The overall regression coefficient for all wind directions combined equals 0.85 or 85%. The overall correlation coefficient exceeds the threshold value of 0.75 or 75%. It can be concluded that the ERA5 database represents the local wind speeds sufficiently.

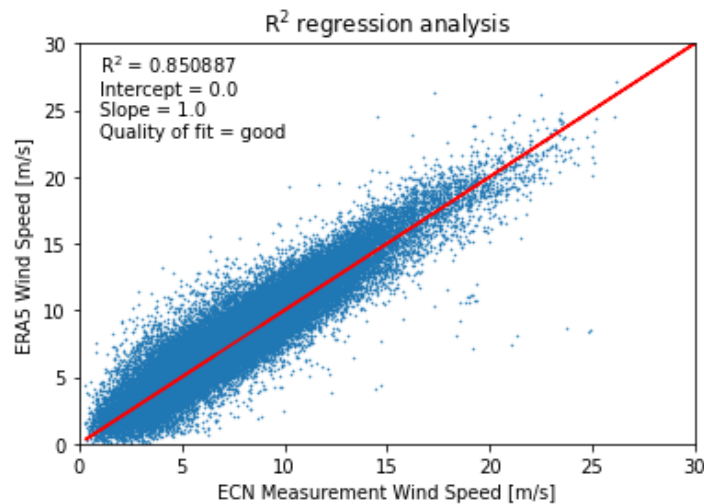


Figure 3.4: Residual plot R^2 regression analysis for all wind directions

Second regression analysis for each wind direction is performed to determine if the two neighbouring turbines influence the ECN measurement data. The wind direction is divided into 16 sections. As expected, the correlation coefficient for the North-West and North-East directions cannot meet the threshold. An overview of all correlation coefficients for each wind direction is given in Table 3.3. In Figure 3.5 and Figure 3.6 the residual plot of the wind direction with the highest correlation coefficient and the wind direction with the lowest correlation coefficient is shown, respectively. A bias can be observed in the graph with the lowest correlation coefficient. The bias is located above the regression line. This bias implies that the ERA5 database returns higher wind speeds for the same timestamp than the ECN Meteomast measurements. The bias is an expected result as for the North-East and North-West wind direction, the ECN meteomast wind speed measurements are distorted, and the wind speed is reduced due to the wake effect of the two neighbouring wind turbines. In Figure 3.4 the residual plot for all wind data is shown. In this research, the ERA5 dataset is assumed to represent local climate data and is used to analyse wind turbine locations further and perform power production calculations.

The Jensen wake model is adopted to model the effect of the neighbouring wind turbines on the wind speed. For each neighbouring wind turbine, the reduction in wind speed at the location of the hydrogen turbine is determined by Equation 3.4. The equation is derived from the Jensen Wake Model equation discussed in subsection 2.1.2. In Table 3.4 an overview is given for the distance and bearing

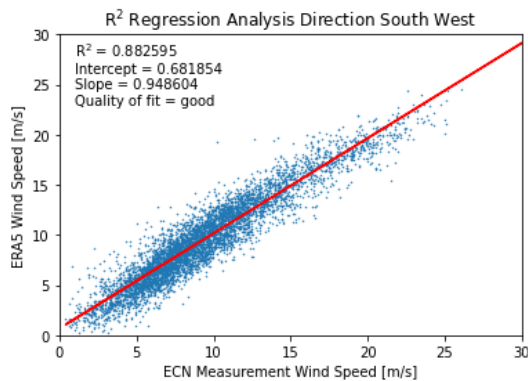


Figure 3.5: Residual plot of R^2 regression analysis for wind direction with highest correlation coefficient

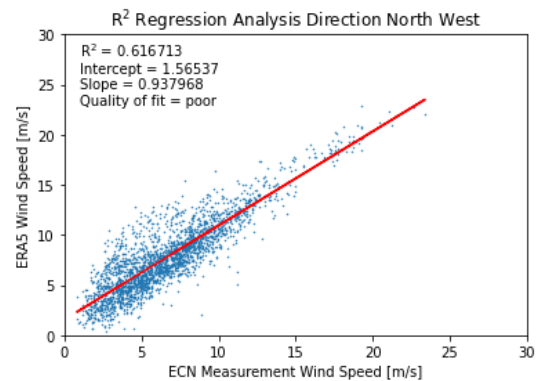


Figure 3.6: Residual plot of R^2 regression analysis for wind direction with lowest correlation coefficient

Wind Direction	R^2 coefficient	Quality of fit
North	0.7882	Good
North-NorthEast	0.7727	Good
North-East	0.6226	Poor
East-NorthEast	0.6555	Poor
East	0.8480	Good
East-SouthEast	0.8251	Good
South-East	0.8414	Good
South-SouthEast	0.8678	Good
South	0.8596	Good
South-SouthWest	0.8000	Good
South-West	0.8826	Good
West-SouthWest	0.8720	Good
West	0.8416	Good
West-NorthWest	0.8426	Good
North-West	0.6167	Poor
North-NorthWest	0.6979	Poor
Total	0.8509	Good

Table 3.3: ECN meteomast measurements and ERA5 reanalysis database R^2 regression coefficient per wind direction

in degrees about the hydrogen wind turbine for the ECN Wieringermeer wind park location. For the Port of Amsterdam, the distance, bearing and locations of the neighbouring wind turbines, which are taken into account in the case study, are shown in Table 3.5. The climate model calculates the reduction in wind speed by each turbine according to the formula shown in Equation 3.4.

The wake width can be calculated by Equation 3.5 where k_w is the wake decay constant. x is the distance between the two turbines, and R_d is the rotor diameter. The total angle of the wake cone and the bearing of the neighbouring wind turbine about the hydrogen turbine result in a wind direction range where the hydrogen turbine is located inside the wake cone of the neighbouring wind turbine. The Jensen wake model assumes a uniform wind speed reduction in both vertical and horizontal directions in the cone of the wake. It is assumed that if the hydrogen turbine is located in the wake cone of a neighbouring turbine, the wind speed reduction is equal to the difference of the ERA5 dataset and the new wind speed determined by Equation 3.4.

In the case of multiple wind turbines with a similar bearing and all contributing a portion to the wake

effect on the hydrogen turbine, the principle of superposition is adopted. The principle of superposition results in a total wind speed reduction equal to the wind speed reduction by every turbine summed. Gunn et al. (2016) has researched the limitations of the principle of superposition in the calculation of power production in a wind turbine park. It is shown that the principle of superposition does not depict the actual reduction in wind speed due to the wake effect but is assumed sufficient and adopted in this research. Three neglected effects were essential to correctly model wind speed and power production by the wind turbine. The first effect is the shortening of the wake when turbines are aligned relative to comparing it with a single turbine. Secondly, when wakes are adjacent, each will be lengthened due to reduced mixing. Finally, the pressure field of downstream turbines can modify and move wakes. The superposition overall results in a slight overestimation of the power production. In this research, the simplicity of the superposition principle is chosen over complex CFD modelling to correctly model wake effects on the hydrogen turbine. The real rotor diameter of the neighbouring turbine is taken into account if known. If not known, the rotor diameter of the specific turbine location is set equal to the rotor diameter for the 4MW ENERCON wind turbine.

$$U_w = U - U \left(\frac{1 - \sqrt{1 - C_t}}{\left(1 + \frac{k_w x}{R_d}\right)^2} \right) \quad (3.4)$$

$$W_w = k_w x + R_d \quad (3.5)$$

Wind Turbine	Latitude	Longitude	Distance to hydrogen turbine [km]	Bearing [deg]
WT10	52.414281	4.800022	-	-
WT01	52.408685	4.831787	2243	251
WT02	52.410339	4.828471	1979	255
WT03	52.412368	4.826151	1785	261
WT04	52.393779	4.805752	2313	188
WT05	52.396306	4.803253	2011	185
WT06	52.398877	4.801418	1715	182
WT07	52.404044	4.800056	1138	180
WT08	52.407562	4.800047	747	180
WT09	52.410780	4.800032	389	180
WT11	52.426452	4.813346	1627	328
WT12	52.412285	4.779633	1401	100
WT13	52.417187	4.779633	1420	75
WT14	52.421045	4.774861	1865	64
WT15	52.422724	4.79204	1084	27

Table 3.4: Port of Amsterdam wind turbine locations in geographical coordinates, distance and bearing in reference to the hydrogen turbine

3.1.3. Wind & Power Output Modelling

The wind speed calculated by the climate data model for both wind turbine locations is used as the input for the power production of the wind turbine. The power curve depicts the relationship between the power output of the wind turbine and the wind speed. The power curve for the Enercon E-126 EP3 wind turbine is shown in Figure 3.7. The site analysis report by Pondera consult has provided an overview of the general system efficiency losses at the ECN Wieringermeer wind park. Table 3.6 shows an overview of all efficiency loss factors on the annual power production. The loss factors defined by the site analysis report will be used in the power production calculations in this research. Wind turbine

Wind Turbine	Latitude	Longitude	Distance to hydrogen turbine [km]	Bearing [deg]
WT05	52.832064	5.073605	-	-
WT01	52.830447	5.102333	1.94	265
WT02	52.830816	5.095166	1.46	265
WT03	52.831197	5.088001	0.97	265
WT04	52.831569	5.080823	0.49	265
WT06	52.832384	5.066615	0.47	87
WT07	52.832678	5.059321	0.96	87
WT08	52.833046	5.052154	1.45	87
WT09	52.833435	5.044978	1.93	87
WT10	52.833801	5.037797	2.41	87
WT11	52.816583	5.100404	2.49	235
WT12	52.816954	5.093248	2.14	227
WT13	52.81733	5.086066	1.84	215
WT14	52.81769	5.078909	1.64	197
WT15	52.818094	5.071111	1.56	171
WT16	52.818493	5.063351	1.66	147
WT17	52.81887	5.055895	1.89	131
WT18	52.837472	5.095357	1.58	286
WT19	52.839722	5.065827	1	40
WT20	52.839469	5.050182	1.78	69
WT21	52.823649	5.081105	1.06	216
WT22	52.826775	5.060823	1.04	116
WT23	52.824837	5.040348	2.37	105

Table 3.5: ECN Wieringermeer wind park wind turbine locations in geographical coordinates, distance and bearing in reference to the hydrogen turbine

hysteresis is considered not present as Enercon E-126-EP3 utilises a soft cut-out wind speed. Electrical losses are set at 1.0%. Electrical losses include power losses due to power conversion processes in the power electronics of the wind turbine and ohmic losses in the power cables. The turbine consumes 0.3% of the produced power to operate. There are two types of blade contamination considered. The first type of blade contamination is ice forming on the wind turbine blades. Ice built-up only occurs at low wind speed and low temperatures. To simplify the power calculations, the loss factor is considered present at all times with an average reduction in power output of 0.3%. The second form of blade contamination is debris built-up, insects and dust accumulation on the airfoil. A 0.5% loss factor is assumed for onshore wind turbines. The final loss factor considered is shadow flicker. Shadow flicker is casting shadows by the wind turbine on particular areas or buildings. The wind turbine is curtailed in the case of excess shadow flicker. The Pondera report state that for the ECN Wieringermeer location, shadow flicker curtailment only accounts for one hour per year. This results in a negligible power loss factor. It is assumed insignificant and not taken into account in this research (Pondera Consult, 2019). At the location of the second turbine in the Port of Amsterdam, the curtailment of shadow flicker is expected to be higher due to the surrounding buildings at the wind turbine location. However, the shadow flicker loss factor is neglected in the power calculations for both wind turbine locations. An overview of all system loss factors is given in table Table 3.6.

As discussed in subsection 2.1.2 the final loss category is caused by turbine unavailability due to scheduled maintenance and unexpected wind turbine failure. This loss factor can be described as a time-based reliability factor. The time-based reliability factor describes the percentage for which the

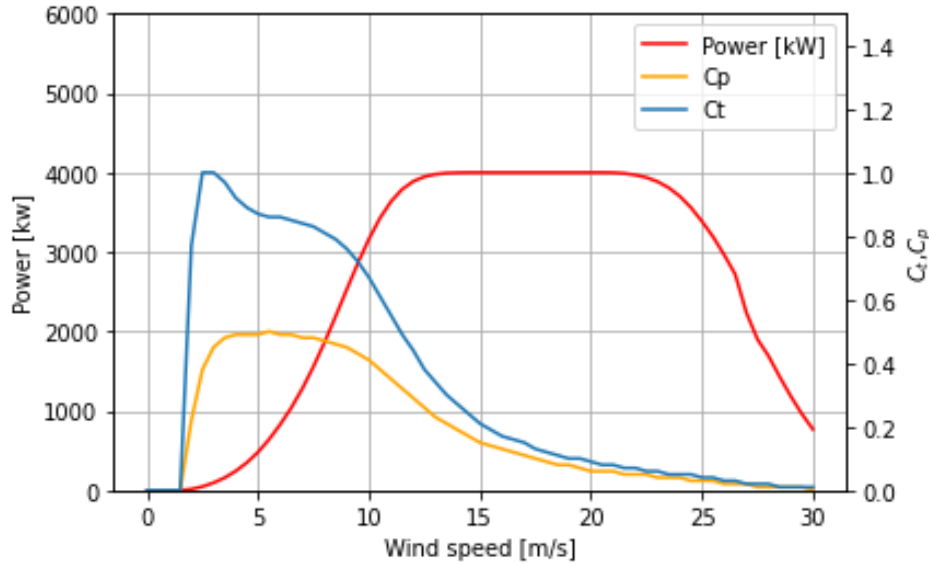


Figure 3.7: Power Curve ENERCON E-126-EP3 4000 [kW] Wind Turbine

General System Loss Parameters	ECN Wieringermeer Wind park	Port of Amsterdam
Wake losses	x%	x%
Wind Turbine Reliability	5.0%	5.0%
Wind Hysteresis	0.0%	0.0%
Electrical Losses	1.0%	1.0%
Electricity Use Wind Turbine	0.3%	0.3%
Blade Degradation Due To Icing	0.3%	0.3%
Blade Degradation Due To Contamination	0.5%	0.5%
Shadow Flicker	0.0%	0.0%

Table 3.6: Site specific wind turbine efficiency losses by Pondera Consult for the ECN Wieringermeer wind turbine location

turbine is operational. The research of Pfaffel et al. (2017) has concluded that turbine reliability reaches 95% on average, based on historical failure and maintenance data of multiple wind parks. The turbine manufacturer Enercon also ensures a 95% reliability factor. In this research, a time-based reliability factor of 95% is adopted. This results in a 5% downtime due to scheduled maintenance operations and unexpected failure. The downtime events due to scheduled maintenance are optimised and planned during minimal power production periods, and the potential power loss is reduced. Unexpected turbine failure often occurs at high wind speeds when the wind turbine is operating at total capacity. This research makes no distinction between scheduled maintenance and unexpected turbine failure. The reliability factor is modelled on an event basis. Random events are simulated throughout the wind turbine operation to simulate curtailment due to maintenance or breakdown. According to Dao et al. (2019) downtimes for onshore wind turbines are on average 3.9 hours per event. Every downtime event modelled in the power output time series equals 3.9 hours. In Figure 3.8 the power output curve of the wind turbine and a breakdown period of 72 hours is shown. Breakdown or maintenance during periods of high demand for hydrogen in combination with periods of insignificant power production by the wind turbine will result in a larger system storage capacity and more interaction with the grid. More interaction with the grid and larger storage capacity in the value chain can significantly impact the total system cost.

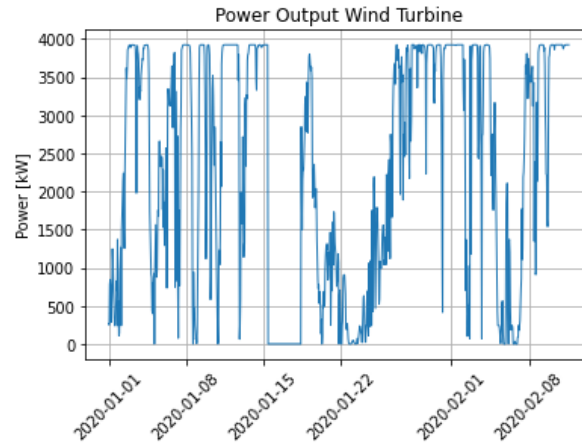


Figure 3.8: Power output Enercon E-126-EP3 first months of 2020

3.1.4. Wind Turbine Cost Components

The wind turbine capital cost and operational cost define the total cost function of the wind turbine. The CAPEX and OPEX costs of the wind turbine are based on actual cost information obtained from the wind turbine installed at the Wieringermeer wind park. The wind turbine's CAPEX cost is divided into the total cost of the wind turbine and the cost of the foundation. Both cost parameters include investment costs for the components, including labour and commissioning costs. The CAPEX of the wind turbine includes all power electronics, cabling and transformers to supply a 20kV connection compatible with the local electricity grid. An overview of the cost components is given in Table 3.7. Annual fixed OPEX costs define the OPEX cost of the wind turbine. Fixed operational costs are yearly costs that ensure the wind turbine's operation, such as scheduled operation and maintenance costs. The wind turbine OPEX includes O&M costs and land lease costs. All CAPEX and OPEX costs for the wind turbine are obtained from HYGRO. For both wind turbine locations, a similar cost structure is considered.

Component	CAPEX	Fixed OPEX	Variable OPEX
Wind Turbine	€3.480.000	€150.000	-
Foundation	€400.000	-	-

Table 3.7: CAPEX, fixed OPEX and Variable OPEX cost overview for the 4MW wind turbine installation (HYGRO, 2021)

An annuity factor is determined and applied to obtain the annual investment cost of the wind turbine. The annuity factor expresses the annual cost in a present value. The annuity factor discounts the total investment cost over the lifetime of the wind turbine. The annuity factor is calculated with the Weighted Average Cost of Capital (WACC) and described by Equation 3.8. r presents the WACC, and n presents the lifetime of the wind turbine. The lifetime of the wind turbine is 20 years. The wind turbine cost function of CAPEX and fixed OPEX cost for the entire value chain is the sum of all Capex and fixed OPEX cost components of every wind turbine location. The wind turbine cost function is shown in Equation 3.9 where p depicts the location of each wind turbine in the value chain.

$$Capex_{WT} = CAPEX_{turbine} + CAPEX_{foundation} \quad (3.6)$$

$$OPEX_{fixed,WT} = OPEX_{O\&M} + OPEX_{landlease} \quad (3.7)$$

$$a_{WT} = \frac{1 - (1 + r)^{-n_{WT}}}{r} \quad (3.8)$$

$$TC_{WT} = \sum_{p \in \mathbf{P}} \frac{CAPEX_{WT}}{a_{WT}} + OPEX_{fixed,WT} \quad (3.9)$$

3.2. Grid Connection

This section discusses the technical and economic constraints of the grid connection used in the case study. The grid connection size, cost structure and interaction with the electricity grid are defined in the following sections. The day-ahead electricity prices are obtained from the EPEX Spot market, and the grid connection technical and economic parameters are obtained from the local DSO for each wind turbine individually. Finally, an overview is given for all technical and economic constraints.

3.2.1. Technical Parameters Grid Connection

The grid connection size for the hydrogen production location is determined by total system cost optimisation conducted by HYGRO. The grid connection size for both wind turbine locations in the case study is 2.5 MW. In Figure 3.9 a map is shown of all DSO operators in the Netherlands. The red dots show that both wind turbine locations are located in the same DSO district. The distribution operator for both wind turbine locations is Liander.

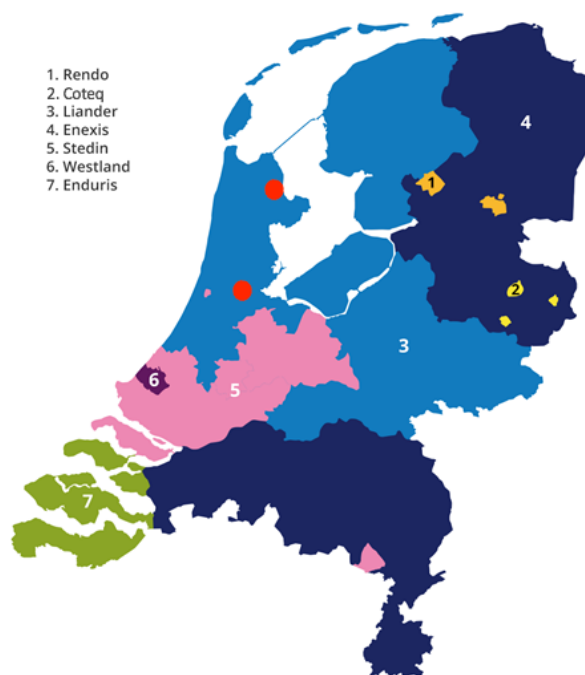


Figure 3.9: Map of Distribution System Operators (DSO) in the Netherlands (EnergieLeveranciers, 2021)

The DSO is responsible for managing and controlling the energy flow in the transmission lines on the local distribution scale. The DSO operators regulate the bi-directional flow of power and secure the availability of low to medium voltage grids. The wind turbines at both locations are connected to the 20 kV medium voltage grid and interact with the local DSO. Due to grid congestion, the DSO could pose limitations on the maximum power drawn or sold to the grid. Grid congestion results from the capacity limitations of the local transmission lines. With grid congestion, a distinction is made between purchase and selling capacity. In Figure 3.10 and Figure 3.11 a map is shown for grid congestion of the Liander DSO district. Figure 3.10 shows grid limitations for purchasing energy from the grid, while Figure 3.11 shows grid congestion levels for selling power to the electricity grid. Both turbine locations are shown with a blue dot. The red area in the figures depict locations where no transport capacity is available, and yellow indicates limited transport capacity. Area without colour indicates sufficient transport capacity within the local DSO power grid. For the Wieringermeer wind park grid, congestion could occur for selling electricity to the power grid. However, no limitations are present for purchasing electricity. The power consumption could be restricted for the wind turbine location in the Port of Amsterdam, whereas there is enough grid capacity available to sell surplus power. No grid congestion is assumed in the

case study, and the total capacity of the grid connection can be utilised.

Technical input parameter	Unit
Grid power capacity	2.5 MW
Availability	Infinite
Type connection	20 kV Medium voltage grid
Grid Congestion	None

Table 3.8: Considered grid connection constraints

The technical constraints of the grid connection for both wind turbine locations are shown in Table 3.8. The grid connection size is 2.5 MW, and the availability is infinite. The local grid voltage level is 20 kV, and no transformer between the hydrogen production site and the grid is required. No efficiency losses between the grid connection and the hydrogen production site's power system are assumed as the grid connection is only a switching substation. A 20kV to 360 kV step-down transformer is needed for the electrolyser. This transformer is placed at the electrolyser system to minimise the length of the low voltage power transmission cables at the production site and minimise the ohmic losses in the power system. For both locations, the same technical constraints are assumed.

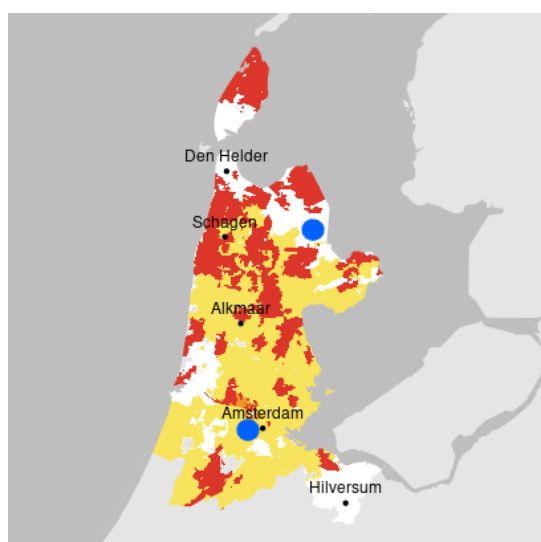


Figure 3.10: Map North-Holland grid congestion consumption of power

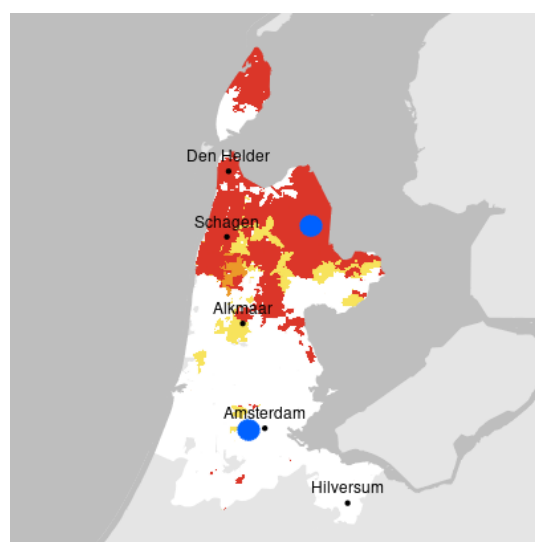


Figure 3.11: Map North-Holland grid congestion selling power

3.2.2. Cost Structure Grid Connection

As discussed in subsection 2.2.2 a shallow cost structure is adopted in this research. The shallow cost structure includes all cost components to ensure a secure grid connection. The value chain developer does not account for unnecessary transmission system expansion and reinforcement beyond the value chain's boundaries. The cost structure of the grid connection is divided into upfront installation cost, annual fixed operations, management and operation cost and power transmission costs. The CAPEX cost for a grid connection includes all power electronic components and installation costs to install and commission a secure grid connection at the hydrogen production site. The annual fixed cost includes the management and necessary maintenance of the grid connection. The transmission cost is based on the interaction with the electricity grid and is proportional to the amount of power sold or purchased. The cost structure, including the periodic cost defined by the local DSO, Liander, is shown in Table 3.10. The variable transmission cost proportional to the interaction with the grid is shown in Table 3.9. LV, MV, IV and HV imply, low voltage [1 kV], medium voltage [20 kV], intermediate voltage [50 kV] and high

voltage [>50 kV], respectively. The grid connection at the turbine locations is 20 kV and is defined in the cost structure of Liander by MV/HV. The cost structure for the MV/HV connection type is applied in the case study for both wind turbine locations.

Connection type	Monthly tariff [€]	CAPEX [€]
> 1 MVA , < 2MVA	91,00	36.500
> 2 MVA , < 5MVA	594,00	237.700
> 5 MVA , < 10MVA	706,00	287.700

Table 3.9: Periodic cost structure & CAPEX Liander grid connection, as of 2021 (Liander, 2021)

Connection Type	Contracted Transported Power [kW]	Monthly Fixed rate [€]	Per kWh - High [€]	Per kWh - Low [€]	Per kW per Month - kW Contract [€]	Monthly kW Max [€]
LV	< 50	1,50	0,0356	0,0183	0,76	-
MV/LV	> 50 , < 136	36,75	0,0105	0,0105	1,93	1,74
MV	> 136 , < 2.000	36,75	0,0105	0,0105	1,23	1,74
IV/MV or HV/MV	> 2.000	230,00	-	-	2,01	2,50
IV	> 2.000	230,00	-	-	1,92	2,43
HV	> 2.000	230,00	-	-	0,97	1,23

Table 3.10: Electricity distribution cost structure Liander (Liander, 2021)

An overview of the costs for the 2.5 MW grid connection applied in the case study is given by Table 3.11. For the 2.5 MW grid connection either the monthly contracted power drawn from the grid or the monthly maximum power drawn from the grid define the variable cost. No costs regarding each delivered kWh is applied for the considered grid connection size. The contracted power is the expected pre-determined monthly maximum power drawn from the grid and paid monthly. The second option includes the cost associated with the maximum monthly power drawn, determined after the monthly periods. The production location operator either pays the fixed monthly tariff for a given contracted power or pays a variable monthly fee based on the maximum power drawn from the grid in each month. The total variable OPEX is determined based on the grid connection size and the monthly cost tariff shown in Table 3.11.

Cost type	Tariff
Annual Fixed Opex	9.888 €
Variable OPEX Monthly High	2.01 [$\frac{€}{kW}$]

Table 3.11: OPEX cost structure case study

3.2.3. Electricity Market

The revenue or cost associated with power grid interaction is determined by the power drawn or supplied to the grid. The day-ahead electricity price determines the price of a kWh. The hourly day-ahead electricity price is obtained from the ENTSOE Transparency platform (ENTSOE, 2021). Open-source data for the Netherlands is available from 05-01-2015 until the present. A graph showing the day-ahead electricity prices for a single day is shown in Figure 3.12.

Two sections define the total cost function corresponding to the interaction with the electricity grid. The first section is compiled from the CAPEX and the second section by the OPEX cost parameters of the grid connection and defined by Equation 3.10 and Equation 3.11. The OPEX comprises the annual fixed costs defined by the annual O&M costs, the cost for maximum power drawn, and the contracted capacity cost. The two latter are multiplied by the grid connection size for model simplification. The CAPEX cost is adjusted with an annuity factor defined by Equation 3.12 where r is the WACC and n the lifetime of the grid connection. The lifetime of the grid connection is assumed to equal the lifetime of the wind turbine. The p portraits each hydrogen production location. The total cost function for the grid connections present in the value chain equals the sum of each hydrogen production location.

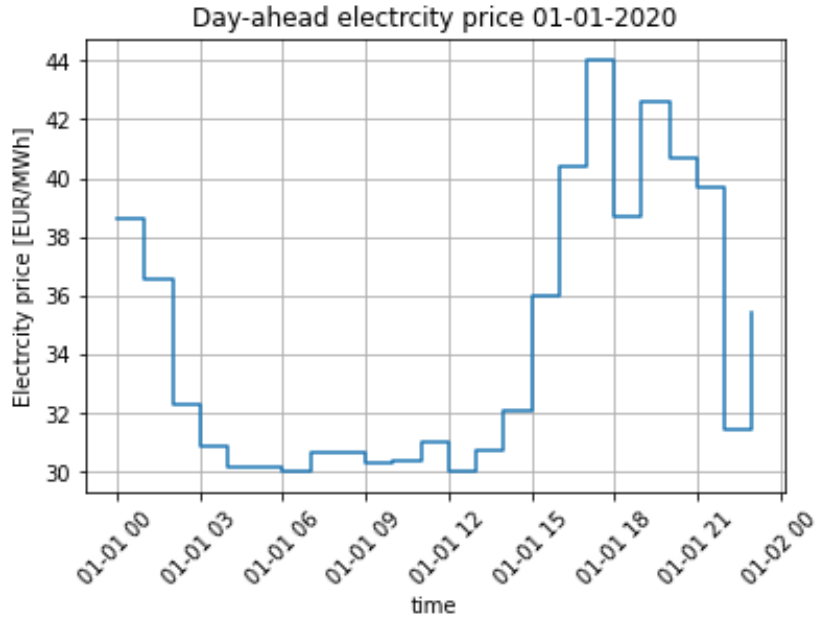


Figure 3.12: Hourly day-ahead electricity price 01-01-202 (ENTSOE, 2021)

$$CAPEX_{Grid} = CAPEX_{Installation} \quad (3.10)$$

$$OPEX_{Fixed,Grid} = OPEX_{O\&M} + OPEX_{MonthlyHigh} \cdot Power_{DrawnMaxMonthly} \quad (3.11)$$

$$a_{Grid} = \frac{1 - (1 + r)^{-n_{Grid}}}{r} \quad (3.12)$$

$$TC_{Grid} = \sum_{p \in \mathbf{P}} \frac{CAPEX_{Grid}}{a_{Grid}} + OPEX_{Grid,p} \quad (3.13)$$

3.3. PEM Electrolyser

This section discusses the entire electrolyser system adopted in the case study. The overall conversion efficiency and hydrogen production rate of the electrolyser system is discussed, whereafter the system size and cost components that built up the cost function adopted in the case study are presented. Finally, an overview of the electrolyser system with the corresponding model input parameters are shown.

The electricity is supplied to the electrolyser via a step-down power converter and regulated by the electrolyser's internal power electronics. A simplified single line diagram of the power conversion steps from the medium voltage cable to the low voltage internal power system as shown in Figure 3.13. The power fed by either the grid connection or the wind turbine has a voltage level of 20kV. The electrolyser system runs on a voltage level of 360V. A step-down converter is necessary to adjust the medium voltage power supply to the low voltage operating range. After voltage reduction, the AC input power is split into an AC power supply for the BOP of the electrolyser system components and a DC supply for the electrolyser stacks. In this research, a 3-phase active AC-DC rectifier is chosen to minimise the power harmonics and maximise the conversion efficiency (Yodwong et al., 2020). A DC-DC converter adjusts and controls the operating voltage of the electrolyser stacks. By adjusting the operating voltage, indirectly, the power density is adjusted and, therefore, the hydrogen production flow rate. The power conversion process from medium to low voltage range is not modelled in this research. The power to hydrogen conversion model with the conversion efficiencies of the power electronics and all BOP components created by HYGRO is incorporated.

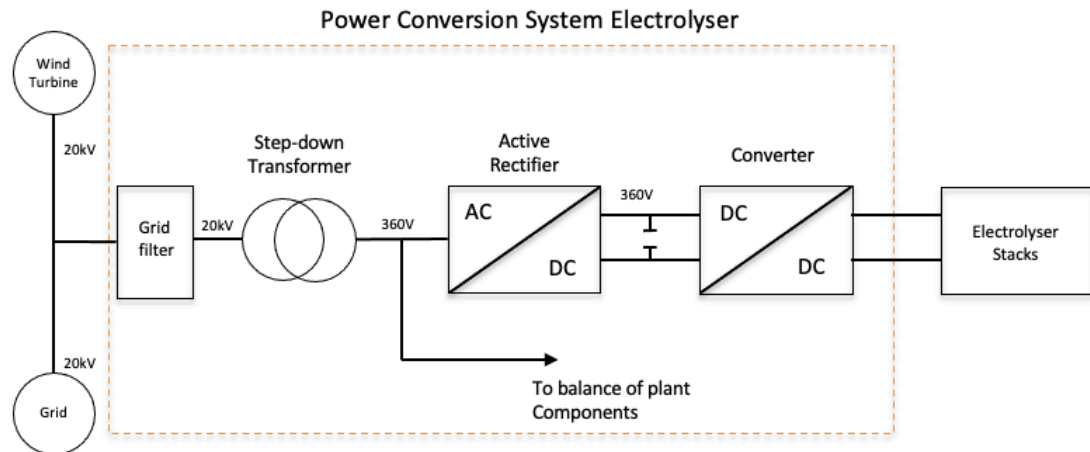


Figure 3.13: Single line diagram power conversion system

3.3.1. PEM Technical Constraints

The overall performance of the electrolyser is pre-determined and modelled by HYGRO, whereafter implemented in this research. Figure 3.15 and Figure 3.16 shows the conversion from power in kilowatt-hours to kilograms of hydrogen and oxygen, respectively. The entire process from power conversion of AC to DC power up to the purified hydrogen obtained at the electrolyser's outlet is included in the power to hydrogen production curve. The pressure of the hydrogen gas at the output of the PEM electrolyser is equal to 30 bar. The efficiency of the entire electrolyser process based on the HHV is shown in Figure 3.14. Two electrolyser operation stages can be identified in the electrolyser efficiency curve.

1. Stand-by stage
2. Operational stage

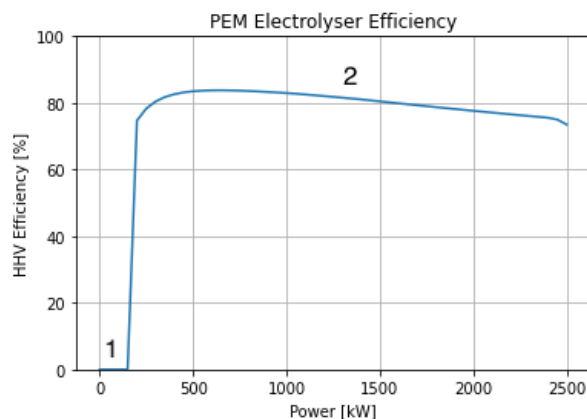


Figure 3.14: PEM electrolyser system efficiency (HYGRO, 2021)

In Figure 3.14 the two stages are shown with their corresponding number. In the range of 0-200kW input power, no hydrogen is produced. The choice to not produce hydrogen at 0-10% of the electrolyser's power capacity is related to the working principles of several BOP components. At low operating levels, the power electronic conversion efficiency from AC to DC power is decreased significantly (Yod-wong et al., 2020). The decrease of power conversion efficiency at 0-10% of the dynamic range results

in an electrolyser operating range of 10-100%. A solution to the inefficient low partial load power conversion problem could be parallel connected converters. Parallel connection of the DC-DC converters ensures modular stack operation by controlling each individual stack by a single DC-DC converter. The energy efficiency of each DC-DC converter is optimised due to lower duty cycles, and the total system efficiency increases (Yodwong et al., 2020). It is possible to run only a single electrolyser stack when the partial load is obtained from the wind turbine. A significant drawback is an increase in conversion system components and, therefore, an increase in total system cost. Next to the efficiency decrease at low partial loads, all BOP system components combined also require a minimum power input to be functional. For the electrolyser system adopted in this case study, a minimum power input threshold of 200kW is applied.

The second stage of the electrolyser is the operational stage as the power input to the electrolyser system increases the current density, and therefore the hydrogen production rate increases proportionally (Scheepers et al., 2020). Due to an increased current density applied to the PEM electrolyser system, the overall cell efficiency decreases, as was discussed in chapter 2. The decrease in efficiency of the electrolyser system at higher input power levels can be observed in Figure 3.14 The PEM system's optimum operating efficiency is reached at roughly 600 kW and reaches a maximum system efficiency of 83.7%. The total system's efficiency is calculated by Equation 3.14. The Higher Heating Value (HHV) for water electrolysis is multiplied by the amount of kg of H₂ produced, divided by the total power input to the electrolyser system and all BOP components. The higher heating value of 1 kg of hydrogen is equal to 141.9 MJ or 39.4 kWh ("National Research Council and National Academy of Engineering", 2004).

$$\eta_{PEM} = \frac{HHV_{H_2} \cdot kg_{H_2}}{E_{in}} \quad (3.14)$$

As the hydrogen production rate is proportional to the power density applied to the electrolyser system, almost a linear correlation between the produced hydrogen in kg and power input in kW can be observed in Figure 3.15. The shown ratio between power input in kWh and kilograms of hydrogen produced will be used as input for the power to the hydrogen conversion process in the optimisation model. Similar to hydrogen production, the exact correlation between oxygen production and power input can be observed in Figure 3.16. As mentioned in chapter 2 this research does not apply any purpose for the oxygen produced at the electrolysis process, and the production of oxygen is therefore neglected. The water supplied for the electrolyser process is assumed to be infinite. The technical parameters for the electrolyser system applied in this case study are shown in Table 3.12.

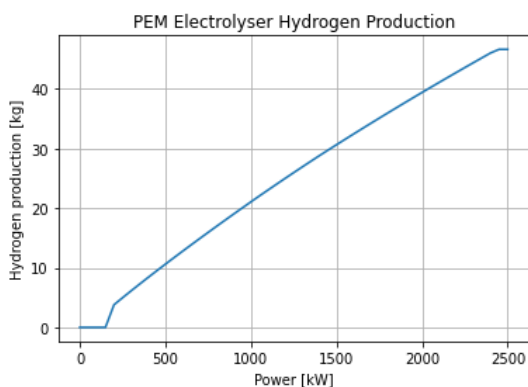


Figure 3.15: Hydrogen production PEM electrolyser

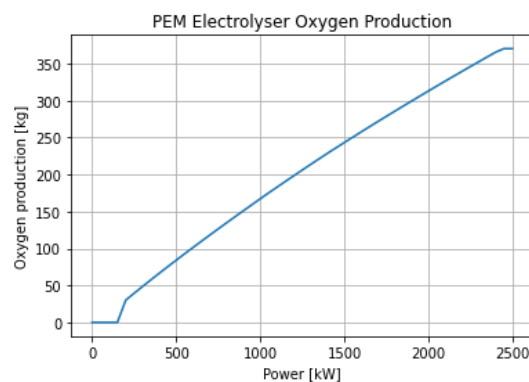


Figure 3.16: Oxygen production PEM electrolyser

Parameter	Constraint
Capacity	2.5 MW
Min Operating Power	0.2 MW
Max Current Density	2.00 A/cm ²
Operating Range	8-100%
Average Power Consumption	49.3 $\frac{kWh}{kg_{H_2}}$
Average Water Consumption	15 $\frac{liter}{kg_{H_2}}$
Input Voltage	360V
Input pressure H ₂ O	1 bar
Output Pressure H ₂	30 bar
Hydrogen Output Purity	99.999%
Average H ₂ Efficiency (HHV)	80.1%
Electrolyser Stacks	2
Number of PEM Cells	400
Power conversion	Active Front end rectifier + DC-DC converter

Table 3.12: Technical data of the adopted electrolyser (HYGRO, 2021)

3.3.2. PEM Cost Components

The PEM electrolyser cost structure can be broken down into three sections. The first section is the electrolysers systems CAPEX. The CAPEX cost considered in this research includes the stack costs, BOP costs, the costs associated with the power electronics system and the civil works needed to connect the electrolyser to the electrical side of the value chain and the hydrogen side of the value chain. The electrical side consists of the grid connection and the wind turbine, while the hydrogen side of the PEM electrolyser system is connected to the next echelon in the value chain, the compression module. An overview of the CAPEX cost components is given by Table 3.13. All cost parameters are obtained from Hygro. The total CAPEX costs of the electrolyser system developed by HYGRO is equal to 1556 €/kW. CAPEX_{Stacks} consist of the initial PEM electrolyser stack costs and stack replacement costs, CAPEX_{BOP} are the costs associated with the balance of the plant's water and gas systems. The CAPEX_{PE} include all costs with the power electronic conversion systems, and CAPEX_{Civil} are the costs developed by the civil works necessary to have the PEM Electrolyser system operational. The CAPEX costs for the PEM electrolyser are annualised with an annuity factor. The annuity factor is calculated according to Equation 3.19, where the annuity factor is the WACC and denoted by r , n_{PEM} is the lifetime of the electrolyser. The electrolyser system costs for all hydrogen production locations are assumed similar.

Cost Component	CAPEX [€]
PEM Stacks	1.870.000
BOP	1.500.000
Power Electronics	370.000
Civil Works	150.000
Total	3.890.000

Table 3.13: CAPEX cost structure 2.5 MW PEM electrolyser system (HYGRO, 2021)

The lifetime of a PEM electrolyser BOP is estimated at around 20 years (Lee et al., 2020). For simplicity in this research, the lifetime of the BOP, power electronic equipment and the system components by the civil works are assumed similar to the lifetime of the wind turbine, 20 years. The electrolyser stacks have an operational lifetime of between 50.000-80.000 hours before replacement is necessary (IRENA, 2020b). The electrolyser stacks can be interchanged and replaced with new PEM electrolyser

stacks. The average annual cost reduction for PEM electrolyser stack is set equal to 2% determined by the expected cost reduction from Deloitte Monitor (2021).

The amount of hours of annual operation for the electrolyser system is a function of hydrogen demand and is defined by the value chain configuration. The full load capacity of the 2.5MW PEM electrolyser system is equal to 46.63 kg/h. An average lifetime of 80.000 full load hours is assumed for the electrolyser stacks (Barei et al., 2019), this results in the total production of roughly 4,000,000 kg in the electrolyser systems stack lifetime. To determine the lifetime of the electrolyser stacks, the annual average demand is divided by the total equivalent full-load operating hours required by the PEM electrolyser to supply the demand. The lifetime and, therefore, the year of replacement of the stacks has to be determined for each specific demand scenario. n_{Stacks} describes the lifetime of the stacks and varies per scenario. The annuity factor of stack replacement for a single production location is given by Equation 3.16, where r is the WACC, and n_{Stacks} is the number of years after which the stacks have to be replaced, taking into account a maximum system lifetime of 20 years. Equation 3.17 defines the total CAPEX cost for the PEM electrolyser system for each production location. For each location, the same cost structure is assumed.

$$CAPEX_{Stacks} = CAPEX_{Stacks} \quad (3.15)$$

$$a_{Stacks} = \frac{1 - (1 + r)^{-n_{Stacks}}}{r} \quad (3.16)$$

$$CAPEX_{PEM} = CAPEX_{BOP} + CAPEX_{PE} + CAPEX_{Civil} \quad (3.17)$$

The second section of the PEM electrolyser system cost structure is the fixed OPEX cost and consist of the total yearly operational & maintenance cost to have the PEM electrolyser fully operational. The optimal maintenance strategy for the PEM electrolyser is during periods of low hydrogen demand and when little wind energy is available. In the combination of the intermittent energy produced by the wind turbine, sufficient moments of not producing hydrogen are assumed to conduct the electrolyser scheduled maintenance. In this research, therefore, no downtime as a result of scheduled maintenance is assumed. The total annual fixed OPEX cost for the 2.5 MW PEM electrolyser system, including the power conversion electronics, is equal to €25,000. The fixed OPEX costs are denoted by $OPEX_{O\&M}$ in Equation 3.20. For each production location, the fixed annual OPEX is considered equal.

The third and final cost section for the PEM electrolyser system contains the variable OPEX costs. The variable OPEX costs considered in this research are the costs associated with the electricity demand for the hydrogen production and the cost associated with the water supply for the hydrogen production and water circulation system for thermal management. When considering the water consumption of the electrolysis process stoichiometrically, the water consumption for a single kilogram of hydrogen is 9 kilograms. However, more water has to be circulated through the electrolyser system. An excess of water is circulated through the electrolyser system due to cooling properties and to provide excess water to the stack to improve the water to hydrogen conversion. Simoes et al. (2021a) has researched the water availability, purification and water management system components for multiple water sources. The assessment for the most suitable water source was based on cost and reliability. Simoes et al. (2021a) concluded that the use of public water from the local water supply network is most suitable in almost all cases if an extensive water supply network is available. In this research, all production locations are onshore and located in the Netherlands, where an extensive public water supply network is available. Security of supply, therefore, poses no issue and limitations on water availability for the electrolysis process. The cost of a single m³ of drinking water in the Netherlands for commercial use is equal to €0.35 (PWN). Average water consumption of 15 litres is assumed per kg produced H₂ (Simoes et al., 2021a). Therefore, for each kg of H₂ produced, the variable cost is €0.005. The price for water for a single produced kg of hydrogen is therefore almost negligible, and for the model, simplification is not incorporated in this research.

The second variable cost component of a single kilogram of hydrogen is the cost of energy. The cost of the energy supplied by either the wind turbine or the power grid is defined by $\frac{\text{€}}{\text{kWh}}$. When the power for the production of hydrogen is supplied by the wind turbine, no variable cost is considered. The wind turbine cost objective function applied in this research already incorporates all costs associated with the wind turbine as is discussed in Equation 3.9. If the power is supplied by the grid connection, the day-ahead market price for that specific moment in time is used as a price variable defined in $\frac{\text{€}}{\text{kWh}}$. The cost of electricity consumed by the electrolyser is not defined in the total cost function of the PEM electrolyser but incorporated in the cost function on grid interaction (Equation 4.2). The cost function of the PEM electrolyser system adopted in this research is given by Equation 3.20, where p represents the production location.

$$OPEX_{Fixed,PEM} = OPEX_{Fixed} \quad (3.18)$$

$$a_{PEM} = \frac{1 - (1 + r)^{-n_{PEM}}}{r} \quad (3.19)$$

$$TC_{PEM} = \sum_{p \in \mathbf{P}} \frac{CAPEX_{PEM}}{a_{PEM}} + \frac{CAPEX_{Stacks}}{a_{Stacks}} OPEX_{Fixed,PEM} \quad (3.20)$$

3.4. Compressor

This section defines the technical and economic constraints of the compressor module. As discussed in section 2.4 the diaphragm compressor is selected as the most suitable option for compression of the hydrogen up to high-pressure levels.

For all MEGCs, the pressure level is assumed to be 640 bar. The diaphragm compressor technical characteristics are shown in Table 3.14. The diaphragm compressor is not able to ramp up and ramp down its speed and power consumption. Therefore operational characteristic is assumed that the diaphragm compressor is either on or off. This results in constant power consumption when the electrolyser is operational to compress the hydrogen from 30 bar to 640 bar. The variable OPEX of the compressor module is, therefore, a function of the power consumption, amount of operational hours and the cost of electricity.

Parameters	Howden
Compression stages	3
Rated Power	84 kW
Inlet pressure range	20-400 bar
Approximate flow rate	44 kg/h
Max. Compression pressure	640 bar
Ambient Operating Temperature	-20°C to +45°C
Electricity consumption	1.9 $\frac{\text{kWh}}{\text{kg}}$
Adiabatic Compressor efficiency	79%
Compressor lifetime	20 years
CAPEX Cost	€500.000
Fixed OPEX	€20.000

Table 3.14: Technical Parameters Howden 64MPa diaphragm compressor (HYGRO, 2021)

The cost function of the compressor module is depicted by Equation 3.23. The CAPEX cost is adjusted with an annuity factor defined by Equation 3.22 where r is the WACC and n_{Comp} the lifetime of the Compressor module. The total cost function for the compressor modules in the value chain

equals to the sum of the compressors at each hub refuelling station location. The operational cost regarding compression of hydrogen is further discussed in chapter 4.

$$OPEX_{Fixed,Comp} = OPEX_{Fixed} \quad (3.21)$$

$$a_{Comp} = \frac{1 - (1 + r)^{-n_{Comp}}}{r} \quad (3.22)$$

$$TC_{Comp} = \sum_{h \in \mathbf{H}} \left(\frac{CAPEX_{Comp}}{a_{Comp}} + OPEX_{Fixed,Comp} \right) \quad (3.23)$$

3.5. Distribution Network and Storage

This section defines the technical and economic constraints of the distribution network layout and adopted non stationary storage technology applied in the case study. Two non stationary storage technologies are applied in this case study as discussed in chapter 2.

Both MEGC and HPSC are considered an integral part of the storage system for the hub refuelling station location and the satellite refuelling station location. The total storage capacity for the entire value chain is defined by the number of MEGC or HPSC units present in the value chain. An overview of the possible transportation configurations considered in the case study is provided by Table 3.15. An simplified representation of the different distribution routes can be seen in Figure 3.17.

Trailer Configurations				
Trailer Size	Transport Technology	Trailer Configuration	Routing	Loading/Unloading Mechanism
20ft trailer	MEGC	1 unit; 20ft MEGC	Direct	Trailer Swap
20ft trailer	HPSC	10 units; HPSC	Indirect	Transportable forklift

Table 3.15: Overview transportation configurations



(a) Topology 1 hub & satellite non-flexible

(b) Topology 2 hub & satellite flexible

Figure 3.17: Distribution network topology example, 1 production location three refuelling stations (flexible/non-flexible)

3.5.1. Transportation - MEGC

The technical and economic data for the MEGCs is based on the compressed hydrogen transportation technology developed by NPROXX (2021). For all storage configurations, the application of the Type IV composite pressure vessel is assumed. NPROXX manufactures two different sized containerised transportation units. The first container unit is a 10ft sized container. The second container unit is an ISO sized 20ft sized container. The 40ft sized trailers consider two 20ft containerised transportation units, as it is not possible to provide enough structural integrity and comply with safety regulations to

manufacture a single 40ft MEGC. This research only assumes the 20ft MEGC.

The MEGC is assumed either fixed or detachable to the trailer. The time taken by the truck driver to swap a single trailer or a single unit is different for all MEGC and trailer configurations. The swap time for the MEGCs is based on the expected trailer handling time by HYGRO. A distinction is made between handling time at the refuelling station and the production location. At the refuelling station, a full MEGC is dropped off, and an empty MEGC is loaded onto the trailer. At the production location, an empty trailer is dropped off, and a full trailer is obtained by the truck driver. Therefore the handling time at the hub location is considered slightly less than the handling time at the refuelling station. The handling time for the MEGC at the hub location and the satellite refuelling station is depicted in Table 3.16. The values for handling time are obtained from a handling time analysis conducted by HYGRO based on all actions required to comply with all transport and safety regulations.

Trailer Configuration	Handling time	Handling time	Handling time
	entire trailer at production location	Single unit at production location	Single unit at refuelling station
units	minutes	minutes	minutes
20ft trailer; 20ft MEGC	11.8	14	14

Table 3.16: Handling time 20ft MEGC

Parameter	MEGC Configuration
	20ft
ISO Container	20ft
Trailer Dimensions (LxWxH)	6.10x2.44x2.89 m
Operating pressure	20-500 bar
Vessel Type	Type IV TPED / EN 12245 Certification
Usable Payload (20-500 bar)	510 kg
Payload (640 bar)	635 kg
Usable Payload (20% back haul factor)	557 kg
Usable Payload (40% back haul factor)	393 kg
Number of vessels	48
Vessel Weight	9.801 kg
Water Volume at 500 bar	16.800 liter

Table 3.17: Technical constraints MEGC configuration based on NPROXX Transportation technology (NPROXX, 2021)

The operating pressure for the MEGCs stated by the manufacturer ranges between 20 and 500 bar. Technical data on the trailers applied in this research are shown in Table 3.17. The lower pressure limit of the MEGC provided by the manufacturer is not the pressure level obtained when taking into account a cascade overflow system at the HRS.

The lack of a compressor unit reduces the pressure-induced overflow capacity of the MEGCs. As the hydrogen is removed from the pressure vessels, the volume relative to the amount of hydrogen stored increases. The increase in relative volume results in a pressure drop in the pressure vessels. The lower pressure limits the cascade overflow mechanism to use all stored hydrogen for refuelling and resulting in hydrogen transportation from the HRS back to the production location. The ratio between the total payload and the payload that is transported back to the production location is defined in this research as the backhaul factor.

The backhaul factor is dependent on many parameters during the filling process. Several parameters that influence the cascade filling process are ambient temperature, dimensions, material properties,

operating temperature and pressure of both FCEV and MEGC storage vessels, the maximum allowable mass flow, operating range of the control valve and also the amount of pre-cooling of the hydrogen at the dispenser (Rothuizen et al., 2013). A different parameter that defines the backhaul factor is an agreement between the customer and the refuelling station regarding the minimum required State of Charge (SOC) of the vehicle leaving the HRS. The SOC is defined as the ratio between the energy density of the hydrogen stored in the vehicle fuel tank and the energy density of hydrogen at 350 bar and 20 C°. Extensive flow analysis of a cascade filling system at the HRS is conducted by HYGRO, taking into account the MEGC as an integral part of the storage bank and filling system. When considering an agreement that all vehicles must be filled up to 100% SOC, a backhaul factor of 30% is expected. When considering a minimum SOC of 50% for the vehicles leaving the HRS, a backhaul factor up to 15% can be considered. In this research, a backhaul factor of 30% is assumed.

The non-ideal gas law is applied and takes into account the compressibility factor of hydrogen at different pressure levels. Equation 3.24 determines the compressibility factor and corresponds to the method applied in (Rothuizen et al., 2013). The empirical Equation of State (EOS) allows for the calculation of the compressibility factor dependent on pressure and temperature, $Z(P, T)$. Ambient temperature conditions of 15 C° are assumed. The density of the hydrogen in the storage vessels is calculated according to Equation 3.25, derived from the non-ideal gas law. Where M is the molar mass of hydrogen in kg/mol , P is the pressure in Pa , T the temperature in K , Z the compressibility factor defined by Equation 3.24 and R the gas constant in $\frac{m^3 Pa}{mol K}$. Due to the expected regulation change in the ADR for the transportation of compressed gasses, the upper limit operating pressure of 640 bar is adopted. The density of H_2 at 640 bar is equal to $37.78 \frac{kg}{m^3}$. The usable payload is calculated according to Equation 3.26. $\rho_{H_2, P_{max}}$ is the density related to the maximum operating pressure of the storage vessels, V_{unit} is the total volume of the MEGC unit in m^3 and BF defines the backhaul factor in %. An overview of the usable payload adopted in this case study is given by Table 3.18.

$$Z(P, T) = \sum_{i=1}^9 \sum_{j=1}^5 (v_{i,j} * P^{i-1} * (\frac{100}{T})^{j-1}) \quad (3.24)$$

$$\rho_{H_2, P} = \frac{MP}{ZRT} \quad (3.25)$$

$$Payload_{MEGC} = \rho_{H_2, P_{max}} V_{unit} * (1 - BF) \quad (3.26)$$

Parameter	MEGC Configuration
	20ft
Water Volume at 500 bar	16.800 liter
Payload (640 bar, 15 C°)	635 kg
Usable Payload (40% back haul factor)	381 kg
Usable Payload (15% back haul factor)	540 kg

Table 3.18: Usable payload MEGC configuration based on NPROXX MEGC Transportation Technology (NPROXX, 2021)

3.5.2. Transportation - HPSC

The high-pressure swappable container units are based on storage technology developed by NPROXX (2021). The transportation mode utilising the HPSCs can be distinguished by a 20ft trailer containing 10 HPSCs. Type IV composite pressure vessels are used. A single containerised unit holds four pressure vessels capable of holding 13.23 kg each, resulting in a total storage capacity of 53 kg under a storage pressure of 640 bar. The HPSCs are not permanently fixed to the trailer. The estimated handling time for the HPSC is assumed to be 10.8 min per container at the satellite station, whereas swapping an entire trailer with 22 HPSC units at the production location will take 33 minutes (HYGRO, 2021). The handling process beholds the loading and unloading of the containerised units with a portable forklift.

The weight of a full HSPC is <1.5t, which is a typical weight limit of a portable forklift. Each HSPC unit connects to the valve panel individually, at either the HRS or production location. An overview of the handling time for the HSPC containers is given in Table 3.21. The same assumption is made with the MEGCs. No handling time reduction is assumed by delivering more than a single HSPC at the refuelling station. The total handling time of the HSPC is a function of the handling time of an entire trailer at the production location, and the amount of HSPC swapped during a single route.

Parameter	HPSC
Container Dimensions (LxWxH)	1.2x1.2x2.7 m
Operating pressure	10-500 bar
Vessel Type	Type IV TPED / EN 12245 Certification
Usable Payload (20-500 bar)	43 kg
Number of vessels	4
Vessel Weight	1400 kg
Water Volume at 500 bar	1400 Liter

Table 3.19: Technical constraints HPSC based on NPROXX transportation technology (NPROXX, 2021)

Technical data on the HPSC applied in this research are shown in Table 3.19. The HPSCs are an integral part of the storage system, and the containers are used as part of the cascade filling system described previously in chapter 2. Similar to the MEGCs, the lower pressure limit for a storage bank composed of HPSCs is increased by applying a cascade filling system compared to the minimum pressure level provided by the manufacturer. The same approach for the MEGC is taken to calculate the usable payload for a single HPSC unit. The compressibility factor is calculated by Equation 3.24, the density of the hydrogen stored in the HPSC as a function of the pressure by Equation 3.25 and the usable payload for a single HPSC is calculated by Equation 3.26. The usable payload for an HSPC unit is shown in Table 3.20. .

Parameter	HPSC
Water Volume at 500 bar	1400 Liter
Payload (640 bar)	52.9 kg
Usable Payload (20% back haul factor)	42.2 kg
Usable Payload (10% back haul factor)	47.7 kg

Table 3.20: Usable payload HSPC configuration based on NPROXX MEGC Transportation Technology (NPROXX, 2021)

Trailer Configuration	Handling time entire trailer at production location	Handling time Single unit at production location	Handling time Single unit at refuelling station
units	minutes	minutes	minutes
20ft trailer; 10x HSPC units	20	10.8	10.8

Table 3.21: Handling time HPSC

3.5.3. Transportation - Pipeline

Important design parameters for the pipeline distribution network between the production location and the hub refuelling station are the pipeline dimensions, maximum allowable pressure and minimum allowable pressure in the pipeline system, where the first defines the CAPEX cost of the pipeline and a combination of the three parameters defines the total line packing volume of the distribution network.

The same pipeline is considered in the entire value chain.

The pipeline adopted in the case study between the production location and the hub refuelling station is shown in Figure 3.18. A four-layer polyethylene pipeline is considered. The pipeline technical data is shown in Table 3.22. The compressor unit at either hub has a lower pressure limit of 20 bar. The maximum operating pressure of the pipeline is considered at 42 bar defined by the manufacturer. Nominal operating pressure is assumed at 30 bar. The total line packing volume for the hydrogen pipeline is defined by Equation 3.27, and defined in $\frac{Nm^3}{m}$ (Gondal, 2016).

P_m and $P_{m'}$ are the upper and lower mean operating pressures, respectively. K_m and $K_{m'}$ are the corresponding compressibility factors of the hydrogen gas. p_n and T_n are the pressure and temperature considered at ambient conditions, T is the temperature of the hydrogen gas in the pipeline and assumed equal to ambient conditions (288.15 K). V_{geom} is the geometric volume of the pipeline. The total line pack storage capacity in kg_{H_2} can be calculated with Equation 3.28, where $V_{storage}$ is the line pack volume per meter and L_{pipe} the total length of the pipeline. The line pack volume per meter for the pipeline considered in this research is equal to $0.165 \frac{Nm^3}{m}$, which results in $0.014 \frac{kg_{H_2}}{m}$. Due to the low line pack storage capacity and the short distance pipelines considered with minimal pressure ranges, the storage capacity of the pipeline is not taken into account in this research

$$V_{storage} = V_{geom} \left(\frac{P_m}{K_m} - \frac{P_{m'}}{K_{m'}} \right) \frac{1}{p_n} \frac{T_n}{T} \quad (3.27)$$

$$Storage_{linepack} = V_{storage} * L_{pipe} \quad (3.28)$$



Figure 3.18: Solforce Hydrogen Pipeline (HYGRO, 2021)

3.5.4. Transport/Storage Cost breakdown

For both MEGCs and the HPSC, a similar cost structure applies. The CAPEX cost structure of compressed hydrogen transportation by road is defined by the investment cost regarding trucks and the trailers, where the demand at each of the HRS determines the total need of storage units in the distribution system.

The OPEX of the distribution system by road is mainly dependent on the total distribution network size. The total distribution network size defines the cost associated with fuel consumption and labour costs regarding a trip between the production location and HRS or between two refuelling stations. Increased distance between the production location and the HRS results in higher distribution cost per trip.

CAPEX Transport/Storage

Parameter	Pipeline
Diameter (Inner)	120 mm
Diameter (Outer)	149 mm
Operating temperature range	-40 C° - 65 C°
Maximum operating pressure, Compressibility factor	42 bar, 1.025
Minimum operating pressure, Compressibility factor	20 bar, 1.012
Nominal operating pressure	30 bar
Operating temperature	15 C°
Design life (surface)	20 years
Design life (buried)	50 years
Line pack volume	0.165 $\frac{Nm^3}{m}$
Density Hydrogen (ambient)	0.084 $\frac{kg}{m^3}$
Line pack storage capacity	0.014 $\frac{kg}{m}$

Table 3.22: Technical parameters hydrogen pipeline (HYGRO, 2021)

Parameter	Pipeline
CAPEX Material	125 $\frac{€}{m}$
CAPEX Installation	100 $\frac{€}{m}$
CAPEX Land lease	250 $\frac{€}{m}$
Fixed OPEX	0 $\frac{€}{m}$

Table 3.23: Economic parameters hydrogen pipeline (HYGRO, 2021)

Truck & Trailer	
Parameter	Assumption
CAPEX Truck	100.000 €
CAPEX Trailer	65.000 €
Average Speed	50 $\frac{km}{h}$
Fuel Consumption (20ft, 40ft trailer)	35 $\frac{L}{100km}$
Truck Availability	24 h
Fuel Price	1.5 $\frac{€}{liter}$
Lifetime	10 years
Fixed OPEX Truck	12 %
Fixed OPEX Trailer	2%
Total Fixed OPEX Truck + Trailer	8%

Table 3.24: Investment constraints truck & trailer (Lahnaoui et al., 2019; Meszler et al., 2018; Teichmann et al., 2012; Yang & Ogden, 2007)

In this research, a distinction is made between the number of transport vehicles and storage vessels. The CAPEX cost of a truck and trailer is described by Equation 3.29. The total capital cost for the entire vehicle fleet is defined by the amount of purchased truck and trailer combinations. The investment costs regarding each truck and trailer configuration are shown in Table 3.24.

$$CAPEX_{Vehicle} = CAPEX_{Truck} + CAPEX_{Trailer} \quad (3.29)$$

The assumption is that the costs and truck type associated with the truck pulling the trailers with MEGC or HPSC is considered equal for all trailer configurations. An overview of the tractor pulling

the MEGC is presented in Table 3.24. A typical truck can travel in between 1 and 1.5 million kilometres (Oostdam, 2019). Multiple EU studies on truck lifetime and distance travelled result in an average lifetime of between 8-12 years (Meszler et al., 2018). In this research, a lifetime of 10 years is assumed.

The economic constraints regarding the pipeline connection are shown in Table 3.23. The CAPEX cost for the pipeline is defined per km and contains three components, the material costs, the cost for installation of the pipeline and the land lease cost. The CAPEX cost function for the entire value chain regarding pipeline distribution is defined by Equation 3.30, where $distance_{pipeline}$ is the total pipe length present in the entire value chain between the production locations and hub refuelling stations. Equation 3.31 presents the cost function for the vehicle and trailer combination used. N_{trucks} defines the number of trucks available in the value chain. For all scenarios, two distribution trucks and trailers are taken into account.

$$CAPEX_{Pipeline} = Distance_{pipeline} \cdot CAPEX_{pipe} \quad (3.30)$$

$$CAPEX_{Vehicle} = N_{trucks} \cdot (CAPEX_{Truck} + CAPEX_{Trailer}) \quad (3.31)$$

The CAPEX costs regarding the MEGC and HSPC units is shown in Table 3.25. The total cost of hydrogen storage is calculated by evaluating the maximum storage needed during the considered time horizon and is determined post optimisation. The total CAPEX of hydrogen storage is defined by Equation 3.32, where $Storage_{Max}$ relates to the number of storage vessels present in the value chain and $CAPEX_{storage}$ depicts the cost of a single storage unit, regarding the type of storage considered, 20ft MEGC or the HSPC. Further elaboration on the calculation of the amount of storage required in the value chain is discussed in chapter 4.

Storage Vessel	Capex	OPEX
20ft MEGC	450.000	2%
HPSC	75.000	2%

Table 3.25: Investment parameters MEGC and HPSC units (HYGRO, 2021)

$$CAPEX_{Storage} = Storage_{Max} \cdot CAPEX_{Storage} \quad (3.32)$$

OPEX Transport/Storage

For each truck and trailer configuration, the fixed OPEX is considered a percentage of the CAPEX cost. According to Teichmann et al. (2012) the fixed OPEX cost for a truck is 12%, and for the different trailer configurations, the fixed OPEX is estimated at 2% of the CAPEX. Similar assumptions are adopted in this study. Taking the estimation of Teichmann et al. (2012) into account, a combined fixed OPEX percentage is set for the truck and trailer at 8%. Each MEGC or HPSC storage unit has an additional 2% fixed OPEX component based on the CAPEX cost of the MEGC or HPSC. The total fixed OPEX for transportation of hydrogen is defined by Equation 3.34. Equation 3.35 describes the fixed OPEX regarding the storage containers.

$$OPEX_{Fixed,Pipeline} = Distance_{pipeline} \cdot OPEX_{Fixed,pipeline} \quad (3.33)$$

$$OPEX_{Fixed,Vehicle} = N_{Trucks} \cdot (OPEX_{Fixed,vehicle} + OPEX_{Fixed,Trailer}) \quad (3.34)$$

$$OPEX_{Fixed,MEGC} = Storage_{Max} \cdot OPEX_{Fixed,MEGC} \quad (3.35)$$

The variable OPEX can be distinguished by the cost regarding the logistics of the compressed hydrogen and the labour cost associated with the truck driver. The logistic cost refers to costs associated with the fuel consumption by the truck. Fuel consumption is dependent on speed, weight, and distance. In this research, the distance combined with the average fuel consumption per distance travelled defines the fuel consumption costs.

(Delgado et al., 2016) has researched the fuel consumption for truck-trailer and rigid truck combinations worldwide. An extensive simulation model on fuel consumption based on transportation on 50% regional roads and 50% highways with an average speed of 50 km/h for European trucks resulted in an approximation for fuel consumption for the weight ranges of 10.000 kg and 20.000 kg corresponding to the weights of the 20ft and 40ft trailers with either MEGC or HPSC of 35 and 45 $\frac{L}{100km}$, respectively. The approximation of road transportation with a 50/50 division between regional roads and highways is assumed plausible when considering the environment of the hydrogen distribution network in the province of North Holland, the Netherlands. The total fuel consumption in $\frac{L}{100km}$ for a 20ft trailer is considered at 35 $\frac{L}{100km}$.

The average fuel price for the recent five years (2017-2021) is equal to 1,17 $\frac{\text{€}}{\text{Liter}}$. The fuel price for diesel as of 2021 for the Netherlands has increased to roughly 1.50 $\frac{\text{€}}{\text{Liter}}$ diesel (CBS, 2021; EVOFENEDEX, 2021). The fuel price trend for the past five years shows a sharp increase. It is assumed that the fuel price will keep rising in the upcoming years (EVOFENEDEX, 2021). In this research, therefore, a fuel price of 1.50 $\frac{\text{€}}{\text{Liter}}$ for diesel is assumed.

The labour cost regarding a truck driver with ADR certification is estimated at €35 per hour (Teichmann et al., 2012). The average travel speed for each truck is defined 50 $\frac{km}{h}$ (Meszler et al., 2018). The labour cost, therefore, for each travelled kilometre when only considering the travel time is 0.70 $\frac{\text{€}}{km}$. However, an unloading and loading time for swapping the MEGCs or HPSC at the hydrogen production location or the HRS must be considered. The truck driver is expected to perform all handling operations regarding swapping the MEGCs and HPSCs. The implementation of both fuel consumption and total costs regarding labour by travel time and handling time of the containers is further elaborated in chapter 4.

3.5.5. Distribution Topology

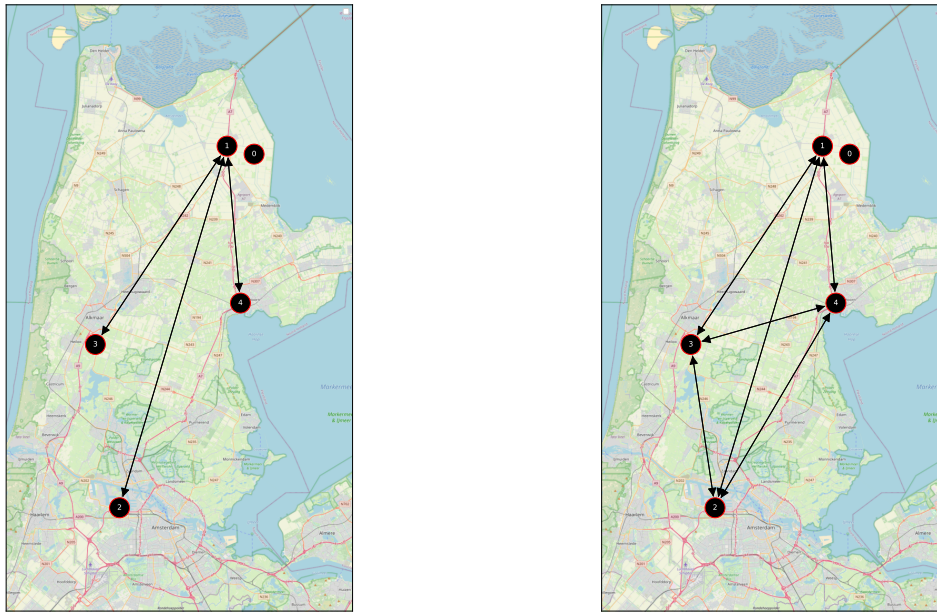
An overview of the different distribution network topologies and their corresponding route options is given by Figure 3.19a and Figure 3.19b. These figures show an example distribution network with a single wind turbine and three refuelling stations. The blue dot presents the wind turbine combined with the hydrogen production location. The hydrogen produced at the production location is transported to the hub station via pipeline and from the hub station further distributed towards regional satellite stations with either MEGC or HPSC with indirect or direct delivery.

3.6. Hydrogen Refuelling Station

This section contains an overview of the two types of refuelling stations considered in this research based on the 'Hub' and 'Satellite' approach defined by HYGRO.

3.6.1. Hub Refuelling Station

Figure 3.20 shows a Piping and Instrumentation Diagram (PID) of the hub station considered in this research. The hub station consists of 2 hydrogen dispensers a compression module to compress the delivered hydrogen from the pipeline connection up to the appropriate pressure level of 640 bar for the MEGC or HSPC containers. A booster compressor and 980 bar high-pressure stationary storage are present for the hydrogen dispenser, filling vehicles up to 700 bar. For the hydrogen dispenser, a filling speed of 7.2 $\frac{kg_{H_2}}{min}$ is assumed according to the SAE J2601-2 protocol with a filling pressure up



(a) Distribution Network Type - Fixed

(b) Distribution Network Type - Flexible

Figure 3.19: Example of distribution network routes for MEGC (left) and HPSC (right) containers

to 350 bar. As the hydrogen dispenser is not able to continuously operate for an entire hour, an average operating time of the hydrogen dispensers of 55% is assumed, which results in a maximum filling capacity of $476 \frac{kgH_2}{hour}$ per hydrogen dispenser. The maximum hydrogen dispensed in a single hour per dispenser is considered equal for all refuelling stations.

The cost overview for the hub refuelling station is shown in Table 3.26. The refuelling station’s total CAPEX and OPEX cost is based on the maximum hourly demand obtained from the demand model discussed in the following section. If the maximum hourly demand of the refuelling station exceeds the filling capacity of the hydrogen dispensers considered in the PID, two in the case of the hub refuelling station, an extension of the refuelling system must be considered. The extension of the refuelling station is considered to have increments equal to the PID shown in Figure 3.20. Consequently, the total CAPEX and OPEX costs for a single hub refuelling station is equivalent to the increments of a single PID.

The PID shows two connection points for the MEGCs or HPSCs. The cost of extending a refuelling station with an extra connection point for either a MEGC or HSPC is negligible for the entire refuelling station. Therefore, the amount of possible connection points is assumed to be unlimited at the refuelling station without the need for expansion. Therefore, the number of connection points does not limit the total storage capacity at the refuelling station in the optimisation model.

Component	Capex	Fixed OPEX
Installation	1.200.000	40.000
Civil works	150.000	
Grid connection	30.000	600
Land Lease	-	15.000
Total	1.380.000	55.600

Table 3.26: Cost overview hub refuelling station

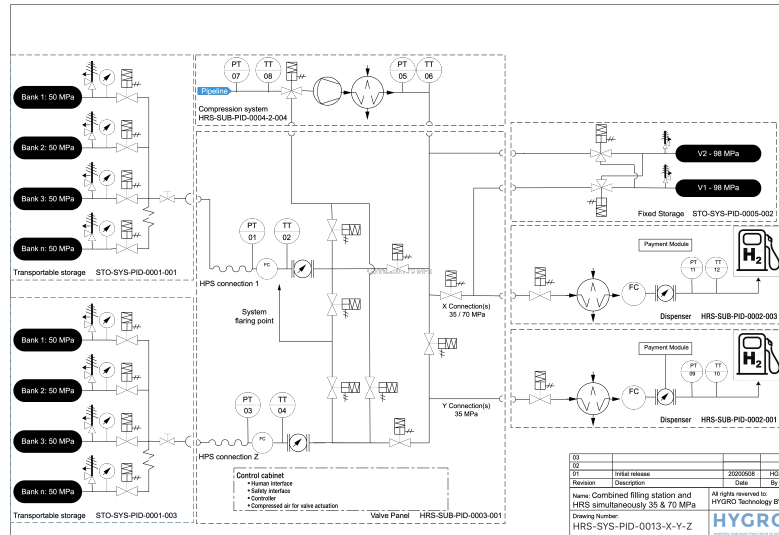


Figure 3.20: PID Hub Station

3.6.2. Satellite Station

Figure 3.21 shows a Piping and Instrumentation Diagram (PID) of the satellite station. The satellite station consists of a single hydrogen dispenser and a valve panel that controls the hydrogen flow from the MEGC or HPSC to the hydrogen dispenser. Similar to the hub refuelling station, a filling speed of $7.2 \frac{kgH_2}{min}$ is assumed according to the SAE J2601-2 protocol with a filling pressure up to 350 bar.

Also, an operational time of 55% is assumed, which results in a filling capacity of $238 \frac{kgH_2}{hour}$. A cost overview for the satellite station is shown in Table 3.27. A similar procedure of determining the CAPEX and OPEX costs for the satellite refuelling station is considered as described previously for the hub refuelling station. Equal to the hub refuelling station, no capacity limit is assumed for storage as the cost for additional connection points for MEGC or HPSC is negligible to the remainder of the satellite station's costs.

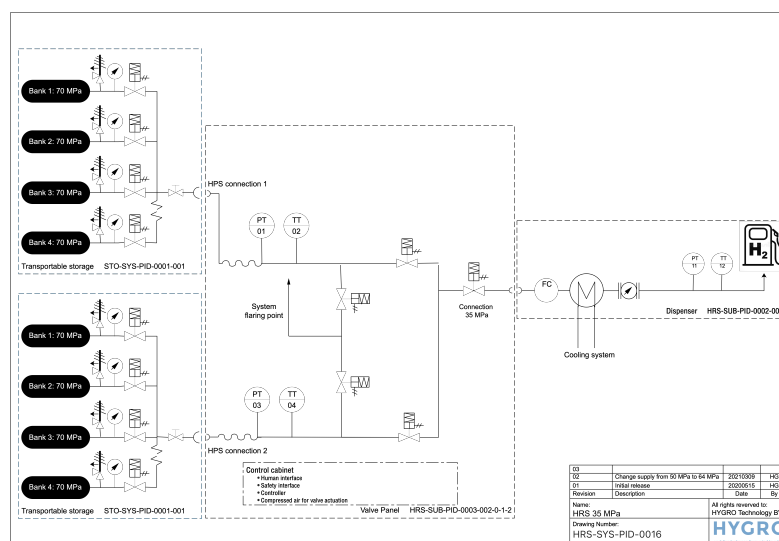


Figure 3.21: PID Satellite Station

Component	Capex	Fixed OPEX
Installation	500.000	10.000
Civil works	75.000	
Grid connection	20.000	600
Land Lease	-	15.000
Total	595.000	25.600

Table 3.27: Cost overview satellite refuelling station

3.7. Demand Model

This section describes the adopted modelling approach to define the hydrogen demand at each HRS location. Actual refuelling data from diesel-powered vehicles is translated into a hydrogen demand pattern. Where after the equivalent hydrogen demand pattern for both end-user categories is presented.

The assumption is made that the refuelling behaviour remains constant. The current diesel demand in litres is converted to an equivalent hydrogen demand in kg based on energy content. The conversion factor for diesel in litres to hydrogen in kg is represented by Equation 3.36. The energy content of a liter diesel is equivalent to $43.4 \frac{MJ}{kg}$ with a density of $0.84 \frac{kg}{L}$ at 20 C° (Navas-Angueta et al., 2019). The higher heating value of hydrogen is equivalent to $141.9 \frac{MJ}{kg}$ ("National Research Council and National Academy of Engineering", 2004). The conversion factor from diesel to hydrogen is equal to $0.268 \frac{kg_{H_2}}{L_{diesel}}$.

$$CF_{H_2,Diesel} = \frac{EnergyDensity_{Diesel} \cdot \rho_{Diesel}}{EnergyDensity_{H_2}} \quad (3.36)$$

When adopting a different drive train technology, the change in Tank-To-Wheel (TTW) energy efficiency must be taken into consideration. A decrease in energy consumption of 35% for the FCET is assumed based on findings from Röck et al. (2020). No change in TTW efficiency for the dual-fuel vehicle category is assumed.

The hydrogen demand for both end-user categories is calculated according to Equation 3.37 and Equation 3.38. Where $CF_{H_2,Diesel}$ is the conversion factor from diesel to kg hydrogen. $diesel_l$ is the number of litres of diesel fuel. $CF_{TTW,FCET}$ and $CF_{TTW,DFV}$ is the change in TTW energy efficiency. $Injection_{DF}$ represents the injection fraction of the hydrogen-diesel mixture adopted by the DF vehicle category. The average hydrogen-diesel fuel mixture for the H2DualPower tractor is assumed 40% hydrogen and 60% diesel fuel (Scholman & Scholman, 2020). The supply of diesel is not considered in this research.

$$H_{2(Demand,FCET)} = CF_{H_2,Diesel} \cdot Diesel_l \cdot (1 - CF_{TTW,FCET}) \quad (3.37)$$

$$H_{2(Demand,DF)} = CF_{H_2,Diesel} \cdot Diesel_l \cdot (1 - CF_{TTW,DF}) \cdot Injection_{DF} \quad (3.38)$$

3.7.1. FCET Demand

Refuelling data from a waste collection company is taken as a reference to calculate the hydrogen demand for the FCET category. For model simplification no distinction is made between refuelling data for the different vehicle types. The dataset adopted in this case study contains four different vehicle

types. The vehicle types considered are rigid trucks, collecting household waste and wheeled containers. Secondly, hook lifts and skips trucks collect large waste containers. The final vehicle type is tractor-trailer combinations utilised for goods transportation for the waste collection company. An overview providing insight into the distribution of vehicle types and amount of vehicles included in the dataset is given by Table 3.28.

FCET End-User Category	
Vehicle type	Amount
Household waste, wheeled container	320
Hook Lift, Skip Truck	442
Tractor - Trailer	276
Total	1038

Table 3.28: Distribution vehicles waste recollection company data

Two essential parameters that define the demand pattern at the refuelling station is the demand per filling event and the timestamp of the filling event. The timestamp represents the time of the day and the day of the week that the refuelling event has taken place.

Figure 3.22 shows the probability distribution of diesel demand at each refuelling event for the waste collection company vehicles. The average diesel per filling event is equal to 190.4 litres. Adopting Equation 3.37 the hydrogen demand per filling event can be determined.

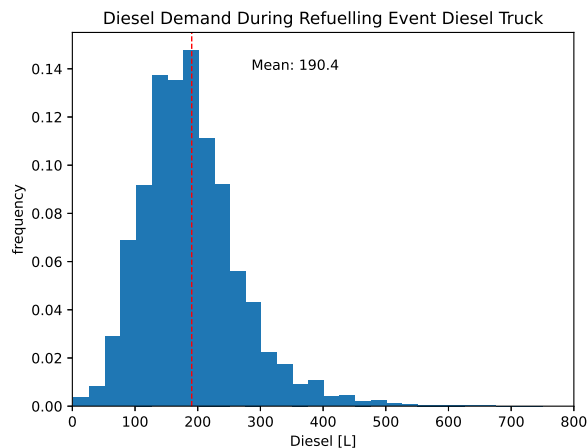


Figure 3.22: Normalized distribution amount of litres diesel per fill event waste collection company

As discussed in chapter 2 the Hyzon Motors HyMax 450 is taken as a reference to model the hydrogen demand. The fuel tank capacity of the Hyzon HyMax 450 is considered 35 kg. Upon arrival, it is assumed that all FCET's have 5 kg left in the hydrogen storage tank. The residual hydrogen inside the storage vessels results in a maximum demand of 30 kg. Translating the current diesel demand from litres to hydrogen demand, result in fill events exceeding the maximum 35 kg tank capacity. Therefore the hydrogen demand for a single fill event larger than 35 kg is split into multiple fill events. The probability distribution for the quantity of hydrogen demand during a fill event adjusted for the maximum storage tank capacity is shown in Figure 3.23. An increase of 7.6% in the number of fill events is observed.

The second parameter is the time step when each refuelling event takes place. The time step of each refuelling event defines the frequency of filling events per time step interval. In this research, the refuelling data analysis is done hourly. Figure 3.24 shows the frequency of fill events for a single week

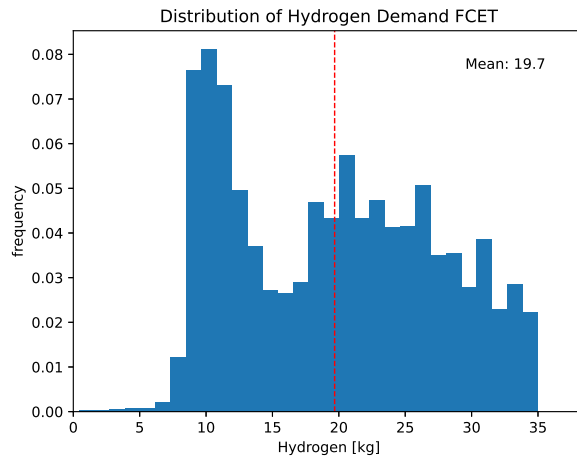


Figure 3.23: Distribution of adjusted hydrogen demand FCET

on an hourly basis for the waste collection company. It can be noticed that most fill events occur during weekdays between 5-7 AM and 2-5 PM. A small number of fill events occur on Saturday, and fewer fill events occur on Saturday and Sunday.

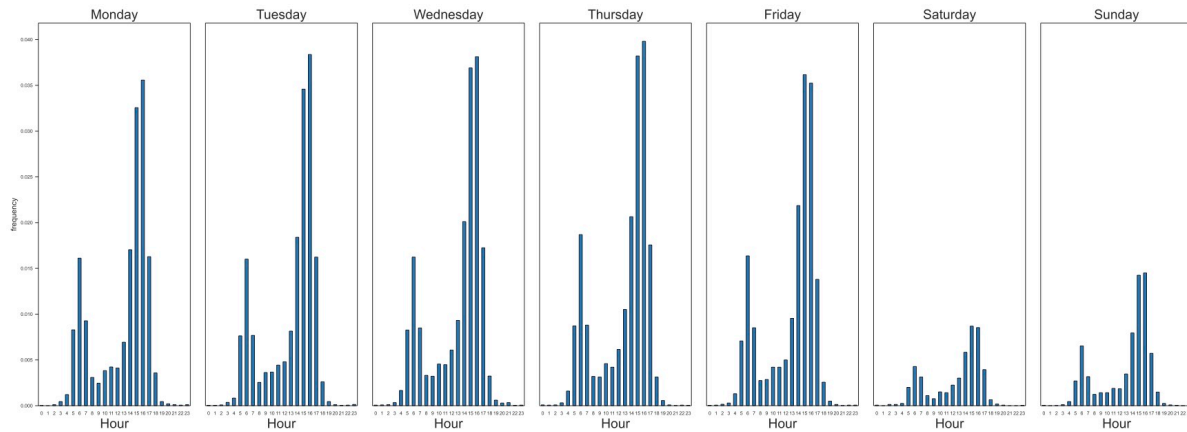


Figure 3.24: Probability distribution of hourly fill events from the waste collection company

3.7.2. Dual-Fuel demand

For the second hydrogen end-user category adopting the dual-fuel ICE, fuel event data from a contractor is taken as a reference. Similar to the first end-user category, no distinction is made based on the technical parameters of the different tractors.

Figure 3.25 shows the probability distribution of diesel demand at each refuelling event. The average amount diesel demand per filling event is equal to 56.0 litres. Adopting Equation 3.38 the hydrogen demand per filling event can be determined.

In chapter 2 the hydrogen dual-fuel tractor developed by H₂ DualPower is taken as a reference to model the dual-fuel hydrogen demand. Technical details on the dual-fuel tractor are shown in Table 2.8. The fuel tank capacity of the H₂DualPower dual-fuel tractor is 11.5 kg. Upon arrival, it is assumed that all dual fuel tractors have a minimum of 0 kg hydrogen left in the hydrogen storage tank. An empty hydrogen storage tank is possible as the dual-fuel tractor can operate on purely diesel fuel. This results in a maximum filling capacity of 11.5 kg.

Similar to the FCET end-user category translating the current diesel demand from litre to hydrogen

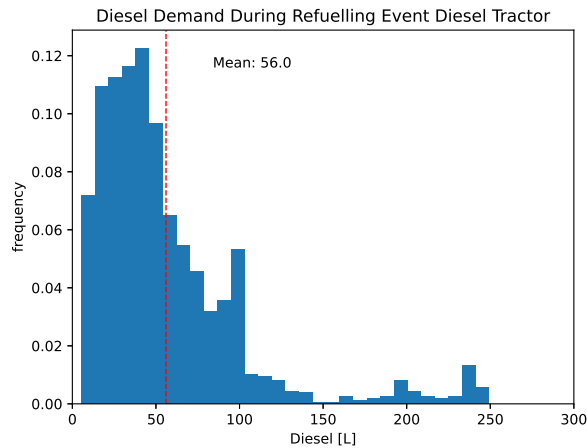


Figure 3.25: Distribution Liters fueled diesel tractors

demand in kg per fill event results in fill events exceeding the maximum 11.5 kg tank capacity. Therefore the hydrogen demand for a single fill event larger than 11.5 kg is split into multiple equal amounts fill events with reduced hydrogen demand to comply with the assumption that the total energy demand for the vehicles remains constant and an average hydrogen injection rate of 40% is reached. The probability distribution of the adjusted hydrogen demand is shown in Figure 3.26. When considering an average injection rate of 40% and maximum filling capacity, the average weekly fill event rate is increased by 8.1%.

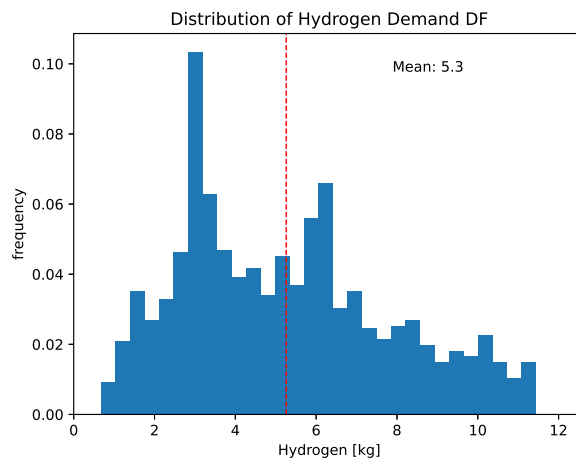


Figure 3.26: Distribution adjusted hydrogen demand DFV

Figure 3.27 shows the frequency of fill events for a single week on an hourly basis for the contractor considering the timestamps of the fuelling events. It can be noticed that similar to the FCET end-user category. Most fill events occur during weekdays between 5-7 AM and 3-5 PM. A small number of fill events occur on Saturday, and almost no fill events occur on Sunday.

3.7.3. Refuelling Station Demand Model

This research adopts a similar approach to determine a hourly hydrogen demand pattern as is described in Kurtz et al. (2020). The demand model predicts the future hydrogen demand for both end-user categories at the HRS. As discussed in the previous section the amount of vehicles arriving at the refuelling station and the demand of each vehicle define the demand pattern.

Firstly, for each hour of the day the amount of vehicles arriving at the refuelling station must be

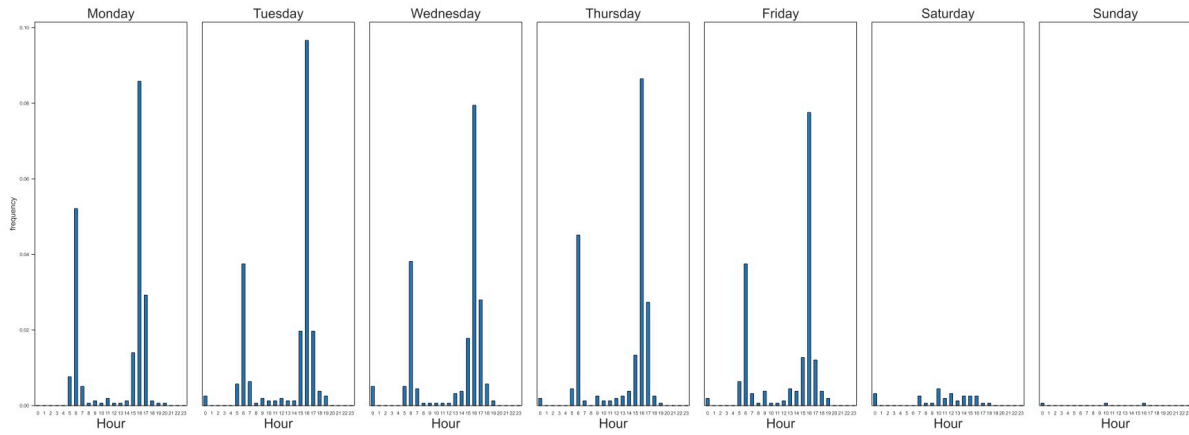


Figure 3.27: Probability distribution of hourly fill events from the contractor company

Figure 3.28: Poisson distribution

determined. In this research, a fill event is considered a discrete event. A Poisson counting process is adopted to determine the number of arrivals of vehicles at a hourly time interval. A counting process is a stochastic process that keeps count of the number of events that have occurred within a time interval (Boxma & Yechiali, 2007). The arrival of vehicles is modelled as a non-homogenous Poisson process as the average rate of arrival is not constant through time, and can be observed in Figure 3.24 and Figure 3.27. The poisson probability distribution is described by Equation 3.39. Where λ is the expected number of events during a single hourly time interval and k is the number of events during that specific time interval.

Both Figure 3.24 and Figure 3.27 depict the frequency of a fill event occurring in that specific hourly time interval. The probability of events occurring in each specific time interval combined with the average total weekly fill events, ensures the ability to determine the hourly mean vehicle arrival rate. Each hour of the week can be described by its specific Poisson distribution which is used to determine the amount of vehicles arriving at each refuelling station for a single year on a hourly time scale.

$$f(k; \lambda) = \frac{\lambda^k e^{-\lambda}}{k!} \quad (3.39)$$

Secondly, the amount of dispensed kg of hydrogen for each fill event must be determined to obtain a realistic demand profile at the HRS. According to Kurtz et al. (2020); 'the amount of hydrogen and rate per fill depends on the vehicle's on-board storage volume, its state of charge, and the station's ability to complete a full fill'. In this research, a simplified model is proposed compared to Kurtz et al. (2020). Only the amount of hydrogen demand expressed in kg is taken into account.

A Kernel-Density Estimation (KDE) is adopted to define the underlying Probability Density Function (PDF) of the hydrogen demand per filling event for both end-user vehicle categories from the given dataset. The KDE is described by Equation 3.40. A Gaussian Kernel is used in this research. Every data point in the hydrogen demand dataset is represented by a Gaussian distribution where h defines the bandwidth. The average sum of all Gaussian distribution result in the overall PDF of the dataset. Shown in Figure 3.29 for both vehicle categories. The demand per fill event is sampled from the shown PDF distributions.

$$f(x) = \frac{1}{nh} \sum_{i=1}^n K\left(\frac{x - x_i}{h}\right) \quad (3.40)$$

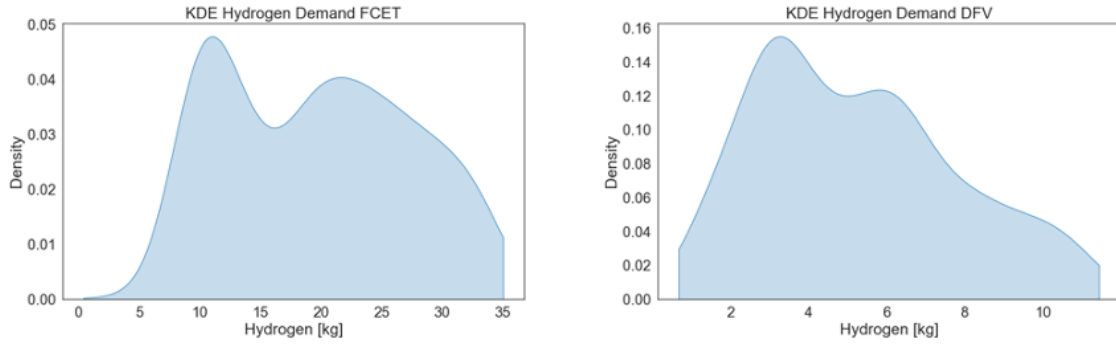


Figure 3.29: Kernel Density Estimation on adjusted FCET & DFV demand data

The combination of determining the number of vehicles arriving each hour at the refuelling station according to the non-homogeneous Poisson distribution and the sampled hydrogen demand from the KDE for each vehicle independently results in a realistic hourly demand profile. Figure 3.30 shows an example of a demand curve at an HRS with a 50:50 distribution of both end-user categories. An average daily hydrogen demand of 400 kg is assumed in Figure 3.30. The illustrated week represents the first week of 2019 and starts from Wednesday. It is shown that the weekend has almost no demand, while weekdays return demand in the morning and the afternoon as is seen in Figure 3.24.

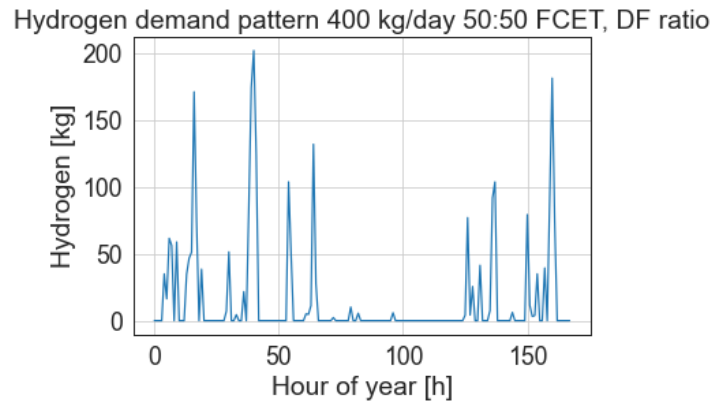


Figure 3.30: Hydrogen demand profile for a single week

4

Optimisation Model

This chapter introduces the single objective MILP cost optimisation model regarding the hydrogen value chain with multiple production locations, hub refuelling stations and satellite refuelling stations. This chapter starts with describing the general approach to determine the total annual cost and LCOH of the hydrogen value chain. Secondly, the objective function that minimises the operational costs concerning hydrogen production and distribution in combination with the investment cost of the total storage capacity is discussed in section 4.2. The objective function can be divided into three sections describing hydrogen production, storage and distribution. The output of the optimisation model is used to determine the total cost of the hydrogen value chain. The total cost function described in section 4.7 in combination with the total annual demand results in the ability to calculate the LCOH. Finally, section 4.8 provides an overview of all 'parameters' and 'variables' utilised in the optimisation model and LCOH calculations. A total overview of the objective function and the constraints is shown in Appendix B.

4.1. Modelling Approach

First, the power production capacity of the entire optimisation planning horizon of the considered wind turbines is determined by the model described in subsection 3.1.2. Secondly, the hydrogen demand at each refuelling station is determined independently, as described in section 3.7. Both the power production profile and the demand profile in combination with the overall scenario boundaries result in the ability to formulate the Mixed Integer Linear Programming (MILP) optimisation problem. The objective function to determine the optimal solution is described in section 4.2.

The commercial optimisation solver Gurobi (Gurobi, 2021) is used to determine the optimal solution. The commercial solver adopts a branch and bound approach to solving the Mixed Integer Linear Programming (MILP) model. From the available optimisation algorithms provided by the Gurobi software package, the barrier algorithm has proven to achieve the best performance.

The barrier algorithm is often fast for large and complex MILP problems such as the model considered in this research. However, it requires large memory and sufficient computational power. The optimality gap for all scenarios is set to 5% to decrease the run time to find the optimal solution. The optimisation algorithm is terminated after 3600 seconds, independent if the optimality gap of less than 5% from the optimal solution is reached.

Detailed research towards the available optimisation algorithms and their corresponding influence on optimisation performance is outside the scope of this study.

In Figure 4.1 an overview of the workflow to derive the LCOH of a hydrogen value chain is shown. The workflow from scenario definition to the LCOH visualisations is depicted, where the boundary of the Python model is illustrated by the blue dotted box.

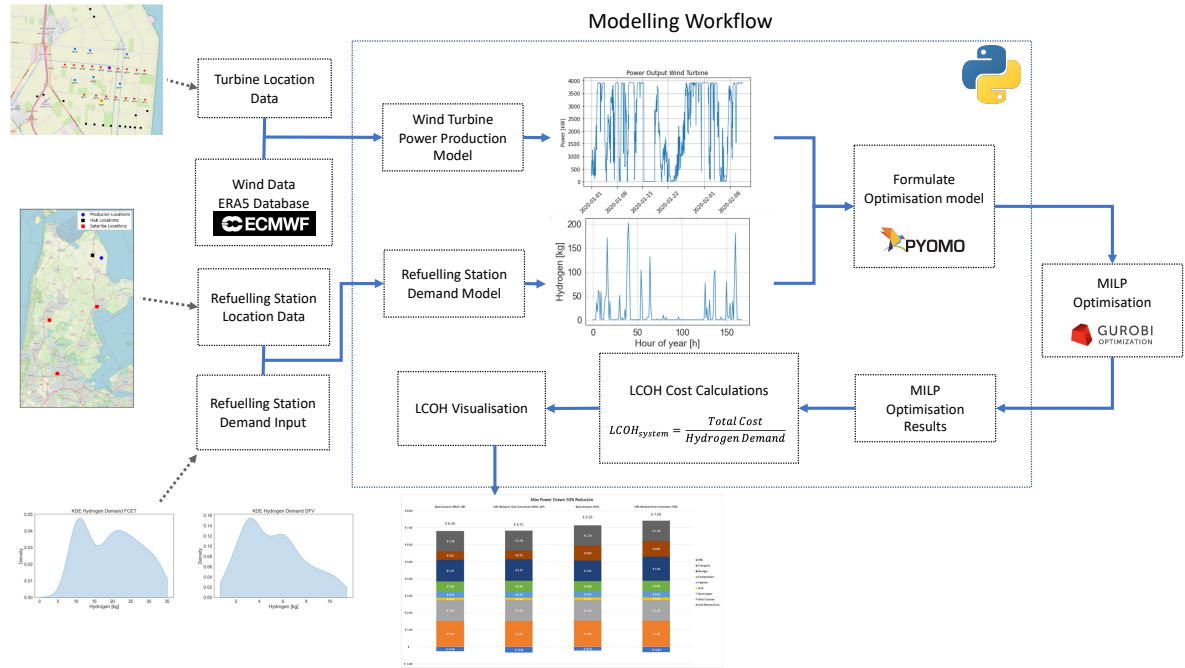


Figure 4.1: Schematic Overview of workflow to determine the LCOH

4.2. Objective Function

The objective function is described by Equation 4.1. Equation 4.1a describes the operational cost concerning energy bought from and sold to the electricity grid, denoted by variable $E_{grid,pt}$. This section of the objective function is dependent on the decision variable $Q_{Hydrogen,pt}$. $Q_{Hydrogen,pt}$ describes the production quantity of hydrogen per time step per production location. The constraints defining the production of hydrogen are discussed in section 4.3

The second section of the objective function, Equation 4.1b, describes the total investment cost for the required storage capacity to satisfy the hydrogen demand. The variable $Storage_{max}$ is dependent on all three decision variables, $Q_{Hydrogen,pt}$, Q_{skhdt} and x_{ijkht} , where Q_{skhdt} describes the quantity of hydrogen delivered to each satellite station and x_{ijkht} describes the routes travelled by the distribution vehicles. The constraints that define the total required storage capacity are further discussed in section 4.4.

The final section of the objective function described by Equation 4.1c, defines the operational cost of hydrogen distribution and is dependent on the decisions variables, Q_{skhdt} and x_{ijkht} . The operational distribution cost can be split into travel costs and handling time costs. All constraints concerning the distribution of hydrogen are discussed in section 4.5.

$$\min_{Q_{Hydrogen,pt}, Q_{skhdt}, x_{ijkht}} \left(\sum_{t \in \mathbf{T}} \sum_{p \in \mathbf{P}} -E_{Grid,pt} \cdot C_{GridEnergy,pt} \cdot C_{Imbalance,pt} \right) \quad (4.1a)$$

$$Storage_{max} \cdot CAPEX_{MEGC} + \quad (4.1b)$$

$$\sum_{(i,j) \in \mathbf{E}} \sum_{k \in \mathbf{K}} \sum_{h \in \mathbf{H}} \sum_{t \in \mathbf{T}} c_{ij} \cdot x_{ijkht} + \sum_{k \in \mathbf{K}} \sum_{h \in \mathbf{H}} \sum_{t \in \mathbf{T}} Ht_{kht} \cdot Wage_{Driver} \quad (4.1c)$$

4.3. Hydrogen Production

The first decision variable is the quantity of hydrogen production per time step at each production location ($Q_{Hydrogen,pt}$). p represents the hydrogen production location, and t represents the time step. The

quantity of hydrogen produced is always limited to the maximum production quantity of the electrolyser, $Q_{HydrogenMax}$. The total operational cost regarding hydrogen production depends on the amount of available wind energy and energy bought and sold, from and to the grid.

The wind energy production per time step ($E_{WT,pt}$) is defined for each production location p . The wind energy production capacity is determined for each location before optimisation by the wind energy production model discussed in subsection 3.1.2. The energy production capacity is based on historical data of a single year between 2015 and 2020. The coordinates of the production location are described by adopting the geographic coordinate system. The parameter x_p describes the latitude coordinate, and the parameter y_p describes the production location's longitude coordinate. The location of p is described by $p(x_p, y_p)$

The variable $E_{Grid,pt}$ quantifies the amount of energy bought or sold at time step t at production location p . The variable $E_{Grid,pt}$ is subjected to Equation 4.2 and is negative when energy is bought from the grid and positive when energy is sold to the grid. The variable $E_{Curtilment,pt}$ represents the wind energy that is neither used for the production of hydrogen nor sold to the grid.

The quantity of hydrogen produced is expressed in kg . The energy required for hydrogen production is expressed in kWh . The variable $E_{Hydrogen,pt}$ describes the energy required for the electrolyser to produce the quantity, $Q_{Hydrogen,pt}$ and is subjected to Equation 4.3. The function describing the energy required for hydrogen production from kg of hydrogen to kWh is piecewise linear fitted to the conversion graph shown in Figure 3.15. All conversion losses from the wind turbine to the electrolyser output are included.

In this model, an extra cost component is added for power sold to the grid. The energy trading company implies a 10% fee on all power sold by the turbine to cover the cost for selling energy on the electricity markets ($Factor_{Imbalance}$). If energy is sold to the grid, the variable $C_{Imbalance,pt}$ is equal to 0.9. When energy is bought, the variable $C_{Imbalance,pt}$ is equal to one. The binary variable $Z_{PEM,pt}$ is equal to one if hydrogen is produced at time step t at the production-hub location p , and 0 otherwise.

This optimisation model assumes that all hydrogen is directly compressed up to the required pressure for hydrogen storage. Due to the working principle of the diaphragm compressor considered in this research, it is either operational or off. The maximum energy consumption of the compressor is taken into account when hydrogen is produced tracked by the binary variable $Z_{PEM,pt}$. It is assumed that a separate grid connection is present at the refuelling station supplying energy for the compression of hydrogen. The cost of compression of the hydrogen is calculated post optimisation and is discussed in section 4.7.

The following constraints are used in the optimisation model regarding the production of hydrogen:

$$E_{Grid,pt} = E_{WT,pt} - E_{Hydrogen,pt} - E_{Curtilment,pt} \quad \forall p, \quad \forall t \quad (4.2)$$

$$E_{Hydrogen,pt} = f(Q_{Hydrogen,pt}) \quad \forall p, \quad \forall t \quad (4.3)$$

$$E_{Grid,pt} \leq Z_{Grid,pt} \cdot BigM \quad \forall p, \quad \forall t \quad (4.4)$$

$$E_{Grid,pt} \geq (Z_{Grid,pt} - 1) \cdot BigM \quad \forall p, \quad \forall t \quad (4.5)$$

$$C_{Imbalance,pt} = 1 - (Z_{Grid,pt} \cdot (1 - Factor_{imbalance})) \quad \forall p, \quad \forall t \quad (4.6)$$

$$Q_{Hydrogen,pt} \geq Z_{PEM,pt} \quad \forall p, \quad \forall t \quad (4.7)$$

$$Q_{Hydrogen,pt} \leq Z_{PEM,pt} \cdot BigM \quad \forall p, \quad \forall t \quad (4.8)$$

$$Q_{Hydrogen,pt} \leq Q_{HydrogenMax} \quad \forall p, \quad \forall t \quad (4.9)$$

$$E_{Hydrogen,pt} \leq E_{HydrogenMax} \quad \forall p, \quad \forall t \quad (4.10)$$

$$E_{Grid,pt} \geq -E_{GridCapacity} \quad \forall p, \quad \forall t \quad (4.11)$$

$$E_{Grid,pt} \leq E_{GridCapacity} \quad \forall p, \quad \forall t \quad (4.12)$$

$$C_{Imbalance,pt} = [0, 1] \quad \forall p, \quad \forall t \quad (4.13)$$

$$Z_{PEM,pt} \in \{0, 1\} \quad \forall p, \quad \forall t \quad (4.14)$$

$$Z_{Grid,pt} \in \{0, 1\} \quad \forall p, \quad \forall t \quad (4.15)$$

$$Q_{Hydrogen,pt} \geq 0 \quad \forall p, \quad \forall t \quad (4.16)$$

$$E_{Hydrogen,pt} \geq 0 \quad \forall p, \quad \forall t \quad (4.17)$$

$$E_{Curtailment,pt} \geq 0 \quad \forall p, \quad \forall t \quad (4.18)$$

4.4. Hydrogen Storage

The required storage capacity of the hydrogen value chain is the sum of the inventory at all hydrogen refuelling station locations. The locations of the hydrogen refuelling station are determined before optimisation and are based on the scenario considered. Each refuelling station location is described by the geographical coordinate system, similar to the production locations. x_h and x_s represent the latitude coordinates for the hub refuelling stations and satellite refuelling stations, respectively, and y_h , y_s represent the longitude coordinates.

The MEGCs or HPSCs at each location provides the ability to store hydrogen. Integrating an inventory component into the multi-period model is based on the inventory routing problem. The inventory allows demand satisfaction across multiple time steps without needing a vehicle arriving at each refuelling station. Demand can be satisfied from the delivered hydrogen at or before time step $t - 1$. Compared to a vehicle routing problem (VRP), the demand of every time step must be satisfied by the delivered hydrogen at the same time step.

Each production location is connected to a hub station via a pipeline connection. No inventory is assumed at the production location as all produced hydrogen is directly transported towards the hub refuelling station. Therefore, the production location and hub refuelling station inventory are considered the same, and therefore hydrogen is distributed between the hub refuelling stations and the satellite stations.

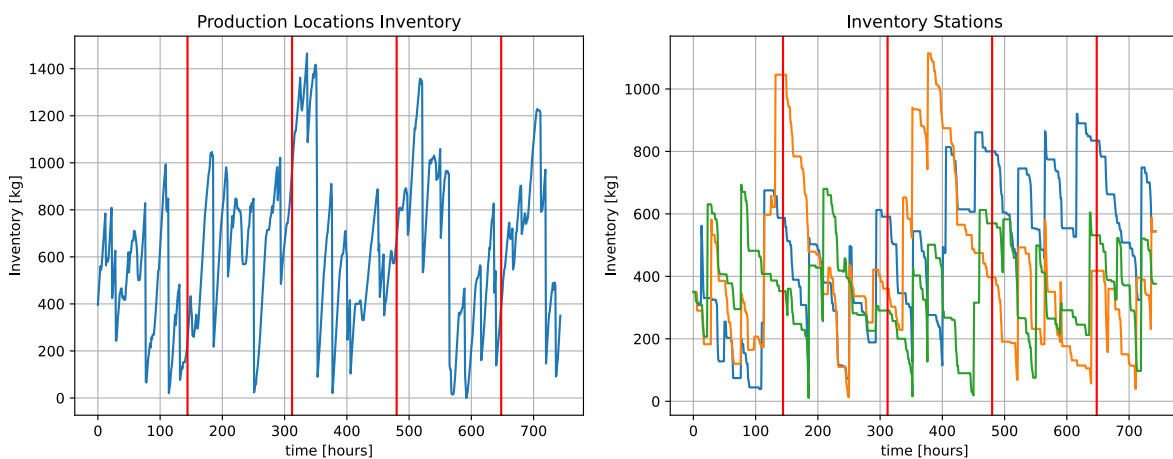
The demand for every refuelling station is determined before the optimisation based on the considered scenario. The parameter that defines the demand profile is the total average daily hydrogen demand and is defined as $demand_{Daily}$ expressed in $\frac{kgH_2}{day}$. The demand is considered to be equal for each refuelling station location. The daily demand pattern is stochastically modelled described by the demand model in section 3.7

The inventory balance constraints at each hub refuelling station is described by Equation 4.19, Equation 4.20, Equation B.49 and for the satellite stations by constraints Equation 4.21, Equation 4.22, Equation B.50. I_{ht} describes the inventory level in kg hydrogen. $Q_{hydrogen,pt}$ is the amount of hydrogen produced which is directly delivered from the production location. $(Q_{skhat} \cdot MEGC_{kg,d})$ is the amount of hydrogen delivered to each satellite refuelling station. Index d denotes the amount of MEGC or HPSC units delivered. $d_{FCET,ht}$ and $d_{DF,ht}$ is the demand for FCET and DFV at the hub refuelling station, respectively. And $d_{FCET,st}$ and $d_{DF,st}$ describes the demand at the satellite refuelling station.

The planning horizon of the single year is divided into weekly optimisation problems that run from Monday 00:00 to Sunday 23:00. The inventory at all locations of the previous week is used as input

for the next week. The considered year of optimisation is optimised on a weekly interval to reduce the optimisation problem's solution space and ensure the model's solvability in a reasonable period. The weekly optimisation approach does not consider the required hydrogen for the following week and trends to sell electricity to the grid without producing hydrogen for the upcoming week. This results in insufficient hydrogen at each location when the consecutive weeks are optimised. To ensure continuity throughout the year between the weekly optimisation problems, an arbitrary continuity equation must be determined. This equation defines the required inventory at the end of the planning horizon of the weekly optimisation problem and ensures the availability of hydrogen at the beginning of the upcoming week.

To determine the arbitrary inventory continuity equation and reduce the influence of the equation on the overall optimisation and the LCOH results, The optimisation model is first to run for a single month without any weekly intervals. Figure 4.2a and Figure 4.2b show the inventory of the hub refuelling stations and satellite refuelling stations for a monthly optimisation period, respectively. A scenario with a single hub and three satellite stations is shown. The red vertical lines in the graph represent the cuts made by the weekly optimisation process to ensure faster run time and solvability of the model. The impact of the weekly optimisation model compared to a yearly optimisation process is further discussed in chapter 6.



(a) Inventory hub refuelling station, first month 2019, MEGC 20ft

(b) Inventory Satellite refuelling stations, first month 2019, MEGC 20ft

Figure 4.2: Inventory of refuelling station locations (monthly optimisation period)

Separate equations for the hub refuelling stations and the satellite stations are derived from Figure 4.2a and Figure 4.2b. The required inventory by the end of the weekly planning horizon for the hub refuelling stations is described by Equation 4.23. The constraint regarding the satellite refuelling stations is described by Equation 4.24. The inventory at the hub refuelling stations must equal the average daily demand, plus the average daily demand at the satellite refuelling station multiplied by the ratio between the number of refuelling stations and hub refuelling stations present in the value chain.

The required inventory at the satellite refuelling stations must be equal to the average daily demand by the end of the weekly planning horizon. The average daily demand is multiplied by the factor, $Inventory_{continuity}$ and scales the described continuity equations to match the inventory levels shown in Figure 4.2a and Figure 4.2b. The $Inventory_{continuity}$ is determined to be 1.5 for all scenarios considered described in chapter 5.

For every time step the inventory at each hub refuelling station is subjected to Equation 4.19, Equation 4.20 and Equation B.49. The inventory for each satellite station subjected to Equation 4.21, Equation 4.22 and Equation B.50. The integer variable $Storage_{Max}$ (Equation 4.28) tracks the maximum amount of MEGC or HPSC units required in the entire planning horizon of a single year. The integer variable is presented in the objective function as the total storage required to fully satisfy demand and

therefore minimised to determine the lowest LCOH. The integer variable $Storage_{Max}$ is used in the LCOH calculations to determine the total CAPEX and OPEX regarding the required storage in the entire hydrogen value chain.

The following constraints are used in the optimisation model to determine the required inventory for the hydrogen value chain:

$$I_{start,h} + Q_{Hydrogen,pt} = \sum_{s \in \mathbf{S}} \sum_{k \in \mathbf{K}} \sum_{d \in \mathbf{D}} Q_{skhdt} \cdot MEGC_{kg,d} + d_{FCET,ht} + d_{DF,ht} + I_{ht} \quad \forall h, t = t_{start}, p = h \quad (4.19)$$

$$I_{ht-1} + Q_{Hydrogen,pt} = \sum_{s \in \mathbf{S}} \sum_{k \in \mathbf{K}} \sum_{d \in \mathbf{D}} Q_{skhdt} \cdot MEGC_{kg,d} + d_{FCET,ht} + d_{DF,ht} + I_{ht} \quad \forall h, \forall t \neq t_{start}, p = h \quad (4.20)$$

$$I_{start,s} + \sum_{s \in \mathbf{S}} \sum_{k \in \mathbf{K}} \sum_{d \in \mathbf{D}} Q_{skhdt} \cdot MEGC_{kg,d} = d_{FCET,st} + d_{DF,st} + I_{st} \quad \forall s, t = t_{start} \quad (4.21)$$

$$I_{st-1} + \sum_{s \in \mathbf{S}} \sum_{k \in \mathbf{K}} \sum_{d \in \mathbf{D}} Q_{skhdt} \cdot MEGC_{kg,d} = d_{FCET,st} + d_{DF,st} + I_{st} \quad \forall s, \forall t \neq t_{start} \quad (4.22)$$

$$I_{ht} \geq Inventory_{Continuity} \cdot (Demand_{HRS} + \left(\frac{|\mathbf{S}|}{|\mathbf{P}|}\right) \cdot Demand_{HRS}) \quad \forall h, t = t_{end} \quad (4.23)$$

$$I_{st} \geq Inventory_{Continuity} \cdot Demand_{HRS} \quad \forall s, t = t_{end} \quad (4.24)$$

$$Inventory_{Hub,t} = \sum_{h \in \mathbf{H}} \frac{I_{ht}}{Payload_{MEGC}} \quad \forall t \quad (4.25)$$

$$Inventory_{Sat,t} = \sum_{s \in \mathbf{S}} \frac{I_{st}}{Payload_{MEGC}} \quad \forall t \quad (4.26)$$

$$Inventory_{Transit,t} = \sum_{s \in \mathbf{S}} \sum_{k \in \mathbf{K}} \sum_{h \in \mathbf{H}} \sum_{d \in \mathbf{D}} \frac{Q_{skhdt} \cdot MEGC_{kg,d}}{Payload_{MEGC}} \quad \forall t \quad (4.27)$$

$$Storage_{Max} \geq Inventory_{Hub,t} + Inventory_{Sat,t} + Inventory_{Transit,t} \quad \forall t \quad (4.28)$$

$$I_{ht} \geq 0 \quad \forall h, \forall t \quad (4.29)$$

$$I_{st} \geq 0 \quad \forall s, \forall t \quad (4.30)$$

$$Inventory_{Hub,t} \geq 0 \quad \forall t \quad (4.31)$$

$$Inventory_{Sat,t} \geq 0 \quad \forall t \quad (4.32)$$

$$Inventory_{Transit,t} \geq 0 \quad \forall t \quad (4.33)$$

4.5. Hydrogen Transportation

The transport of the hydrogen between the hub refuelling station and the satellite refuelling stations, together with the quantity delivered to each refuelling station, define the operational distribution cost and have an influence on the overall required storage capacity. Adopting various production locations hub and satellite refuelling stations increases the complexity of the supply chain network.

The travel distance is based on the existing road network obtained from OpenStreetMap (OSM). The route between two locations is based on the shortest available travel distance via the existing road network between two geographical locations. The method to solve the distribution of the hydrogen fuel and routing of transport vehicles is based on the implementation of the inventory routing problem with multiple 'depots' and multiple 'demand' locations derived from (Bertazzi et al., 2019).

The inventory routing problem is derived from a vehicle routing problem, where additionally, the inventory of all locations is taken into account. Demand is satisfied based on the available inventory or supplied hydrogen at or before time step $t - 1$. The distribution system locations and available distribution routes considered in each scenario are described by an undirected graph $\mathbf{G}(\mathbf{V}, \mathbf{E})$, where $\mathbf{V} = \{1, \dots, H + S\}$ is a set of vertices and describes all hub and satellite locations. Set \mathbf{E} describes all edges that can be traversed by the vehicles (Bertazzi et al., 2019). $\mathbf{H} = \{1, \dots, H\}$, describes all vertices representing the hub refuelling stations and $\mathbf{S} = \{1, \dots, S\}$, describes the satellite stations present in the value chain. The edges in \mathbf{E} are defined differently for both container technologies. The complete set of edges between all refuelling station locations is described by $\mathbf{E} = \{\mathbf{V} \times \mathbf{V}\}$. For the scenarios considering the 20ft MEGC, only direct routes between the hub refuelling stations and the satellite stations are permitted. Considering the HPSC storage units, all edges are allowed to be traversed.

A homogeneous transportation fleet is considered, defined by set $\mathbf{K} = \{1, \dots, K\}$, where K represents the number of transport vehicles available in the entire supply chain. The maximum transport capacity of the vehicles is based on the maximum amount of MEGC or HPSC fitted on the 20ft trailer. The quantity of MEGCs or HPSCs delivered to each refuelling station is stated by the binary decision variable Q_{skhdt} , where s represents the refuelling station, k represents the transport vehicle used, h represents the hub refuelling station location the hydrogen originates from, and t defines the time step. d represents the index of the amount of MEGC units delivered. The parameter $MEGC_{kg,d}$ represents a list corresponding to the amount of kg of hydrogen stored for the number of MEGC's or HPSCs on the back of the trailer denoted by d . The total quantity delivered by a single round trip cannot exceed the inventory at the hub refuelling station of the previous time-step, described by Equation 4.34 and Equation 4.35.

An important parameter to be considered is the transportation of hydrogen from the satellite station back to the hub refuelling station. A residual amount of hydrogen is left in the storage containers due to the application of a cascade filling process. The absolute storage capacity of the MEGCs or the HPSCs can not be fully utilised. The total storage capacity is therefore divided into an absolute storage capacity and a relative storage capacity, described by the *BackhaulFactor*. $MEGC_{kg,d}$ is adjusted to represent the relative storage capacity of the MEGCs or HPSCs in the hydrogen distribution calculations.

To define the total cost of transportation, the vertices traversed by all vehicles across the entire planning horizon is described by the decision variable x_{ijkht} . All elements of variable x_{ijkht} describe a binary matrix which defines all edges $(i, j) \in \mathbf{E}$, that are traversed by the vehicles k originating from hub refuelling station location h at time each step t . The constraint describing x_{ijkht} is shown by Equation 4.41.

The binary variable Z_{skht} is introduced, where Z_{skht} is equal to 1 if vertex s is visited by vehicle k from hub refuelling station h in time step t (Bertazzi et al., 2019). A refuelling station is visited if the delivered quantity is larger than zero (Equation 4.37) and forces Z_{skht} to be equal to one. To ensure only a single vehicle can be assigned to a single production location, the constraint described in Equation 4.36 is added. The binary matrix of elements x_{ijkht} contains an edge entering the refuelling station and an edge leaving the refuelling station s , if Z_{skht} is equal to one.

When solving an inventory routing problem, it could occur that a travelled route does not include the hub refuelling station location while still complying with the constraint of each vertex having a single inbound and single outbound edge being traversed. A simplified visualisation of sub tour elimination is shown in Figure 4.3. P represents the hub refuelling station location, and R is a satellite refuelling station. In Figure 4.3a a sub tour is depicted, and in Figure 4.3b the sub tour is no longer present. As can be observed, the route begins and ends at the production location. Equation 4.42 represents the sub-tour elimination constraint. The constraint describes that the number of traversed edges has to be equal to or larger than the number of refuelling stations visited in \mathbf{E} (De & Di Summa, 2018).



(a) Route where a subtour is present

(b) Route where no subtour is present

Figure 4.3: Subtour example

The operational cost of transportation of the hydrogen is composed of three components. The first component is the cost of the driver regarding the travel time between the two locations. The second factor is cost regarding the fuel consumption of the delivery truck between two locations. The third component is the handling time cost regarding the MEGC or HSPC at the hub location and satellite refuelling station.

A non-negative travel time matrix described by $Transport_{time,ij}$, with $(i,j) \in \mathbf{E}$ represents the travel time between the considered locations in *hours*. A non-negative fuel consumption matrix described by $Transport_{Fuel,ij}$ with $(i,j) \in \mathbf{E}$ represents the fuel consumption in *liters* between the production locations. Both matrices are based on the case study input parameters discussed in chapter 3. A total cost matrix for travel time and fuel consumption is described by Equation 4.61. The handling time cost depends on the quantity of hydrogen delivered by each route travelled. The total handling time Ht_{kht} for a single route by vehicle k in a time step t originating from the production location h is described by Equation 4.44. Ht_{kht} is a function of the amount units delivered at the satellite stations in the travelled route, multiplied with the handling time of a single storage unit at each satellite station, $Ht_{unit,sat}$. The handling time of a full trailer ($Ht_{unit,hub}$) at the hub location is added. The total cost function for transportation is described in the objective function (Equation 4.1c), where the operational cost of transportation is minimised.

The total duration of a distribution trip of a vehicle can exceed the time step of the optimisation model. The binary variable $Z_{Busy,kt}$ is introduced to determine if a distribution vehicle k is still occupied delivering hydrogen to the satellite stations and cannot be used during the considered time step. The continuous variable $Operational_{time,kht}$ described by Equation 4.45 tracks the total operational time of each vehicle k , per time step t originating from hub location h in *hours*. If larger than zero, the operational time variable decreases by a single hour per consecutive time step. If the variable $Operational_{time,kht}$ is larger than zero, it forces binary variable $Z_{Busy,kt}$ to be equal to one. The binary variable is adopted in Equation 4.48, where it implies that the total hydrogen delivered by vehicle k in time step t is equal to zero if the binary variable $Z_{Busy,kt}$ is equal to one.

The following constraints are used in the optimisation model to determine the operational costs re-

garding hydrogen distribution:

$$\sum_{s \in \mathbf{S}} \sum_{k \in \mathbf{K}} \sum_{d \in \mathbf{D}} Q_{skhdt} \leq I_{start,h} \quad \forall h, t = t_{start} \quad (4.34)$$

$$\sum_{s \in \mathbf{S}} \sum_{k \in \mathbf{K}} \sum_{d \in \mathbf{D}} Q_{skhdt} \leq I_{Hub,ht-1} \quad \forall h, t \neq t_{start} \quad (4.35)$$

$$\sum_{k \in \mathbf{K}} \sum_{d \in \mathbf{D}} Q_{skhdt} \leq 1 \quad \forall s, \forall h, \forall t \quad (4.36)$$

$$\sum_{d \in \mathbf{D}} Q_{skhdt} \cdot MEGC_{kg,d} \leq Z_{skht} \quad \forall s, \forall k, \forall h, \forall t \quad (4.37)$$

$$\sum_{s \in \mathbf{S}} \sum_{d \in \mathbf{D}} Q_{skhdt} \cdot MEGC_{kg,d} \geq Z_{kth} \quad \forall h, \forall t \quad (4.38)$$

$$\sum_{h \in \mathbf{H}} Z_{kth} \leq 1 \quad \forall k, \forall t \quad (4.39)$$

$$\sum_{k \in \mathbf{K}} \sum_{h \in \mathbf{H}} Z_{skht} \leq 1 \quad \forall s, \forall t \quad (4.40)$$

$$\sum_{j \in I:(j,i) \in \mathbf{E}} x_{ijkht} + \sum_{j \in I:(i,j) \in \mathbf{E}} x_{ijkht} = 2 \cdot Z_{skht} \quad \forall s, \forall k, \forall h, \forall t \quad (4.41)$$

$$\sum_{i,j \in \mathbf{E}} x_{ijkht} \leq |\mathbf{E}| - 1 \quad \forall \mathbf{E} \subset \mathbf{V} : 2 \leq |\mathbf{E}| \leq |\mathbf{V}|, \forall k, \forall h, \forall t \quad (4.42)$$

$$Transport_{time,kht} = \sum_{(i,j) \in \mathbf{E}} x_{ijkht} \cdot Duration_{travel,ij} \quad \forall k, \forall h, \forall t \quad (4.43)$$

$$Handling_{time,kht} = \sum_{s \in \mathbf{S}} \sum_{d \in \mathbf{D}} \frac{Q_{skhdt} \cdot MEGC_{kg,d}}{Payload_{MEGC}} \cdot Ht_{unit,sat} + Z_{kth} \cdot Ht_{unit,hub} \quad \forall s, \forall k, \forall h, \forall t \quad (4.44)$$

$$Operational_{time,kht} = Handling_{time,kht} + Transport_{time,kht} \quad \forall k, \forall h, \forall t \quad (4.45)$$

$$Operational_{time,kht} \leq Z_{Busy,kt} \cdot BigM \quad \forall k, \forall h, \forall t \quad (4.46)$$

$$Z_{Busy,kht} \leq Operational_{time,kht} \quad \forall k, \forall h, \forall t \quad (4.47)$$

$$\sum_{d \in \mathbf{D}} Q_{skhdt} \leq BigM \cdot (1 - Z_{Busy,kt-1}) \quad \forall s, \forall k, \forall h, \forall t \quad (4.48)$$

$$Q_{skhdt} = \{0, 1\} \quad \forall s, \forall k, \forall h, \forall d, \forall t \quad (4.49)$$

$$Z_{skht} = \{0, 1\} \quad \forall s, \forall k, \forall h, \forall t \quad (4.50)$$

$$Z_{kth} = \{0, 1\} \quad \forall k, \forall h, \forall t \quad (4.51)$$

$$Z_{Busy,kt} = \{0, 1\} \quad \forall k, \forall t \quad (4.52)$$

$$I_{MEGC,d} \in \{0, \dots, N_{TrailerMax} \cdot Payload_{MEGC} \cdot (1 - BackhaulFactor)\} \quad (4.53)$$

$$I_{Hub,ht} \geq 0 \quad \forall h, \forall t \quad (4.54)$$

$$Transport_{time,kht} \geq 0 \quad \forall k, \forall h, \forall t \quad (4.55)$$

$$Handling_{time,kht} \geq 0 \quad \forall k, \forall h, \forall t \quad (4.56)$$

$$Operational_{time,kht} \geq 0 \quad \forall k, \forall h, \forall t \quad (4.57)$$

An overview of the objective function and all constraints considered in the optimisation model is shown in Appendix B

4.6. Total Cost Function

After optimisation of the operational system cost function for a considered scenario, the total annual cost of the hydrogen value chain can be determined. This section describes the total cost function for the hydrogen value chain. The total system cost function can be divided into the following components:

- Production Location Cost
- Refuelling Station Cost
- Distribution Cost
- Storage Cost

The total cost function is described by Equation 4.58. The total cost function returns the total annual cost for owning and operating the entire hydrogen value chain from well-to-tank [$\frac{\text{€}}{\text{annum}}$].

$$TC_{system} = TC_{ProdLoc} + TC_{HRS} + TC_{Distribution} + TC_{Storage} \quad (4.58)$$

The first component includes all investment costs associated with the production location, including the wind turbine, the grid connection, PEM electrolyser and the pipeline connection between the production location and the hub refuelling station. The second component describes all costs associated with the refuelling stations present in the value chain, including the total investment cost of all hub stations and satellite stations and the energy cost regarding pre-cooling of hydrogen for the dispenser. The refuelling station and, therefore, the investment cost scales modular with the expected daily hydrogen demand as discussed in section 3.6. The third cost component cost is associated with the distribution of the hydrogen. It includes the driver costs for the total operational time and fuel consumption of the distribution vehicles. The final component describes the cost associated with the required number of containers in the value chain to satisfy the demand according to the defined constraints. A detailed description of each part of the total cost function is described in the following sections.

4.6.1. Hydrogen Production Location Cost

The total cost function for all production locations p is described by Equation 4.59. The CAPEX cost for the wind turbine, PEM electrolyser, grid connection, compressor module, and the pipeline connection to the nearby hub station is considered for every production location. The CAPEX cost of each component is annualised with the corresponding annuity factor. The second cost component in the total cost function is the fixed OPEX. The third cost component of the production location is equal to the costs associated with grid interaction. $C_{GridEnergy,t}$ represents the electricity cost based on the day-ahead market price of the specific hour of the considered year. The grid interaction cost depends on the hydrogen quantity produced at time step t and is minimised by the optimisation model. The final costs are associated with the energy cost to operate the hydrogen compressor and are dependent on the binary variable $Z_{PEM,pt}$ as a result of the optimisation process.

$$\begin{aligned}
TC_{ProdLoc} = & \sum_{p \in \mathbf{P}} \left(\frac{CAPEX_{WT}}{a_{WT}} + \frac{CAPEX_{PEM}}{a_{PEM}} + \frac{CAPEX_{Stacks}}{a_{Stacks}} + \frac{CAPEX_{Grid}}{a_{Grid}} + \frac{CAPEX_{Comp}}{a_{Comp}} \right. \\
& + OPEX_{Fixed,WT} + OPEX_{Fixed,PEM} + OPEX_{Fixed,Grid} + OPEX_{Fixed,Comp} \\
& + Distance_{Pipeline} \cdot \left(\frac{CAPEX_{Pipeline}}{a_{Pipeline}} + OPEX_{Fixed,Pipeline} \right) \\
& + \sum_{p \in \mathbf{P}} \sum_{t \in \mathbf{T}} (-E_{Grid,pt} \cdot C_{GridEnergy,t} \cdot C_{Imbalance,pt}) \\
& \left. + \sum_{p \in \mathbf{P}} \sum_{t \in \mathbf{T}} Z_{pem,tp} \cdot E_{Comp} \cdot E_{EnergyHRS} \right) \quad (4.59)
\end{aligned}$$

4.6.2. Hydrogen Refuelling Station Cost

The total cost function for all refuelling stations considered in the value is described by Equation 4.60. The hub stations are denoted by h and the satellite stations by s . The cost of energy for compression is incorporated in the cost function described in Equation 4.59. The cost function of the refuelling stations contains the CAPEX, the fixed OPEX and the OPEX regarding energy cost of the amount of kg hydrogen dispensed.

$$\begin{aligned}
TC_{HRS} = & \sum_{h \in \mathbf{H}} \frac{CAPEX_{Hub}}{a_{Hub}} + OPEX_{FixedHub} \\
& + \sum_{h \in \mathbf{H}} \sum_{t \in \mathbf{T}} (d_{FCET,ht} + d_{DF,ht}) \cdot E_{dispenser} \cdot E_{EnergyHRS} \\
& + \sum_{s \in \mathbf{S}} \frac{CAPEX_{Sat}}{a_{Sat}} + OPEX_{FixedSat} \\
& + \sum_{s \in \mathbf{S}} \sum_{t \in \mathbf{T}} (d_{FCET,st} + d_{DF,st}) \cdot E_{dispenser} \cdot C_{EnergyHRS} \quad (4.60)
\end{aligned}$$

4.6.3. Hydrogen Distribution Cost

The total cost function regarding the transportation of hydrogen is described by Equation 4.62. Equation 4.61 describes the cost regarding fuel and driver wage to travel from location i to j . The first component in the total distribution cost function describes all costs associated with travel time and fuel consumption across the planning horizon. The second component considers the driver's cost regarding the loading and unloading time of the MEGCs of HSPC transported. The final component describes all investment costs en fixed OPEX costs regarding the distribution vehicle fleet.

$$c_{ij} = Transport_{time,ij} \cdot C_{Driver} + Transport_{Fuel,ij} \cdot C_{Fuel} \quad (4.61)$$

$$\begin{aligned}
TC_{transport} = & \sum_{i,j \in \mathbf{E}} \sum_{k \in \mathbf{K}} \sum_{h \in \mathbf{H}} \sum_{t \in \mathbf{T}} c_{ij} \cdot x_{ijkht} \\
& + \sum_{k \in \mathbf{K}} \sum_{h \in \mathbf{H}} \sum_{t \in \mathbf{T}} Ht_{kht} \cdot C_{Driver} \quad (4.62) \\
& + \sum_{k \in \mathbf{K}} \left(\frac{CAPEX_{vehicle}}{a_{vehicle}} + \frac{CAPEX_{trailer}}{a_{trailer}} + OPEX_{Fixed,vehicle} + OPEX_{Fixed,trailer} \right)
\end{aligned}$$

4.6.4. Hydrogen Storage Cost

Different from the 'classical' inventory routing problem where the cost of storage is often described as a fixed cost component per unit stored multiplied by the inventory at each time step t , this research incorporates the inventory cost based on the amount of MEGC or HPSC required to obtain the optimal solution. The inventory cost is calculated based on the maximum amount of MEGC or HPSC present in the system across all time steps, described by Equation 4.63. The amount of MEGC or HPSC present in the system is based on the inventory at the refuelling stations and the containers in transit at every time step t .

$$TC_{inventory} = Storage_{Max} \cdot \left(\frac{CAPEX_{MEGC}}{a_{MEGC}} + OPEX_{Fixed,MEGC} \right) \quad (4.63)$$

4.7. LCOH Cost Function

To compare several hydrogen value chain configurations, the LCOH of each value chain must be determined. The LCOH describes the cost of hydrogen from Well-To-Tank (WTT) in $\frac{\text{€}}{\text{kgH}_2}$.

In this research, a slightly different approach to the LCOH is considered. The sales of excess electricity to the grid for the day-ahead market price results in a revenue stream that can not be neglected when determining the most optimal storage solution and the scenario with the lowest LCOH. As described in subsection 4.6.1 the variable $E_{Grid,pt}$ describes the amount of energy sold to and bought from the electricity grid.

The LCOH is calculated by Equation 4.64 and presets the hydrogen value in $[\frac{\text{€}}{\text{kgH}_2}]$.

$$LCOH_{system} = \frac{TC_{ProdLoc} + TC_{HRS} + TC_{Distribution} + TC_{Storage}}{\sum_{h \in \mathbf{H}} \sum_{t \in \mathbf{T}} (d_{FCET,ht} + d_{DF,ht}) + \sum_{s \in \mathbf{S}} \sum_{t \in \mathbf{T}} (d_{FCET,st} + d_{DF,st})} \quad (4.64)$$

Five wind-based hydrogen value chain sizes and spatial configurations are compared. The first hydrogen value chain consists of a single wind turbine with a single hub refuelling station and a single satellite station. The first scenario gives insight into a small-sized hydrogen value chain with a high average daily demand at each refuelling station. For the second hydrogen value chain, the same wind turbine location and satellite refuelling station are considered. Additionally, two satellite station locations are added. For the third, fourth and fifth configurations, a turbine location is added where a single refuelling station is converted to a hub refuelling station. The fifth scenario represents a similar system setup compared to scenario one. The benefit of a larger but similar value chain configuration regarding distribution can therefore be determined. The spatial configurations of scenarios three, four and five are the same. However, a different annual demand is considered for each scenario. All scenarios combined pose an example of a gradual demand increase in the development of the hydrogen value chain through time. The increase in system size and total annual demand for all scenarios combined gives insight into the LCOH development of a hydrogen value chain based on wind energy. The outcome of the optimisation and the LCOH cost calculations are discussed in the next chapter.

4.8. Parameter Overview

Sets

Undirected Graph	G(V, E)
Set of vertices in considered in the optimisation model	V = {1, ..., V}
Set of possible edges to be traversed (dependent on the non-stationary storage type chosen)	E = { V × V }
Set of production locations	P = {1, ..., P}
Set of hub refuelling station locations	H = {1, ..., H}
Set of satellite refuelling station locations	S = {1, ..., S}
Set of optimisation model time horizon	T = { $t_{start}, \dots, t_{end}$ }
Set of distribution vehicles considered	K = {0, ..., K}
Set of amount containers stored on the back of the distribution vehicle's trailer	D = {0, ..., $N_{TrailerMax}$ }

Decision Variables

$Q_{Hydrogen,pt}$	Hydrogen production per time step, per production location	kg_{H_2}
Q_{skhdt}	Number of hydrogen storage units delivered at each refuelling station	–
x_{ijkht}	1, if edge from i to j is traversed by vehicle k , from hub refuelling station h , in time step t 0, Otherwise	–

Continuous Variables

$E_{Hydrogen,pt}$	Hydrogen production energy requirement per time step, per production location	kWh
$E_{Grid,pt}$	Energy bought/sold to the grid per time step, per production location	kWh
$E_{Curtailment,pt}$	Wind turbine energy curtailed per time step, per production location	kWh
$C_{Imbalance,pt}$	Imbalance factor per time step, per production location	–
$I_{Hub,ht}$	Inventory at hub refuelling station, per time step	kg_{H_2}
$I_{Sat,ht}$	Inventory at satellite refuelling station, per time step	kg_{H_2}
$Transport_{time,kht}$	Travel time for vehicle k , from hub refuelling station h , per time step t	$hour$
$Handling_{time,kht}$	Handling time for vehicle k , from hub refuelling station h , per time step t	$hour$
$Operational_{time,kht}$	Total operational time for vehicle k , from hub refuelling station h , per time step t	$hour$

Integer Variables

$Inventory_{Hub,t}$	Number of MEGC or HPSC storage units at hub refuelling station, per time step	–
$Inventory_{Sat,t}$	Number of MEGC or HPSC storage units at satellite refuelling station, per time step	–
$Inventory_{Transit,t}$	Number of MEGC or HPSC storage units in transit, per time step	–
$Storage_{Max}$	Maximum number of MEGC or HPSC storage units in the entire optimisation planning horizon	–

Binary Variables

$Z_{PEM,pt}$	1, if hydrogen is produced at production location p , at time step t 0, Otherwise	
$Z_{Grid,pt}$	1 if energy is sold to the grid at production location p , at time step t 0, if energy is bought to the grid at production location p , at time step t	
Z_{skht}	1, if satellite refuelling station is visited by vehicle k , from hub h , at time step t 0, Otherwise	
Z_{kht}	1, if vehicle k from hub refuelling station h is used in time step t 0, Otherwise	$Z_{Busy,kt}$
	1, if vehicle k is busy at time step t 0, Otherwise	

Indexed Parameters

x_p	Latitude coordinate of production location	°
y_p	Longitude coordinate of production location	°
x_h	Latitude coordinate of hub refuelling station location	°
y_h	Longitude coordinate of hub refuelling station location	°
x_s	Latitude coordinate of satellite refuelling station location	°
y_s	Latitude coordinate of satellite refuelling station location	°
$E_{WT,pt}$	Energy production capacity wind turbine, per turbine location, per time step	kWh
$I_{start,h}$	Starting inventory hub refuelling station	kg_{H_2}
$I_{start,s}$	Starting inventory satellite refuelling station	kg_{H_2}
$MEGC_{kg,di}$	List describing total storage on the back of the distribution trailer, in reference to the amount of MEGC units	kg_{H_2}
$d_{FCET,ht}$	FCET demand at hub refuelling station h , in time step t	kg_{H_2}
$d_{DFV,ht}$	DFV demand at hub refuelling station h , in time step t	kg_{H_2}
$d_{FCET,st}$	FCET demand at satellite refuelling station s , in time step t	kg_{H_2}
$d_{DFV,st}$	DFV demand at hub refuelling station s , in time step t	kg_{H_2}
$C_{GridEnergy,t}$	Day-Ahead market price of grid energy	$\frac{\text{€}}{kWh}$
$Transport_{time,ij}$	Total travel time from location i to j	hour
$Transport_{Fuel,ij}$	Total distance from location i to j	km
c_{ij}	Total distribution cost from location i to j	€

Parameters

$BigM$	Large Number	–
$Factor_{Imbalance}$	Percentage of revenue subtracted to pay to energy company	%
$Q_{HydrogenMax}$	Maximum production capacity electrolyser	kg_{H_2}
$E_{HydrogenMax}$	Maximum energy capacity electrolyser, per hour	kWh
$E_{GridCapacity}$	Maximum energy capacity grid connection, per hour	kWh
t_{start}	Hour of the year optimisation start point	hour
t_{end}	Hour of the year optimisation end point	hour

$Payload_{MEGC}$	Absolute storage capacity single MEGC unit	kg_{H_2}
$Ht_{unit,hub}$	Handling time MEGC unit at the hub refuelling station	hour
$Ht_{unit,sat}$	Handling time MEGC at the Satellite refuelling station	hour
$Inventory_{Continuity}$	Inventory continuity factor	–
$Demand_{HRS}$	Average daily demand at each refuelling station	kg_{H_2}
$N_{TrailerMax}$	Maximum number of MEGC units on a single 20ft trailer	–
$BackhaulFactor$	Percentage of MEGC storage capacity that is unused due to cascade filling process	%
$CAPEX_{WT}$	Investment cost wind turbine	€
$CAPEX_{PEM}$	Investment cost PEM electrolyser BOP	€
$CAPEX_{Stacks}$	Investment cost PEM electrolyser stacks	€
$CAPEX_{Grid}$	Investment cost grid connection	€
$CAPEX_{Comp}$	Investment cost diaphragm compressor	€
$CAPEX_{Pipeline}$	Investment cost pipeline	$\frac{€}{m}$
$CAPEX_{MEGC}$	Investment cost single non-stationary storage unit	€
$CAPEX_{vehicle}$	Investment cost distribution vehicle	€
$CAPEX_{trailer}$	Investment cost distribution trailer	€
$CAPEX_{Hub}$	Investment cost hub refuelling station	€
$CAPEX_{Sat}$	Investment cost sSatellite refuelling station	€
$OPEX_{Fixed,WT}$	Fixed operational cost wind turbine	$\frac{€}{annum}$
$OPEX_{Fixed,PEM}$	Fixed operational cost PEM electrolyser BOP	$\frac{€}{annum}$
$OPEX_{Stacks}$	Fixed operational cost PEM electrolyser stacks	$\frac{€}{annum}$
$OPEX_{Fixed,Grid}$	Fixed operational cost grid connection	$\frac{€}{annum}$
$OPEX_{Fixed,Comp}$	Fixed operational cost diaphragm compressor	$\frac{€}{annum}$
$OPEX_{Fixed,Pipeline}$	Fixed operational cost hydrogen pipeline	$\frac{€}{annum \cdot m}$
$OPEX_{Fixed,MEGC}$	Fixed operational cost single non-stationary storage unit	$\frac{€}{annum}$
$OPEX_{Fixed,vehicle}$	Fixed operational cost distribution vehicle	$\frac{€}{annum}$
$OPEX_{Fixed,trailer}$	Fixed operational cost distribution trailer	$\frac{€}{annum}$
$OPEX_{Fixed,Hub}$	Fixed operational cost hub refuelling station	$\frac{€}{annum}$
$OPEX_{Fixed,Sat}$	Fixed operational cost satellite refuelling station	$\frac{€}{annum}$
a_{WT}	Annuity factor wind turbine	–
a_{PEM}	Annuity factor PEM electrolyser BOP	–
a_{Stacks}	Annuity factor PEM electrolyser stacks	–
a_{Grid}	Annuity factor grid connection	–
a_{Comp}	Annuity factor diaphragm compressor	–
$a_{Pipeline}$	Annuity factor hydrogen pipeline	–
a_{MEGC}	Annuity factor non-stationary storage unit	–
$a_{vehicle}$	Annuity factor distribution vehicle	–
$a_{trailer}$	Annuity factor distribution trailer	–
a_{Hub}	Annuity factor hub refuelling station	–
a_{Sat}	Annuity factor satellite refuelling station	–
$Distance_{Pipeline}$	Total haversine distance between production locations and hub refuelling stations	m
E_{Comp}	Energy consumption diaphragm compressor	kWh
$E_{Dispenser}$	Energy consumption hydrogen dispenser	kWh
$C_{EnergyHRS}$	Cost of energy at the hydrogen refuelling station	$\frac{EUR}{kWh}$
C_{Driver}	Driver wage	$\frac{€}{hour}$
C_{Fuel}	Fuel cost	$\frac{€}{liter}$

5

Results

The main research question answered in this research as discussed in chapter 1 is "What impact does the type of non-stationary storage unit have on the levelised cost of hydrogen in the wind dominated hydrogen value chain?". To answer the main research question, the choice is made to optimise five separate hydrogen value chain configurations that describe a gradual implementation of a hydrogen value chain in the province of North-Holland. The results generated by the optimisation model and subsequent cost calculations are presented in this chapter.

The chapter starts by describing the five hydrogen value chain scenarios in section 5.1. In section 5.2, the five hydrogen value chain configurations are analysed based on the choices made in hydrogen production process (subsection 5.2.1), the total required non-stationary storage units and consequently the hydrogen distribution (subsection 5.2.2), and the LCOH of the entire value chain (subsection 5.2.3). The value chain scenarios are distinguished by the number of operated wind turbines and the operational refuelling stations, together, with an set average daily demand at each refuelling station. For all value chain scenarios, both the MEGC20ft and the HPSC containers are compared to provide insight into the utilisation of the different non-stationary storage technologies.

The remainder of this chapter describes a scenario analysis in section 5.3. The scenario analysis is conducted on the second scenario described in section 5.1. The second scenario is chosen for the scenario analysis as it is expected to represent the first implementation of the proposed hydrogen value chain.

Finally, in section 5.4 a sensitivity analysis is performed on two system parameters, the WACC and the total annual demand. The decisions made by the optimisation model are solely based on the minimisation of the cost function discussed in the previous chapter. Other objectives are not taken into account but should be reflected upon when interpreting the outcome of the optimisation model.

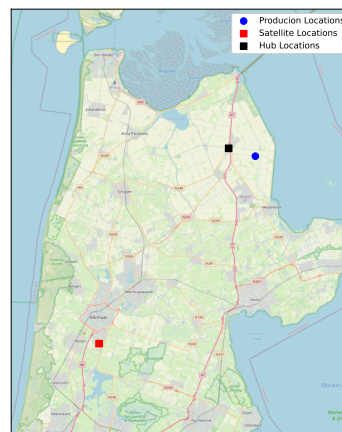
5.1. Optimisation Scenarios

Table 5.1 shows an overview of the considered number of production locations, hub refuelling stations and satellite refuelling stations for all considered scenarios in this research.

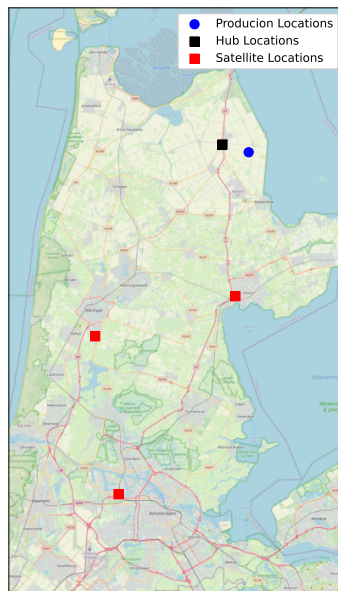
Scenario Information	Scenario 1	Scenario 2	Scenario 3	Scenario 4	Scenario 5
Wind turbines	1	1	2	2	2
Hub refuelling stations	1	1	2	2	2
Satellite refuelling stations	1	3	2	2	2
Total number of refuelling stations	2	4	4	4	4
Average daily hydrogen demand at HRS [$\frac{kgH_2}{day}$]	350	175	175	262.5	350
Non-stationary storage units considered	20ft MEGC/HPSC				
Length distribution trailer	20ft	20ft	20ft	20ft	20ft

Table 5.1: Overview of scenario configurations

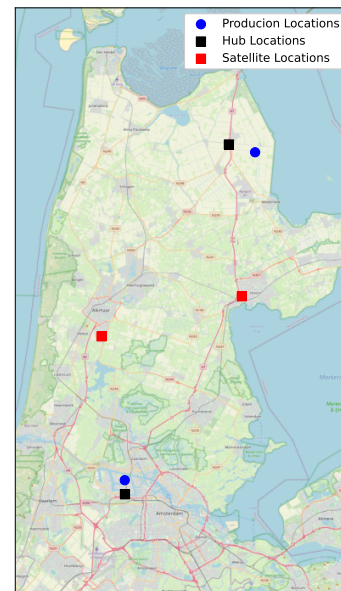
Five wind-based hydrogen value chain sizes and spatial configurations are compared. The first hydrogen value chain consists of a single wind turbine with a single hub refuelling station and a single satellite station. The first scenario gives insight into a small-sized hydrogen value chain with a high average daily demand at each refuelling station. For the second hydrogen value chain, the same wind turbine location and satellite refuelling station are considered. Additionally, two satellite station locations are added. For the third, fourth and fifth configurations, a turbine location is added where a single refuelling station is converted to a hub refuelling station. The final three scenarios represents a similar system setup compared to scenario one. The spatial configurations of all scenarios are shown in Figure 5.1. The spatial configurations of scenarios three, four and five are the same. However, a different annual demand is considered for each scenario. All scenarios combined pose an example of a gradual demand increase in the development of the hydrogen value chain through time. The increase in system size and total annual demand for all scenarios combined gives insight into the LCOH development of a hydrogen value chain for both non-stationary storage applications.



(a) Spatial Configuration Scenario 1



(b) Spatial Configuration Scenario 2



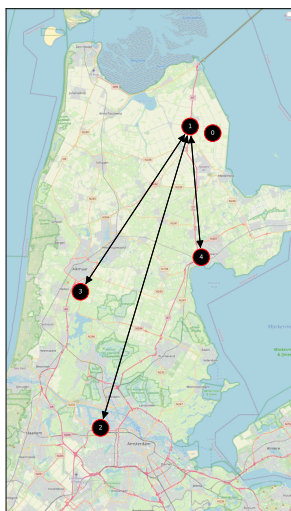
(c) Spatial Configuration Scenario 3, 4 and 5

Figure 5.1: Overview Spatial Configurations

The average daily demand at each refuelling station for each separate scenario is considered equal. The average daily demand is used to create the demand profile at each refuelling station independently with the demand model described in section 3.7. For each refuelling station the average daily demand

is equal to $350 \frac{kg}{day}$, $175 \frac{kg}{day}$, $175 \frac{kg}{day}$, $262.5 \frac{kg}{day}$ and $350 \frac{kg}{day}$ for scenario one to five, respectively. For scenarios one, two and three, the output of the demand model results in total annual system wide demand of roughly 250.000 kg of hydrogen. The annual demand for scenario four is equates to roughly 375.000 kg of hydrogen. The annual demand for the final scenario is close to 500.000 kg.

In each scenario, the implementation of a truck with a 20ft trailer is assumed. Only direct deliveries between the hub refuelling station and the satellite refuelling stations are performed when utilising a 20ft trailer with a 20ft MEGC container. The 20ft trailer with the HPSCs is able to supply multiple refuelling stations in a single trip. As an example, the routing options of scenario two are shown in Figure 5.2. As discussed in chapter 3, real routing based on the local road network is used to calculate the distance the distribution vehicle has to travel and the total duration for travelling between each location. Only for scenario one, the available routes are equal for both container technologies due to the single hub and single satellite station setup of the considered hydrogen value chain.



(a) Traversable routes by truck scenario 2 MEGC 20ft



(b) Traversable routes by truck scenario 2 MEGC 20ft

Figure 5.2: Routing options for MEGCs and HPSCs

5.2. Main Scenario Results

This section describes the results from the optimisation model and the LCOH calculations for all five considered scenarios. First the decision making process for hydrogen production is compared between all scenarios. Secondly key parameters of required storage capacity and cost regarding distribution to supply the hydrogen to each refuelling station is analysed. Finally the LCOH of all five scenarios are compared for both non-stationary storage technologies.

5.2.1. Hydrogen Production Process Comparison

This subsection reviews the output of the optimisation model with a focus on the production process of hydrogen compared to the available wind energy and interaction with the electricity grid. Table 5.2 shows the general output of the optimisation model regarding hydrogen demand and key hydrogen production parameters. The hydrogen demand is slightly different due to the stochastic modelling of the demand at each refuelling station independently. The output values are depicted for each scenario and distinguished per container technology. The total available power produced by the wind turbine is equal to 15.1 *GWh* for the production location located in the Wieringermeer and 13.2 *GWh* for the production location in the Port of Amsterdam, equating to 3376 and 3304 wind turbine full load hours, respectively. The capacity factor of the wind turbine in the Wieringermeer is therefore 0.43 in 2019.

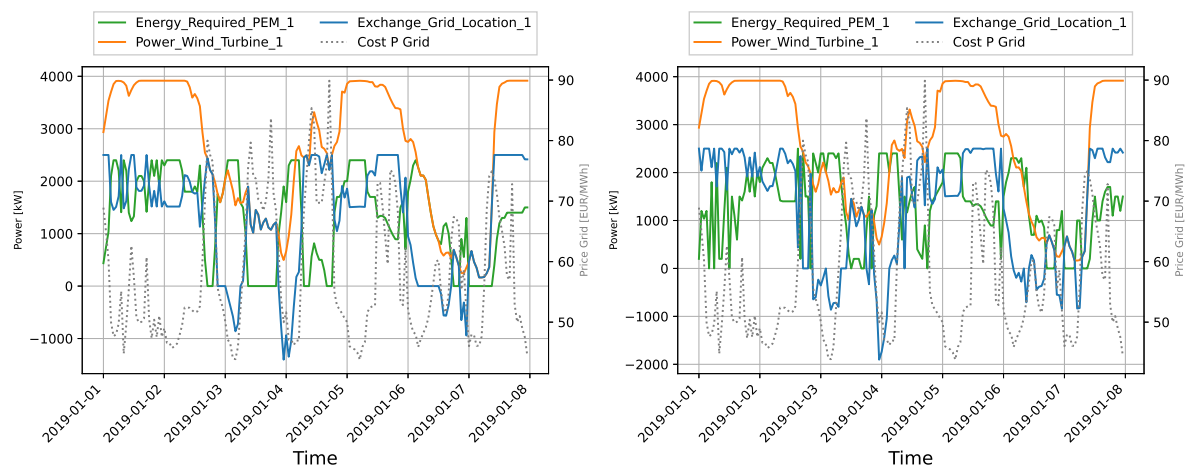
The capacity factor for the region where the turbine is located is verified by the regional wind power report from TNO (Pian et al., 2021).

Parameter	Units	Scenario 1		Scenario 2		Scenario 3		Scenario 4		Scenario 5	
		MEGC 20ft	HPSC	MEGC 20ft	HPSC						
Total Hydrogen Demand	Tonne	252.44	252.44	253.48	252.62	252.14	252.74	378.89	379.20	504.4	505.5
Total Energy Required Hydrogen Production	GWh	12.71	12.67	12.80	12.73	12.42	12.34	18.90	18.88	25.44	25.47
Average Full Load Hours Electrolyser	hr	5084	5068	5119	5093	2482	2467	3779	3525	5088	5093
Total Wind Turbines Energy Production Available For Hydrogen Production	GWh	15.11	15.11	15.11	15.11	28.33	28.33	28.33	28.33	28.33	28.33
Average Full Load Hours Wind turbines	hr	3777	3777	3777	3777	3540	3540	3540	3540	3540	3540
Total Energy Curtailed	GWh	0.08	0.22	0.08	0.20	1.22	1.54	0.73	1.01	0.28	0.69
Average Full Load Hours Curtailed	hr	20.07	55.2	19.4	50.0	152	192	50.0	126	71.0	100.0
Total Energy Bought from the Electricity Grid	GWh	3.89	3.98	3.91	4.02	2.90	3.13	5.52	5.51	4.1	4.17
Total Energy Sold to the Grid	GWh	6.21	6.19	6.14	6.19	17.6	17.6	14.22	13.98	11.34	11.15
Total Energy Used for Hydrogen Production from Grid Connection	GWh	3.89	3.98	3.91	4.02	2.90	3.13	5.52	5.51	4.1	4.17
Total Energy Used for Hydrogen Production from Wind Turbines	GWh	8.82	8.69	8.89	8.72	9.51	9.20	13.33	13.33	16.7	16.49
Percentage Power Used for Hydrogen Production from Wind Turbine	%	69.37	68.61	69.45	68.45	79.26	77.24	70.68	73.11	68.35	67.63
Percentage Power Used for Hydrogen Production from Grid Connection	%	30.63	31.39	30.55	31.54	20.73	22.76	29.23	26.96	31.65	32.37

Table 5.2: Overview key parameters production, transport and storage

In all scenarios, the total energy required for the production of hydrogen is less than the total available yearly energy production capacity of the wind turbine. It can be noticed that almost a negligible amount of available wind energy is curtailed. The optimisation process results in optimally scheduling the hydrogen production quantity per time step in combination with the energy production capacity of the wind turbine and the grid connection capacity.

Figure 5.3 illustrates the first week of hydrogen production, power production and power exchange with the grid for scenario 1 for both container technologies. First, despite minor deviations on the hourly time scale, the overall trend in hydrogen production quantity for each time step for both container technologies is similar. Secondly, the correlation coefficient between the hydrogen production quantity for the value chain considering the 20ft MEGC and the HPSC oriented value is 0.8. This implies that hydrogen is mainly produced during periods when energy is produced by the wind turbine. Thirdly, the trend in Figure 5.3 also shows a high correlation with the price fluctuations of the power grid.



(a) First week, Wind turbine power production, Electrolyser power requirement, Exchange power grid, Electricity grid price MEGC 20ft
(b) First week, Wind turbine power production, Electrolyser power requirement, Exchange power grid, Electricity grid price HPSC

Figure 5.3: Correlation matrices scenario 1, MEGC 20ft HPSC

As from Figure 5.3 it is noticed that there are time steps when the energy required for hydrogen production exceeds the power generation capacity of the wind turbine, which consequently result in power drawn from the grid. It can also be noticed at certain time steps there is sufficient wind power available and unused electrolyser capacity to produce hydrogen. However, excess electricity is sold to

the grid. When investigating the output of the optimisation model, roughly 70% of the power required by the hydrogen production process is directly provided by the wind turbine, 30% of the power required for hydrogen production is drawn from the grid despite the excess of total yearly energy production of the wind turbine.

An important observation is that the optimisation process solely based on the cost optimisation of the revenue/cost regarding the power exchange with the grid, consequently drives the decision making process towards utilising the grid to increase overall revenue. It is more cost-effective to sell higher valued wind energy to the grid and buy grid power at reduced tariff at a later time step in the week, than using only self produced wind energy for the production of hydrogen.

A larger storage capacity is required in the case of minimising the amount of hydrogen produced by power bought from the grid and increasing the overall LCOH. It can be concluded that the main parameters that drive the production process of hydrogen production are the price of electricity from the grid and the power production capacity of the wind turbine, in combination with the available grid connection capacity.

The optimisation model does not take into account the origin of electricity drawn from the grid and the extra cost or revenue obtained from producing, and the need to acquire green energy certificates. The shown effect based on cost optimisation should be taken into account when designing a future hydrogen value chain with the production of green hydrogen. Also, the optimisation process is based on a weekly interval and, therefore, is not able to foresee and act on the weekly or monthly or seasonal mismatch between energy production and energy demand for the production of hydrogen. The limitations of the model will be further discussed in chapter 6.

The linear correlation matrix of several production parameters for scenario one is shown in Figure 5.4. The correlation matrices for all other scenarios can be found in Appendix C. The correlation matrix is created by adopting the Pearson correlation coefficient (Equation 5.1). The correlation matrix reflects the correlation between the time series of the grid electricity price, the available power production of the wind turbine, the exchange of power with the electricity grid and the hydrogen production throughout the optimisation planning horizon. A negative correlation between the electricity price and the hydrogen production of 0.60 is observed from the correlation matrix. A lower positive correlation of 0.28 is shown between the power production of the wind turbine and the production of hydrogen. This implies that the hydrogen production process is more dependent on the electricity price fluctuations of the power grid than the power production of the wind turbine. This is in line with observations seen in Table 5.2. It can therefore be concluded, as also shown in Figure 5.4 that production of hydrogen is solely based on cost optimisation is highly dependent on the price fluctuations of the electricity grid on the short-time scale) and the wind power availability on a larger time scale.

$$\rho(X, Y) = \frac{cov(X, Y)}{\sigma(X)\sigma(Y)} \quad (5.1)$$

Both Table 5.2 and Figure 5.4 show that the production process of hydrogen is to a small extent dependent on the choice of storage technology. Comparing a single turbine value chain with a different number of satellite stations but the same total daily demand shows almost no impact on the correlation of the hydrogen production decision process at each time step. The slight differences in each scenario are the result of the stochastic modelling approach of the demand profile for each scenario and each storage technology independently.

Considering the same total demand in the hydrogen value chain of 250.000 kg and adding a wind turbine and hub refuelling station location shifts the decision-making process of the optimisation model. It can be noticed that a hydrogen value chain with reduced demand in relation to the number of production locations compared to the other scenarios result in a higher utilisation rate of produced wind energy for the production process of hydrogen. A more detailed overview of the production process

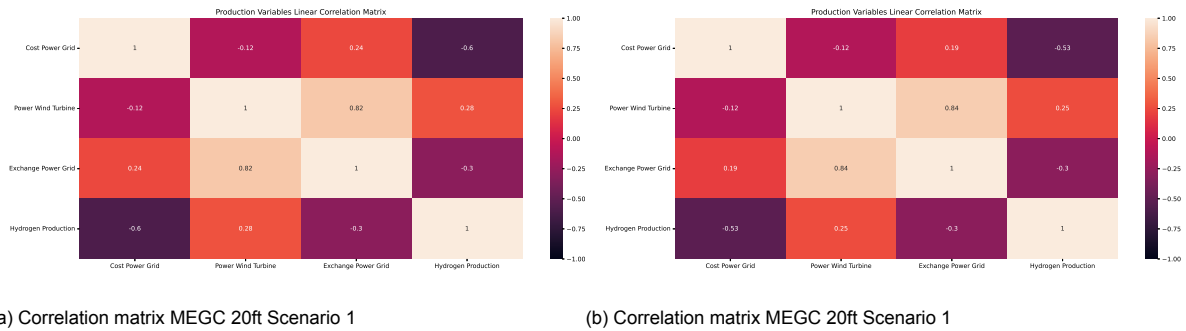


Figure 5.4: Correlation matrices scenario 1, MEGC 20ft HPSC

parameters per wind turbine location for scenario three, scenario four and scenario five is shown in Table 5.3. The detailed overview confirms the almost negligible impact of different storage technologies on the decision making process on the production side of the hydrogen value chain.

Analysing the detailed production parameters for both scenarios three, four and five, it can be noticed that for scenario 3, the most amount of energy is curtailed due to the excess power production by the wind turbines in comparison with the energy requirement for the hydrogen production and the grid connection size. Due to revenue losses when power production of the wind turbine is curtailed, the total curtailed energy throughout the planning horizon is minimised as a consequence of the optimisation process. By adjusting the hydrogen production quantity at each time step, the overall energy utilisation rate of the wind energy production capacity either sold to the grid or used for hydrogen production is maximised. In order to minimise the curtailed energy and maximise the revenue of the excess produced electricity in scenario three, a shift is noticed towards more hydrogen production directly from the wind turbine to overcome the difference between the grid connection power capacity (2.5 MW) and the wind turbine power capacity (4 MW).

The ratio between the energy source for the produced hydrogen for scenario 3 compared to the other scenarios is almost 80/20, with 80% of the hydrogen being directly produced from wind energy, whereas for the other scenarios, this ratio is close to 70/30. With the gradual increase of total annual demand for scenarios 3, 4 and 5, the shift towards 70/30 can be noticed. Overall a larger amount of energy curtailed regarding the HPSC units can be noticed. This is a result of the optimised storage capacity to reduce the storage CAPEX therefore, no excess storage capacity is available compared to the 20ft MEGC scenario due to the required investment in the 20ft MEGC units to provide distribution flexibility.

For the wind turbine corresponding to location 2, located in the Port of Amsterdam, a difference in total annual energy production capacity is shown of roughly 2 GWh in 2019. The overall hydrogen production based on total weight is slightly biased towards the production location with the higher yearly wind energy yield. This is in line with the previously mentioned shift of hydrogen production when the turbine power production exceeds the grid connection size, and the most cost-optimal process is to minimise the total power curtailed throughout the planning horizon. The total difference of hydrogen production compared to the total energy production capacity of both turbine locations of 14% results in a higher utilisation rate of the grid connection for the production location in the Port of Amsterdam compared to the production location in the Wieringermeer.

It can be concluded that the cost optimisation approach by the model shows an overall trend in the production decision process whereby the choice of the storage technology or the value chain spatial configuration has a negligible impact when considering the same total annual hydrogen demand. The total power curtailed in combination with the overall cost of grid interaction is minimised and shows a leading role in the hydrogen production quantity and time step decision-making process.

Parameter	Units	Scenario 3				Scenario 4				Scenario 5			
		MEGC 20ft		HPSC		MEGC 20ft		HPSC		MEGC 20ft		HPSC	
		Location 1	Location 2										
Hydrogen Produced	kg	129.89	122.27	127.17	123.58	196.76	181.26	194.17	183.7	257.64	245.29	254.66	249.03
Full Load Hours Electrolysis	hr	2554.67	2410.14	2505.58	2430.81	3924.8	3604.6	3880.8	3670.7	5219.4	4957.96	5154.28	5033.1
Energy Required Hydrogen Production	GWh	6.39	6.03	6.26	6.08	9.81	9.01	9.70	8.18	13.05	12.39	12.89	12.58
Energy Produced Wind Turbines	GWh	15.11	13.22	15.11	13.22	15.11	13.22	15.11	13.22	15.11	13.22	15.11	13.22
Full Load Hours Wind turbine	hr	3776.65	3304.77	3776.65	3304.65	3776.65	3304.77	3776.65	3304.65	3776.65	3304.77	3776.65	3304.65
Energy Curtailed	GWh	0.57	0.64	0.86	0.68	0.14	0.15	0.52	0.48	0.15	0.13	0.35	0.34
Full Load Hours Curtailed	hr	142.66	161.17	215.79	169.61	34.89	37.31	53.33	46.67	37.53	33.45	87.74	84.54
Energy Bought from the Grid	GWh	1.32	1.58	1.43	1.71	2.46	2.57	2.61	2.94	4.13	4.62	4.17	4.82
Energy Sold to the Grid	GWh	9.47	8.13	9.4	8.18	7.62	6.62	7.49	6.50	6.04	5.13	6.04	5.12
Energy Used for Hydrogen Production from Grid	GWh	1.32	1.58	1.43	1.71	2.46	2.57	2.61	2.94	4.13	4.62	4.17	4.82
Energy Used for Hydrogen Production from Wind Turbine	GWh	5.06	4.45	4.84	4.36	7.35	6.45	7.09	6.24	8.92	7.78	8.72	7.77
Percentage Power Used for Hydrogen from Wind Turbine	%	79.26	73.77	77.24	71.82	74.92	71.53	73.11	67.99	68.35	62.76	67.63	61.72
Percentage Power Used for Hydrogen from Grid	%	20.74	26.23	22.76	28.18	25.08	28.03	26.98	32.01	31.65	37.24	32.37	38.28

Table 5.3: Detailed Overview Key Parameters Hydrogen Production, Scenario 3 and Scenario 4

5.2.2. Storage Capacity and Hydrogen Distribution Comparison

The major differences between the scenarios regarding the choice in storage technologies can be found in the absolute storage capacity, costs associated with handling time and transportation costs. For all five scenarios Table 5.4 depicts the optimal storage size expressed in required storage units and the corresponding absolute storage capacity in *kg*. The adopted backhaul factor in the optimisation model for each storage technology is shown. The total CAPEX corresponding to each storage technology is in favour of the HPSC technology for the first three scenarios. The OPEX regarding handling time and transportation of the containers is, however, significantly higher for the HPSC technology. The handling time costs contains the driver wage in combination with the total hours of handling time required to load and unload the specific containers at each location. The total transport cost contains the cost of fuel and the cost of the driver's wage for transporting the hydrogen storage unit between refuelling station locations.

The relative large storage capacity for the first three scenarios with distribution via the 20ft MEGC storage systems is a result of required flexibility in terms of the number of storage units to be delivered and storage units used as inventory across the refuelling station locations. This consequently results in an almost doubled absolute storage capacity in *kg* compared to the HPSC based scenario for scenarios 1, 2 and 3. With increased total demand and an equal amount of refuelling stations considered in the hydrogen value chain, it can be noticed that the absolute storage capacity difference in scenarios 4 and 5 is reduced compared to the first three scenarios.

Parameter	Units	Scenario 1		Scenario 2		Scenario 3		Scenario 4		Scenario 5	
		MEGC 20ft	HPSC								
Storage Units Required	#	6	38	8	46	7	44	9	76	10	95
Storage Capacity	kg	3930	2014	5240	2438	4585	2332	5895	4028	6550	5035
Backhaul Factor	%	30	20	30	20	30	20	30	20	30	20
Storage CAPEX	EUR	2,700,000	2,660,000	3,600,000	3,220,000	3,150,000	3,080,000	4,050,000	5,700,000	4,500,000	6,650,000
Handling Time OPEX	EUR	7,043	39,658	10,681	62,017	7,120	41,667	10,732	67,678	14,112	75,256
Transport OPEX	EUR	39,082	53,112	66,187	104,818	33,078	54,080	50,064	74,088	65,477	64,077

Table 5.4: Overview scenario storage sizing, storage cost and distribution costs

It shows that for a hydrogen value chain with four refuelling stations, a minimum of 7-8 20ft MEGCs are required to provide enough flexibility in the system to ensure full demand satisfaction. A general observation can be made that in the case of a value chain based on the 20ft MEGC each added refuelling station to the value chain requires at least two units, whereas overall, an extra unit is required that will be transit in between the refuelling stations. Considering the same hydrogen value chain size and spatial configuration, doubling demand only required two extra 20ft MEGC containers to cope with the increased daily demand at each refuelling station.

Doubling the total hydrogen demand in scenario four shows a doubling of the required HPSC units. Flexibility to distribute the units across the refuelling station poses no restrictions for the HPSC units as

it is possible to deliver half-full truckloads of HPSC units. The negative impact of the overall smaller total storage in the value chain is the increased transport costs as half-full truckloads offset the investment benefit of the reduced amount of HPSC storage units. A trade-off is therefore noticed between extra distribution trips with less total system storage capacity or more storage capacity and fewer distribution trips.

It can therefore be concluded when considering the 20ft MEGCs the flexibility of the distribution system is an important criterion for system sizing. Whereas a value chain focused on the distribution of hydrogen via the HPSC units, the overall capacity and cost regarding the distribution of the HPSC units is an important factor due to the CAPEX difference between the two storage technologies.

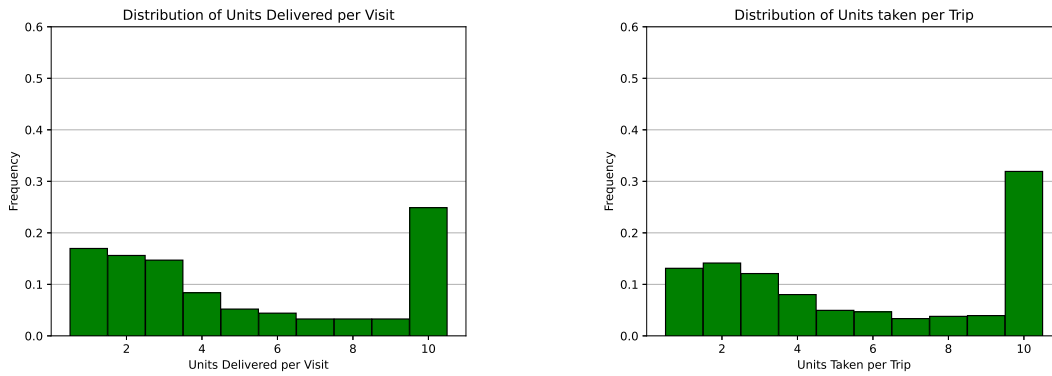
Several key indicators regarding the distribution of hydrogen for all five scenarios is shown in Table 5.5. It should be taken into account that the optimisation model simultaneously minimises the CAPEX and OPEX regarding the storage units in the hydrogen value chain and the OPEX regarding the distribution and handling time of the storage units. For the first scenario, the routing options are exactly similar for both container technologies due to the consideration of a single satellite station. The output of the optimisation model shows that for a system with the same distribution routing options but a different container technology, the optimal distribution strategy for the HPSC units is to depart the production site with a 4/5 filled truck on average and to complete more trips throughout the year compared to increasing the total system storage capacity size and weight until full truckloads are available.

Parameter	Units	Scenario 1		Scenario 2		Scenario 3		Scenario 4		Scenario 5	
		MEGC 20ft	HPSC								
Total Trips	#	273	371	414	686	276	478	414	638	547	552
Total Traveled Distance	km	19,969	27,138	33,885	52,917	16,801	27,114	25,432	37,199	33,265	32,103
Average Trip Distance	km	73.2	73.2	81.9	77.1	60.88	56.73	61.43	58.31	60.81	58.16
Total Trip Duration	hr	408	552	691	1100	276	569	512	779	685	675
Average Trip Duration	hr	1.5	1.5	1.7	1.6	1.27	1.19	1.27	1.22	1.25	1.22
Average Yearly Deliveries per Station	#	273	371	138	294	138	563	208	415	274	299
Average Weekly Deliveries per Station	#	5.25	7.13	2.65	5.66	2.65	5.42	4.02	8.32	5.26	7.74
Average Delivered Units	#	1	8.05	1	4.73	1	5.31	1	5.96	1	7.40
Average Distributed Units per Trip	#	1	8.05	1	5.71	1	5.63	1	6.02	1	7.40

Table 5.5: Overview detailed scenario distribution results

For the second scenario and third scenario, a similar trend of half-full truck distribution is also noticed. Looking at the total annual distribution costs for the multi-satellite value chain of scenario four, the advantage of split delivery between two or more refuelling stations during a single round trip is shown. Figure 5.16a illustrates the distribution of the number of units delivered at each refuelling station upon arrival, and Figure 5.16b shows the number of storage units taken upon departure from the hub refuelling station for scenario 2 when considering the HPSC storage units. In the scenario analysis, the storage of the hydrogen container's present value chain will be fixed where the decision-making process of the hydrogen production and distribution will be further analysed solely based on the cost of distribution and the cost of production. It is expected that a fixed storage capacity will influence the distribution scheduling and the number of storage units distributed during a single trip. With more storage units, more efficient routing can be scheduled due to the ability to wait for more filled storage units at the production locations.

The overall conclusion regarding the distribution of the HPSC containers can be made that for a system with 250.000 kg of annual hydrogen production, half-full truckloads deliveries allow an overall smaller total storage capacity and therefore counteract the CAPEX cost difference between both container technologies, as will be discussed in subsection 5.2.3. For the 500.000 kg annual hydrogen value chain with two satellite stations, the total required storage capacity exceeds the need for flexibility, thereby reducing the total storage capacity difference for both container technologies. This results in showing the large overall cost advantage for the 20ft MEGC units.



(a) Distribution of HPSC units delivered per visit by the distribution vehicle for scenario 2 (b) Distribution of HPSC units taken by the distribution vehicle from the hub station for scenario 2

Figure 5.5: Distributions of HPSC units delivered and taken by the distribution for scenario 2

For all scenarios, due to the assumed handling time of the small containers by the utilisation of a transportable forklift on the back of the trailer, A significant difference in OPEX regarding handling time is observed between the two container technologies. Where the total handling time OPEX are in favour of the 20ft MEGC unit for every scenario.

5.2.3. Levelised Cost Of Hydrogen Comparison

Table 5.6 depicts the contribution towards the total LCOH per value chain compartment and the total LCOH from well-to-tank. The model output regarding the levelised cost of hydrogen is compared for both container technologies for each scenario. Figure 5.7 shows an overview of the LCOH cost distribution for all scenarios considered in this research.

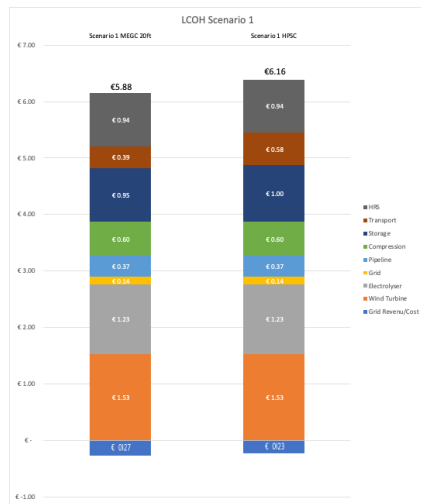
Also, the LCOH is compared for parity with diesel fuel as of 2022. The LCOH analysis contains all costs associated with the hydrogen value chain from energy up to the tank of the vehicle (Well-to-tank). The cost of hydrogen is compared to the current cost of diesel at the refuelling stations without Value Added Tax (VAT) but including excise duties. As of 2022, the average cost of diesel without tax is equal to 1.36 in the Netherlands. The assumption is made that the use of 1 kg hydrogen in fuel cell trucks equates to the use of 5 litres of diesel in a diesel-fuelled truck. Taking into account a 10% profit margin for the refuelling station operator, the LCOH must be less than $6.40 \frac{\text{€}}{\text{kg}_{H_2}}$ to reach cost parity with diesel fuel as of 2022.

Hydrogen Value Chain Component	Scenario 1		Scenario 2		Scenario 3		Scenario 4		Scenario 5	
	20ft MEGC	HPSC								
Grid Revenue/Cost	-0.27	-0.23	-0.25	-0.21	-2.05	-2.00	-0.76	-0.79	-0.09	-0.02
Wind Turbine	1.53	1.53	1.52	1.53	3.06	3.06	2.03	2.03	1.53	1.53
PEM Electrolyser	1.23	1.23	1.23	1.23	2.47	2.47	1.64	1.64	1.23	1.23
Grid Connection	0.14	0.14	0.14	0.14	0.28	0.28	0.19	0.19	0.14	0.14
Hydrogen Pipeline	0.37	0.37	0.37	0.37	0.58	0.58	0.39	0.39	0.29	0.29
Hydrogen Compression	0.60	0.60	0.59	0.60	0.97	0.98	0.72	0.75	0.59	0.60
Storage	0.95	1.00	1.27	1.21	1.11	1.16	0.95	1.33	0.80	1.25
Distribution	0.39	0.58	0.51	0.87	0.37	0.59	0.30	0.54	0.26	0.38
Refuelling Stations	0.94	0.94	1.18	1.19	1.36	1.37	1.24	1.24	0.94	0.94
Total LCOH	5.88	6.16	6.56	6.93	8.15	8.49	6.70	7.32	5.69	6.34

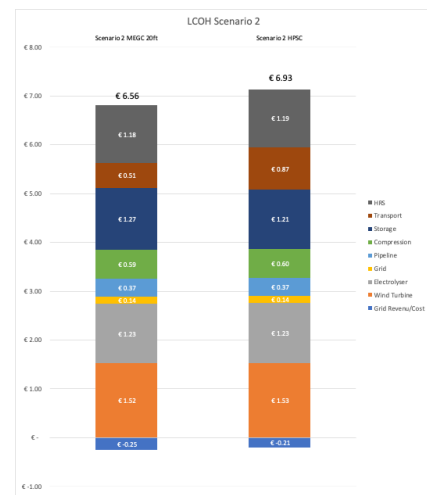
Table 5.6: Overview LCOH calculations all main scenarios

Non-Stationary Storage Technology Cost Comparison

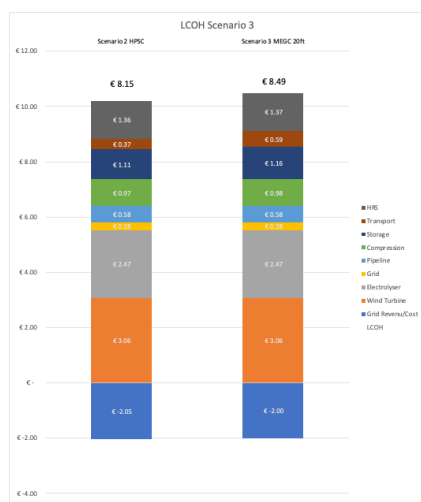
The LCOH cost distribution obtained from the optimisation process for each container technology



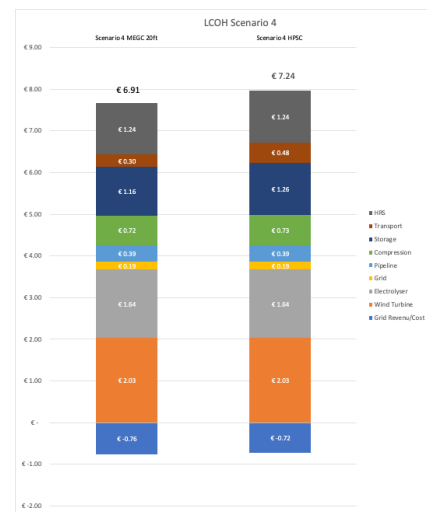
(a) LCOH Cost Distribution Scenario 1



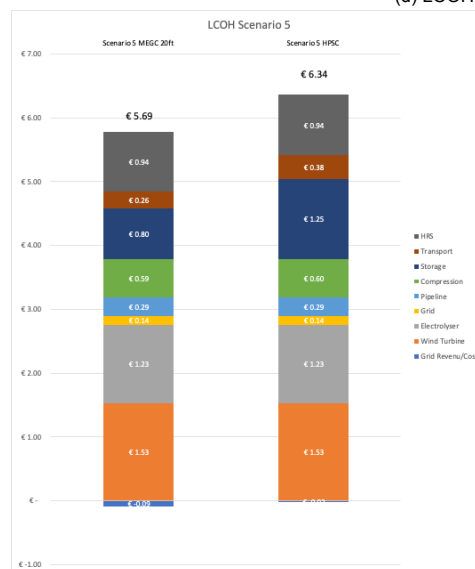
(b) LCOH Cost Distribution Scenario 2



(c) LCOH Cost Distribution Scenario 3



(d) LCOH Cost Distribution Scenario 4



(e) LCOH Cost Distribution Scenario 5

Figure 5.6: Overview LCOH Container technology Comparison

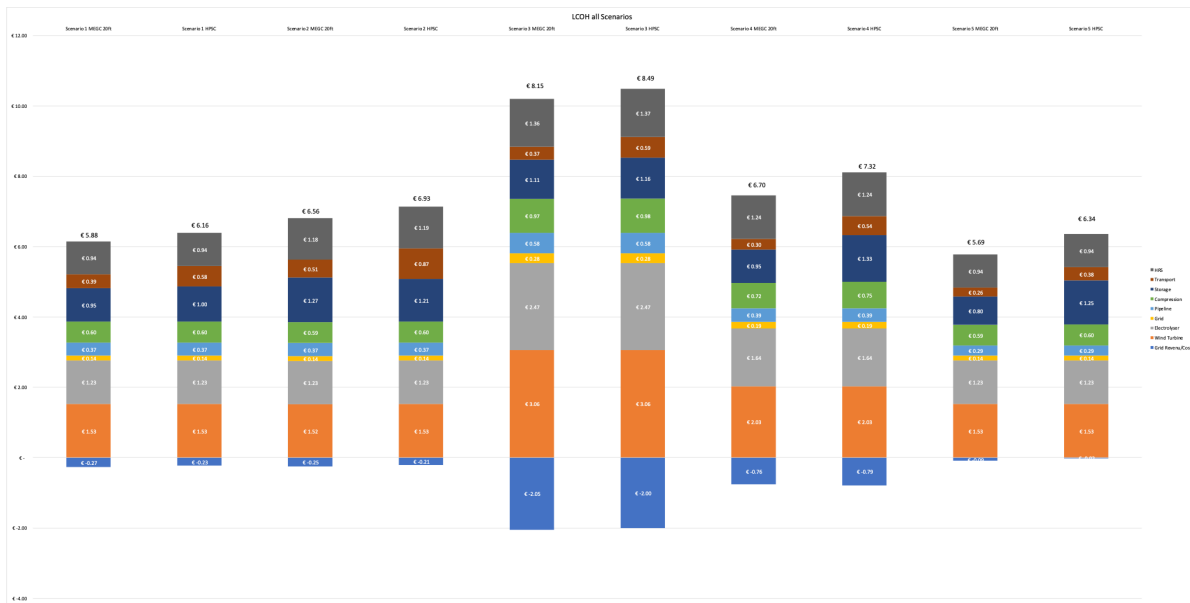


Figure 5.7: LCOH overview Scenario 1 - 5

and scenario configuration is shown in Figure 5.6. A more detailed cost overview, including The total annual cost per value chain section expressed in € and $\frac{\text{€}}{\text{kg}}$ is shown Appendix D. In Figure 5.6 the distribution of the value chain cost components expressed in $\frac{\text{€}}{\text{kg}}$ are shown. Each section contains both the annualised CAPEX and OPEX components.

The first observation is the minor difference between the total LCOH for each scenario. For each scenario, based on current market prices. Secondly, the 20ft MEGC outperforms the HPSC units in every scenario. The two components that define the overall cost advantage for the MEGC 20ft units are the investment costs and the costs regarding the distribution of the hydrogen storage containers. It is expected that the cost difference between the HPSC container and the MEGC unit will decrease in the future due to technological development and economics of scale. The reduction of the cost difference between both container technologies is discussed in subsection 5.3.2.

Taking into account the gradual development of a hydrogen value chain, the overall LCOH of hydrogen varies between € 8.35 and € 5.69 for the 20ft MEGC container and € 8.49 and € 6.16 for the HPSC storage unit. Figure 5.8 shows the cost trend from scenarios 3 to 5, where the same spatial configuration is considered. Thirdly, it is shown that the overall LCOH in the hydrogen value chain diverges when comparing both container technologies with increasing total annual demand. Therefore it can be concluded regarding the increase of annual demand for the same spatial configuration. The LCOH cost difference will increase. The cost distribution efficiency regarding the HPSC units does not outweigh the extra cost by increased handling time and the large CAPEX difference between both container technologies.

Fourthly, observing the cost development regarding the distribution of the hydrogen storage units across the value chain as the second contributor to the cost difference between container technologies, it can be noticed that the rate of decrease of contribution to the total LCOH for the HPSC units is larger than the MEGC 20ft containers. Figure 5.9 shows the cost development of the distribution cost compared against the increased total annual demand between scenarios 3, 4 and 5. The overall cost component for transportation of the HPSC storage units is larger for all scenarios, where a significant cost driver for the HPSC distribution network is the cost regarding the required handling time. The convergence of transportation cost is, however, an interesting development. It shows the cost reduction potential of visiting multiple refuelling stations per round-trip by the distribution vehicle. As previously shown in Table 5.4, the total travelled distance in scenario 5 for the HPSC units is less while assuming

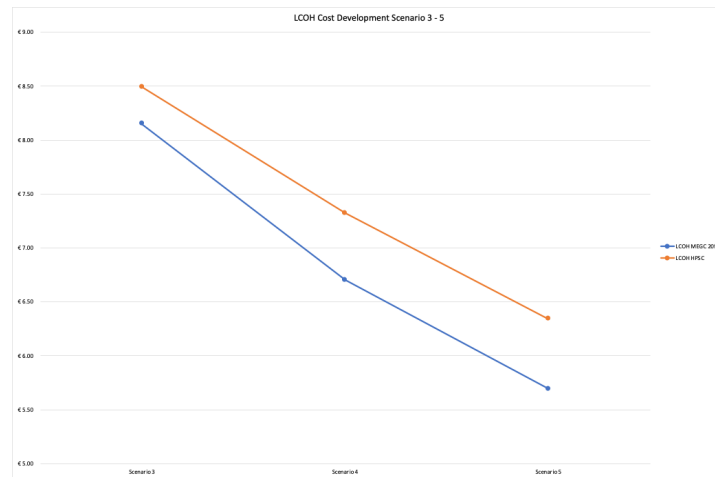


Figure 5.8: LCOH Cost Development Scenario 3 - 5

an increased demand in the hydrogen value chain. As this research only includes an early-stage hydrogen value chain, the potential cost-benefit of multiple deliveries for both container technologies in a single trip is further discussed in chapter 6.

Finally, despite the convergence of the transport cost component for both container technologies, the overall LCOH diverges due to the high CAPEX difference of the HPSC units.

Comparing the LCOH for each scenario with diesel parity, it can be concluded that diesel parity is reached when the value chain is fully utilised, and the annual demand is greater than 250.000 kg per production location for current market pricing of the value chain system components. The future cost development of several value chain components is further discussed in chapter 6, where also the potential for each container technology expressed in an expected LCOH is examined.

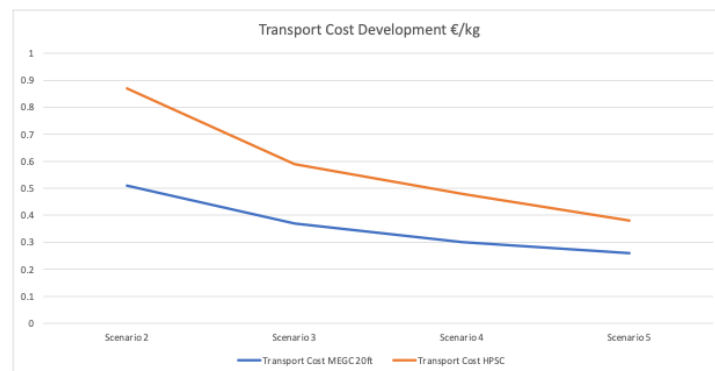


Figure 5.9: Cost Development LCOH Transport Component

5.3. Scenario Analysis

In this section several input parameters of the optimisation model are varied to determine the relative impact on the decision-making process of the hydrogen production process, distribution planning, required storage capacity, the choice of most suitable container technology and the overall LCOH. The second scenario is used in the scenario analysis as it is expected that scenario two represents a first implementation of the proposed hydrogen value chain.

5.3.1. Power Availability Grid

The first input parameter varied in the optimisation model is the maximum power to be withdrawn from the grid. The operator at the production location has to pay grid distribution costs concerning the maximum monthly power drawn from the grid. In the Netherlands, the cost structure of power distribution is only applicable to consumers and not for producers of power. As the production location is both, it is preferred to maximise the ability to sell power and minimise the costs concerning the peak power drawn from the grid.

The reduction in maximum power drawn from the grid will reduce the overall grid connection OPEX while still being able to sell the excess produced electricity to the grid when necessary. In this scenario analysis, the power drawn from the grid is reduced to 50% and 25% of the assumed grid connection. The capacity of the grid connection considered is 2.5 MW for all scenarios.

The expected result is an increased requirement of overall storage capacity to overcome periods with reduced power production by the wind turbine and where the grid connection is not able to aid the production process of hydrogen. This leads to a shift in the ratio between the source of energy for the hydrogen production process. The shift will drift towards more direct consumption of wind energy compared to the base scenario.

Table 5.7 shows the most important key parameters regarding the production of wind energy and hydrogen at the production location. The table also includes the ratio between energy sources used by the electrolyser. Also, the OPEX component regarding the grid connection distribution cost and the total revenue/cost by utilising the grid connection is shown for every case. In Table 5.8 the required storage capacity and key parameters regarding hydrogen distribution is shown.

The first noticeable result is the infeasible optimisation process of the 25% reduced maximum power drawn from the grid scenario. This scenario sheds light on the limitation of the optimisation model used in this research. The infeasibility of the 25% case is the application of optimising each week compared to the consideration of a yearly optimisation time horizon. The yearly optimisation would increase the computational time and the required CPU and Memory resources beyond a realistic size. The model is not able to include the use of extra storage to overcome weekly/monthly/seasonal effects. It is therefore shown that this particular optimisation model is limited by the arbitrary choice of inventory size by the end of each weekly optimisation process as discussed in chapter 3. Therefore only a maximum reduction of 50% in maximum power drawn from regarding the total grid connection capacity is being analysed.

Parameter	Units	Base Scenario		50% Reduction Max Power Drawn Grid	
		MEGC 20ft	HPSC	MEGC 20ft	HPSC
Energy Production Wind Turbine	GWh	15.11	15.11	15.11	15.11
Energy Required PEM	GWh	12.8	12.73	12.75	12.62
Energy Curtailed	GWh	0.08	0.2	0.08	0.18
Energy Sold To The Grid	GWh	6.14	6.19	5.83	5.87
Energy Bought From The Grid	GWh	3.91	4.02	3.56	3.57
Energy Used Hydrogen Production From Grid	GWh	3.91	4.02	3.56	3.57
Energy Used Hydrogen Production From Wind Turbine	GWh	8.89	8.72	9.2	9.05
Percentage Energy Used Hydrogen Production From Grid	%	30.55	31.54	27.9	-502,278
Percentage Energy Used Hydrogen Production From Wind Turbine	%	69.45	68.46	72.1	292,631
OPEX Grid Connection Distribution	EUR	60281.67	60300	30,150	30,510
OPEX Grid Total	EUR	-183,689	-174,330	-143,705	-142,077

Table 5.7: Overview results production process scenario analysis 50% reduction max power drawn

For the adjusted scenario, the total grid distribution OPEX is reduced by 50%, as expected. However, the net revenue obtained regarding the interaction with the electricity grid shows an increase for both container technologies compared to the base scenario. This is in line with the expected shift in the ratio between the energy source for the production of hydrogen. Due to the ability to sell hydrogen

at 100% grid capacity, no change in the amount of curtailed energy is noticed.

It can be seen that for the HPSC oriented scenario with a 50% reduction in maximum power drawn from the grid, 17% more storage units are required to overcome the mismatch between power production of the wind turbine and being able to use the grid as a backup source. Regarding the MEGC 20ft containers, the excess storage capacity in the entire value chain is able to absorb this mismatch, and no extra containers are required.

Parameter	Units	Base Scenario		50% Reduction Max Power Drawn Grid	
		MEGC 20ft	HPSC	MEGC 20ft	HPSC
Total Storage Required	#	8	46	8.0	54
Storage CAPEX	EUR	3,600,000	3,220,000	3,600,00	3,780,000
Handling Time OPEX	EUR	10,681	62,017	10,681	62,571
Distribution OPEX	EUR	66,187	104,818	66,187	114,443
Total Trips	#	414	686	414	718
Total Distance Travelled	km	33,885	52,197	33,885	57,782
Average Trip Distance	km	81.85	77,14	81.85	80.5
Total Trip Duration	hr	691.4	1100,5	691.4	1201
Average Trip Duration	hr	1.67	1.6	1.67	1.67
Average Deliveries Per Refuelling Station Weekly	#	2.65	5.54	2.65	6.43
Average Stations Delivered Per Trip	#	1	1.29	1	1.4
Average Delivered Units	#	1	5.06	1	4.46
Average Units Distributed Per Trip	#	1	5.71	1	5.04

Table 5.8: Overview results storage sizing and distribution scenario analysis 50% reduction max power drawn

Figure 5.10 illustrates the comparison between the LCOH of the base scenario and the scenario with the reduced capacity of power drawn from the grid. The LCOH distribution shows an economic advantage in the overall revenue regarding the grid interaction component for both new scenarios as fewer costs are associated with the utilisation of the grid connection. For the HPSC oriented hydrogen value chain, the increased amount of HPSC units results in an increase in the revenue of power sold to the grid. However, the requirement for more storage units increases the storage cost component of the total LCOH. This results in an overall higher LCOH for the hydrogen value chain. Also, due to the application of more storage units, the overall distribution costs are increased.

It can be concluded that reducing the maximum power drawn from the grid increases the energy consumption of the wind turbine for the production process of hydrogen marginally and results in a negligible reduction or even an increase of the overall LCOH when considering the HPSC units. The reduction of grid utilisation should therefore only be considered if there is enough excess storage capacity present in the value chain, and it will not lead to extra investment in storage units. The limitations of this optimisation model result in not being able to reduce the maximum power drawn from the grid by more than 50%.

5.3.2. Cost Reduction HPSC

For all previously shown scenarios, it should be taken into account that the overall cost of storage is equal to $687 \frac{\text{€}}{\text{kg}}$ for a single 20ft MEGC unit and $1320 \frac{\text{€}}{\text{kg}}$ for a single HPSC unit. The cost of both container storage units depicts the market price as of 2022.

The expected cost development in the price difference price of the storage container technologies per kg will decrease to a marginal cost difference and will be mainly related to the cost of the materials for each container due to the economics of scale. The current pricing of both storage technologies includes technological development costs, which will decrease when taking into account economics of scale in future scenarios.

In this research, both container technologies are compared by considering a reduced cost of stor-



Figure 5.10: LCOH Distribution Reduction of Maximum Power drawn from grid

age per kg of hydrogen for the HPSC units. The expected future cost difference between the 20ft MEGC units and HPSC units will be dominated by the number of valves required. The HPSC unit with four sections will require a single valve per gas cylinder to ensure the application of the cascade filling process. The 20ft MEGC is also divided into four sections per container and requires a single valve per section. Forty more valves are required when considering a 20 ft trailer with HPSC units compared to a single MEGC 20ft unit. The cost difference per kg of hydrogen storage is expected to be around $200 \frac{\text{€}}{\text{kg}}$. The new assumed cost in this scenario analysis will be $687 \frac{\text{€}}{\text{kg}}$ and $887 \frac{\text{€}}{\text{kg}}$ for the MEGC 20ft and HPSC container, respectively.

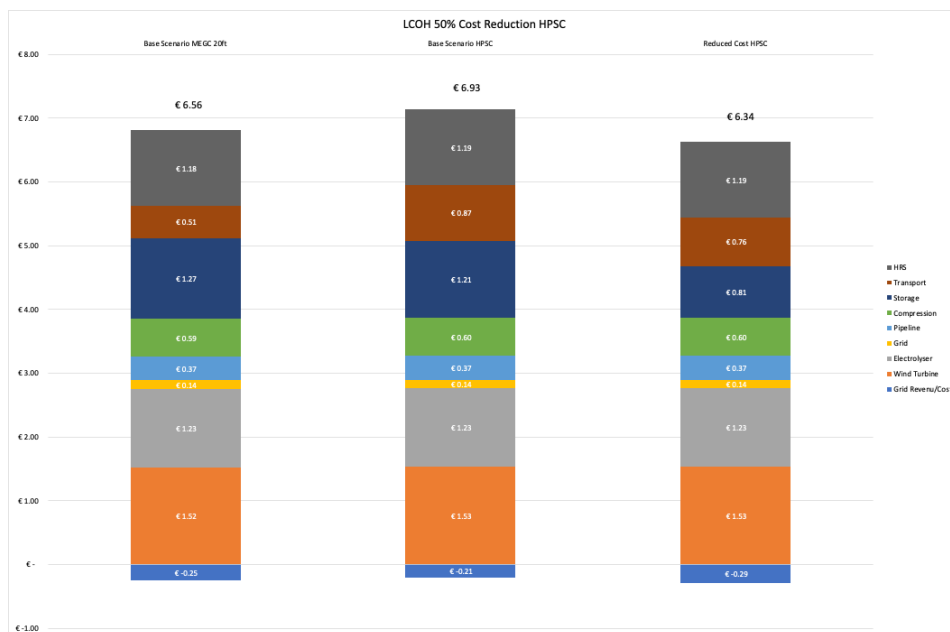


Figure 5.11: HPSC cost reduction LCOH overview

Figure 5.11 illustrates the LCOH distribution for scenario 2 for the base scenario and the adjusted CAPEX component for the HPSC storage units. Reducing the CAPEX difference per kg hydrogen stor-

age for both container technologies results in the HPSC oriented hydrogen value chain outperforming the MEGC 20ft oriented value chain by 0.22 cents per kg on LCOH, and a 3% LCOH cost reduction is reached compared to the current pricing of the HPSC units. Next to the overall cost reduction of the LCOH for the considered scenario, a decrease in overall transport cost is shown. The decrease in transport cost is a result of the decision to invest in more HPSC units due to the decreased CAPEX cost, reflecting upon the trade-off between more transport movements or investment in more storage units. Figure 5.12 shows despite the minor overall cost reduction seen for scenario two. The overall cost difference is in favour of the 20ft MEGC units when considering an increased demand.

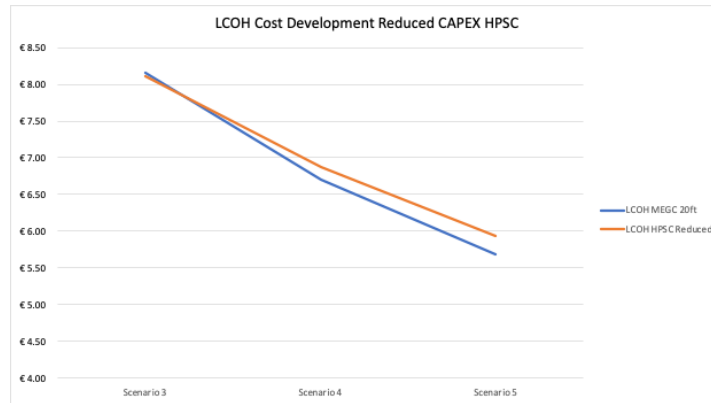


Figure 5.12: LCOH Cost reduction scenario 3 - 5, reduced CAPEX difference

It can be concluded when considering the economic potential for the cost reduction of the HPSC unit, the overall difference in LCOH between the two container technologies is very small. The application for the HPSC units, therefore, is more suitable for a hydrogen value chain with many small-sized refuelling stations with low demand. The extra benefit when demand increases are the flexibility in the distribution network. However, it can be concluded that for a refuelling station network, the current market pricing of the MEGC 20ft outperforms the flexibility and added cost of the HPSC unit. When station demand increases and the throughput per production location increases from a single turbine to multiple turbines per production location, the required amount of 20ft, MEGCs will provide enough flexibility to the distribution system for optimally scheduling distribution. Figure 5.13 shows all scenarios considering the reduced CAPEX difference between the HPSC and the MEGC 20ft unit.

5.3.3. Fixed Storage

The simultaneous optimisation process of the production planning, total storage capacity and distribution of hydrogen to the satellite station results in the minimal amount of storage required to optimally distribute the hydrogen for the specified year of optimisation. Taking into account uncertainty and the variability of the wind turbine power production capacity in combination with the stochastic nature of demand at the refuelling station, a safety factor regarding the number of storage units available in the value chain should be considered when sizing the hydrogen value chain. In this subsection, a scenario with a safety factor regarding a total storage capacity of 1.25 times the optimal storage capacity is assumed.

For the base scenario, it is known that for 2019 the minimum value of hydrogen storage units required to satisfy the demand for the second scenario is equal to 8 units for the 20ft MEGC units and 46 for the HPSC units. An increase of 1.25x will result in the application of 10, 20ft MEGC units and 60 HPSC units. Due to the fixed storage capacity during the optimisation process, the inventory optimisation will be excluded from the objective function and therefore simplifies the optimisation model.

Figure 5.15 shows the distribution of the LCOH for the base scenario with the optimised inventory size and the two scenarios, including the fixed storage capacity. The final LCOH distribution shown in the figure illustrates the LCOH distribution with equal CAPEX cost for both storage technologies as discussed in the previous section in combination with the fixed storage factor.

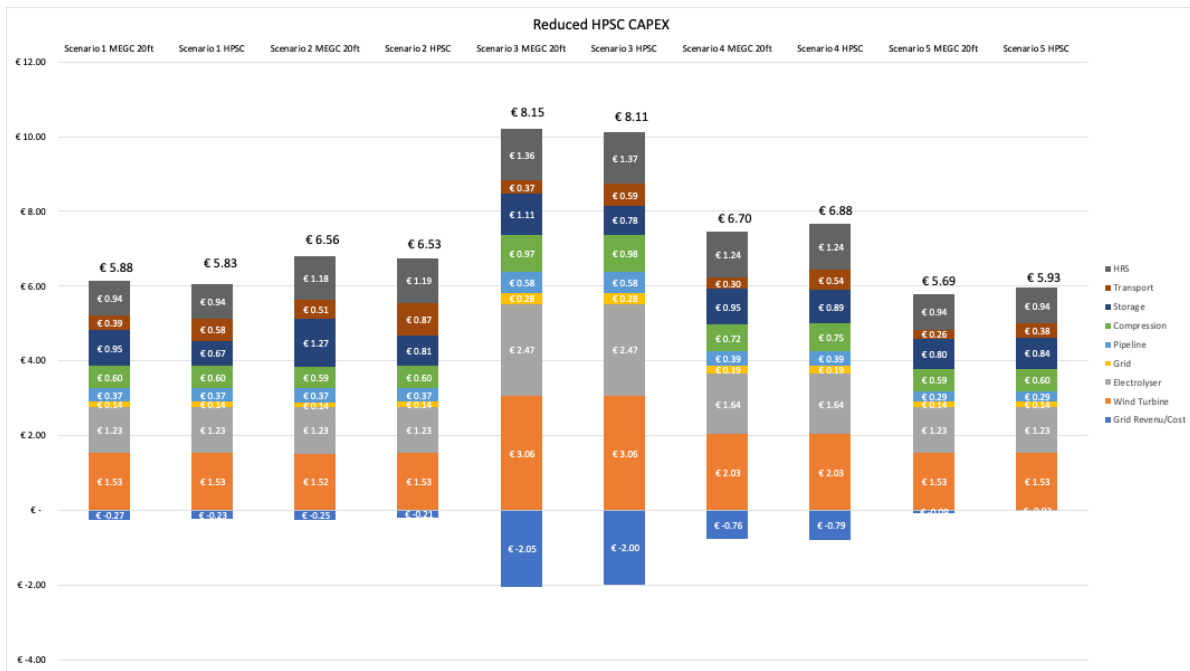
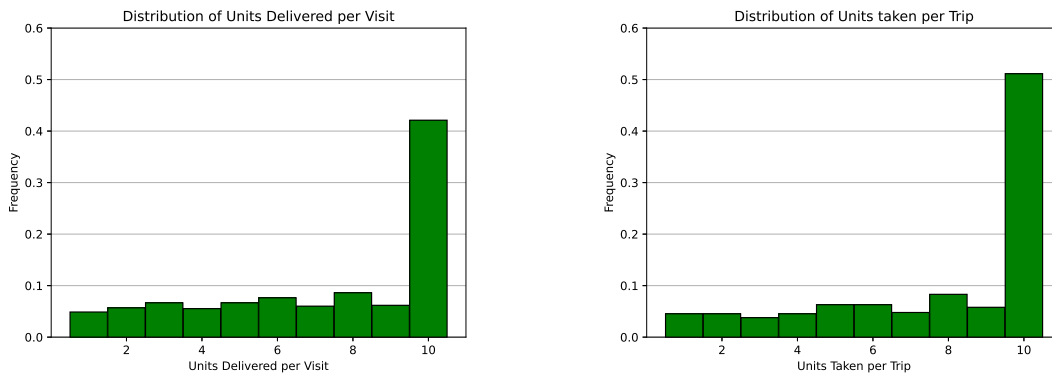


Figure 5.13: LCOH overview reduced HPSC CAPEX cost



(a) Distribution of HPSC units delivered per visit by the distribution vehicle for scenario 2, Fixed Storage (60 units) (b) Distribution of HPSC units taken by the distribution vehicle from the hub station for scenario 2

Figure 5.14: Distributions of HPSC units delivered and taken by the distribution for scenario 2, Fixed Storage (60 units)

Due to the optimisation process based solely on total system cost and the increased overall storage capacity, the application of selling higher valued wind energy and buying reduced grid electricity for the production of hydrogen is increased. The increased revenue obtained by grid interaction reduces the increase in overall LCOH for the fixed storage scenarios. However, the overall LCOH of hydrogen is increased for both storage technologies due to the increased available storage units. An increase of 6% and 5% for the 20ft MEGC and HPSC oriented value chain is observed, respectively.

The final LCOH distribution illustrated in Figure 5.15 shows the LCOH distribution for the HPSC scenario with an equal cost of storage per kg hydrogen as the 20ft MEGC units. Similar to the previous section, it is observed that the HPSC outperforms the MEGC 20ft oriented value chain by 7% when considering the fixed storage capacity with a factor of 1.25x the optimal storage capacity.

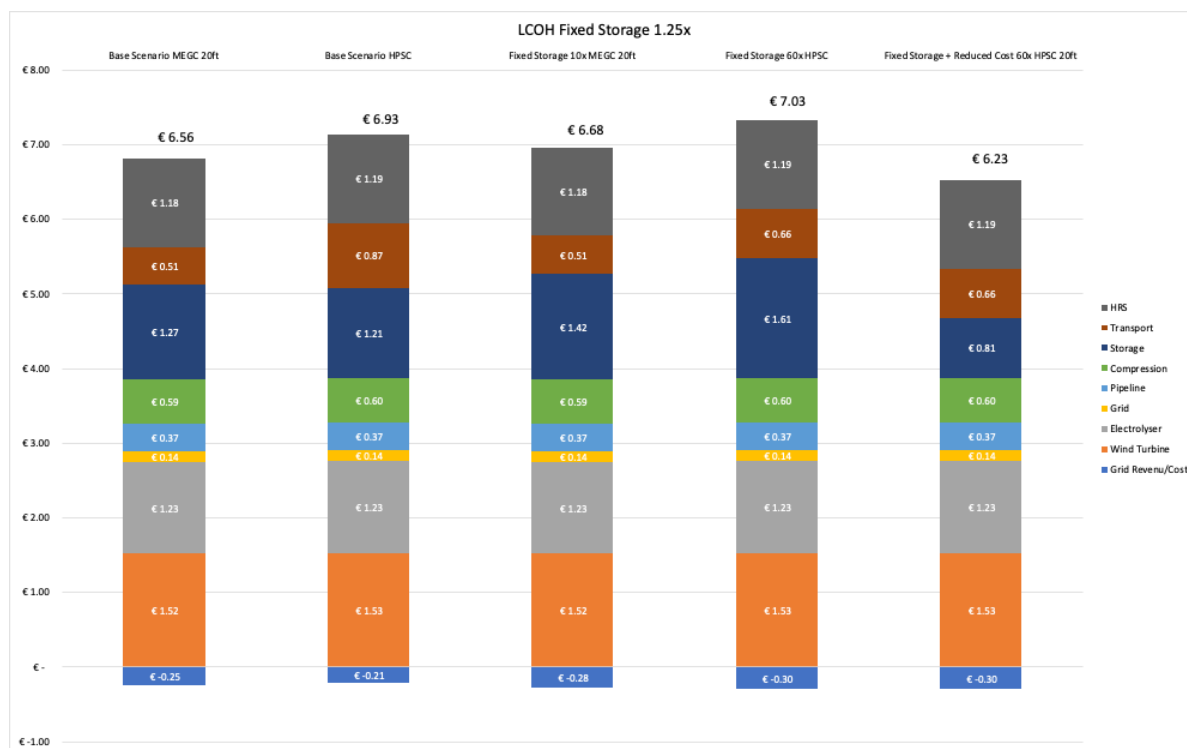


Figure 5.15: LCOH Distribution Fixed Storage

5.3.4. Grid Electricity Price

For all optimisation scenarios, 2019 is taken as a reference year. 2019 is the year with the most average annual wind speed of the past five years for which historical price data is available. Figure 5.17 shows the price development of the grid electricity price from 2019 and onwards until February 2022. A 100-day moving average is shown by the dark orange line. The light orange area shows the hourly fluctuations of the day ahead electricity price taken from ENTSOE transparency platform (ENTSOE, 2021).

From 2020 two observations are noticed. Firstly, the increase in electricity price and secondly, the price fluctuations increases in magnitude and intensify. The increased electricity price is the result of the rapid economic rebound after the first year of the Covid-19 pandemic. Parallel to the rapid demand growth for energy, 2021 has shown more extreme weather conditions resulting in higher power fluctuations from renewable energy sources. A 20% increase in renewable generating capacity is realised in Europe from 2020 to 2021. The installed capacity of renewable energy sources increased for solar from 7 GW to 10 GW in 2019 to 2020 and for installed wind capacity from 4.5 GW to 6.5 in 2020. With an expected installed capacity of 30 GW solar and 15 GW wind energy generation capacity by 2025 the influence of renewable energy sources on the electricity grid price is expected to rise.

The average electricity price for 2019 and 2020 was $48 \frac{\text{€}}{\text{MWh}}$ and $51 \frac{\text{€}}{\text{MWh}}$, respectively. The impact of the increased renewable energy production capacity will lead to more frequent and large power fluctuations resulting in high price fluctuations on the electricity market.

In this research, two scenarios are analysed with an on average increased electricity price and increased magnitude of price fluctuations. The electricity price of 2019 is multiplied by a factor of 2 and 3 to simulate different price increments. The price fluctuations of 2019 are multiplied to sustain the correlation between wind speed and price fluctuations of the energy price. The correlation between the power price fluctuations and the power production capacity is equivalent to 0.12 for 2019 as discussed in section 5.1.

Table 5.9 shows an overview of the average electricity price and standard deviation of the grid

(a) Distribution of HPSC units delivered per visit by the distribution vehicle (b) Distribution of HPSC units taken by the distribution vehicle from the hub station for scenario 2

Figure 5.16: Distributions of HPSC units delivered and taken by the distribution for scenario 2

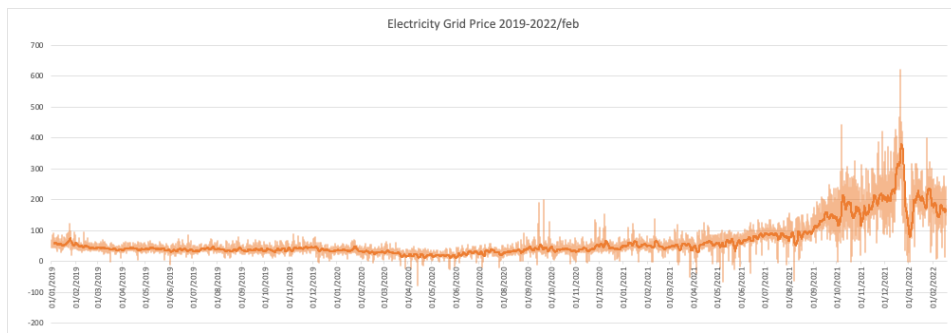


Figure 5.17: Grid Electricity Price 2019 - 2022/feb

Parameter	Average Price [$\frac{\text{€}}{\text{MWh}}$]	Standard Deviation [$\frac{\text{€}}{\text{MWh}}$]
Cost of Electricity 2019	41.19	11.28
Cost of Electricity 2019 x2	82.38	22.57
Cost of Electricity 2019 x3	123.57	33.86

Table 5.9: Increased electricity price 2019

electricity price for 2019 together with the increased grid electricity price and corresponding standard deviation.

The LCOH regarding the increased grid electricity price is shown in Figure 5.18 for all scenarios. The only factor influenced by the increased electricity price is the total revenue/cost regarding the interaction with the grid. It can be concluded that the LCOH of hydrogen is resilient against increased price fluctuations of the electricity grid. The increased electricity price fluctuations result in a lower overall LCOH due to extra revenue by the larger cost differences between the power bought at time steps when the grid electricity price is low and selling excess produced power from the wind turbine at time steps when the electricity price is high.

5.4. Sensitivity analysis

A sensitivity analysis is performed to determine how the variation of certain parameters, which are assumed constant for all previously discussed scenarios, affect the output of the optimisation model. The

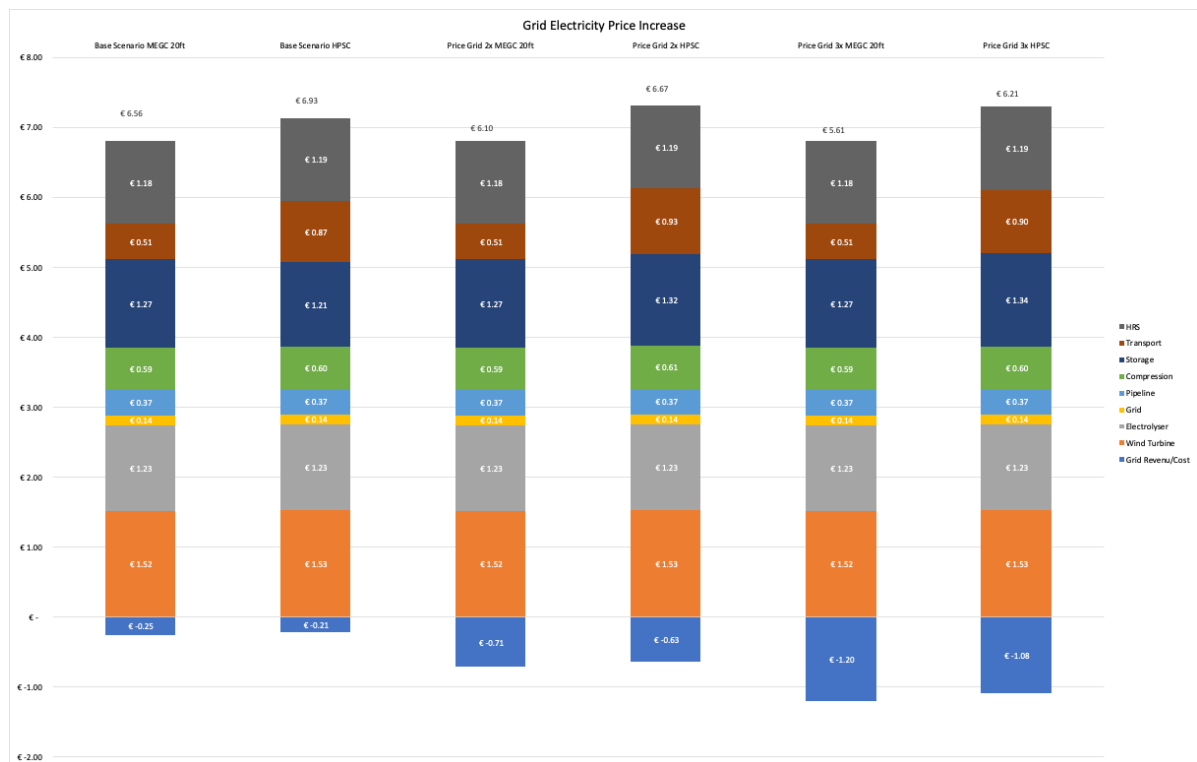


Figure 5.18: LCOH overview increased grid electricity price

sensitivity analysis for the economic optimisation model is similar to the scenario analysis performed in the previous section. The difference between the performed scenario analysis and the sensitivity analysis is the relative variation of input certain input parameters. In the sensitivity analysis, minor variations are examined to determine the stability and sensitivity of the optimisation model. The variables adjusted in the sensitivity analysis are the WACC and the total annual demand. By varying the model with small increments, the outcome of the model for a certain range regarding the considered variable in the sensitivity analysis can be predicted.

5.4.1. WACC

The first parameter varied in the sensitivity analysis is the Weighted Average Cost of Capital. For all previously examined scenarios, a WACC of 4% is assumed. The optimisation model incorporates the annualised cost of the total CAPEX for each asset. The annuity factor for each component of the value is affected by the alteration of the percentage of the WACC. The WACC of 4% represents an 80-20 debt/equity ratio, where the expected cost of equity is 10% and the cost of debt 2.5%. The values for the WACC are taken from an industry survey on renewable energy sources for each country in Europe by Auctions for Renewable Energy Support (AURES) backed by the European Union. The value chain is based on on-shore wind energy, and therefore the cost of equity and cost of debt is assumed similar for all value chain components.

Figure 5.19 shows a range from 3% to 5% where three optimisation result are used to interpolate the linear trend for a WACC between 3% and 5%. On average, the LCOH for the value chain considering 20ft MEGC containers is increased by € 0.45 per increased WACC percentage. The change of WACC for the MEGC 20ft storage units shows no difference in the number of storage units required.

Figure 5.20 shows the range of WACC from 3% to 5% for the HPSC oriented value chain. Overall a linear trend is observed with an average cost increase of € 0.15 per increased percentage of WACC. In comparison to the 20ft MEGC oriented value chain, a different sizing of storage capacity is noticed

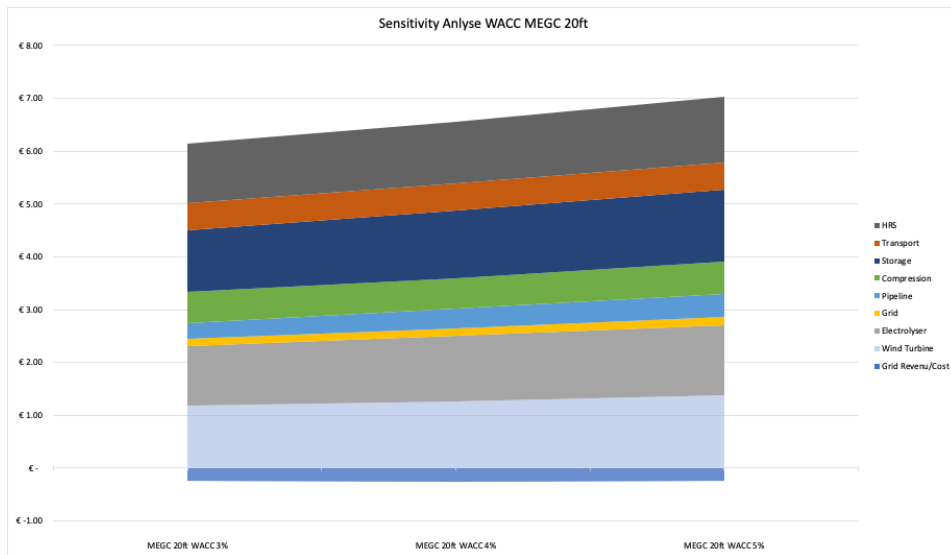


Figure 5.19: Sensitivity analysis WACC range 3 - 5% MEGC 20ft

with increased WACC. It is shown that less storage is purchased with a larger assumed WACC, as the WACC impacts the annualised CAPEX cost regarding the storage units. The choice is made to deliver more half-full truckloads with consequently more restocking of the refuelling station to reduce the required investment in the HPSC storage units and therefore reduce the overall LCOH increment per increased percentage for the WACC.

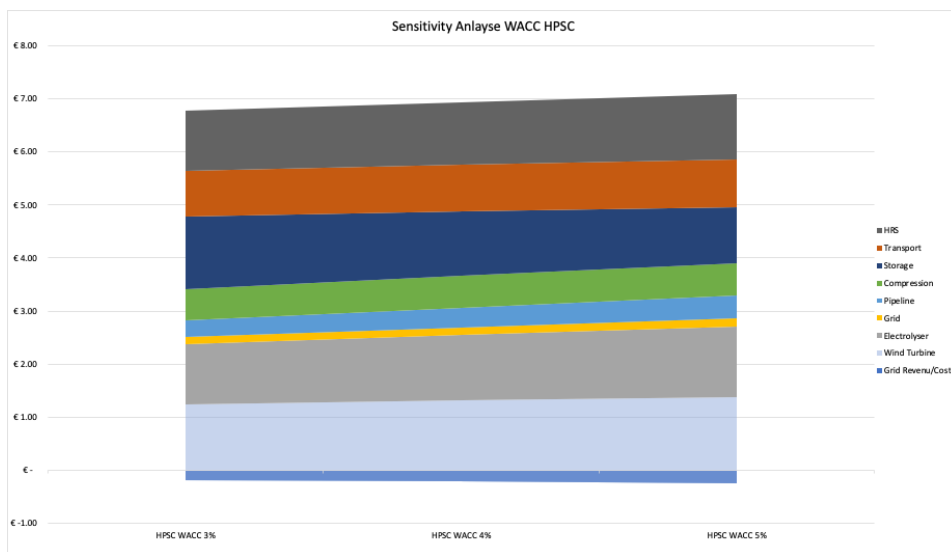


Figure 5.20: Sensitivity analysis WACC range 3 - 5% HPSC

5.4.2. Demand

The second parameter varied in the sensitivity analysis is spread in total annual demand according to the stochastic demand model discussed in chapter 2. Figure 5.21 shows the boxplot for the demand varies according to the stochastic demand model adopted in this research. The boxplot includes 50 data points for each demand scenario. All demand time series for each refuelling station are modelled independently. The total maximum spread of total annual demand is equal to 8000 kg.

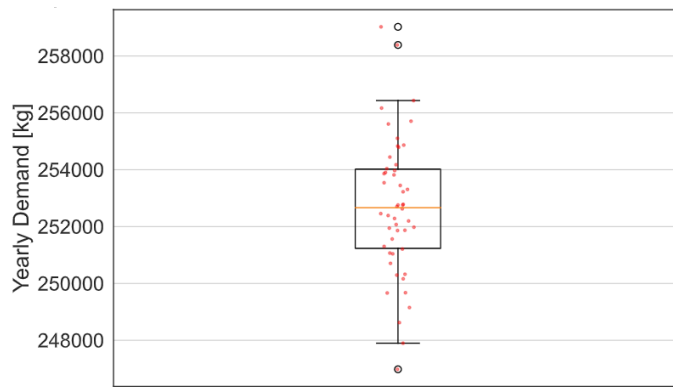


Figure 5.21: Boxplot demand distribution, 250.000 kg annual demand, 4 refuelling stations

For the sensitivity analysis, the minimum, maximum and median of the stochastic demand are compared. Figure 5.22 shows the output of the sensitivity analysis for the hydrogen value chain considering 20ft MEGC units. Similar when varying the WACC, the system sizing for each demand scenario remains constant for the MEGC 20ft oriented value chain due to the excess storage capacity available to ensure system distribution flexibility.

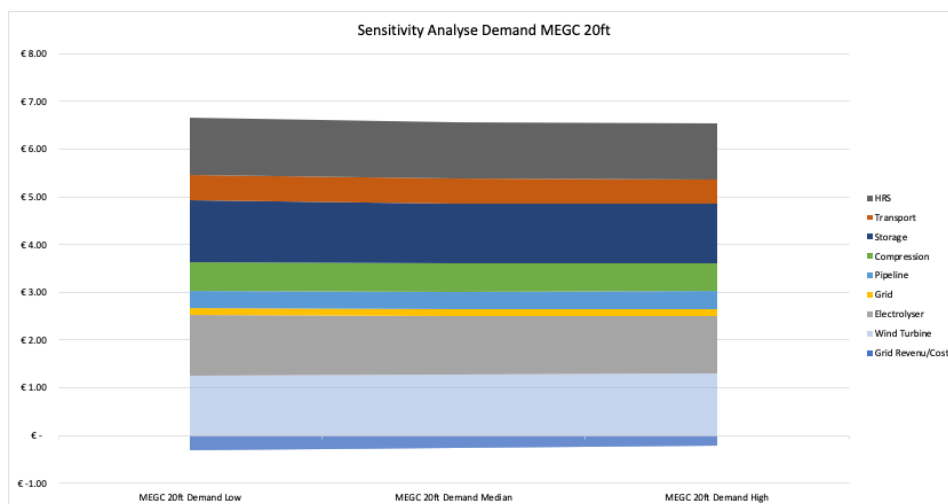


Figure 5.22: Sensitivity analyse demand Low,Median,High 20ft MEGC storage, 250,000 kg average annual demand

Figure 5.23 shows the output of the sensitivity analysis regarding the same demand distribution shown in Figure 5.21 for the HPSC oriented value chain.

In comparison to the scenario considering the 20ft MEGC the LCOH increases when considering the maximum bound of the annual demand variation. The increase is caused by the need for extra HPSC units in the hydrogen value chain. Regarding the sensitivity of the hydrogen value chain on the expected stochastic demand, it can be concluded that the total LCOH is expected to change minimally. For both container technologies. For the HPSC unit oriented value chain, it can be concluded that the requirement of extra HPSC units remains within the safety factor discussed in subsection 5.3.3 in the scenario analysis. The optimal value of storage containers for the given scenario varies between 42 and 50 HPSC units. Corresponding to a $\pm 8\%$ of the scenario considering the median of the demand distribution shown in Figure 5.21.

Furthermore, it can be noticed for an increased total annual demand, less power is sold to the grid,

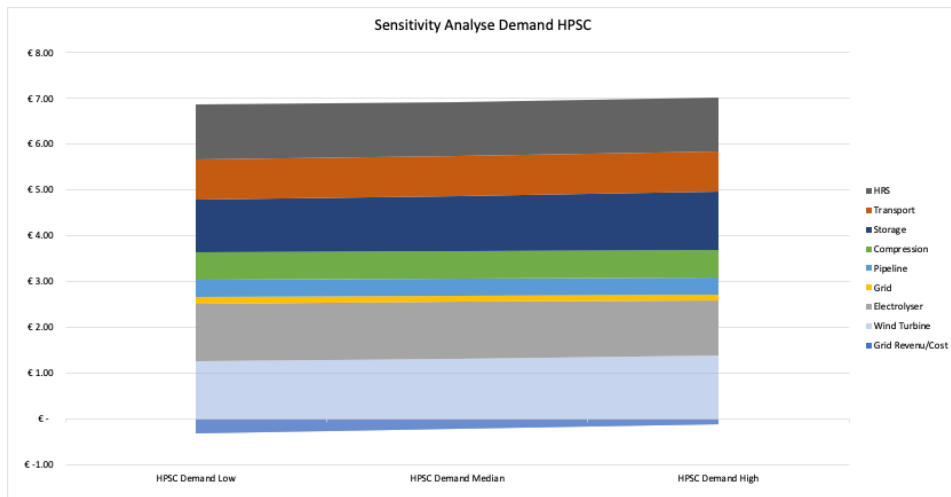


Figure 5.23: Sensitivity analysis demand Low, Median, High HPSC storage, 250,000 kg average annual demand

and the total revenue of power sold decreases for both storage technology-oriented value chains.

6

Discussion

This thesis research aimed to develop a model to give insight into the Levelised Cost Of Hydrogen (LCOH) from Well-To-Tank (WTT) in the wind dominated hydrogen value chain, supplying gaseous hydrogen to refuelling stations for the mobility sector. The main research question to answer in this research was: "What impact does the choice of non-stationary storage unit have on the levelised cost of hydrogen in the wind dominated hydrogen value chain?" The results show that the choice in non-stationary storage technology mainly influences two LCOH cost components. Firstly, the cost of storage. Secondly, the cost of distribution. It can be concluded that the MILP optimisation model provides the desired insight into the total LCOH and determine the most suitable storage technology. However, limitations on the results generated by the model based on the inputs should be taken into account while interpreting the outcome. This discussion reflects on the relative impact of both considered container technologies on the hydrogen production process, hydrogen storage sizing and distribution routing. The overall limitations of the adopted optimisation model are discussed at the end of this chapter.

6.1. Hydrogen Production

An important finding is the relatively small impact of non-stationary storage container type on the hydrogen production decision-making process. Figure 6.1 shows that for a similar value chain configuration, the same trend in hydrogen production quantity is observed for both non-stationary storage technologies.

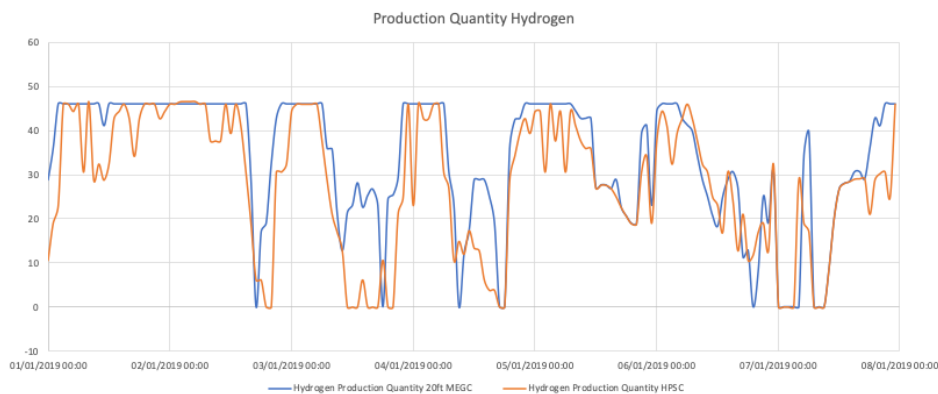


Figure 6.1: Hydrogen production quantity for both non-stationary containers types considering the same scenario

The decision-making process for hydrogen production is mainly dependent on four parameters which are not influenced by the type of storage container. The combination of the wind turbine production capacity, electrolyser power capacity, grid connection power capacity and cost of electricity defines the overall production and quantity and moment.

The sizing of the grid connection has an essential role in storage sizing. This research assumed that electricity bought from the grid is green and, therefore, the hydrogen produced will be green. An optimal ratio of 70/30 was found between directly utilised wind energy and grid energy to produce hydrogen. Future regulations could impose that it is not allowed to use grid energy to produce hydrogen, as it is difficult to prove the origin and determine if the grid electricity is produced green. This will increase storage requirement to overcome periods with less wind and, therefore, negatively impact the LCOH.

Secondly, the same setup is used for all scenarios, a single wind turbine of 4MW, grid connection of 2.5MW and an electrolyser of 2.5MW. Different sizing of these components will lead to different decision making in the production process. Due to the complexity of the decision-making process, it is hard to predict the overall change in LCOH when considering different production location setups.

Thirdly, the cost of grid electricity plays a significant role in the decision-making process. The results show that the production of hydrogen and the price of grid electricity have a strong negative correlation. The sensitivity analysis shows that with an increased electricity price and increased price fluctuations, a decrease in LCOH is observed. This concludes that the value chain is resilient against an increased implementation of renewable energy sources in the energy grid. A decreased LCOH results from selling higher valued wind energy and buying back lower-cost electricity from the grid to produce hydrogen, hence the average 70/30 ratio between directly consumed wind energy and energy consumption of grid power.

The scenario analysis considers the price fluctuations based on the year 2019. What is observed is that the correlation factor between wind energy production and the electricity price is only 0.12. However, this correlation is expected to increase significantly for future energy systems containing mainly renewable energy sources. More renewable energy generation capacity than fossil fuel-based energy generation capacity will result in low energy prices during windy periods and high electricity prices when there is less wind. Taking advantage of the electricity price differences will reduce significantly or not be present at all. More research must be conducted towards the impact of increased renewable energy generation capacity and the impact on the LCOH.

6.2. Hydrogen Storage

Two different trends are observed between the sizing of the considered non-stationary storage units. The first trend is the storage sizing being dominated by the required storage distribution flexibility. This trend is mainly shown for 20ft MEGC storage units in the small scale hydrogen value chain configurations. The second trend observed is the storage sizing based on a trade-off. There is a trade-off between the required non-stationary storage units and the hydrogen distribution cost. Due to the high CAPEX of the small HPSC units, it is more cost-effective to drive around more often with half-full truck loads than investing in more storage capacity and reducing the overall distribution cost. A rule of thumb can be formulated for minimum storage requirement for all container types: '2-3 storage units are required per refuelling station to provide enough distribution flexibility'.

The required distribution flexibility results in a hydrogen storage over-capacity. Despite the over-capacity, investing and using the 20ft MEGC storage containers will result in a lower LCOH. This is a result of the significant cost difference between the container technologies.

For an increased refuelling station demand, the value chain storage capacity for the 20ft MEGC will no longer be based on required system flexibility. Storage over-capacity is no longer present, and all available storage capacity is utilised efficiently. The current market price difference between the two container types will lead to an increased difference in the LCOH between both storage technologies when considering more significant total system demand.

The results in this research are all based on the assumptions of the current market pricing of both considered non-stationary storage technologies. The future price difference between both storage containers is expected to decrease dramatically. As shown in the scenario analyse, a reduced CAPEX

price difference of up to $200 \frac{\text{€}}{\text{kg}}$ shows a shift in the lowest obtained LCOH between the HPSC and 20ft MEGC for small-sized hydrogen value chains. Further analysis between the future cost development of the two storage technologies is required to optimally define the tipping point between the choice of correct storage container size.

Further research towards the tipping point between the optimal choice of container type for each value chain configuration is dependent on two factors. The first factor is the considered target market. This research only focused on 2 to 4 hydrogen refuelling stations, per installed wind turbine, with demand between 175 and $350 \frac{\text{kg}}{\text{day}}$. It is expected that for hydrogen refuelling stations, demand will grow beyond $350 \frac{\text{kg}}{\text{day}}$. A daily demand of 350 kg equates to refuelling roughly 10-15 FCETs.

For other target markets such as supplying hydrogen to power fuel-cell generators, it is expected that investing in the 20ft MEGC container compared to the smaller HPSC unit is not a suitable approach. This research, however, does not include the results to determine the impact on the LCOH for both non-stationary storage technologies when, for example, ten demand locations in combination with a single wind turbine location is taken into account. This will equate to an average maximum daily demand of 35 kg per demand location. It is expected that the HPSC unit will outperform the 20ft MEGC, even with current market price differences.

The second focus point is the cost difference between the considered non-stationary storage containers. Currently, the market price for each non-stationary storage technology dictates a 2x cost difference per kg_{H_2} stored, in favour of the 20ft MEGC container. Future cost development could shift the choice between optimal container technology based on the lowest LCOH.

6.3. Hydrogen Distribution

From the results, it is shown that two parameters dictate the cost of distribution. The first parameter is the number of distribution trips which result in the total distribution cost regarding moving hydrogen from location to location. The second parameter is the total handling time of each non-stationary storage unit.

In this research, the handling time of each container is assumed by a simplified equation. The handling time for each container is determined by a constant handling time per delivered container. The considered handling time per container includes the handling time of the distribution truck arriving and leaving at a refuelling station site. This simplification of the handling time results in an overestimation of the handling time required for the HPSC storage unit if more than one HPSC unit is delivered and, therefore, negatively influence the LCOH.

As discussed in the previous section, the storage sizing for the small container is heavily dependent on the trade-off between the total cost of distribution and the investment cost per container. While the total distribution cost decreases for both container types, the difference between distribution costs converges for both non-stationary storage units with increased system size and demand.

The convergence of the overall distribution cost for the HPSC units results from a higher distribution efficiency resulting from the requirement of fewer distribution trips as more refuelling stations can be supplied during a single trip. Increased distribution efficiency is expected for the smaller HPSC storage units for large hydrogen value chain network configurations. It could outweigh the marginal future expected CAPEX cost difference between both storage technologies and the increased handling time cost for the HPSC unit. Designing and developing the hydrogen value chain and determining the optimal container type depends on the expected final size of the distribution system. If the system size increases sufficiently and the demand of the value chain remains relatively low at each refuelling station, the HPSC unit could outperform the 20ft MEGC unit.

A more detailed study on larger hydrogen value chain systems must be conducted to determine the tipping point at which the increased distribution efficiency will outweigh the storage CAPEX difference

and added cost of handling time for the HPSC units.

6.4. Model Limitations

The first point for discussion is the time step chosen for the optimisation model. The time step of the model influences the complexity of the optimisation problem and consequently determines the maximum length of the considered planning horizon. The differentiation in time step results in the ability to conclude the decision making process of hydrogen production and distribution of the hydrogen to the refuelling stations on a strategic decision level or an operational decision level. Developing a model on the operational level resulted in a large and complex optimisation problem due to the large solution space created by the extended planning horizon of a single year based on an hourly time interval. Multiple computational methods have been considered during this research to increase the optimisation model's performance and reduce the overall required run time. Solving a single year time horizon at once on a high performance computing cluster could not return a result within a reasonable period due to the NP-hard nature of a MILP problem which results in an exponential increase in problem complexity for an increased planning horizon. The decision was made to reduce the optimisation problem complexity by reducing the considered planning horizon for a single optimisation problem and providing an arbitrary function that defines continuity throughout the entire planning horizon of a single year.

A single week was determined to be the optimal planning horizon to ensure higher usability of the optimisation model. This resulted in an average run time for the 20ft MEGC container scenarios of 2 hours and 12-24 hours for the scenarios considering the HPSC units. The increased run time for the HPSC units results from a more extensive solution space created by the increased choice for the number of units distributed per distribution vehicle for each time step. It can be argued if the approach adopting a MILP optimisation model is the most suitable method taking into account a very short timestep with a long planning horizon. The applied arbitrary rule to ensure continuity is expected to impact the overall results of the weekly optimisation and should therefore be carefully determined when using the current model for strategic decision making regarding system sizing and the overall results on LCOH.

The second point for discussion is the distribution strategy adopted for both container technologies. As discussed, only direct distribution from the hub refuelling station towards the satellite refuelling station is considered for the MEGC 20ft container. For the HPSC units, distribution between satellite stations is possible. The developed optimisation model is based on the travelling salesman problem, implying that the distribution vehicle starts and ends at the same hub location. The results show that the hydrogen is distributed more efficiently with the HPSC than the 20ft MEGC for large value chain configurations regarding the available refuelling stations locations. Considering a more complex distribution strategy for both storage container technologies, allowing different start endpoints and taking into account the location of each vehicle at every time step could change the dynamic of the distribution network decision-making process and overall cost regarding hydrogen distribution. Taking empty and full hydrogen containers simultaneously would lead to a more accurate result. However, simultaneously considering empty and full containers in a MILP introduces more complexity and will harm the overall model run time. This would lead to an even shorter planning horizon with more influence on the arbitrary continuity equations for the inventory at each location.

Dividing the planning horizon of a single year into multiple consecutive optimisation problems and ensuring continuity between each optimisation process removes the ability to consider weekly, monthly and seasonal effects on the system sizing components and hydrogen production process. Therefore, it is expected that optimisation based on a two-weekly interval or a monthly basis would yield a different result than the weekly optimisation model proposed in this research.

6.5. Uncertainty

Three uncertainty categories in the value chain can be identified. Supply uncertainty regarding the production process of hydrogen, uncertainty concerning the reliability of the value chain components

and demand uncertainty of the total hydrogen demand at each refuelling station. In the current optimisation model, uncertainty is only included in the stochastic demand model and is based on the current refuelling characteristics of diesel-fuelled trucks and tractors. The stochastic demand model results in a realistic hydrogen demand profile at each refuelling station for every scenario independently. To base demand uncertainty on the refuelling characteristics of diesel-fuelled vehicles could lead to different results as future hydrogen demand patterns are expected to change due to the hydrogen refilling process characterisations as increased cooling capacity requirements for fast back to back refilling of hydrogen vehicles has negative impact on the LCOH.

Leaving out the supply uncertainty regarding the reliability of system components results in an underestimation of required storage units as it is assumed that no safety stock is required to overcome periods with no hydrogen production. Incorporating supply uncertainty would lead to a more robust sizing of the required storage units in the hydrogen value chain and could implement a certain safety stock level at each production or refuelling station location. The distribution in the optimisation model is based on on-time delivery as the total storage size in the value chain for each time step is minimised. This results in no safety stock required or assumed at each hub or satellite refuelling station in this research regarding demand uncertainty. This leads to underestimating the required storage units in the entire value chain and should be considered when reviewing the results. Incorporating more uncertainties at different echelons of the value chain in the optimisation model will lead to an improved outcome.

6.6. Multi-Objective Optimisation

The results of the current model and considered scenarios show that despite the wind turbine's available annual energy production capacity exceeding the annual energy requirement for the production of hydrogen, not all hydrogen is produced by the power from the wind turbine directly. This is a result of the inability to oversee weekly and seasonal effects by the weekly optimisation process and the single objective optimisation process based on the lowest cost. The model is focused on optimising the total cost regarding the hydrogen value chain and results in the optimal interaction with the electricity grid by selling high valued wind energy and buying lower-valued energy from the grid. The example of the exposed trade-off between the investment in the amount of HPSC units compared to the higher distribution cost of driving around more often with half-full truckloads, thereby increasing the total distribution cost, reflects on the impact of considering only cost optimisation as the model objective.

Incorporating several optimisation objectives in the model will result in a different decision-making process regarding the entire value chain. The weight of several optimisation objectives will result in better strategic decision making on system sizing and overall cost expectation on the LCOH. Two proposed objectives for the model could be incorporating an environmental objective or a system reliability objective. The Environmental objective could result in the more direct use of wind turbine energy for hydrogen production, maximising the amount of green hydrogen production. Incorporating an optimisation objective to maximise reliability or minimise downtime per value chain component will result in more required storage units. Varying the input parameters such as the number of distribution vehicles would also impact the multi-objective optimisation results.

The optimisation model will result in a non-trivial optimisation problem, where not all objectives can be optimised simultaneously. The objective functions will be conflicting and result in a distribution described as a Pareto front. The Pareto will represent trade-offs between different optimisation objectives. For example, taking into account a multi-objective optimisation with two objectives regarding the total cost assumed in this research and the total system reliability. It would describe how much the desired hydrogen value chain reliability would impact the overall LCOH of the hydrogen supplied to the refuelling stations.

7

Conclusion

The entire hydrogen value chain from well-to-tank was considered to give insight into the Levelised Cost of Hydrogen (LCOH) for the mobility market. Firstly a theoretical study on the available system components and corresponding costs was conducted. The optimal choice of technology for each echelon of the value chain resulted in a general design of a wind dominated hydrogen value chain. To analyse and draw conclusions on the optimal configuration and sizing strategy based on the proposed value chain design, a single objective MILP cost optimisation model was created and resulted in the following conclusions based on the results shown in chapter 5.

Table D.1 displays the results obtained from the optimisation model for each value chain component expressed in total annual cost in euros and contribution towards the LCOH expressed in $\frac{\text{€}}{\text{kg}}$. The following can be concluded on the contribution towards the total LCOH per value chain component. (1) The total annual cost for the production of hydrogen contribute 45-65% of the total LCOH. Taking into account the interaction with the grid connection by optimally selling and buying energy, the total cost contribution of the production of hydrogen results in 40% towards the total LCOH for all scenarios. (2) The hydrogen pipeline between the production location and hub refuelling station contributes 2% towards the total LCOH for all scenarios. (3) 5-7% of the LCOH is a result of the requirement to compress hydrogen to 640 bar. (4) Storage cost varies between 13-20% of the total LCOH and is heavily dependent on the storage technology and considered scenario. (5) For both container technologies, the total cost of transport regarding the handling time and distribution costs lead to a contribution of % of the LCOH. (6) Finally, the refuelling stations have a contribution of 15-17% to the total LCOH.

Overall, it can be concluded that the LCOH for single turbine production locations with a single hub and single satellite refuelling station value chain topology, the LCOH will be less than € 8.50 according to current market prices. Increased value chain size will lead to a lower LCOH due to more efficient hydrogen distribution and the ability to split production between production locations. The maximum impact on the LCOH for adding a single turbine production location is 25%. The impact on the LCOH by adding an extra production location reduces with increased hydrogen value chain size and the number of production locations already present.

For current market prices for all value chain components, diesel price parity is only reached when the hydrogen value chain is used at maximum capacity, when considering single turbine production locations with single hub and single satellite refuelling stations, at 250.000 kg of hydrogen production per wind turbine and electrolyser pair. Potential cost reduction of multiple hydrogen value chain components such as electrolyser stacks, storage containers and cost of hydrogen refuelling stations will result in reaching parity with diesel for small hydrogen value chain configurations with single turbine production locations.

Hydrogen Production Process

The decision-making process of hydrogen production based on cost optimisation is negligibly im-

pacted by the spatial configuration of the hydrogen value chain amount of refuelling stations considered or considered storage technology. It can be concluded that the hydrogen production process is mainly dependent on four parameters. (1) The total demand within a specified time frame. (2) Price fluctuations of the electricity market. (3) The energy production capacity of the wind turbine at each time step. (4) The considered grid connection capacity for the maximum power sold or bought to and from the grid, respectively.

Reducing the grid connection capacity increases the LCOH as less revenue is obtained when a low annual demand is considered in reference to the available energy and hydrogen production capacity. Reducing the grid connection capacity regarding power drawn from the grid will lead to the investment of more storage units and an overall higher LCOH. It is therefore crucial to size the correct grid connection capacity in combination with the turbine power capacity and the electrolyser capacity. The cost-optimal hydrogen production process is to not use all wind energy directly for the production of hydrogen but sell high valued wind energy and buy back low-cost electricity from the grid at other time steps. The optimal ratio between wind energy directly used for hydrogen production and grid energy for hydrogen production varies between 80/20 and 70/30 in relation to increased demand in reference to the wind energy production capacity.

Hydrogen Storage & Distribution

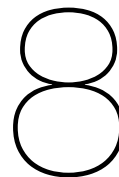
For all scenarios, the storage and distribution of hydrogen via the 20ft MEGC container result in a lower LCOH. It can be concluded that the storage capacity sizing regarding the 20ft MEGC units is based on the required flexibility in the hydrogen value chain in early market adoption. The sizing of the HPSC units is based on a trade-off between the total investment cost and the distribution cost of all hydrogen containers. The trade-off is heavily influenced by three parameters. (1) The total distribution cost regarding the distance between the value chain locations. (2) the handling time cost of a single HPSC unit. (3) The CAPEX of an HPSC unit.

From the scenario analysis, it can be concluded that reducing the cost difference between the 20ft MEGC and the HPSC based on future expectations will reduce the LCOH difference between both container technologies. However, with increased value chain size and refuelling station demand, less handling time and the available distribution flexibility outweighs the HPSC container distribution efficiency.

The LCOH is mainly CAPEX driven. The increased price fluctuations and the average cost of grid energy will have a positive effect on the LCOH of the hydrogen value chain. The revenue obtained from selling high valued wind energy and producing hydrogen from low-cost grid electricity is increased with larger price fluctuations. In combination with the increased revenue obtained from excess produced wind energy, the LCOH reduces.

From the sensitivity analysis, it can be concluded that the change in WACC has a larger impact on the LCOH for the 20ft MEGC than the HPSC units. The optimisation model takes into account the higher overall cost regarding the upfront investment, which influences the total trips by the distribution vehicles and the total required HPSC storage units.

To answer the main research question, it can be concluded that the 20ft MEGC container will have a cost advantage based on the LCOH in the start-up phase of a wind-based hydrogen value chain. Also, with increased value chain size and increased demand per refuelling station location, the value chain using the 20ft MEGC will outweigh the distribution advantage of the HPSC container significantly and result in a lower overall LCOH. Therefore the 20ft MEGC is a better option to be implemented in the hydrogen refuelling station network for the future mobility market than the HPSC units. The HPSC units are applicable to a hydrogen refuelling network considering many locations that will change dynamically across time, with each very low hydrogen demand per specified time period. If the cost difference between both container technologies decreases significantly and extra required handling time for the HPSC unit reduces, it should be reconsidered as viable option as it could outperform the 20ft MEGC for large value chain configurations by increased distribution efficiency.



Recommendations

In this research, the choice of integrated storage technology for a wind dominated hydrogen value chain based on current market pricing has been compared. The single objective cost MILP optimisation model has given exploratory insights into applying both storage technologies based on the LCOH of the well-to-tank hydrogen value chain. The research has clearly shown what container type should be used for the mobility market refuelling infrastructure. The model, however, includes many assumptions. The model adopted could be extended, or a different modelling approach could be considered for future research. The following areas for future research can be considered:

- **Model Extension:** The single objective MILP cost optimisation model has shown that the 20ft MEGC storage unit is the most suitable option for refuelling the hydrogen mobility market. Future research could adopt and extend the current optimisation model by only considering the MEGC 20ft container and increasing the complexity of the distribution model by considering empty and full containers simultaneously. This results in the ability to consider separate pickup and drop-off locations optimising the distribution of the 20ft MEGC container compared to only direct delivery. A separate model extension could be multi-objective optimisation reducing the interaction with grid connection at each production location and increasing direct wind energy consumption for hydrogen production.
- **Energy market modelling:** The current model adopts the day-ahead market electricity price to calculate the revenue/cost of grid energy. More extensive market modelling considering different energy markets could lead to a different production decision-making process, and the impact on the LCOH of hydrogen for operating on different energy markets could be evaluated. The additional markets could be actively traded on the imbalance market and the reservation of excess electrolyser power capacity or scaling up/scaling down turbine power capacity on the balancing markets, including Frequency Containment Reserve (FCR), automatic Frequency Restoration Reserve (aFRR) and the manual Frequency Restoration Reserve (mFRR) markets.
- **Modelling Approach:** The current single objective optimisation model is based on the optimisation on historical data. Therefore, the model optimises the value chain based on the basis that everything is known in advance. This modelling approach could lead to the underestimation of the LCOH. A more realistic and robust modelling approach would be based on forecasting models. Models such as Auto-Regressive Integrated Moving Average (ARIMA) or Machine Learning (ML) models would base the decision making process for the entire hydrogen value chain on the available data at each time step. Thereby incorporating many uncertainty parameters could lead to an overall higher LCOH.
- **Target market:** This Exploratory research on the optimal container choice for the hydrogen refuelling market for the mobility sector resulted in the 20ft MEGC. Other research explore several new target markets. A target market for future research could be the expected LCOH for a value chain considering many temporary dynamically changing locations with low hydrogen demand, such as events and building sites, including a fuel cell generator where the HPSC container could pose a viable solution.

Bibliography

- Abdelrasoul, A. (2020). *Advances in Membrane Technologies*.
- ACEA (2021). Vehicles in use, Europe - January 2021. Tech. Rep. 01.
URL <https://www.acea.auto/files/report-vehicles-in-use-europe-january-2021-1.pdf>
- Ackermann, T. (2012). *Wind Power in Power Systems, Second Edition*. John Wiley and Sons.
- Ahmad, A., & Azam, T. (2019). Water Purification Technologies. *Bottled and Packaged Water*, (pp. 83–120). doi: 10.1016/B978-0-12-815272-0.00004-0.
- Aka, B. A., Godwin, N., Jacob, C., & O, E. E. (2017). Estimating Pressure Drop in Natural Gas Pipeline : (A Case Study of Rumuji – Bonny NLNG Pipeline). *International Journal of Scientific & Engineering Research*, 8(1), 1–9.
- Aldén, L., & Barney, A. (2015). Decommissioning of Wind Farms-Ensuring Low Environmental Impact.
URL <http://www.ewea.org/events/workshops/wp-content/uploads/Tech16a-Session-5-01-Alden-Uppsala-University.pdf>
- Almansoori, A., & Shah, N. (2006). Design and operation of a future hydrogen supply chain: Snapshot model. *Chemical Engineering Research and Design*, 84(6 A), 423–438. doi: 10.1205/cherd.05193.
- Alsubal, S., Alaloul, W. S., Shawn, E. L., Liew, M. S., Palaniappan, P., & Musarat, M. A. (2021). Life Cycle Cost Assessment of Offshore Wind Farm: Kudat Malaysia Case. *Sustainability*, 13(14), 7943. doi: 10.3390/su13147943.
- Apata, O., & Oyedokun, D. T. (2020). An overview of control techniques for wind turbine systems. *Scientific African*, 10, e00566. doi: 10.1016/J.SCIAF.2020.E00566.
- Arar, Ö., Yüksel, Ü., Kabay, N., & Yüksel, M. (2014). Various applications of electrodeionization (EDI) method for water treatment—A short review. *Desalination*, 342, 16–22. doi: 10.1016/J.DESAL.2014.01.028.
- ASTM (2021). ASTM International - Standards Worldwide.
URL <https://www.astm.org/>
- Badgett, A., Ruth, M., James, B., & Pivovar, B. (2021). Methods identifying cost reduction potential for water electrolysis systems. *Current Opinion in Chemical Engineering*, 33, 100714. doi: 10.1016/J.COCH.2021.100714.
- Bareiß, K., De La Rua, C., Möckl, M., & Hamacher, T. (2019). Life cycle assessment of hydrogen from proton exchange membrane water electrolysis in future energy systems. doi: 10.1016/j.apenergy.2019.01.001.
- Barthélémy, H. (2012). Hydrogen storage - Industrial perspectives. *International Journal of Hydrogen Energy*, 37(22), 17364–17372. doi: 10.1016/j.ijhydene.2012.04.121.
- Barthelemy, H., Weber, M., & Barbier, F. (2017). Hydrogen storage: Recent improvements and industrial perspectives. *International Journal of Hydrogen Energy*, 42(11), 7254–7262. doi: 10.1016/j.ijhydene.2016.03.178.
- Barthelmie, R. J., Shepherd, T. J., Aird, J. A., & Pryor, S. C. (2020). Power and Wind Shear Implications of Large Wind Turbine Scenarios in the US Central Plains. *Energies*, 13(6), 1–21. doi: 10.3390/en13164269.

- Barton, M., Soriano, L., Stahley, J., Talakar, A., & Energy, S. (2020). Under Pressure: The Challenges of Hydrogen Compression. (August 2021).
 URL <https://assets.siemens-energy.com/siemens/assets/api/uuid:d985fced-fb7e-4881-a1b9-87cd6d7eac63/se-he-august2021-challenges-hydrogencompression.pdf>
- Bauer, A., Mayer, T., Semmel, M., Guerrero Morales, M. A., & Wind, J. (2019). Energetic evaluation of hydrogen refueling stations with liquid or gaseous stored hydrogen. *International Journal of Hydrogen Energy*, 44(13), 6795–6812. doi: 10.1016/J.IJHYDENE.2019.01.087.
- Berro Ramirez, J. P., Halm, D., Grandier, J. C., Villalonga, S., & Nony, F. (2015). 700 bar type IV high pressure hydrogen storage vessel burst – Simulation and experimental validation. *International Journal of Hydrogen Energy*, 40(38), 13183–13192. doi: 10.1016/J.IJHYDENE.2015.05.126.
- Bertazzi, L., Coelho, L. C., De Maio, A., & Laganà, D. (2019). A matheuristic algorithm for the multi-depot inventory routing problem. *Transportation Research Part E: Logistics and Transportation Review*, 122, 524–544. doi: 10.1016/J.TRE.2019.01.005.
- Bessarabov, D., & Millet, P. (2018). *PEM water electrolysis*, vol. 1. Academic Press.
- Blanco, M. I. (2009). The economics of wind energy. *Renewable and Sustainable Energy Reviews* 13 2009, Vol. 13, Page 1372-1382. doi: 10.1016/j.rser.2008.09.004.
- Bloch, H. P. (2006). *A practical guide to compressor technology*. John Wiley & Sons.
- Bossel, B., Ulf Eliasson (2004). *The Hydrogen Economy*. National Academies Press.
- Boxma, O. J., & Yechiali, U. (2007). *Poisson processes, ordinary and compound*. Citeseer.
- Burckhardt Compression (2021). Compressor solutions for oil-free high-pressure piston compressors.
 URL <https://www.burckhardtcompression.com/solution/industrial-gases/h2-power-to-x-mobility/h2-trailer-filling/>
- CBS (2021). Pompprijzen motorbrandstoffen; locatie tankstation, brandstofsoort.
 URL <https://www.cbs.nl/nl-nl/cijfers/detail/81567NED>
- Cernat, A., Pana, C., Negurescu, N., Gheorghe, L., Nutu, C., & Fuiurescu, D. (2020). Hydrogen—an alternative fuel for automotive diesel engines used in transportation. *Sustainability*, 12, 9321. doi: 10.3390/su12229321.
- Cheng, X., Shi, Z., Glass, N., Zhang, L., Zhang, J., Song, D., Liu, Z. S., Wang, H., & Shen, J. (2007). A review of PEM hydrogen fuel cell contamination: Impacts, mechanisms, and mitigation. *Journal of Power Sources*, 165(2), 739–756. doi: 10.1016/J.JPOWSOUR.2006.12.012.
- Chisholm, G., & Cronin, L. (2016). Hydrogen From Water Electrolysis. *Storing Energy: With Special Reference to Renewable Energy Sources*, (pp. 315–343). doi: 10.1016/B978-0-12-803440-8.00016-6.
- Colmenar-Santos, A., Campiñez-Romero, S., Enriquez-Garcia, L., & Pérez-Molina, C. (2014). Simplified analysis of the electric power losses for on-shore wind farms considering weibull distribution parameters. *Energies*, 7, 6856–6885. doi: 10.3390/en7116856.
- Contreras Montoya, L. T., Hayyani, M. Y., Issa, M., Ilinca, A., Ibrahim, H., & Rezkallah, M. (2021). Wind power plant planning and modeling. *Hybrid Renewable Energy Systems and Microgrids*, (pp. 259–312). doi: 10.1016/B978-0-12-821724-5.00012-X.
- Coutanceau, C., Baranton, S., & Audichon, T. (2018). Hydrogen Production From Water Electrolysis. *Hydrogen Electrochemical Production*, (pp. 17–62). doi: 10.1016/B978-0-12-811250-2.00003-0.
- Cunanan, C., Tran, M.-K., Lee, Y., Kwok, S., Leung, V., & Fowler, M. (2021). A Review of Heavy-Duty Vehicle Powertrain Technologies: Diesel Engine Vehicles, Battery Electric Vehicles, and Hydrogen Fuel Cell Electric Vehicles. *Clean Technologies*, 3(2), 474–489. doi: 10.3390/cleantechnol3020028.

Dao, C., Kazemtabrizi, B., & Crabtree, C. (2019). Wind turbine reliability data review and impacts on levelised cost of energy. *Wind Energy*, 22(12), 1848–1871. doi: 10.1002/we.2404.

Dasilveira, R. (2002). Advanced technologies for reciprocating compressors with respect to performance and reliability. *Mycological Research*, 106(11), 1323–1330.

De, L., & Di Summa, G. M. (2018). Methods and Models for Combinatorial Optimization Exact methods for the Traveling Salesman Problem.

Delgado, O., Miller, J., Sharpe, B., & Muncrief, R. (2016). Estimating the fuel efficiency technology potential of heavy-duty trucks in major markets around the world. *Working Paper*, (14).

DeliverHy (2013). Final Report Summary - DELIVERHY (Optimisation of Transport Solutions for Compressed Hydrogen) | FP7 | CORDIS | European Commission.
URL <https://cordis.europa.eu/project/id/278796/reporting>

Deloitte Monitor (2021). Fueling the future of mobility: hydrogen electrolyzers. (January).

Diaz-Dorado, E., Carrillo, C., Cidras, J., & Albo, E. (2007). Estimation of energy losses in a wind park. (pp. 1–6). doi: 10.1109/EPQU.2007.4424125.

Du, Z., Liu, C., Zhai, J., Guo, X., Xiong, Y., Su, W., & He, G. (2021). A review of hydrogen purification technologies for fuel cell vehicles. *Catalysts*, 11(3), 1–19. doi: 10.3390/catal11030393.

EEA (2017). Greenhouse gas emissions from transport in Europe — European Environment Agency.
URL <https://www.eea.europa.eu/data-and-maps/indicators/transport-emissions-of-greenhouse-gases/transport-emissions-of-greenhouse-gases-12>

EEA (2020). New registrations of electric vehicles in Europe.
URL <https://www.eea.europa.eu/data-and-maps/indicators/proportion-of-vehicle-fleet-meeting-5/assessment>

ELGA (????).

Emile, M. S., Ojong, T., Georg, I., Gutachter, M., Hans, I., Krautz, J., Heinz, I., & Berg, P. (2018). Characterization of the Performance of PEM Water Electrolysis Cells operating with and without Flow Channels, based on Experimentally Validated Semi-empirical Coupled-Physics Models 1976 in Kumba-Kamerun. (pp. 1–174).
URL https://publica.fraunhofer.de/eprints/urn_nbn_de_kobv_col-opus4-46504.pdf

EnergieLeveranciers (2021). Overzicht Netbeheerders stroom en gas in Nederland.
URL <https://www.energieleveranciers.nl/netbeheerders/overzicht-netbeheerders/>

ENTSOE (2021). ENTSO-E Transparency Platform.
URL <https://transparency.entsoe.eu/dashboard/show>

ENTSOE, GIE, & Hydrogen Europe (2021). How To Transport and Store Hydrogen – Facts and Figures. (p. 16).
URL https://www.gie.eu/wp-content/uploads/filr/3429/entsog_{ }gie_{ }he_{ }QandA_{ }hydrogen_{ }transport_{ }and_{ }storage_{ }210521.pdf

EPEX SPOT (2021). Basics of the Power Market | EPEX SPOT.
URL <https://www.epexspot.com/en/basicspowermarket#day-ahead-and-intraday-the-backbone-of>

EU (2021). Vehicle categories | Interne Markt, Industrie, Ondernemerschap en Midden- en Kleinbedrijf.
URL https://ec.europa.eu/growth/sectors/automotive/vehicle-categories_nl

- EU Commission (2018). A Clean Planet for all A European strategic long-term vision for a prosperous, modern, competitive and climate neutral economy. Tech. rep.
URL https://climatecooperation.cn/wp-content/uploads/2019/06/com_2018_733_analysis_in_support_en_0.pdf
- EVOFENEDEX (2021). Dieselprijzen Nederland - overzicht van dieselprijzen per week of jaar.
URL <https://www.evofenedex.nl/kennis/vervoer/dieselprijs>
- Fallah, S. (2014). *Electric and Hybrid Vehicles - Technologies, Modeling and Control: A Mechatronic Approach*.
- Garcia-Sanz, M., & Houppis, C. H. (2012). *Wind energy systems: control engineering design*. CRC press.
- Ghiassi-Farrokhfal, Y., Ketter, W., & Collins, J. (2021). Making green power purchase agreements more predictable and reliable for companies. *Decision Support Systems*, 144, 113514. doi: 10.1016/J.DSS.2021.113514.
- Glenk, G., & Reichelstein, S. (2019). Economics of converting renewable power to hydrogen. *Nature Energy*, 4(3), 216–222. doi: 10.1038/s41560-019-0326-1.
- Gondal, I. (2016). Hydrogen transportation by pipelines. *Compendium of Hydrogen Energy*, (pp. 301–322). doi: 10.1016/B978-1-78242-362-1.00012-2.
- Gunn, K., Stock-Williams, C., Burke, M., Willden, R., Vogel, C., Hunter, W., Stallard, T., Robinson, N., & Schmidt, S. R. (2016). Limitations to the validity of single wake superposition in wind farm yield assessment. *Journal of Physics: Conference Series*, 749(1). doi: 10.1088/1742-6596/749/1/012003.
- Gurobi (2021). Mixed-Integer Programming (MIP) – A Primer on the Basics.
URL <https://www.gurobi.com/resource/mip-basics/>
- H2DualPower (2021). H2 Dual Power | De allereerste waterstofftrekker ter wereld.
URL <https://h2dualpower.com/nl>
- Handwerker, M., Wellnitz, J., & Marzbani, H. (2021). Comparison of Hydrogen Powertrains with the Battery Powered Electric Vehicle and Investigation of Small-Scale Local Hydrogen Production Using Renewable Energy. *Hydrogen*, 2(1), 76–100. doi: 10.3390/hydrogen2010005.
- He, G., Mallapragada, D. S., Bose, A., Heuberger, C. F., & Gencer, E. (2021). Hydrogen Supply Chain Planning with Flexible Transmission and Storage Scheduling. *IEEE Transactions on Sustainable Energy*. doi: 10.1109/TSTE.2021.3064015.
- Hjelkrem, O. A., Arnesen, P., Aarseth Bø, T., & Sondell, R. S. (2020). Estimation of tank-to-wheel efficiency functions based on type approval data. *Applied Energy*, 276, 115463. doi: 10.1016/J.APENERGY.2020.115463.
- Hochgraf, C. (2009). APPLICATIONS – TRANSPORTATION | Electric Vehicles: Fuel Cells. *Encyclopedia of Electrochemical Power Sources*, (pp. 236–248). doi: 10.1016/B978-044452745-5.00863-7.
- Howden (2021). Compressors | Products and Services | Howden.
URL <https://www.howden.com/en-gb/products/compressors>
- Hu, Y., Xu, X., & Wang, W. (2017). A new cavity profile for a diaphragm compressor used in hydrogen fueling stations. *International Journal of Hydrogen Energy*, 42(38), 24458–24469. doi: 10.1016/J.IJHYDENE.2017.08.058.
- Humpage, S. (2000). An introduction to regression analysis. *Sensors (Peterborough, NH)*, 17(9), 68–74. doi: 10.1002/9781118267912.ch6.
- Hurskainen, M., & Ihonen, J. (2020). Techno-economic feasibility of road transport of hydrogen using liquid organic hydrogen carriers. *International Journal of Hydrogen Energy*, 45(56), 32098–32112. doi: 10.1016/j.ijhydene.2020.08.186.

- Hydrogen Council (2020). Path to hydrogen competitiveness: a cost perspective. (January), 88.
URL https://hydrogencouncil.com/wp-content/uploads/2020/01/Path-to-Hydrogen-Competitiveness_Full-Study-1.pdf
- Hydrogen Europe (2020). Strategic Research and Innovation Agenda Final Draft. (October), 157.
URL https://www.eosc.eu/sites/default/files/EOSC-SRIA-V1.0_15Feb2021.pdf
- HYGRO (2021). Hydrogen as primary energy carrier | HYGRO.
URL <https://hy-gro.net/nl>
- HyLAW (2019). Horizontal Position Paper Transport and Distribution of Compressed Hydrogen by Road Quantity and Pressure Limitations. (February), 1–5.
- ICCT (2020). Assessment of Hydrogen Production Costs from Electrolysis: United States and Europe. *International Council on Clean Transportation (ICCT)*, (pp. 1–73).
URL https://theicct.org/sites/default/files/publications/final_{_}icct2020_{_}assessment_{_}of_{_}hydrogen_{_}production_{_}costsv2.pdf
- IRENA (2020a). *Green Hydrogen Cost Reduction: Scaling up Electrolysers to Meet the 1.5 C Climate Goal*.
URL [/publications/2020/Dec/Green-hydrogen-cost-reduction{%}0Ahttps://www.irena.org/-/media/Files/IRENA/Agency/Publication/2020/Dec/IRENA_{_}Green_{_}hydrogen_{_}cost_{_}2020.pdf](https://www.irena.org/-/media/Files/IRENA/Agency/Publication/2020/Dec/IRENA_{_}Green_{_}hydrogen_{_}cost_{_}2020.pdf)
- IRENA (2020b). *Green Hydrogen Cost Reduction: Scaling up Electrolysers to Meet the 1.5 C Climate Goal*.
URL [/publications/2020/Dec/Green-hydrogen-cost-reduction{%}0Ahttps://www.irena.org/-/media/Files/IRENA/Agency/Publication/2020/Dec/IRENA_{_}Green_{_}hydrogen_{_}cost_{_}2020.pdf](https://www.irena.org/-/media/Files/IRENA/Agency/Publication/2020/Dec/IRENA_{_}Green_{_}hydrogen_{_}cost_{_}2020.pdf)
- Jelavić, M., Petrović, V., Barišić, M., & Ivanović, I. (2013). Wind turbine control beyond the cut-out wind speed. *European Wind Energy Conference and Exhibition, EWEC 2013*, 1, 343–349.
- Jensen, N. O. (1983). *A note on wind generator interaction*. Citeseer.
- Karagöz, Y., Sandalci, T., Yüksek, L., Dalkılıç, A. S., & Wongwises, S. (2016). Effect of hydrogen-diesel dual-fuel usage on performance, emissions and diesel combustion in diesel engines. *Advances in Mechanical Engineering*, 8(8), 1–13. doi: 10.1177/1687814016664458.
- Karlsdóttir, S. N. (2012). Corrosion, Scaling and Material Selection in Geothermal Power Production. *Comprehensive Renewable Energy*, 7, 241–259. doi: 10.1016/B978-0-08-087872-0.00706-X.
- Karolytė, R. (2017). Hydrogen with CCS for decarbonised heat in the Scottish context. (August), 1–14.
URL https://www.climatechange.org.uk/media/2123/hydrogen_for_decarbonised_heat.pdf
- Kasem Alaboudy, A. H., Daoud, A. A., Desouky, S. S., & Salem, A. A. (2013). Converter controls and flicker study of PMSG-based grid connected wind turbines. *Ain Shams Engineering Journal*, 4(1), 75–91. doi: 10.1016/J.ASEJ.2012.06.002.
- Kato, T., Kubota, M., Kobayashi, N., & Suzuoki, Y. (2005). Effective utilization of by-product oxygen from electrolysis hydrogen production. *Energy*, 30(14), 2580–2595. doi: 10.1016/J.ENERGY.2004.07.004.
- Keçebaş, A., Kayfeci, M., & Bayat, M. (2019). Electrochemical hydrogen generation. *Solar Hydrogen Production: Processes, Systems and Technologies*, (pp. 299–317). doi: 10.1016/B978-0-12-814853-2.00009-6.
- Khan, M. A., Al-Attas, T., Roy, S., Rahman, M. M., Ghaffour, N., Thangadurai, V., Larter, S., Hu, J., Ajayan, P. M., & Kibria, M. G. (2021). Seawater electrolysis for hydrogen production: a solution looking for a problem? *Energy & Environmental Science*, (pp. 5–7). doi: 10.1039/d1ee00870f.

- Khatib, F. N., Wilberforce, T., Ijaodola, O., Ogungbemi, E., El-Hassan, Z., Durrant, A., Thompson, J., & Olabi, A. G. (2019). Material degradation of components in polymer electrolyte membrane (PEM) electrolytic cell and mitigation mechanisms: A review. *Renewable and Sustainable Energy Reviews*, *111*, 1–14. doi: 10.1016/J.RSER.2019.05.007.
- Kollwitz, J. (2016). Defining the Wake Decay Constant As a Function of Turbulence Intensity To Model Wake Losses in Onshore Wind Farms. (p. 59).
URL <http://www.diva-portal.org/smash/get/diva2:1044398/FULLTEXT01.pdf>
- Krokoszinski, H.-J. (2003). Efficiency and effectiveness of wind farms—keys to cost optimized operation and maintenance. *Renewable Energy*, *28*, 2165–2178. doi: 10.1016/S0960-1481(03)00100-9.
- Kurtz, J., Bradley, T., Winkler, E., & Gearhart, C. (2020). Predicting demand for hydrogen station fueling. *International Journal of Hydrogen Energy*, *45*(56), 32298–32310. doi: 10.1016/j.ijhydene.2019.10.014.
- Lahnaoui, A., Wulf, C., Heinrichs, H., & Dalmazzone, D. (2019). Optimizing hydrogen transportation system for mobility via compressed hydrogen trucks. *International Journal of Hydrogen Energy*, *44*(35), 19302–19312. doi: 10.1016/J.IJHYDENE.2018.10.234.
- Lee, H., Jin, Y., & Hong, S. (2016). Recent transitions in ultrapure water (UPW) technology: Rising role of reverse osmosis (RO). *Desalination*, *399*, 185–197. doi: 10.1016/J.DESAL.2016.09.003.
- Lee, H., Lee, B., Byun, M., & Lim, H. (2020). Economic and environmental analysis for PEM water electrolysis based on replacement moment and renewable electricity resources. *Energy Conversion and Management*, *224*(June), 113477. doi: 10.1016/j.enconman.2020.113477.
- Lehner, M., Tichler, R., Steinmüller, H., & Koppe, M. (2014). *Power-to-Gas: Technology and Business Models*. Springer Link.
- Li, X. J., Allen, J. D., Stager, J. A., & Ku, A. Y. (2020). Paths to low-cost hydrogen energy at a scale for transportation applications in the USA and China via liquid-hydrogen distribution networks. *4*(1), 26–47. doi: 10.1093/ce/zkz033.
URL <https://academic-oup-com.tudelft.idm.oclc.org/ce/article/4/1/26/5812776>
- Liander (2021). Tarieven | Grootzakelijk | Liander.
URL <https://www.liander.nl/grootzakelijk/aansluitingen/tarieven2021/?ref=22608>
- Ligen, Y., Vrabel, H., & Girault, H. (2020). Energy efficient hydrogen drying and purification for fuel cell vehicles. *International Journal of Hydrogen Energy*, *45*(18), 10639–10647. doi: 10.1016/J.IJHYDENE.2020.02.035.
- Liu, X., Reddi, K., Elgowainy, A., Lohse-Busch, H., Wang, M., & Rustagi, N. (2020). Comparison of well-to-wheels energy use and emissions of a hydrogen fuel cell electric vehicle relative to a conventional gasoline-powered internal combustion engine vehicle. *International Journal of Hydrogen Energy*, *45*(1), 972–983. doi: 10.1016/j.ijhydene.2019.10.192.
- Lugo-Méndez, H., Lopez-Arenas, T., Torres-Aldaco, A., Torres-González, E. V., Sales-Cruz, M., & Lugo-Leyte, R. (2021). Interstage pressures of a multistage compressor with intercooling. *Entropy*, *23*(3), 1–14. doi: 10.3390/e23030351.
- Mair, G. W., Thomas, S., Schalaus, B., & Wang, B. (2021). Safety criteria for the transport of hydrogen in permanently mounted composite pressure vessels. *International Journal of Hydrogen Energy*, *46*(23), 12577–12593. doi: 10.1016/J.IJHYDENE.2020.07.268.
- Makridis (2016). Hydrogen storage and compression. *Methane and Hydrogen for Energy Storage*, (June), 1–28. doi: 10.1049/pbpo101e_c.h1.

- Marcinkoski, J., Vijayagopal, R., Kast, J., & Duran, A. (2016a). Driving an industry: Medium and heavy duty fuel cell electric truck component sizing. *World Electric Vehicle Journal*, 8(1), 78–89. doi: 10.3390/wevj8010078.
- Marcinkoski, J., Vijayagopal, R., Kast, J., & Duran, A. (2016b). Driving an industry: Medium and heavy duty fuel cell electric truck component sizing. *World Electric Vehicle Journal*, 8(1), 78–89. doi: 10.3390/wevj8010078.
- Mayyas, A., Ruth, M., Pivovar, B., Bender, G., Wipke, K., Mayyas, A., Ruth, M., Pivovar, B., Bender, G., & Wipke, K. (2019). Manufacturing Cost Analysis for Proton Exchange Membrane Water Electrolyzers. *National Renewable Energy Laboratory*, (August), 65.
URL <https://www.nrel.gov/docs/fy10osti/72740.pdf>.
- Meeus, L. (2020). *The evolution of electricity markets in Europe*. Edward Elgar Publishing.
- Mellein, B. R., Scurto, A. M., & Shiflett, M. B. (2021). Gas solubility in ionic liquids. *Current Opinion in Green and Sustainable Chemistry*, 28. doi: 10.1016/j.cogsc.2020.100425.
- Meszler, D., Delgado, O., Rodríguez, F., & Muncrief, R. (2018). EUROPEAN HEAVY-DUTY VEHICLES: COST-EFFECTIVENESS OF FUEL-EFFICIENCY TECHNOLOGIES FOR LONG-HAUL TRACTOR-TRAILERS IN THE 2025-2030 TIMEFRAME.
URL https://theicct.org/sites/default/files/publications/ICCT_EU-HDV-tech-2025-30_20180116.pdf
- Meyers, J., & Meneveau, C. (2012). Optimal turbine spacing in fully developed wind farm boundary layers. *Wind Energy*, 15, 305 – 317. doi: 10.1002/we.469.
- Miguel, N. D., Acosta, B., Commission, E., Moretto, P., & Commission, E. (2017). Analysis of out-of-spec events during refueling of on-board hydrogen tanks ANALYSIS OF OUT-OF-SPEC EVENTS DURING REFUELING OF ON-BOARD HYDROGEN TANKS. (January 2019).
- Millet, P., & Grigoriev, S. (2013). Water Electrolysis Technologies. *Renewable Hydrogen Technologies: Production, Purification, Storage, Applications and Safety*, (pp. 19–41). doi: 10.1016/B978-0-444-56352-1.00002-7.
- Ministerie I&W (2021). Europese overeenkomst voor het internationale vervoer van gevaarlijke goederen over de binnenwateren (ADN).
- Mrčela, I., Sumina, D., Sačić, F., & Bariša, T. (2016). A wind turbine two level back-to-back converter power loss study. (pp. 308–314). doi: 10.1109/EPEPEMC.2016.7752016.
- Mwanyika, H., & Kainkwa, R. (2009). Determination of the power law exponent for southern highlands of Tanzania. *Tanzania Journal of Science*, 32(1). doi: 10.4314/tjs.v32i1.18434.
- ”National Research Council and National Academy of Engineering” (2004). *The Hydrogen Economy: Opportunities, Costs, Barriers, and Ramp;D Needs*. Washington, DC: The National Academies Press.
- Navas-Anguita, Z., García-Gusano, D., & Iribarren, D. (2019). A review of techno-economic data for road transportation fuels. *Renewable and Sustainable Energy Reviews*, 112, 11–26. doi: 10.1016/J.RSER.2019.05.041.
- Netušil, M., & Additional, P. D. (2012). Natural Gas Dehydration - Chapter 1. *Natural Gas - Extraction to End Use*, (pp. 3–22).
- NHN (2021). Home – Noord-Hollandse Energie Noord.
URL <https://energieregionhnl.nl/>
- Niermann, M., Drü, S., Kaltschmitt, M., & Bonhoff, K. (2019). Liquid organic hydrogen carriers (LOHCs)- techno-economic analysis of LOHCs in a defined process chain †. *This journal is Cite this: Energy Environ. Sci*, 12, 290. doi: 10.1039/c8ee02700e.

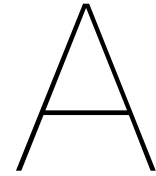
- Nistor, S., Dave, S., Fan, Z., & Sooriyabandara, M. (2016). Technical and economic analysis of hydrogen refuelling. *Applied Energy*, *167*, 211–220. doi: 10.1016/J.APENERGY.2015.10.094.
- NPROXX (2021). Hydrogen Storage for Filling Stations - NPROXX.
URL <https://www.nproxx.com/hydrogen-storage-transport/hydrogen-refuelling-stations/>
- Offer, G. J., Howey, D., Contestabile, M., Clague, R., & Brandon, N. P. (2010). Comparative analysis of battery electric, hydrogen fuel cell and hybrid vehicles in a future sustainable road transport system. *Energy Policy*, *38*(1), 24–29. doi: 10.1016/j.enpol.2009.08.040.
- Omrani, R., & Shabani, B. (2019). Review of gas diffusion layer for proton exchange membrane-based technologies with a focus on unitised regenerative fuel cells. *International Journal of Hydrogen Energy*, *44*(7), 3834–3860. doi: 10.1016/j.ijhydene.2018.12.120.
- Oostdam, M. (2019). Techno-economic assessment of hydrogen fuel-cell tractor semi-trailer: Exploratory research into the feasibility.
URL <https://repository.tudelft.nl/islandora/object/uuid:%7B3A1225ee00-7bb3-4628-8906-e988a4dde2b8>
- OSM (????).
- Parks, G., Boyd, R., Cornish, J., & Remick, R. (2014). Hydrogen Station Compression, Storage, and Dispensing Technical Status and Costs: Systems Integration. *Related Information: Independent review published for the U.S. Department of Energy Hydrogen and Fuel Cells Program*, (May), Medium: ED; Size: 74 pp.
URL <https://www.nrel.gov/docs/fy14osti/58564.pdf>
- Penev, M., Zuboy, J., & Hunter, C. (2019). Economic analysis of a high-pressure urban pipeline concept (HyLine) for delivering hydrogen to retail fueling stations. *Transportation Research Part D: Transport and Environment*, *77*, 92–105. doi: 10.1016/J.TRD.2019.10.005.
- Peschka, W. (2012). *Liquid hydrogen: fuel of the future*. Springer Science & Business Media.
- Petitpas, G., Simon, A. J., Moreno-Blanco, J., & Aceves, S. M. (2018). Liquid Hydrogen Infrastructure Analysis. Tech. rep.
- Pffafel, S., Faulstich, S., & Rohrig, K. (2017). Performance and Reliability of Wind Turbines: A Review. *Energies* *2017*, Vol. 10, Page 1904, *10*(11), 1904. doi: 10.3390/EN10111904.
- Pian, A., Verhoef, J., De Vries, L., & Gonzalez-Aparicio, I. (2021). TNO report 2021 R11177 Measuring and visualizing environmental and social impacts of wind energy projects.
- Platzer, M. F., & Sarigul-Klijn, N. (2021). Hydrogen Compression Technology. *SpringerBriefs in Applied Sciences and Technology*, (pp. 71–72). doi: 10.1007/978-3-030-58244-9_19.
- Pondera Consult (2019). ENERGY YIELD CALCULATION ECN TEST SITE RW05. Tech. rep.
- Pudukudy, M., Yaakob, Z., Mohammad, M., Narayanan, B., & Sopian, K. (2014). Renewable hydrogen economy in Asia – Opportunities and challenges: An overview. *Renewable and Sustainable Energy Reviews*, *30*, 743–757. doi: 10.1016/J.RSER.2013.11.015.
- PWN (????).
- Ratnakar, R. R., Dindoruk, B., & Harvey, A. (2020). Thermodynamic modeling of hydrogen-water system for high-pressure storage and mobility applications. *Journal of Natural Gas Science and Engineering*, *81*, 103463. doi: 10.1016/j.jngse.2020.103463.
- Ratnakar, R. R., Gupta, N., Zhang, K., van Doorne, C., Fesmire, J., Dindoruk, B., & Balakotaiah, V. (2021). Hydrogen supply chain and challenges in large-scale LH2 storage and transportation. *International Journal of Hydrogen Energy*. doi: 10.1016/j.ijhydene.2021.05.025.

- Reddi, K., Elgowainy, A., Rustagi, N., & Gupta, E. (2018). Techno-economic analysis of conventional and advanced high-pressure tube trailer configurations for compressed hydrogen gas transportation and refueling. *International Journal of Hydrogen Energy*, 43(9), 4428–4438. doi: 10.1016/j.ijhydene.2018.01.049.
- Renewable Energy Agency, I. (2012). RENEWABLE ENERGY TECHNOLOGIES: COST ANALYSIS SERIES Volume 1: Power Sector Acknowledgement.
URL www.irena.org/Publications
- Reuß, M., Grube, T., Robinius, M., & Stolten, D. (2019). A hydrogen supply chain with spatial resolution: Comparative analysis of infrastructure technologies in Germany. *Applied Energy*, 247, 438–453. doi: 10.1016/j.apenergy.2019.04.064.
- Röck, M., Martin, R., & Hausberger, S. (2020). *JEC Tank-To-Wheels report v5 : Heavy duty vehicles*.
- Rohatgi, A., & Northwest, P. (2015). III . 11 Investigation of H₂ Diaphragm Compressors to Enable Low-Cost Long-Life Operation. (pp. 53–56).
- Rothlauf, F. (2011). *Optimization Methods*, vol. 25. Springer, Berlin, Heidelberg.
- Rothuizen, E., Mérida, W., Rokni, M., & Wistoft-Ibsen, M. (2013). Optimization of hydrogen vehicle refueling via dynamic simulation. *International Journal of Hydrogen Energy*, 38(11), 4221–4231. doi: 10.1016/J.IJHYDENE.2013.01.161.
- Rothuizen, E., & Rokni, M. (2014). Optimization of the overall energy consumption in cascade fueling stations for hydrogen vehicles. *International Journal of Hydrogen Energy*, 39(1), 582–592. doi: 10.1016/J.IJHYDENE.2013.10.066.
- Ruuskanen, V., Koponen, J., Kosonen, A., Niemelä, M., Ahola, J., & Hämäläinen, A. (2020). Power quality and reactive power of water electrolyzers supplied with thyristor converters. *Journal of Power Sources*, 459, 228075. doi: 10.1016/J.JPOWSOUR.2020.228075.
- Saravanan, N., Nagarajan, G., Sanjay, G., Dhanasekaran, C., & Kalaiselvan, K. M. (2008). Combustion analysis on a DI diesel engine with hydrogen in dual fuel mode. *Fuel*, 87(17-18), 3591–3599. doi: 10.1016/j.fuel.2008.07.011.
- Scheepers, F., Stähler, M., Stähler, A., Rauls, E., Müller, M., Carmo, M., & Lehnert, W. (2020). Improving the efficiency of PEM electrolyzers through membrane-specific pressure optimization. *Energies*, 13(3). doi: 10.3390/en13030612.
- Schelbergen, M., Kalverla, P. C., Schmehl, R., & Watson, S. J. (2020). Clustering wind profile shapes to estimate airborne wind energy production. *Wind Energy Science*, 5(3), 1097–1120. doi: 10.5194/wes-5-1097-2020.
- Schmidt, O., Gambhir, A., Staffell, I., Hawkes, A., Nelson, J., & Few, S. (2017). Future cost and performance of water electrolysis: An expert elicitation study. *International Journal of Hydrogen Energy*, 42(52), 30470–30492. doi: 10.1016/J.IJHYDENE.2017.10.045.
- Scholman, R., & Scholman, A. J. O. S. (2020). Reportage new holland dual power. (p. 2020).
- Schoots, K., Ferioli, F., Kramer, G. J., & van der Zwaan, B. C. (2008). Learning curves for hydrogen production technology: An assessment of observed cost reductions. *International Journal of Hydrogen Energy*, 33(11), 2630–2645. doi: 10.1016/J.IJHYDENE.2008.03.011.
- Schwabe, P., Lensink, S., & Hand, M. (2011). Work Package 1 Final Report IEA Wind Task 26 Multi-national Case Study of the Financial Cost of Wind Energy.
URL <http://www.osti.gov/bridge>
- Scott, R. B., Denton, W. H., & Nicholls, C. M. (2013). *Technology and uses of liquid hydrogen*. Elsevier.
- Sdanghi, G., Maranzana, G., Celzard, A., & Fierro, V. (2019). Review of the current technologies and performances of hydrogen compression for stationary and automotive applications. *Renewable and Sustainable Energy Reviews*, 102, 150–170. doi: 10.1016/J.RSER.2018.11.028.

- Seo, S. K., Yun, D. Y., & Lee, C. J. (2020). Design and optimization of a hydrogen supply chain using a centralized storage model. *Applied Energy*, 262, 114452. doi: 10.1016/j.apenergy.2019.114452.
- Shakoor, R., Hassan, M. Y., Raheem, A., & Wu, Y. K. (2016). Wake effect modeling: A review of wind farm layout optimization using Jensen's model. *Renewable and Sustainable Energy Reviews*, 58, 1048–1059. doi: 10.1016/J.RSER.2015.12.229.
- Sheffield, J. W., Martin, K. B., & Folkson, R. (2014). Electricity and hydrogen as energy vectors for transportation vehicles. *Alternative Fuels and Advanced Vehicle Technologies for Improved Environmental Performance: Towards Zero Carbon Transportation*, (pp. 117–137). doi: 10.1533/9780857097422.1.117.
- Shiva Kumar, S., & Himabindu, V. (2019). Hydrogen production by PEM water electrolysis – A review. *Materials Science for Energy Technologies*, 2(3), 442–454. doi: 10.1016/J.MSET.2019.03.002.
- Silva, J., Ribeiro, C., & Guedes, R. (2007). Roughness length classification of corine land cover classes. *European Wind Energy Conference and Exhibition 2007, EWEC 2007*, 2(January 2007), 828–837.
- Simoes, S. G., Catarino, J., Picado, A., Lopes, T. F., di Bernardino, S., Amorim, F., Gírio, F., Rangel, C. M., & Ponce de Leão, T. (2021a). Water availability and water usage solutions for electrolysis in hydrogen production. *Journal of Cleaner Production*, 315, 128124. doi: 10.1016/J.JCLEPRO.2021.128124.
- Simoes, S. G., Catarino, J., Picado, A., Lopes, T. F., di Bernardino, S., Amorim, F., Gírio, F., Rangel, C. M., & Ponce de Leão, T. (2021b). Water availability and water usage solutions for electrolysis in hydrogen production. *Journal of Cleaner Production*, 315, 128124. doi: 10.1016/J.JCLEPRO.2021.128124.
- Staffell, I., Scamman, D., Abad, A. V., Balcombe, P., Dodds, P. E., Ekins, P., Shah, N., & Ward, K. R. (2019). The role of hydrogen and fuel cells in the global energy system. *Energy & Environmental Science*, 12(2), 463–491. doi: 10.1039/C8EE01157E.
- Stevens, R. J., Gayme, D. F., & Meneveau, C. (2016). Effects of turbine spacing on the power output of extended wind-farms. *Wind Energy*, 19(2), 359–370.
- Stevens, R. J. A. M. (2016). Dependence of optimal wind turbine spacing on wind farm length. *Wind Energy*, 19(4), 651–663. doi: 10.1002/WE.1857.
- Stöckl, F., Schill, W.-P., & Zerrahn, A. (2020). Green hydrogen: optimal supply chains and power sector benefits. Tech. rep.
URL www.diw.de/
- Stolten, D., & Emonts, B. (2016). *Hydrogen Science and Engineering, 2 Volume Set: Materials, Processes, Systems, and Technology*, vol. 1. John Wiley & Sons.
- Swider, D. J., Beurskens, L., Davidson, S., Twidell, J., Pyrko, J., Prügler, W., Auer, H., Vertin, K., & Skema, R. (2008). Conditions and costs for renewables electricity grid connection: Examples in europe. *Renewable Energy*, 33(8), 1832–1842. doi: <https://doi.org/10.1016/j.renene.2007.11.005>.
- Taherian-Fard, E., Sahebi, R., Niknam, T., Izadian, A., & Shasadeghi, M. (2020). Wind turbine drivetrain technologies. *IEEE Transactions on Industry Applications*, 56(2), 1729–1741. doi: 10.1109/TIA.2020.2966169.
- Taylor, M., Ralon, P., & Al-Zoghoul, S. (2020). Renewable Power Generation Costs in 2020. Tech. rep., IRENA.
URL https://www.irena.org/-/media/Files/IRENA/Agency/Publication/2021/Jun/IRENA_Power_Generation_Costs_2020.pdf
- Teichmann, D., Arlt, W., & Wasserscheid, P. (2012). Liquid Organic Hydrogen Carriers as an efficient vector for the transport and storage of renewable energy. *International Journal of Hydrogen Energy*, 37(23), 18118–18132. doi: 10.1016/J.IJHYDENE.2012.08.066.

- Teter, J., Tattini, J., & Petropoulos, A. (2020). Tracking transport 2020. <https://www.iea.org/reports/tracking-transport-2020>.
- The Linde Group (2010). Hydrogen Recovery by Pressure Swing Adsorption. *Engineering*, (pp. 4–8).
- The Linde Group (2020). Linde Ionic Compressor. *Linde Ionic Compressor*, (p. 1).
- Thomson, C., & Harrison, G. P. (2015). Life Cycle Costs and Carbon Emissions of Onshore Wind Power.
URL https://www.climateexchange.org.uk/media/1459/life_cycle_wind_-_executive_summary_.pdf
- Trinke, P., Bensmann, B., & Hanke-Rauschenbach, R. (2017). Current density effect on hydrogen permeation in PEM water electrolyzers. *International Journal of Hydrogen Energy*, 42(21), 14355–14366. doi: 10.1016/J.IJHYDENE.2017.03.231.
- Ursúa, A., Gandía, L. M., & Sanchis, P. (2012). Hydrogen production from water electrolysis: Current status and future trends. *Proceedings of the IEEE*, 100(2), 410–426. doi: 10.1109/JPROC.2011.2156750.
- U.S. DOE, O. o. E. E., & Energy, R. (2017). Energy Efficiency & Renewable Energy - Hydrogen storage (US DOE). *Office of Energy Efficiency and Renewable Energy U.S. Department of Energy*.
URL <https://www.energy.gov/sites/prod/files/2017/03/f34/fcto-h2-storage-fact-sheet.pdf>
- van Sloten, R., Fabius, B., & Aldenkamp, M. (2020). *Transitiestudie verduurzaming wegtransport Transitieonderzoek verduurzaming wegtransport*.
URL <https://open.overheid.nl/repository/ron1-12d8b63b-d93b-499c-b3b1-37e86dddce7c/1/pdf/bijlage-7-transitiestudie-verduurzaming-wegtransport.pdf>
- Veena, R., Manuel, S. M., Mathew, S., & Petra, M. I. (2020). Wake Induced Power Losses in Wind Farms. *International Journal of Engineering and Advanced Technology*, 9(3), 2175–2180. doi: 10.35940/ijeat.c5611.029320.
- Wang, A., Van der Leun, K., Peters, D., & Buseman, M. (2020). European Hydrogen Backbone. (July), 24.
URL https://gasforclimate2050.eu/wp-content/uploads/2020/07/2020_European-Hydrogen-Backbone_Report.pdf
- Werapun, W., Tirawanichakul, Y., & Waewsak, J. (2017). Wind Shear Coefficients and their Effect on Energy Production. *Energy Procedia*, 138, 1061–1066. doi: 10.1016/j.egypro.2017.10.111.
- Wiser, R., Bolinger, M., & Lantz, E. (2019). Assessing wind power operating costs in the United States: Results from a survey of wind industry experts. *Renewable Energy Focus*, 30(April), 46–57. doi: 10.1016/j.ref.2019.05.003.
- Witkowski, A., Rusin, A., Majkut, M., & Stolecka, K. (2017). Comprehensive analysis of hydrogen compression and pipeline transportation from thermodynamics and safety aspects. *Energy*, 141, 2508–2518. doi: 10.1016/J.ENERGY.2017.05.141.
- Wright, A. K., & Wood, D. H. (2004). The starting and low wind speed behaviour of a small horizontal axis wind turbine. *Journal of Wind Engineering and Industrial Aerodynamics*, 92(14-15), 1265–1279. doi: 10.1016/J.JWEIA.2004.08.003.
- Xu, C., Hao, C., Li, L., Han, X., Xue, F., Sun, M., & Shen, W. (2018). Evaluation of the power-law wind-speed extrapolation method with atmospheric stability classification methods for flows over different terrain types. *Applied Sciences (Switzerland)*, 8(9), 1–16. doi: 10.3390/app8091429.
- Yang, C., & Ogden, J. (2007). Determining the lowest-cost hydrogen delivery mode. *International Journal of Hydrogen Energy*, 32(2), 268–286. doi: 10.1016/J.IJHYDENE.2006.05.009.

- Yodwong, B., Guilbert, D., Phattanasak, M., Kaewmanee, W., Hinaje, M., & Vitale, G. (2020). AC-DC converters for electrolyzer applications: State of the art and future challenges. *Electronics (Switzerland)*, 9(6). doi: 10.3390/electronics9060912.
- Zauner, A., Böhm, H., Rosenfeld, D. C., & Tichler, R. (2019). Innovative large-scale energy storage technologies and Power-to-Gas concepts after optimization. D7.7 Analysis on future technology options and on techno-economic optimization. (691797), 1–89.
- Zeng, K., & Zhang, D. (2010). Recent progress in alkaline water electrolysis for hydrogen production and applications. *Progress in Energy and Combustion Science*, (3), 307–326. doi: 10.1016/j.pecs.2009.11.002.
- Zhang, J., Fisher, T. S., Ramachandran, P. V., Gore, J. P., & Mudawar, I. (2005). A review of heat transfer issues in hydrogen storage technologies.
- Zhao, Y., Mao, Y., Zhang, W., Tang, Y., & Wang, P. (2020). Reviews on the effects of contaminations and research methodologies for PEMFC. *International Journal of Hydrogen Energy*, 45(43), 23174–23200. doi: 10.1016/J.IJHYDENE.2020.06.145.



Appendix: Balance OF Plants PEM Elctrolyser

A.0.1. Electrolyser Balance of Plants

This Appendix discusses the PEM electrolyser system adopted in this research. The subsection reviews the balance of plant (BOP) and all necessary system components to obtain high-quality hydrogen for fuel cell applications. The PEM electrolyser production process is examined.

The balance of plant for a PEM electrolyser system is schematically shown in Figure A.1. Before the hydrogen is produced in the electrolyser stack, a few pre-processing steps are required. Two main feedstock components can be defined. The first feedstock component is the power input for the electrolysis process. The power is supplied directly from the wind turbine or the connection to the power grid. A DC power source is required for the electrolyser system, and an AC power supply is necessary for all BOP equipment and processes. The second feedstock can be defined as the water needed for the production of hydrogen.

A PEM electrolyser requires highly purified water to produce hydrogen. A water pre-treatment process purifies the tap water supplied to the system. An oxygen separator system removes the oxygen produced at the cathode of the electrolyser from the water stream outlet. In this research, no application for the produced oxygen is assumed. The water obtained after de gas/water separator is recirculated through a heat exchanger to remove the excess heat produced by the electrolysis process and de-ionised by an internal ion exchange membrane or EDI. As a result of gas crossover in the PEM electrolyser cells, saturation water and oxygen are removed from the downstream hydrogen outlet by drying and de-oxygen purification processes. These processes ensure the production of hydrogen with high purity levels.

An overview of all BOP system components:

- Water Pre-treatment System
- Electrolyser Stack
- Thermal Management
- Oxygen Purification
- Hydrogen Drying
- Power Electronics

Water treatment

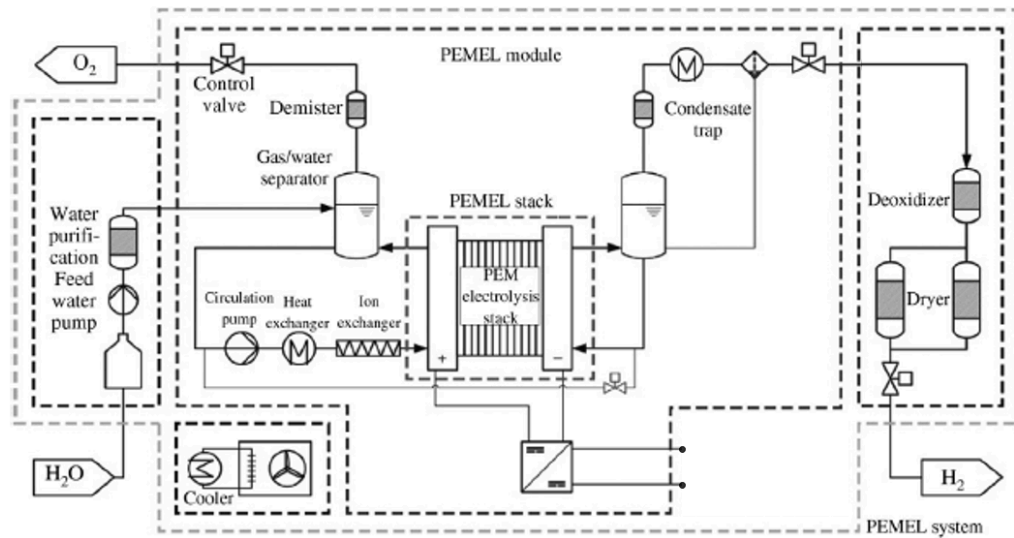


Figure A.1: Balance of plant components electrolyser (Millet & Grigoriev, 2013)

Water for electrolysis can be obtained from multiple sources. Simoes et al. (2021b) has researched treatment processes necessary for different water sources. The water used in the electrolyser starts with the collection process and defining the origin of the water source, which determines the transport of water to the production site, the necessity of water storage, the water treatment processes and the method of disposal of the waste product from the water treatment process. Two water treatment steps can be identified when considering hydrogen production in the wind-based value chain. The first step is necessary when considering offshore wind turbines. Salinated water is obtained from the sea, and a desalination process is necessary to convert the salinated water into drinking water. The second step is to transform the drinking water into ultrapure water, ready to be used in the electrolyser. In this research, the last purification step from drinking water to ultrapure water is required as an onshore wind turbine is considered.

Due to the availability of an adequate water supply network with drinking water quality, no transportation or storage is needed. Purifying water before using it in the electrolysis process is crucial. Impurities in un-purified water can be built up and deposited on the electrode surfaces, preventing ions from permeating the membrane. A result is that the efficiency and lifetime of the electrolyser stack is reduced (Zeng & Zhang, 2010). The electrolyser manufacturer defines the purity of the water required. Either Type I or Type II water is required (Khan et al., 2021). Type I and Type II water define a classification of water purity established by the American Society for Testing and Materials (ASTM, 2021). Type I water is considered as Ultra-Pure Water (UPW). The different types of water classes are defined by the level of conductivity expressed in $[\frac{\mu S}{cm}]$, Resistivity $[M\Omega \cdot cm]$, Total Organic Carbon (TOC) in parts per billion (ppb) or maximum ionic concentrations of certain materials in $[\frac{\mu g}{L}]$. An overview of the different water classes defined by ASTM is shown in Table A.1.

Water type	Conductivity $[\frac{\mu S}{cm}]$	Resistivity $[M\Omega \cdot cm]$	PH	Total Organic Carbon $[\frac{\mu g}{L}]$	Sodium $[\frac{\mu g}{L}]$	Chloride $[\frac{\mu g}{L}]$	Silica $[\frac{\mu g}{L}]$
Type I	<0.056	>18	-	50	1	1	3
Type II	<1	>1.0	-	50	5	5	3
Type III	<0.25	>4.0	-	200	10	10	500
Type IV	<5	>0.2	5.0-8.0	-	50	50	-

Table A.1: Water purification classes defined by the American Society for Testing and Materials (ELGA)

Production of UPW can be defined as a three-stage process. The first process is the pre-treatment process. The pre-treatment process ensures the removal of all solids in the water supply. The second stage is the make-up stage which ensures the removal of salts, organics, fine particles, bacteria and colloidal materials from the water supply. The final stage consists of the polishing stage, which ensures purification up to the desired type I or types II purity level defined by the electrolyser manufacturer (Lee et al., 2016).

To obtain UPW from drinking water, multiple purification processes can be adopted. General purification processes are UV disinfection, ozonation, Membrane technologies, ion exchange filters and electrode ionisation (Ahmad & Azam, 2019). The first two technologies are mainly used to disinfect water of microbes and organic materials and are not suitable to extract materials from the water. Reverse osmosis and membrane distillation are technologies based on a semi-permeable membrane and often applied to salinated water. Ion exchange filter and electrode de-ionisation (EDI) focus on extracting impurities present as ions in the water. Reverse osmosis or membrane distillation is often combined with either ion exchange filters or EDI to obtain high water purities required for the electrolysis process (Khan et al., 2021).

Ordinary filters conduct the removal of solids from the water supply. The second step in water purification is performed by reverse osmosis or membrane distillation. Reverse osmosis is a pressure difference process that forces water under high pressure to diffuse through a membrane. The purpose of reverse osmosis is mainly to remove salts, organics, fine particles, bacteria and colloidal materials (Lee et al., 2016). Pure water molecules can pass the semi-permeable membrane. To be able to purify the water, pressure has to be larger than the osmotic pressure to allow the concentrated water to flow through the semi-permeable membrane (Ahmad & Azam, 2019). The semi-permeable membrane extracts all unwanted impurities from the water, which results in the reject flow. The water flow behind the membrane is permeated. The efficiency of reverse osmosis depends mainly on the water flux and the ability to eliminate salt from the water stream. Reverse osmosis processes can remove up to 99% of the salts from the water (Ahmad & Azam, 2019).

With the process of membrane distillation, salted water is directly in contact with a microporous hydrophobic membrane. A temperature gradient creates a pressure difference between the two sides of the hydrophobic membrane. The pressure difference is the driving force of mass transfer through the membrane. Only water vapour molecules can cross the membrane as the liquid cannot pass through the hydrophobic material. As a result, water vapour condensates on the permeate side of the membrane (Abdelrasoul, 2020). The temperature of the electrolysis process can be used to create the temperature gradient between the membrane and improve the efficiency of the water purification process.

The reverse osmosis process and membrane distillation technologies can supply the core of the water purification process. The final purification step consists of an ion exchange filter or EDI (Khan et al., 2021). Both the ion exchange filter and the EDI work on the principle of ion exchange absorption. An ion exchange filter is generally built up of a fixed-bed polymer membrane containing ion-exchange resins. The ion-exchange resin is an insoluble material that can replace ions present in the water flow with the ions attached to the ion resins. Contaminates present in the water flow are removed in the water stream by placing them on the resin (Khan et al., 2021). The ion exchange process is called de-ionisation. Cations (positively charged ions) in the water flow are interchanged with a hydrogen ion. Anions (negatively charged ions) are interchanged with a hydroxyl ion. The ions in the water stream that are replaced with the hydroxyl and hydrogen ions are recombined to form a water molecule, purifying the water flowing through the ion exchange filter. Two main categories of ion exchange membranes exist. There are acidic cationic resins and anionic base resins. The cationic resins are used to remove positively charged ions from the water flow, whereas anionic resins are used to remove negatively charged ions from the water flow. The cathodic and anoxic resins are separately packed in exchange beds or mixed bed ion exchangers. The ions must be regenerated for both types of ion exchange filters if all hydroxyl and hydrogen ions are replaced with toxic ions.

EDI is a process that combines the previously discussed processes of ion exchange resins from the

ion exchange filter and ion exchange membranes used in electrodialysis. In between electrodes, an anion and cation membrane is placed. Through the middle of the EDI, a compartment is filled with ion exchange resins and reinforce the removal of cations and anions from the unpurified water flow under direct current (Arar et al., 2014). Similar to ion exchange filters, different configurations are available. Either the ion-exchange resins are mixed or in separate sections of the filter. The particular property of the exchange membrane and the direction of the electrical potential gradient results in a purified water flow and a flow with the ion concentration. The ionic resins supply ionic conductivity, which makes the purification process possible. Due to the applied current, the EDI can regenerate, and therefore continuous operation can be adopted. A typical EDI consumes 0.2-3.0 kWh per 4000 litres of water (Arar et al., 2014).

Oxygen separation

The production of hydrogen-oxygen is considered a by-product. When utilising the fundamental equation of water splitting, 1 mole of oxygen is produced for every two moles of water. Per kg H₂ produced, 8 kg of O₂ is generated. The oxygen produced at the electrolyser stack is present in the internal water circuit of the electrolyser system. An oxygen separator removes the oxygen from the water outlet stream of the electrolyser stack. Oxygen is an industrial feedstock used at various processes such as blast furnaces, electric furnaces and glass melting (Kato et al., 2005). Oxygen can therefore be sold and create a revenue stream to reduce the total value chain operating cost. To positively impact the value chain, the economic potential of the oxygen produced as a by-product must outweigh the additional cost factors of the oxygen storage and transportation system. The possible added economic potential of the oxygen produced at the hydrogen production site based on wind energy is outside the scope of this study, and no application for the produced oxygen is assumed.

Stack Operation

An PEM electrolyser stack is built up from multiple PEM electrolyser cells. The composition of a PEM electrolyser stack is shown in Figure A.2. Multiple MEA's are stacked and separated by bipolar separator plates. The bipolar separator plates transport the reactants and products of the electrolysis process from and to the electrolyser cells. Electro technically, the PEM electrolyser cells are connected in series. The total voltage of the electrolyser stack is therefore proportional to the number of stacked electrolyser cells. The electrolyser system is held together with two pressure endplates. An electrolyser stack can either be built as a single stack or on a modular basis. In the case of a single stack, the electrolyser cells are stacked until the desired power capacity for the electrolyser is reached. A modular design adopts a different approach. The modular stack design consists of multiple stacks, each producing a part of the desired electrolyser system size. When considering the option for a single stack or multi-stack system design, several criteria must be considered based on the application of the electrolyser system. The first criteria will be if the ability of continuous operation during maintenance is required. The second criteria are the electrolyser flexibility properties. Thirdly, packaging considerations and, finally, a cost comparison between the two system designs for the specific application. Stolten & Emonts (2016).

The polarisation curve of a single PEM electrolyser cell is shown in Figure A.3. The polarisation curve shows the cell voltage as a function of the applied current density during the operation of the electrolyser. The current density of the electrolyser system is proportional to the power input (Scheepers et al., 2020). The activation losses dominate the efficiency loss in the system for low current densities. For mid-range current densities, ohmic losses are dominant. As for higher current densities, losses are dominated by mass transportation losses (Emile et al., 2018). The electrolyser stack voltage is the sum of the PEM cells stacked together in series.

The electrolyser stack efficiency is dependent on the current density applied and the stack voltage operating level. The thermodynamic efficiency is determined by the amount of power used to generate heat and not hydrogen. The heat production is generated by the overpotential in the electrolysis process and is a function of the current density as can be seen in Figure A.3. The cell potential increases as the current density increases. More heat is generated if a higher current density is applied

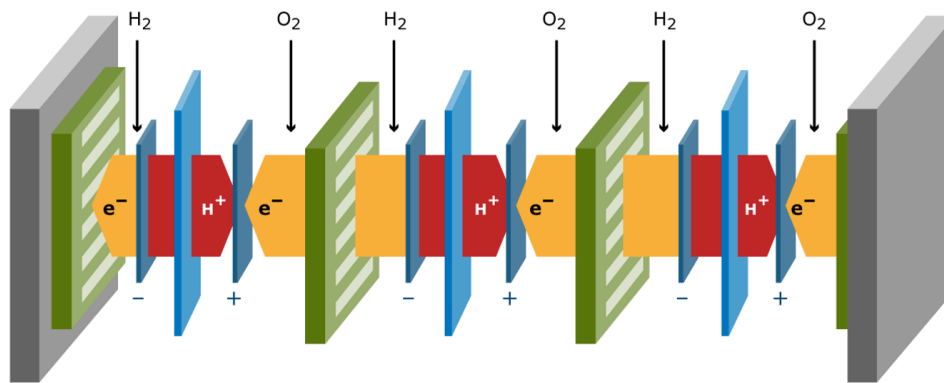


Figure A.2: Composition PEM electrolyser stack

to the electrolyser unit due to increased losses in the electrolysis process. Increased heat production results in lower system efficiency. Higher current densities applied to an electrolyser stack, therefore, reduce the overall system efficiency. To optimise the efficiency of an electrolyser system, a large stack size can be chosen to increase the active surface area of the electrolyser and reduce the total current density during operation. However, the increase of system size results in total electrolyser and BOP system costs increase. An economic optimum is present between the power supply connection size and the electrolyser stack size. Not only does the efficiency of the electrolyser increase, but also the lifetime and efficiency degradation. The two latter are proportional to the current density applied to the electrolyser (Zauner et al., 2019). All parameters that have to be taken into account for the economic optimisation of an electrolyser system are

- System cost components (CAPEX/OPEX)
- Electrolyzer efficiency
- Electrolyzer lifetime
- Efficiency degradation
- Standby power consumption
- Power supply characteristics

Hydrogen purification

The water electrolysis process releases hydrogen at 99.99% purity. The International Organization for Standardization (ISO) released in 2012 a standard for hydrogen purity requirements for the fuel cell application in the mobility sector. Similar to ISO the Society for Automotive Engineers (SAE) released a similar classification in 2015. China adopted the GB/T 37244-2011 qualification for PEM fuel cells. This made a distinction in Pure Hydrogen, High-Pure Hydrogen and Ultrapure hydrogen. However, it did not include all fuel cell performance-limiting qualification measurements. Therefore, In 2018 China altered the GB/T 37244 standard and created the GB/T 37244-2018 standard specifically for fuel cell vehicle applications (Du et al., 2021). An overview of the measured components and the requirements is shown in Table A.2.

Hydrogen fuel cells are dominant in the vehicle industry due to their high power density, low-temperature operation and compact cell structure (Du et al., 2021). High-quality H_2 is required for fuel cell application. It is dependent on the manufacturer which standard is adopted. However, when the highest purity classes are considered, the hydrogen produced with the PEM electrolyser need additional purification steps to obtain 99.999% and 99.9999% hydrogen purity.

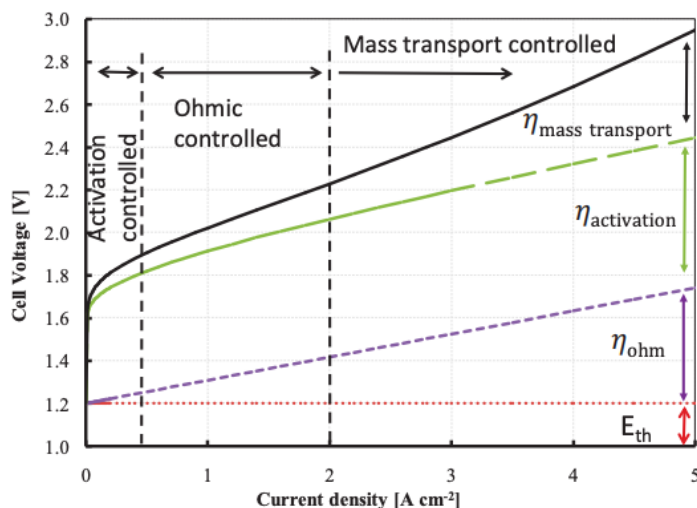


Figure A.3: Polarization curve single PEM electrolysis cell Emile et al. (2018)

Component	GB / T 3634.2-2011			ISO 14687-2:2012	ISO 14687:2019
	Pure H ₂	High Pure H ₂	Ultrapure H ₂	SAE J2719-201511	SAE J2719-202003
H ₂ Purity	99.99%	99.999%	99.9999%	99.97% GB/T 37244-2018	99.97%
Total non-hydrogen gases	-	10 ppm	1 ppm	300 ppm	300 ppm
H ₂ O	10 ppm	3 ppm	0.5 ppm	5 ppm	5 ppm
Total HC	-	-	-	2 ppm	-
Non-methane HC	-	-	-	-	2 ppm
Methane	10 ppm	1 ppm	0.2 ppm	-	100 ppm
O ₂	5 ppm	1 ppm	0.2 ppm	5 ppm	5 ppm
He	-	-	-	300 ppm	300 ppm
N ₂ and Ar	-	-	-	100 ppm	-
N ₂	60 ppm	5 ppm	0.4 ppm	-	300 ppm
Ar	-	-	0.2 ppm	-	300 ppm
CO ₂	5 ppm	1 ppm	0.1 ppm	2 ppm	2 ppm
CO	5 ppm	1 ppm	0.1 ppm	0.2 ppm	0.2 ppm
H ₂ S	-	-	-	0.004 ppm	0.004 ppm
HCHO	-	-	-	0.001 ppm	0.001 ppm
HCOOH	-	-	-	0.2 ppm	0.2 ppm
NH ₃	-	-	-	0.1 ppm	0.1 ppm
Total halide	-	-	-	0.05 ppm	0.05
Maximum particular concentration	-	-	-	1 mg/kg	mg/kg

Table A.2: Hydrogen Purity requirements according to the ISO 14687-2:2012, ISO 14687:2019, SAE J2719-201511, SAE J2719-202003 and the GB/T 3634-2011 and GB/T 37244.2-2018 (Du et al., 2021)

The two main components of impurities in the electrolyser outlet stream are O₂ and H₂O (Bessarabov & Millet, 2018) when considering ultrapure water feed stream to the PEM electrolyser. The gas impurities in the outlet stream are a result of the gas crossover process. The gas crossover process is the permeation of water and oxygen across the membrane of the electrolyser. The three processes determining the amount of gas crossover are diffusion due to concentration gradient, diffusion due to pressure gradient and permeation due to water drag with dissolved hydrogen (Stolten & Emonts,

2016). The processes are dependent on temperature, pressure and membrane thickness. Thicker membranes lead to lower hydrogen production efficiency and higher overpotential due to lower ionic conductivity. Lower temperatures lead to a lower efficiency and a higher pressure gradient leads to more gas cross over. (Stolten & Emonts, 2016).

The hydrogen purification methods can be classified into two categories, physical and chemical purification methods. The first category includes adsorption methods, low-temperature separation methods and membrane separation. The chemical category consists of hydroxide separation and catalysts applications (Du et al., 2021). Oxygen present in the hydrogen gas mixture is typically removed with catalytic recombination of hydrogen and oxygen according to reaction Equation A.1. Oxygen recombination is applied before the hydrogen drying process as the recombination produces water Ligen et al. (2020). Catalytic recombination is an exothermic reaction; however, temperatures are limited due to the low oxygen concentration in the hydrogen stream. No extra cooling process is required. hydrogen losses by the catalytic recombination are around 0.6-0.8% (Ligen et al., 2020).



The hydrogen gas with water impurities outlet is called humid hydrogen (Stolten & Emonts, 2016). The hydrogen gas contains water vapour that must be removed to obtain a high enough hydrogen gas purity. The gas mixture can be described by the law of an ideal humid gas. Water needs to be removed from the hydrogen gas as it can result in a reduction in proton membrane conductivity for the fuel cell and have corrosive effects on the metal parts of the value chains system components (Du et al., 2021) such as compression modules and the transportation methods. In cold temperatures freezing of water can damage pipes and valves (Staffell et al., 2019). Humid hydrogen is treated by condensing the water at reduced temperature, pressure swing adsorption or temperature swing adsorption. To reach ISO standards f hydrogen less than 55 ppm may be present in the H₂ gas.

Pressure swing adsorption utilises high pressure to remove the water impurities from the hydrogen gas. Impure hydrogen is compressed in an adsorption tank where an adsorption material adsorbs the water from the hydrogen gas mixture. The purified hydrogen gas mixture is released and results in the high purity end product. The release of the H₂ gas from the adsorption tank reduces the overall internal pressure. At reduced pressure, the adsorption material regenerates by releasing the water. The water is removed from the tank, whereafter the process repeats itself, and unpurified hydrogen is added to the regenerated adsorption tank. Adsorbents used often include zeolite molecular sieves, activated carbon, activated alumina, and silica gel (Du et al., 2021). The typical pressure range for hydrogen adsorption is between 10 and 40 bar, and regeneration occurs at pressure levels slightly above atmospheric pressure (The Linde Group, 2010). TSA works according to the same principle as the PSA but utilises temperature to adsorb the water from the impure hydrogen gas. The water is adsorbed at low temperatures by the adsorbent material, and the adsorption material is regenerated at high temperatures. The temperature range for the hydrogen purification process utilising TSA is in between ambient temperatures and 200-300 C° for regeneration of the adsorbent material (Ligen et al., 2020).

Two main parameters define the total operation efficiency of the PSA and TSA processes. The recovery rate defines the amount of hydrogen obtained after the PSA or TSA about the amount provided to the drying process. The second parameter is the energy consumption of the PSA and TSA processes. Different PSA and TSA technologies and process steps obtain a recovery rate between 70% and 99%. The highest recovery rates are reached with vacuum aided pressure swing adsorption (Du et al., 2021). Figure A.4 and Figure A.5 show schematic representations of the swing adsorption processes.

Thermal management

Heat is generated by multiple sources in the electrolyser production plant. The first heat source is the heat generated by the overpotential applied in the electrolyser stack. The heat from the electrolysis process is dissipated by the excessive water flow on the cathode side. An internal heat management

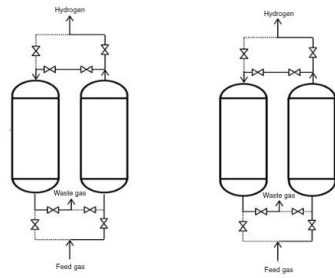


Figure A.4: Schematic configuration of pressure swing adsorption process

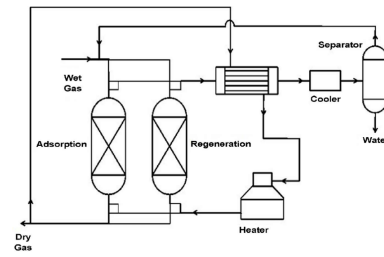


Figure A.5: Schematic configuration of temperature swing adsorption process (Netušil & Additional, 2012)

system reduces the water temperature from the water flow of the electrolyser water outlet. The water needs to be cooled as the internal purification process conducted by the ion exchange filter of EDI often have limited thermal stability, and the water temperature is reduced to a temperature of less than 60°C (Bessarabov & Millet, 2018).

The second heat source in the hydrogen electrolysis plant is the catalytic recombination of oxygen and water in the purification process of hydrogen. The amount of heat produced at this stage in the electrolyser plant is, however, negligible, and no thermal management system is required to maintain temperatures below safe operating conditions.

Power electronics

The power electronics of the hydrogen production plant is defined by the input power connection size and type. In the wind-based value chain, A power transformer converts the voltage level from a medium-voltage range to a low voltage range adjusted for the electrolyser stack operating voltage. The AC power supplied and reduced by the step-down transformer is used to power AI BOP processes and equipment. An active rectifier chops the AC power supply into the DC to be used for the electrolysis process. The amount of energy required for a kg of H₂ is equal to 4.2-5.5 kwh/kg H₂ (Schmidt et al., 2017).

A few important characteristics should be considered considering the adequate power conversion technology for the electrolyser system in combination with the type of power source. According to (Kasem Alaboudy et al., 2013) the most important factors for choosing the right power electronic conversion equipment are:

- Ability to deliver either direct or indirect controlled current to the electrolyser to manage the hydrogen flow rate and electrolyser operating efficiency
- Supply a high enough power quality for efficient electrolyser operation
- AC power supply must meet international quality standards
- Obtain a high-power electronic conversion efficiency
- High system reliability to prevent conversion component failures
- Low cost of the overall power electronic system

For AC-DC rectifiers, two types of conversion technologies can be distinguished. The first technology is the use of thyristor-based rectifiers. The second category is diode-based rectifiers in combination with DC-DC choppers. The thyristor-based rectifiers allow a more accurate current control as a result of the working principle of the rectifier. The control of the rectifier is based on the firing angle. The firing angle is defined as the angle between the start of the diode's forward bias and when the thyristor obtains a pulse. The adoption of control via firing angle for the rectifier leads to increased current harmonics and reactive power production (Yodwong et al., 2020). Consequently, the total power factor of the rectifier is lowered. The electrolysers operate at a high current compared to voltage also, the hydrogen flow rate is proportional to the current applied to the electrolyser stacks. The high current

harmonics caused by the thyristors result in extra losses in the electrolyser cells (Ruuskanen et al., 2020). A solution to the decreased power factor by the current harmonics is passive or active filters. The AC-DC rectifier in combination with a DC-DC chopper allows an increase in power factor without the use of passive filters and makes it a more cost-effective solution (Yodwong et al., 2020). For PEM electrolysers in a low to medium voltage range, AC-DC rectifiers with a DC-DC chopper are most suitable, whereas thyristors converters are applied to high voltage alkaline electrolysers (Yodwong et al., 2020).

A distinction can be made between active and passive front end conversion technology. Both diode and thyristor conversion technologies cannot actively switch on and off the current. The rectifiers conversion processes are based on the grid frequency. The rectifiers are therefore uncontrolled. With the application of an uncontrolled rectifier, a DC-DC converter is added to control the voltage of the electrolyser stacks and therefore, indirectly the input current of the electrolyser. When incorporating an active rectifier, the diodes are replaced with actively controlled switches. The actively controlled switches can reduce the harmonic distortion in the power source, thereby increasing the overall power factor and conversion efficiency. A second advantage is that using an active front end rectifier reduces the need for a heavy grid filter and therefore reduces the overall footprint and cost of the power electronic system. An actively front end controlled power electronics conversion system is a preferred implementation for the PEM electrolyser to maximise conversion efficiency and reduce the economic footprint of the power electronics system. The topology, connection type and size for the wind-based value chain is discussed in chapter 3.

B

Appendix: Model Overview

This appendix displays an overview of the objective function and all constraints considered in the optimisation model.

B.1. Objective function

$$\min_{Q_{Hydrogen,pt}, Q_{skhdt}, x_{ijkht}} \left(\sum_{t \in \mathbf{T}} \sum_{p \in \mathbf{P}} -E_{Grid,pt} \cdot C_{GridEnergy,pt} \cdot C_{Imbalance,pt} \right) \quad (\text{B.1a})$$

$$Storage_{max} \cdot CAPEX_{MEGC} + \quad (\text{B.1b})$$

$$\sum_{(i,j) \in \mathbf{E}} \sum_{k \in \mathbf{K}} \sum_{h \in \mathbf{H}} \sum_{t \in \mathbf{T}} c_{ij} \cdot x_{ijkht} + \sum_{k \in \mathbf{K}} \sum_{h \in \mathbf{H}} \sum_{t \in \mathbf{T}} Ht_{kht} \cdot Wage_{Driver} \quad (\text{B.1c})$$

B.2. Constraints

$$E_{Grid,pt} = E_{WT,pt} - E_{Hydrogen,pt} - E_{Curtailment,pt} \quad \forall p, \quad \forall t \quad (\text{B.2})$$

$$E_{Hydrogen,pt} = f(Q_{Hydrogen,pt}) \quad \forall p, \quad \forall t \quad (\text{B.3})$$

$$E_{Grid,pt} \leq Z_{Grid,pt} \cdot BigM \quad \forall p, \quad \forall t \quad (\text{B.4})$$

$$E_{Grid,pt} \geq (Z_{Grid,pt} - 1) \cdot BigM \quad \forall p, \quad \forall t \quad (\text{B.5})$$

$$C_{Imbalance,pt} = 1 - (Z_{Grid,pt} \cdot (1 - Factor_{Imbalance})) \quad \forall p, \quad \forall t \quad (\text{B.6})$$

$$Q_{Hydrogen,pt} \geq Z_{PEM,pt} \quad \forall p, \quad \forall t \quad (\text{B.7})$$

$$Q_{Hydrogen,pt} \leq Z_{PEM,pt} \cdot BigM \quad \forall p, \quad \forall t \quad (\text{B.8})$$

$$Q_{Hydrogen,pt} \leq Q_{HydrogenMax} \quad \forall p, \quad \forall t \quad (\text{B.9})$$

$$E_{Hydrogen,pt} \leq E_{HydrogenMax} \quad \forall p, \quad \forall t \quad (\text{B.10})$$

$$E_{Grid,pt} \geq -E_{GridCapacity} \quad \forall p, \quad \forall t \quad (\text{B.11})$$

$$E_{Grid,pt} \leq E_{GridCapacity} \quad \forall p, \quad \forall t \quad (\text{B.12})$$

$$I_{start,h} + Q_{Hydrogen,pt} = \sum_{s \in \mathbf{S}} \sum_{k \in \mathbf{K}} \sum_{d \in \mathbf{D}} Q_{skhdt} \cdot MEGC_{kg,d} + d_{FCET,ht} + d_{DF,ht} + I_{ht} \quad \forall h, t = t_{start}, p = h \quad (\text{B.13})$$

$$I_{ht-1} + Q_{Hydrogen,pt} = \sum_{s \in \mathbf{S}} \sum_{k \in \mathbf{K}} \sum_{d \in \mathbf{D}} Q_{skhdt} \cdot MEGC_{kg,d} + d_{FCET,ht} + d_{DF,ht} + I_{ht} \quad \forall h, \forall t \neq t_{start}, p = h \quad (\text{B.14})$$

$$I_{start,s} + \sum_{s \in \mathbf{S}} \sum_{k \in \mathbf{K}} \sum_{d \in \mathbf{D}} Q_{skhdt} \cdot MEGC_{kg,d} = d_{FCET,st} + d_{DF,st} + I_{st} \quad \forall s, t = t_{start} \quad (\text{B.15})$$

$$I_{st-1} + \sum_{s \in \mathbf{S}} \sum_{k \in \mathbf{K}} \sum_{d \in \mathbf{D}} Q_{skhdt} \cdot MEGC_{kg,d} = d_{FCET,st} + d_{DF,st} + I_{st} \quad \forall s, \forall t \neq t_{start} \quad (\text{B.16})$$

$$I_{ht} \geq Inventory_{Continuity} \cdot (Demand_{HRS} + \left(\frac{|\mathbf{S}|}{|\mathbf{P}|}\right) \cdot Demand_{HRS}) \quad \forall h, t = t_{end} \quad (\text{B.17})$$

$$I_{st} \geq Inventory_{Continuity} \cdot Demand_{HRS} \quad \forall s, t = t_{end} \quad (\text{B.18})$$

$$Inventory_{Hub,t} = \sum_{h \in \mathbf{H}} \frac{I_{ht}}{Payload_{MEGC}} \quad \forall t \quad (\text{B.19})$$

$$Inventory_{Sat,t} = \sum_{s \in \mathbf{S}} \frac{I_{st}}{Payload_{MEGC}} \quad \forall t \quad (\text{B.20})$$

$$Inventory_{Transit,t} = \sum_{s \in \mathbf{S}} \sum_{k \in \mathbf{K}} \sum_{h \in \mathbf{H}} \sum_{d \in \mathbf{D}} \frac{Q_{skhdt} \cdot MEGC_{kg,d}}{Payload_{MEGC}} \quad \forall t \quad (\text{B.21})$$

$$Storage_{Max} \geq Inventory_{Hub,t} + Inventory_{Sat,t} + Inventory_{Transit,t} \quad \forall t \quad (\text{B.22})$$

$$\sum_{s \in \mathbf{S}} \sum_{k \in \mathbf{K}} \sum_{d \in \mathbf{D}} Q_{skhdt} \leq I_{start,h} \quad \forall h, t = t_{start} \quad (\text{B.23})$$

$$\sum_{s \in \mathbf{S}} \sum_{k \in \mathbf{K}} \sum_{d \in \mathbf{D}} Q_{skhdt} \leq I_{Hub,ht-1} \quad \forall h, t \neq t_{start} \quad (\text{B.24})$$

$$\sum_{k \in \mathbf{K}} \sum_{d \in \mathbf{D}} Q_{skhdt} \leq 1 \quad \forall s, \forall h, \forall t \quad (\text{B.25})$$

$$\sum_{d \in \mathbf{D}} Q_{skhdt} \cdot MEGC_{kg,d} \leq Z_{skht} \quad \forall s, \forall k, \forall h, \forall t \quad (\text{B.26})$$

$$\sum_{s \in \mathbf{S}} \sum_{d \in \mathbf{D}} Q_{skhdt} \cdot MEGC_{kg,d} \geq Z_{kht} \quad \forall h, \forall t \quad (\text{B.27})$$

$$\sum_{h \in \mathbf{H}} Z_{kht} \leq 1 \quad \forall k, \forall t \quad (\text{B.28})$$

$$\sum_{k \in \mathbf{K}} \sum_{h \in \mathbf{H}} Z_{skht} \leq 1 \quad \forall s, \forall t \quad (\text{B.29})$$

$$\sum_{j \in I:(j,i) \in \mathbf{E}} x_{ijkht} + \sum_{j \in I:(i,j) \in \mathbf{E}} x_{ijkht} = 2 \cdot Z_{skht} \quad \forall s, \forall k, \forall h, \forall t \quad (\text{B.30})$$

$$\sum_{i,j \in \mathbf{E}} x_{ijkht} \leq |\mathbf{E}| - 1 \quad \forall \mathbf{E} \subset \mathbf{V} : 2 \leq |\mathbf{E}| \leq |\mathbf{V}|, \forall k, \forall h, \forall t \quad (\text{B.31})$$

$$\text{Transport}_{time,kht} = \sum_{(i,j) \in \mathbf{E}} x_{ijkht} \cdot \text{Duration}_{travel,ij} \quad \forall k, \forall h, \forall t \quad (\text{B.32})$$

$$\text{Handling}_{time,kht} = \sum_{s \in \mathbf{S}} \sum_{d \in \mathbf{D}} \frac{Q_{skhdt} \cdot \text{MEGC}_{kg,d}}{\text{Payload}_{MEGC}} \cdot Ht_{unit,sat} + Z_{khth} \cdot Ht_{unit,hub} \quad \forall s, \forall k, \forall h, \forall t \quad (\text{B.33})$$

$$\text{Operational}_{time,kht} = \text{Handling}_{time,kht} + \text{Transport}_{time,kht} \quad \forall k, \forall h, \forall t \quad (\text{B.34})$$

$$\text{Operational}_{time,kht} \leq Z_{Busy,kt} \cdot \text{BigM} \quad \forall k, \forall h, \forall t \quad (\text{B.35})$$

$$Z_{Busy,kht} \leq \text{Operational}_{time,kht} \quad \forall k, \forall h, \forall t \quad (\text{B.36})$$

$$\sum_{d \in \mathbf{D}} Q_{skhdt} \leq \text{BigM} \cdot (1 - Z_{Busy,kt-1}) \quad \forall s, \forall k, \forall h, \forall t \quad (\text{B.37})$$

$$I_{MEGC,d} \in \{0, \dots, N_{TrailerMax} \cdot \text{Payload}_{MEGC} \cdot (1 - \text{BackhaulFactor})\} \quad (\text{B.38})$$

$$C_{Imbalance,pt} = [0, 1] \quad \forall p, \quad \forall t \quad (\text{B.39})$$

$$Z_{PEM,pt} \in \{0, 1\} \quad \forall p, \quad \forall t \quad (\text{B.40})$$

$$Z_{Grid,pt} \in \{0, 1\} \quad \forall p, \quad \forall t \quad (\text{B.41})$$

$$Q_{skhdt} \in \{0, 1\} \quad \forall s, \forall k, \forall h, \forall d, \forall t \quad (\text{B.42})$$

$$Z_{skht} \in \{0, 1\} \quad \forall s, \forall k, \forall h, \forall t \quad (\text{B.43})$$

$$Z_{khth} \in \{0, 1\} \quad \forall k, \forall h, \forall t \quad (\text{B.44})$$

$$Z_{Busy,kt} \in \{0, 1\} \quad \forall k, \forall t \quad (\text{B.45})$$

$$Q_{Hydrogen,pt} \geq 0 \quad \forall p, \quad \forall t \quad (\text{B.46})$$

$$E_{Hydrogen,pt} \geq 0 \quad \forall p, \quad \forall t \quad (\text{B.47})$$

$$E_{Curtailment,pt} \geq 0 \quad \forall p, \quad \forall t \quad (\text{B.48})$$

$$I_{ht} \geq 0 \quad \forall h, \forall t \quad (\text{B.49})$$

$$I_{st} \geq 0 \quad \forall s, \forall t \quad (\text{B.50})$$

$$\text{Inventory}_{Hub,t} \geq 0 \quad \forall t \quad (\text{B.51})$$

$$\text{Inventory}_{Sat,t} \geq 0 \quad \forall t \quad (\text{B.52})$$

$$\text{Inventory}_{Transit,t} \geq 0 \quad \forall t \quad (\text{B.53})$$

$$I_{Hub,ht} \geq 0 \quad \forall h, \forall t \quad (\text{B.54})$$

$$\text{Transport}_{time,kht} \geq 0 \quad \forall k, \forall h, \forall t \quad (\text{B.55})$$

$$\text{Handling}_{time,kht} \geq 0 \quad \forall k, \forall h, \forall t \quad (\text{B.56})$$

$$\text{Operational}_{time,kht} \geq 0 \quad \forall k, \forall h, \forall t \quad (\text{B.57})$$

B.3. Total Cost Function

$$TC_{system} = TC_{ProdLoc} + TC_{HRS} + TC_{Distribution} + TC_{Storage} \quad (B.58)$$

$$\begin{aligned}
TC_{ProdLoc} = & \sum_{p \in \mathbf{P}} \left(\frac{CAPEX_{WT}}{a_{WT}} + \frac{CAPEX_{PEM}}{a_{PEM}} + \frac{CAPEX_{Stacks}}{a_{Stacks}} + \frac{CAPEX_{Grid}}{a_{Grid}} + \frac{CAPEX_{Comp}}{a_{Comp}} \right. \\
& + OPEX_{Fixed,WT} + OPEX_{Fixed,PEM} + OPEX_{Fixed,Grid} + OPEX_{Fixed,Comp} \\
& + Distance_{Pipeline} \cdot \left(\frac{CAPEX_{Pipeline}}{a_{Pipeline}} + OPEX_{Fixed,Pipeline} \right) \\
& + \sum_{p \in \mathbf{P}} \sum_{t \in \mathbf{T}} (-E_{Grid,pt} \cdot C_{GridEnergy,t} \cdot C_{Imbalance,pt}) \\
& \left. + \sum_{p \in \mathbf{P}} \sum_{t \in \mathbf{T}} Z_{pem,tp} \cdot E_{Comp} \cdot E_{EnergyHRS} \right) \quad (B.59)
\end{aligned}$$

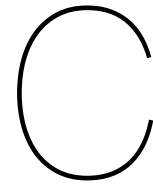
$$\begin{aligned}
TC_{HRS} = & \sum_{h \in \mathbf{H}} \frac{CAPEX_{Hub}}{a_{Hub}} + OPEX_{FixedHub} \\
& + \sum_{h \in \mathbf{H}} \sum_{t \in \mathbf{T}} (d_{FCET,ht} + d_{DF,ht}) \cdot E_{dispenser} \cdot E_{EnergyHRS} \\
& + \sum_{s \in \mathbf{S}} \frac{CAPEX_{Sat}}{a_{Sat}} + OPEX_{FixedSat} \\
& + \sum_{s \in \mathbf{S}} \sum_{t \in \mathbf{T}} d_{FCET,st} + d_{DF,st}) \cdot E_{dispenser} \cdot C_{EnergyHRS} \quad (B.60)
\end{aligned}$$

$$c_{ij} = Transport_{time,ij} \cdot C_{Driver} + Transport_{Fuel,ij} \cdot C_{Fuel} \quad (B.61)$$

$$\begin{aligned}
TC_{transport} = & \sum_{i,j \in \mathbf{E}} \sum_{k \in \mathbf{K}} \sum_{h \in \mathbf{H}} \sum_{t \in \mathbf{T}} c_{ij} \cdot x_{ijkht} \\
& + \sum_{k \in \mathbf{K}} \sum_{h \in \mathbf{H}} \sum_{t \in \mathbf{T}} Ht_{kht} \cdot C_{Driver} \quad (B.62) \\
& + \sum_{k \in \mathbf{K}} \left(\frac{CAPEX_{vehicle}}{a_{vehicle}} + \frac{CAPEX_{trailer}}{a_{trailer}} + OPEX_{Fixed,vehicle} + OPEX_{Fixed,trailer} \right)
\end{aligned}$$

$$TC_{inventory} = Storage_{Max} \cdot \left(\frac{CAPEX_{MEGC}}{a_{MEGC}} + OPEX_{Fixed,MEGC} \right) \quad (B.63)$$

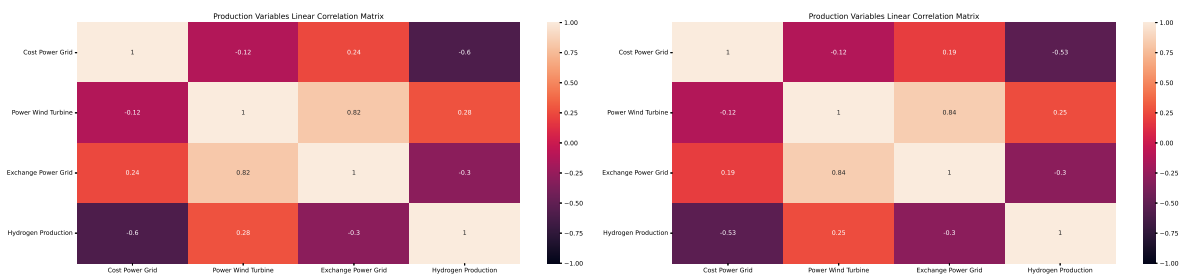
$$LCOH_{system} = \frac{TC_{ProdLoc} + TC_{HRS} + TC_{Distribution} + TC_{Storage}}{\sum_{h \in \mathbf{H}} \sum_{t \in \mathbf{T}} (d_{FCET,ht} + d_{DF,ht}) + \sum_{s \in \mathbf{S}} \sum_{t \in \mathbf{T}} (d_{FCET,st} + d_{DF,st})} \quad (B.64)$$



Appendix: Correlations Matrices

This appendix contains the linear correlation matrices for all four base scenarios discussed in chapter 5.

Correlation matrices scenario 1: One turbine, one hub station, one satellite station. Average daily station demand is equal to 350 kg

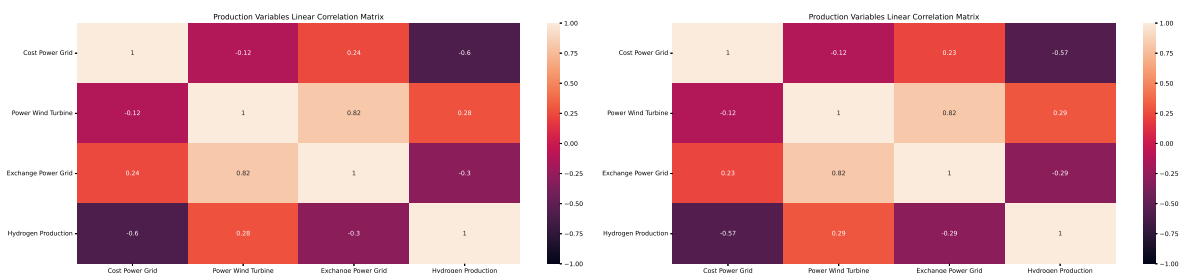


(a) Correlation matrix MEGC 20ft Scenario 1

(b) Correlation matrix MEGC 20ft Scenario 1

Figure C.1: Correlation matrices scenario 1, MEGC 20ft & HPSC

Correlation matrices scenario 2: One turbine, single hub station, three satellite stations. Average daily station demand is equal to 175 kg

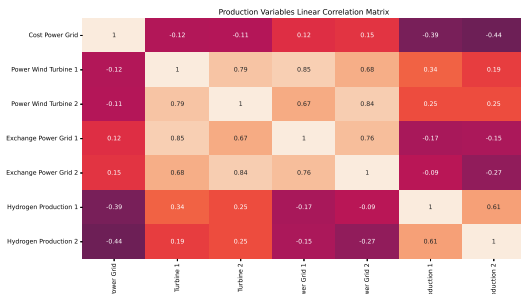


(a) Correlation matrix MEGC 20ft Scenario 2

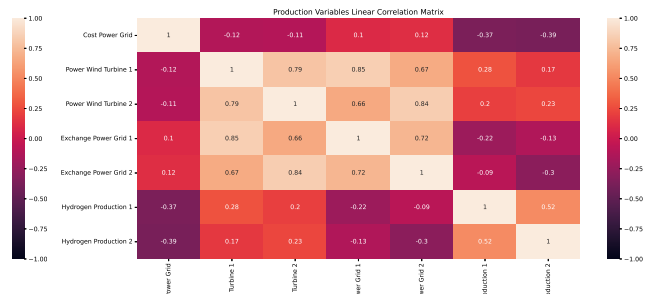
(b) Correlation matrix MEGC 20ft Scenario 2

Figure C.2: Correlation matrices scenario 2, MEGC 20ft & HPSC

Correlation matrices scenario 3: Two turbines, two hub stations, two satellite station. Average daily station demand is equal to 175 kg



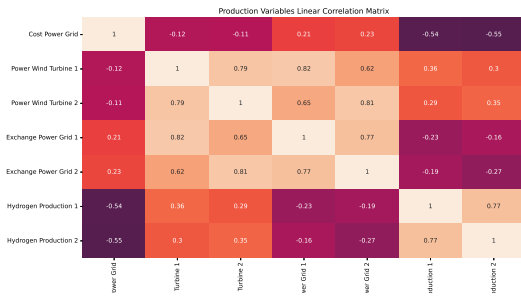
(a) Correlation matrix MEGC 20ft Scenario 3



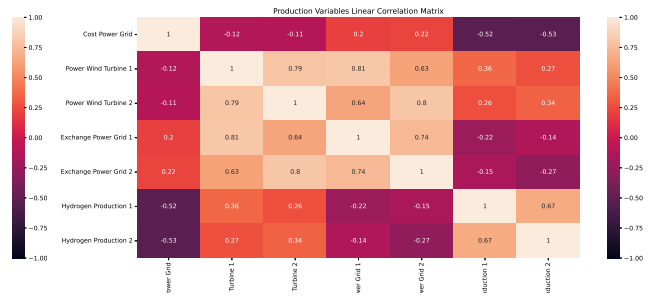
(b) Correlation matrix MEGC 20ft Scenario 3

Figure C.3: Correlation matrices scenario 3, MEGC 20ft & HPSC

Correlation matrices scenario 4: Two turbines, two hub station, two satellite station. Average daily station demand is equal to 262.5 kg



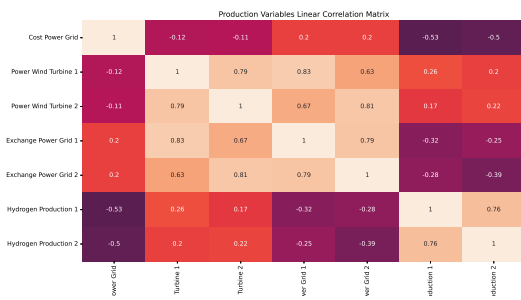
(a) Correlation matrix MEGC 20ft Scenario 4



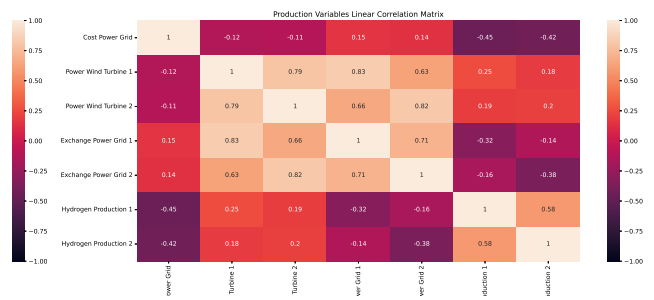
(b) Correlation matrix MEGC 20ft Scenario 4

Figure C.4: Correlation matrices scenario 4, MEGC 20ft & HPSC

Correlation matrices scenario 5: Two turbines, two hub station, two satellite station. Average daily station demand is equal to 350 kg

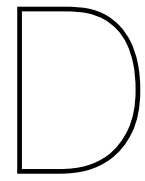


(a) Correlation matrix MEGC 20ft Scenario 5



(b) Correlation matrix MEGC 20ft Scenario 5

Figure C.5: Correlation matrices scenario 5, MEGC 20ft & HPSC



Appendix: Detailed Cost Overview Base Scenarios

Parameter	Scenario 1				Scenario 2				Scenario 3				Scenario 4				Scenario 5			
	MEGC 2011		HFSC		MEGC 2011		HFSC		MEGC 2011		HFSC		MEGC 2011		HFSC		MEGC 2011		HFSC	
	Total Annual Cost [€]	LCOH [$\frac{€}{MWh}$]	Total Annual Cost [€]	LCOH [$\frac{€}{MWh}$]	Total Annual Cost [€]	LCOH [$\frac{€}{MWh}$]	Total Annual Cost [€]	LCOH [$\frac{€}{MWh}$]	Total Annual Cost [€]	LCOH [$\frac{€}{MWh}$]	Total Annual Cost [€]	LCOH [$\frac{€}{MWh}$]	Total Annual Cost [€]	LCOH [$\frac{€}{MWh}$]	Total Annual Cost [€]	LCOH [$\frac{€}{MWh}$]	Total Annual Cost [€]	LCOH [$\frac{€}{MWh}$]	Total Annual Cost [€]	LCOH [$\frac{€}{MWh}$]
Wind Turbine	385,497	1.53	385,497	1.53	385,497	1.53	385,497	1.53	385,497	1.53	385,497	1.53	385,497	1.53	385,497	1.53	385,497	1.53	385,497	1.53
PEM	173,635	0.69	173,635	0.69	173,635	0.69	173,635	0.69	173,635	0.69	173,635	0.69	173,635	0.69	173,635	0.69	173,635	0.69	173,635	0.69
PEM Stacks	137,597	0.55	137,597	0.55	137,597	0.55	137,597	0.55	137,597	0.55	137,597	0.55	137,597	0.55	137,597	0.55	137,597	0.55	137,597	0.55
Pipeline	36,790	0.15	36,790	0.15	36,790	0.15	36,790	0.15	36,790	0.15	36,790	0.15	36,790	0.15	36,790	0.15	36,790	0.15	36,790	0.15
Compression	159,837	0.60	159,837	0.60	159,837	0.60	159,837	0.60	159,837	0.60	159,837	0.60	159,837	0.60	159,837	0.60	159,837	0.60	159,837	0.60
Grid Connection	35,093	0.14	35,093	0.14	35,093	0.14	35,093	0.14	35,093	0.14	35,093	0.14	35,093	0.14	35,093	0.14	35,093	0.14	35,093	0.14
Cell/Revenue Grid	46,821	-0.27	46,821	-0.27	46,821	-0.27	46,821	-0.27	46,821	-0.27	46,821	-0.27	46,821	-0.27	46,821	-0.27	46,821	-0.27	46,821	-0.27
Storage	240,670	0.95	240,670	0.95	240,670	0.95	240,670	0.95	240,670	0.95	240,670	0.95	240,670	0.95	240,670	0.95	240,670	0.95	240,670	0.95
Transport	98,697	0.39	98,697	0.39	98,697	0.39	98,697	0.39	98,697	0.39	98,697	0.39	98,697	0.39	98,697	0.39	98,697	0.39	98,697	0.39
Refueling Stations	236,981	0.94	236,982	0.94	236,982	0.94	236,982	0.94	236,982	0.94	236,982	0.94	236,982	0.94	236,982	0.94	236,982	0.94	236,982	0.94
Total	1,494,185	5.88	1,555,263	6.16	1,696,123	6.92	1,740,107	6.92	1,897,444	8.5	2,054,457	8.5	2,197,744	8.5	2,354,659	8.5	2,501,766	8.5	2,674,426	8.5

Table D.1: Total annual cost and contribution to LCOH for every value chain component